Conference Proceedings of the Society for Experimental Mechanics Series

Steven Mates
Veronica Eliasson
Paul Allison *Editors*

# Dynamic Behavior of Materials, Volume 1

## Proceedings of the 2022 Annual Conference on Experimental and Applied Mechanics

SEM

Springer

# Conference Proceedings of the Society for Experimental Mechanics Series

**Series Editors**

Kristin B. Zimmerman
Society for Experimental Mechanics, Inc.,
Bethel, CT, USA

The Conference Proceedings of the Society for Experimental Mechanics Series presents early findings and case studies from a wide range of fundamental and applied work across the broad range of fields that comprise Experimental Mechanics. Series volumes follow the principle tracks or focus topics featured in each of the Society's two annual conferences: IMAC, A Conference and Exposition on Structural Dynamics, and the Society's Annual Conference & Exposition and will address critical areas of interest to researchers and design engineers working in all areas of Structural Dynamics, Solid Mechanics and Materials Research.

Steven Mates • Veronica Eliasson • Paul Allison
Editors

# Dynamic Behavior of Materials, Volume 1

## Proceedings of the 2022 Annual Conference on Experimental and Applied Mechanics

Springer

*Editors*
Steven Mates
Division, MS 8553
NIST/Material Science and Engineering
Gaithersburg, MD, USA

Veronica Eliasson
Mines Mechanical Engineering
Golden, CO, USA

Paul Allison
Baylor University
Waco, TX, USA

ISSN 2191-5644 ISSN 2191-5652 (electronic)
Conference Proceedings of the Society for Experimental Mechanics Series
ISBN 978-3-031-17452-0 ISBN 978-3-031-17453-7 (eBook)
https://doi.org/10.1007/978-3-031-17453-7



This Springer imprint is published by the registered company Springer Nature Switzerland AG
The registered company address is: Gewerbestrasse 11, 6330 Cham, Switzerland

# Preface

*Dynamic Behavior of Materials* represents one of six volumes of technical papers to be presented at the 2022 SEM Annual Conference & Exposition on Experimental and Applied Mechanics organized by the Society for Experimental Mechanics scheduled to be held June 13–16, 2022. The complete proceedings also include volumes on: *Challenges in Mechanics of Time-Dependent Materials & Mechanics of Biological Systems and Materials*; *Fracture, Fatigue, Failure and Damage Evolution*; *Advancements in Optical Methods, Digital Image Correlation & Micro- and Nanomechanics*; *Mechanics of Composite, Hybrid & Multifunctional Materials*; *and Thermomechanics & Infrared Imaging, Inverse Problem Methodologies and Mechanics of Additive & Advanced Manufactured Materials.*

Each collection presents early findings from experimental and computational investigations on an important area within Experimental Mechanics. Dynamic Behavior of Materials is one of these areas.

The Dynamic Behavior of Materials track was initiated in 2005 and reflects our efforts to bring together researchers interested in the dynamic behavior of materials and structures and to provide a forum to facilitate technical interaction and exchange. Over the years, this track has been representing the ever-growing interests in dynamic behavior to the SEM community, working toward expanding synergy with other tracks and topics, and improving diversity and inclusivity, as evidenced by the increasing number and diversity of papers and attendance.

The contributed papers span numerous technical divisions within SEM, demonstrating its relevance not only in the dynamic behavior of materials community but also in the mechanics of materials community as a whole. The track organizers thank the authors, presenters, organizers, and session chairs for their participation, support, and contribution to this track. The SEM support staff is also acknowledged for their devoted efforts in accommodating the large number of paper submissions making this year's Dynamic Behavior of Materials Track a success.

Gaithersburg, MD, USA — Steven Mates
Golden, CO, USA — Veronica Eliasson
Waco, TX, USA — Paul Allison

# Contents

# Chapter 1
# A Novel Millipede Wave Guide, aka One-Mile SHPB in One-Foot

**Wil Whittington, Trey Leonard, and Ghatu Subhash**

**Abstract** Engineering equipment that uses the principles of longitudinal stress wave propagation often utilizes long slender rods to accommodate long-duration stress pulses. Such designs demand larger footprint and higher cost of infrastructure. To remedy this situation, a revolutionary and innovative design concept called "millipede bar" or "stress waveguide" is being proposed. The concept is introduced in this chapter with preliminary results.

**Keywords** Millipede bar · Stress waveguide · SHPB · 1D stress wave propagation · Impedance matching

## 1.1 Introduction

Many impact machines are comprised of series and parallel components that guide axial and torsional stress waves along straight bars and tubes, called mechanical or stress waveguides. Although these machines can take many forms and range in sizes from meters to hundreds of meters, the basic premise of the operation in these machines is common to each operation with a series of steps: (1) impact from an energy source, (2) stress wave propagation, (3) stress wave transmission, and (4) and energy dissipation into a material or component. Some practical examples include drilling equipment, split Hopkinson pressure bar, jackhammer, etc. [1–3].

Mechanical waveguides (e.g., incident bars, anvils, horns) used in impact are typically made of elastic materials that behave according to well-established stress wave propagation equations developed over the past century [4, 5]. Fundamental relationships regarding stress wave speed and impedance in these waveguides govern much of the wave propagation behavior with strain rate-dependent mechanical properties used to describe the overall durability or strength. While there are many wave modes that can be excited (e.g., bending or Rayleigh waves), impact machines are typically restricted to waves that travel axially along bars (e.g., uniaxial, torsional) for large loads and velocities, constant wave propagation speeds, and low losses. For several applications, the waveguides are designed up to hundreds of meters in length in order to produce the required loading durations [3, 6, 7]; recently, significant strides in folded waveguides, known as "serpentine" and "millipede" bars, have been developed for coaxial and planar waveguides, respectively [8]. Two examples are shown in Fig. 1.1.

Although great strides have been made to guide longitudinal waves in bars, there has been little advancement in generating and manipulating these waves. The current state of the art in stress wave generation is divided into two areas: direct impact and shaped impact. Figure 1.2 illustrates the two scenarios.

Pulse shaping is typically performed either by a nonuniform or mismatched impedance striker and incident bars or by parasitic materials known as "pulse shapers" or "cushions." [9–12]. In either case, the stress wave is shaped into a longer pulse length with a longer rise-time and reduced maximum characteristic frequencies. In the case of nonuniform bar ends or impedances, a significant limitation in maximum load and total energy transfer is apparent, due to reduced contact area and wave reflections, respectively [9]. Alternatively, parasitic pulse shapers require parasitic energy losses to shape pulses via viscoelastic and/or plastic deformation in the shaper materials [9, 12]. Furthermore, significant challenges exist in the usefulness of pulse shaper techniques due to the strong nonlinear dependence on load, velocity,

W. Whittington · T. Leonard
Department of Mechanical Engineering, Mississippi State University, Starkville, MS, USA
e-mail: whittington@me.msstate.edu; ryl4@msstate.edu

G. Subhash (✉)
Mechanical and Aerospace Engineering, University of Florida, Gainesville, FL, USA
e-mail: subhash@ufl.edu



S. Mates et al. (eds.), *Dynamic Behavior of Materials, Volume 1*, Conference Proceedings of the Society for Experimental Mechanics Series, https://doi.org/10.1007/978-3-031-17453-7_1

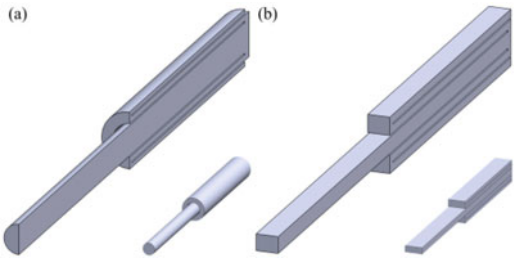


**Fig. 1.1** Examples of (**a**) coaxial and (**b**) planar mechanical waveguide [8]

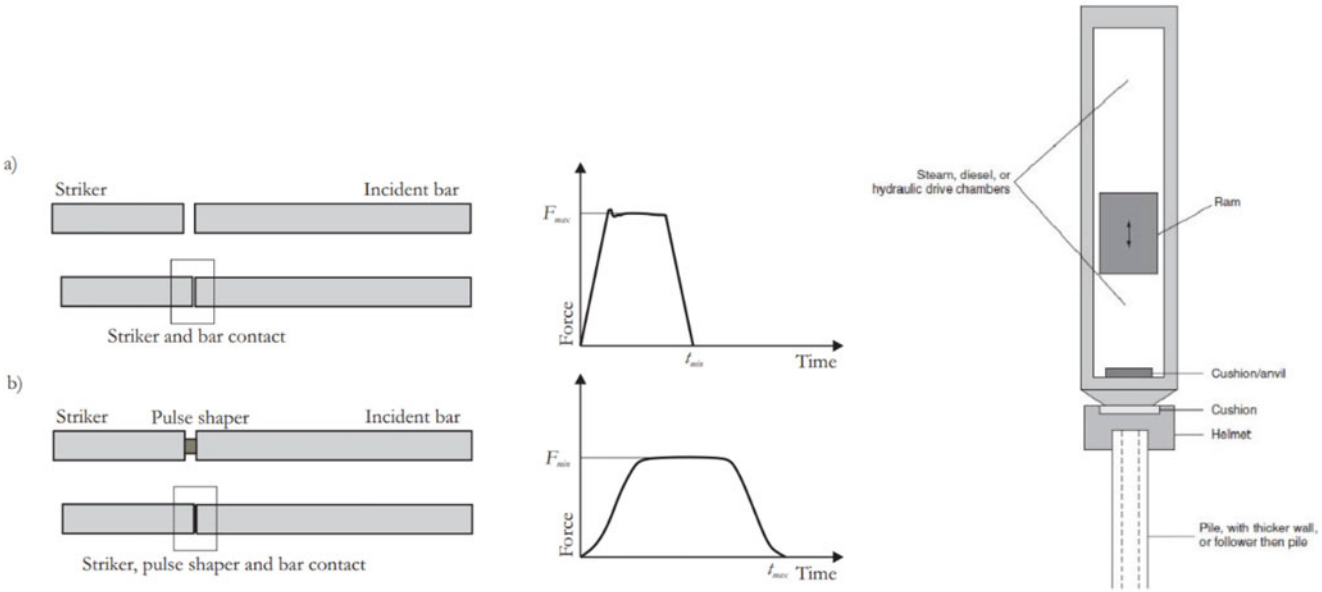


**Fig. 1.2** Contact force in (**a**) "severe" striker-bar impact, (**b**) striker-shaper-bar impact. Example of a pulse shaping "cushion" located in a pile driving hammer used in bridge construction [9, 10]

and bar geometries [12]. Finally, both methods do not allow for stress wave shaping that reduces the pulse length to achieve larger amplitudes and/or shorter rise times. To date, no significant strategy has been proposed to overcome these limitations.

In this study, we propose a millipede-striker bar configuration that overcomes many of the challenges in state-of-the-art pulse shaping with additional benefits, including selectable pulse shapes, digital signaling, pulse amplification, and pulse timing. These exciting opportunities are afforded using the new flexibility offered by folded waveguide techniques and striker bar selection. With this new impact bar configuration, the design space of pulses used in impact is increased and offers many benefits to the world of impact devices and tools.

### *1.1.1 Millipede Bar Principle of Operation*

The design of a planar "millipede bar" waveguide is based on the principle of a waveguide with constant impedance. The bar consists of one primary rod at the center and the desired number of parallel secondary rods extending in either two or three dimensions. The cross-sectional area of each secondary rod is half that of the primary rod. A schematic of a typical bar design is shown in Fig. 1.3 with one central primary rod and four secondary rods on either side. The central rod has a free end (called impact end) on one side where the impact by a striker bar occurs, and on the other side, it branches into two secondary rods that run parallel on either side. These two rods have equal cross-sectional areas (or impedances), but each is half that of the primary rod. The rods are connected at the alternate ends, and this assembly has a width the same as the width of the rod, as shown in the figure. This design feature not only allows smooth transfer of stress waves from the central rod to the two parallel secondary rods without any wave reflection, but it also provides momentum balance that may occur at this end during the wave transfer from the primary rod to the secondary rods. The dimensions of all other connection points are kept the same.

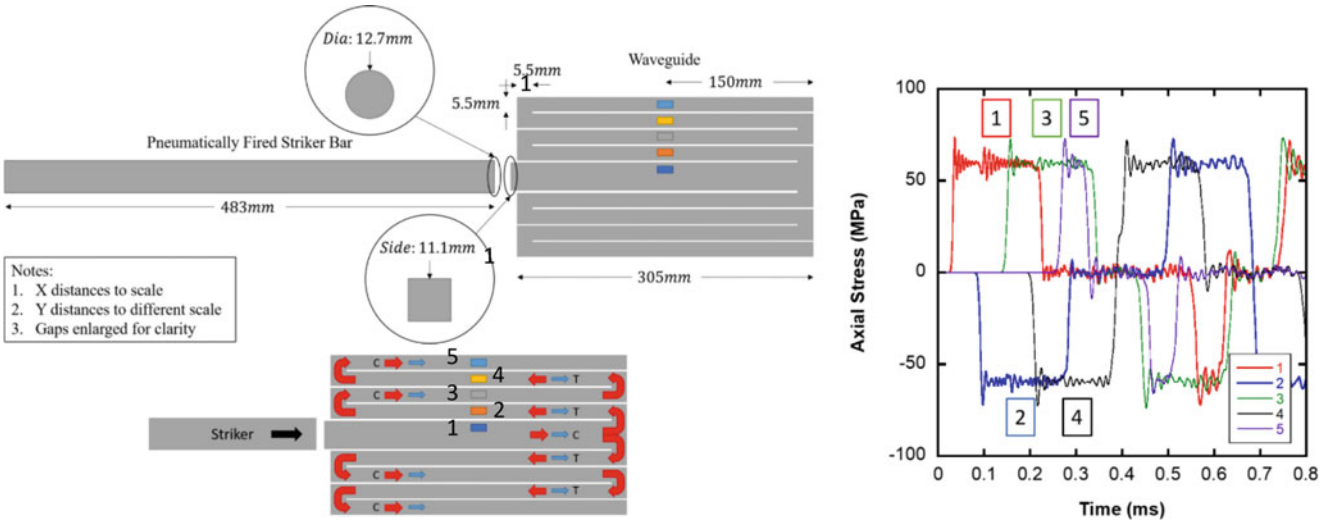


**Fig. 1.3** Millipede bar schematic and the measured wave profiles at the midpoints of rod segments

Preliminary finite element analysis with boundary conditions that prohibit lateral motion of the rods has shown that longitudinal stress wave propagation through the millipede bar is possible without significant dispersion, as shown in the wave profiles measured at the center of the primary and secondary rods (designated as 1,2. . .5) is also shown in Fig. 1.3. One may wonder if such a phenomenon can be extended to tens of such rods arranged in a similar fashion, thus giving rise to a stress wave of several milliseconds duration in a compact three-dimensional space.

## 1.2 Discusion and Conclusions

While the preliminary finite element analysis shows promise for this millipede bar concept, numerous practical issues need to be addressed to make this concept practically viable. Some critical questions that need to be addressed are: How small the gap between the rod segments must be for effective stress transfer from one bar to the next? How to experimentally implement the boundary conditions used in FE simulations? What are the practical limitations on the dimensions of the bar and the longitudinal stress pulse duration for effective functioning of the millipede bar? From a fundamental scientific perspective, why does a stress wave flow through the bend rather than reflect back into the same rod? What is the mechanism that governs this behavior? It is crucial to find answers to these questions to make this concept a reality.

## References

1. Scaccabarozzi, D., Saggin, B.: Measurement of stress waves propagation in percussive drilling. Sensors. **21**, 3677 (2021)
2. Albertini, C., Cadoni, E., Labibes, K.: Precision measurements of vehicle crashworthiness by means of a large Hopkinson bar. J. Phys. IV France. **7**, C3, C3-79-C3-84 (1997)
3. Gilat, A., Seidt, J.D., Matrka, T.A., Gardner, K.A.: A new device for tensile and compressive testing at intermediate strain rates. Exp. Mech. **59**(5), 725–731 (2019)
4. Kolsky, H.: LXXI. The propagation of stress pulses in viscoelastic solids. Philos. Mag. **1**(8), 693–710 (1956)
5. Davies, P.R.M.: Stress waves in solids. Br. J. Appl. Phys. **7**(6), 203–209 (1956)
6. Frank, R., Goble, R.: Wave Mechanics and the Wave Equation. Pile Driving Contractors Association (2000)
7. Albertini, C., Cadoni, E., Labibes, K.: Precision measurements of vehicle crashworthiness by means of a large Hopkinson bar. J. Phys. IV France. **07, C3**, C3-79-C3-84 (1997)
8. Leonard III, R., Luskin, L., Zhang, L., Jinkerson, J., Morse, J., Horstemeyer, M., El Kadiri, H., Rhee, H., Loukus, J., Whittington, W.: Design considerations for joining of tubular members subjected to impact loading. J. Adv. Join. Process. **3** (2021)
9. Baranowski, P., Janiszewski, J., Malachowski, J.: Study on computational methods applied to modelling of pulse shaper in split-Hopkinson bar. Arch. Mech. **66**(6), 429–452 (2014)
10. Take, W.A., Valsangkar, A.J., Randolph, M.F.: Analytical solution for pile hammer impact. Comput. Geotech. **25**(2), 57–74 (1999)
11. Chung, J., Wallerand, R., Hélias-Brault, M.: Pile fatigue assessment during driving. Proc. Eng. **66**, 451–463 (2013)
12. Chen, W., Bo, S.: Split Hopkinson (Kolsky) Bar: Design, Testing and Applications. Springer, New York (2010)

# Chapter 2
# Dynamic Compressive Behavior and Deformation Mechanisms of 3D-Printed Hierarchical Reentrant Honeycomb


**Chi Zhan, Mingzhe Li, and Weiyi Lu**

**Abstract** Hierarchical reentrant honeycombs (H-ReHs) with a 2nd order triangular hierarchy, an emerging type of lightweight but robust structures, have exhibited prominent energy absorption performance under quasi-static compression. However, due to the structural strain rate effect as well as the viscoelastic nature of the printing material, the crushing behavior of H-ReHs under the dynamic loading condition could be completely different from the quasi-static scenario. Therefore, it is necessary to investigate the crushing behavior of H-ReHs under dynamic impacts, the real loading condition in crashworthiness applications. In this study, the dynamic responses of H-ReHs are characterized by a drop tower apparatus and compared with the quasi-static responses. The results show that the linear elastic and nonlinear post-buckling behaviors of the H-ReHs exhibit different levels of strain rate sensitivity. The strain rate-dependent behaviors are attributed to the micro-inertia effect and the localized deformation modes of the 2nd order triangular hierarchy. In addition, the energy absorption capacity of H-ReHs under dynamic impacts can reach two orders of magnitude higher than that of the quasi-static one. These findings revealed the relationship between the dynamic crushing behaviors of H-ReHs and the structural heterogeneity of the hierarchical structure, which provides a design paradigm for lightweight but robust structures.

**Keywords** Dynamic impact · Hierarchical · Re-entrant honeycomb · 3D printing · High-speed DIC

## 2.1 Introduction

In the past few decades, cellular materials such as foams and honeycombs have been proposed for energy absorption and shock mitigation applications, in order to satisfy the increasing demand for impact protection in automotive, aerospace, and defense industries [1–5]. Since then, considerable researches have been conducted to investigate the mechanical responses of cellular materials under quasi-static and dynamic loading conditions [6–8]. It has been demonstrated that the crushing of cellular materials under dynamic loading conditions is distinctive from the quasi-static one, mainly due to the dominated material strain rate effect and the structural inertia effect [9]. Under the dynamic loading condition, the stress required to crush the cellular materials is much higher than the quasi-static cases, and thus the energy absorption capacity of the cellular materials is significantly enhanced [10, 11]. In addition, the deformation patterns of the cellular materials are completely different under the dynamic loading condition, e.g., significant deformation localization than the quasi-static counterpart has been observed [12–14]. Therefore, it is necessary to investigate and compare both dynamic and quasi-static crushing behaviors of the cellular materials and reveal the corresponding strain-rate-dependent deformation mechanisms.

Recently, auxetic reentrant honeycombs (ReHs) with inverted cell walls have been extensively investigated. Due to the unique negative Poisson's ratio effect, ReHs have exhibited superior impact resistance over conventional honeycombs [15, 16]. However, the mechanical properties of the ReHs have not been optimized yet due to the bending-dominated behavior of the ligaments [17]. It has been demonstrated that the hierarchical structure topologies not only have great potential for converting the bending-dominated behavior of cellular materials into the stretching-dominated one, but also exhibit a combination of lightweight and excellent mechanical properties [18–20]. Therefore, by introducing the hierarchical structures into the conventional cell walls, the resulted hierarchical re-entrant honeycombs (H-ReHs) have great potential to possess extraordinary mechanical properties [21].

In our previous work, we have fabricated H-ReHs with triangular hierarchical substructures through 3D printing technique and investigated their crushing behavior under quasi-static compression [22]. The 2nd order triangular hierarchy has a unique

C. Zhan (✉) · M. Li · W. Lu
Department of Civil & Environmental Engineering, Michigan State University, East Lansing, MI, USA
e-mail: zhanchi@msu.edu; limingzh@msu.edu; wylu@egr.msu.edu



S. Mates et al. (eds.), *Dynamic Behavior of Materials, Volume 1*, Conference Proceedings of the Society for Experimental Mechanics Series, https://doi.org/10.1007/978-3-031-17453-7_2

deformation behavior of elastic stretching, buckling, fracture, and densification, which results in a much-enhanced energy absorption capacity over the regular re-entrant honeycombs. It is necessary to investigate the crushing behaviors of H-ReHs under dynamic loading conditions, the real loading conditions for crashworthiness applications. In this study, the mechanical responses of H-ReHs under dynamic impact are investigated and compared with their quasi-static counterparts. It is found that while the stress levels are significantly enhanced for H-ReHs under the dynamic loading condition, the strain rate sensitivity is different in linear elastic and nonlinear post-buckling regions, respectively. In addition, the energy absorption capacity for H-ReHs under the dynamic loading condition is significantly enhanced. These are associated with the micro-inertia effect and the deformation localization of the 2nd order triangular hierarchy in H-ReHs under the dynamic impact.

## 2.2 Materials and Methods

The hierarchical re-entrant honeycomb (H-ReH) specimens were fabricated by the PolyJet 3D printer (Objet Connex 350, Stratasys). The printing material was a mixture of Tangoblack and Verowhite (FLX9870-DM, Stratasys). The overall dimension of H-ReH specimens is 60.4 mm × 35.5 mm × 18 mm (width × height × thickness). The typical printed H-ReH specimen is shown in Fig. 2.1a. H-ReH specimens with three different relative densities—0.17, 0.23, and 0.34—were designed and fabricated in this study. The relative density was adjusted by changing the thickness of the hierarchical struts.

The constitutive behavior of the printing material was first characterized by a uniaxial tensile test (ASTM D638-14). The typical constitutive behavior of the printing material is shown in Fig. 2.2. The tensile strength was 10.5 MPa, and the

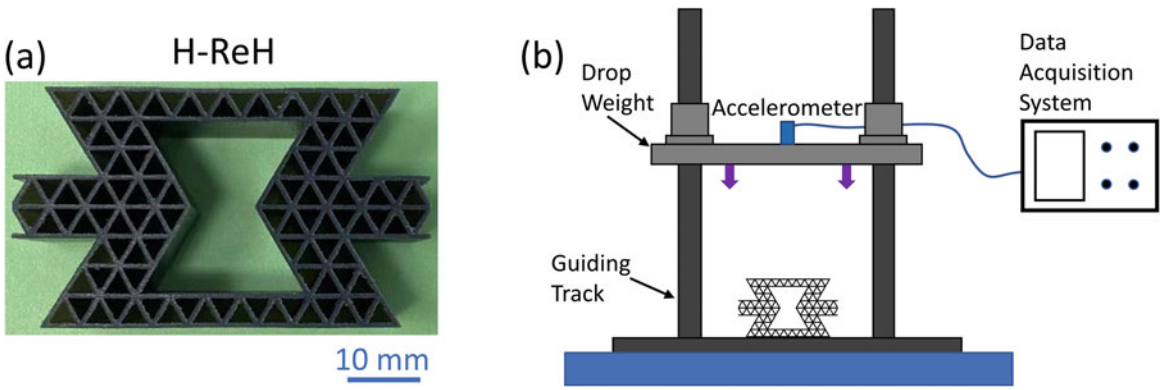


**Fig. 2.1** (**a**) 3D printed hierarchical reentrant honeycomb. (**b**) Schematic of the experimental set-up of the drop tower tests

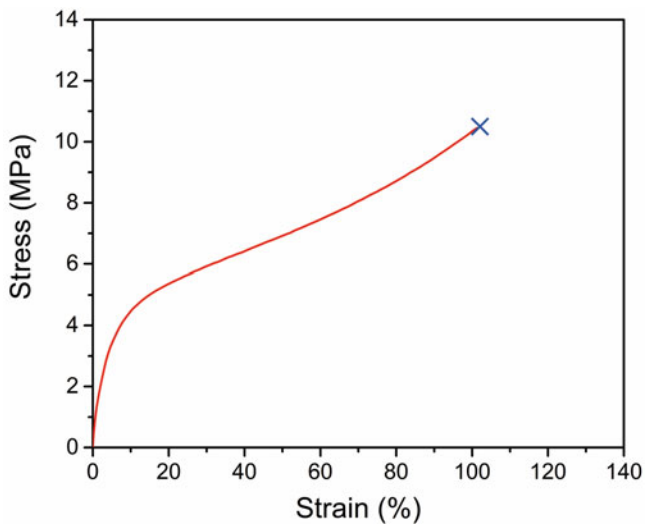


**Fig. 2.2** Standardized uniaxial tensile testing result of the printing material

elongation at break was 100%. The mechanical properties of 3D printed H-ReHs were characterized by quasi-static compression and dynamic impact tests. For the quasi-static compression tests, a universal test machine (Model 5982, Instron) was used with a constant loading rate of 9 mm/min. The applied stress was calculated as $\sigma = F/A$, where $F$ was the force applied by the Instron crosshead and $A$ was the cross-sectional area of the 3D-printed H-ReH. The nominal strain was calculated as $\varepsilon = \delta/h \times 100\%$, where $\delta$ was the Instron machine crosshead displacement, and $h$ was the initial height of the sample. Specific energy absorption (SEA) of H-ReHs was calculated as $\text{SEA} = \frac{\int F \, \mathrm{d}\delta}{m}$, where $m$ was the mass of the H-ReH specimen. For the dynamic impact tests, a customized drop tower apparatus at the Ford Motor Company was used. Fig. 2.1b shows the schematic of the drop tower setup. The incident speed of the dynamic tests was set at 2.5 m/s, and the corresponding free drop height was set at 0.32 m. The drop weight was 8.8 kg. The deceleration time history was collected by an accelerometer attached to the drop weight and then recorded by an oscilloscope (PXIe-5105, National Instruments) at a sampling rate of $10^6$ Hz. The stress applied to the H-ReH specimen was calculated as $\sigma = m_\mathrm{d} \cdot a/A$, where $m_\mathrm{d}$ was the drop weight and $a$ was the deceleration of the drop weight. The displacement was calculated as $\delta = \iint a(t) \, \mathrm{d}^2 t$, where $t$ was the time [23]. The displacement was then converted to the strain of H-ReH by using the sample height.

During the dynamic impact tests, a high-speed camera (Chronos 1.4, Kron Technologies Inc.) was used to capture the local deformation of the H-ReHs at a frame rate of 5903 fps and a resolution of 640 × 360. To analyze the local deformation of H-ReHs under the dynamic impact, the digital image correlation (DIC) technique was employed. All 3D printed H-ReH specimens were firstly spray painted with white 3–7 pixel size surface patterns (flat white, Rust-Oleum) for tracking [21]. After that, the high-speed videos recording the deformation process of H-ReHs during the dynamic impact were collected for the DIC analyses. By importing the high-speed videos into the DIC processing software (Aramis Professional 2019, GOM Company), the deformation contours of the H-ReHs under the dynamic impact were obtained and analyzed.

## 2.3 Results

### 2.3.1 Dynamic and Quasi-static Responses of H-ReHs

The dynamic responses of H-ReHs with different relative densities are shown in Fig. 2.3a. It is observed that all H-ReHs have an elastic response initially. With increasing the relative density, both the elastic modulus and the strength of the H-ReHs are increased. After reaching the strength of the structure, post-buckling plateaus are observed for all H-ReHs. The post-buckling plateaus exhibit a two-step increment for all H-ReHs, which is associated with the localized progressive deformation of the 2nd order triangular hierarchy. The stress level of the post-buckling plateau is increased by increasing the relative density as well. Finally, all H-ReHs exhibit a densification behavior. For comparison, the typical stress-strain curves of H-ReHs under quasi-static compression are shown in Fig. 2.3b. Generally, all H-ReHs exhibit a linear elastic, nonlinear post-buckling, and

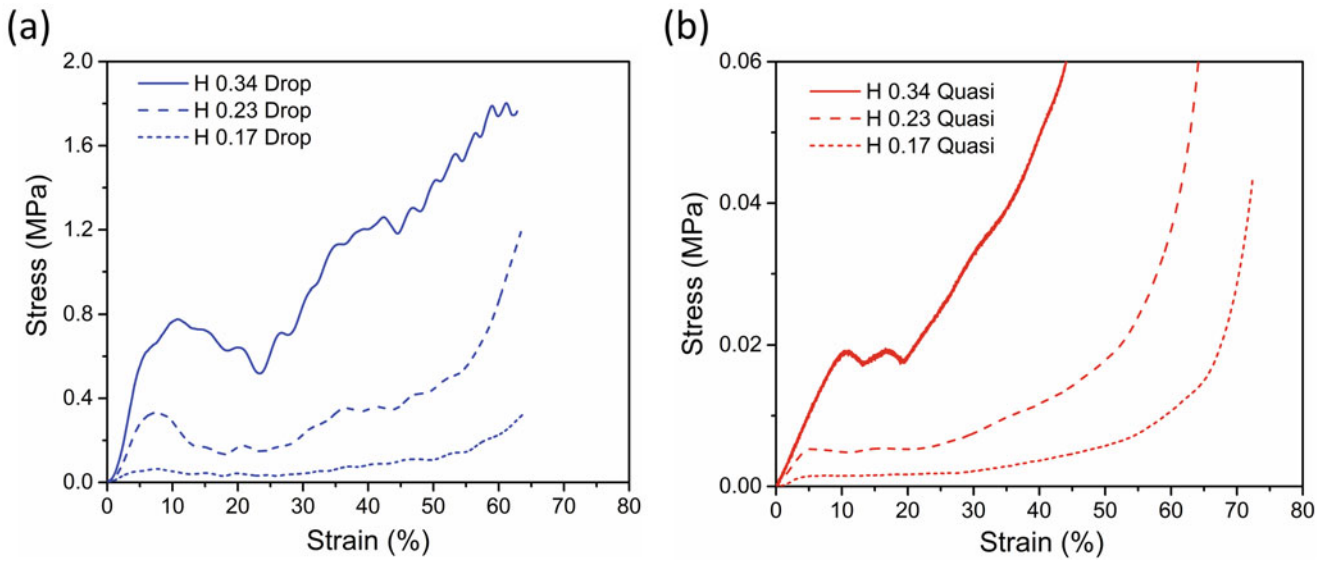


**Fig. 2.3** Typical stress-strain curves of H-ReHs under (**a**) dynamic impact, and (**b**) quasi-static compression

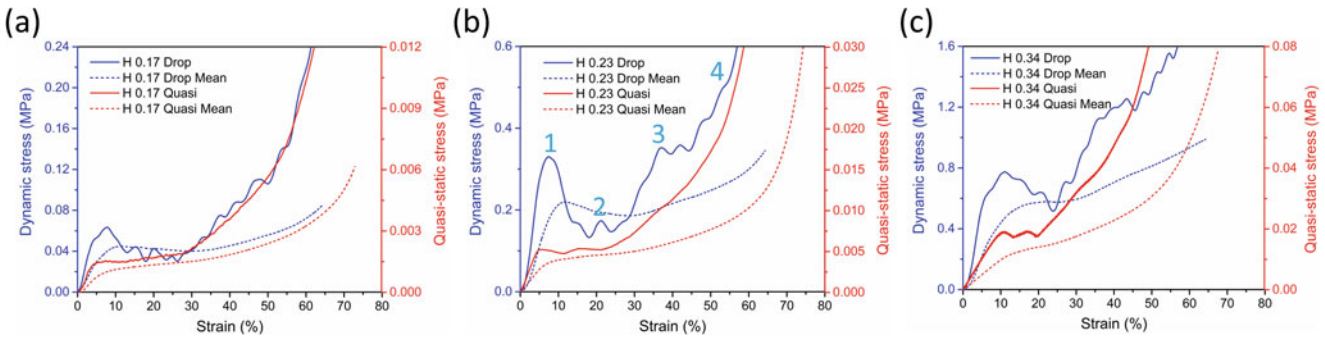


**Fig. 2.4** Comparison of dynamic and quasi-static stress-strain curves of H-ReHs. (**a**) $\overline{\rho} = 0.17$, (**b**) $\overline{\rho} = 0.23$, and (**c**) $\overline{\rho} = 0.34$

**Table 2.1** Elastic modulus and the elastic strain rate sensitivity of H-ReHs

| – | $E_d$ (MPa) | $E_q$ (MPa) | $E_d/E_q$ |
|---|---|---|---|
| H 0.17 | 1.78 | 0.067 | 26.61 |
| H 0.23 | 7.52 | 0.13 | 59.18 |
| H 0.34 | 16.03 | 0.21 | 75.63 |

**Table 2.2** Mean crushing stress at $\varepsilon = 40\%$ and the post-buckling strain rate sensitivity of H-ReHs

| – | $\sigma_{md}$ (MPa) | $\sigma_{mq}$ (MPa) | $\sigma_{md}/\sigma_{mq}$ |
|---|---|---|---|
| H 0.17 | 0.045 | 0.0018 | 24.67 |
| H 0.23 | 0.22 | 0.0061 | 35.25 |
| H 0.34 | 0.71 | 0.023 | 31.06 |

densification behavior. Particularly, the post-buckling stress plateaus of H-ReHs under quasi-static compression have only a one-step increment, which is different from the dynamic scenario. In addition, it is noted that the stress level of the quasi-static responses is much lower than the dynamic ones. These should be associated with the strain rate effect and different deformation mechanisms of the H-ReHs under different loading rates.

In order to directly characterize the strain rate effect of H-ReHs with various relative densities, the dynamic and the quasi-static stress-strain curves for each relative density of H-ReH are plotted together, as shown in Fig. 2.4a–c. In addition, the mean crushing stresses are calculated as $\sigma_m(\varepsilon) = \frac{\int \sigma \, d\varepsilon}{\varepsilon}$ and plotted in Fig. 2.4 as well. The dynamic stress range is 16 times that of the quasi-static one for all these figures. As shown in Fig. 2.4b, for the H-ReH with $\overline{\rho} = 0.23$, the dynamic stress-strain curve initially shows a much higher strength in the elastic region compared to the quasi-static curve, followed by a stress drop at the beginning of the post-buckling region. Afterward, the dynamic post-buckling plateau is close to the quasi-static one, as shown in Fig. 2.4b. These results indicate that the linear elastic and nonlinear post-buckling behaviors of the H-ReHs exhibit different levels of strain rate sensitivity. Similar behavior is also observed when the relative density of H-ReHs is $\overline{\rho} = 0.17$ and $\overline{\rho} = 0.34$, respectively. Therefore, it is critical to characterize the strain rate sensitivity of H-ReHs in elastic and post-buckling regions, respectively. To do that, the ratios between the dynamic mechanical properties and the quasi-static ones are extracted. Firstly, the ratio of the dynamic elastic modulus ($E_d$) to the quasi-static elastic modulus ($E_q$) of H-ReHs is calculated as the elastic strain rate sensitivity of H-ReHs, as shown in Table 2.1. Secondly, the ratio of the dynamic mean stress ($\sigma_{md}$) at 40% strain to the quasi-static mean stress ($\sigma_{mq}$) at the same strain is calculated as the post-buckling strain rate sensitivity of H-ReHs, as shown in Table 2.2. It is observed that the value of $E_d/E_q$ significantly increases with increasing relative density, as shown in Table 2.1. This demonstrates that the elastic strain rate sensitivity of H-ReHs is enhanced when the relative density is increased. By contrast, the value of $\sigma_{md}/\sigma_{mq}$ almost remains constant with the increasing relative density of the H-ReHs. This, on the other hand, shows that the post-buckling strain rate sensitivity of H-ReHs is insensitive to the relative density. Furthermore, by comparing the values of $E_d/E_s$ and $\sigma_{md}/\sigma_{mq}$, it is found that the elastic strain rate sensitivity of H-ReHs is significantly higher than the post-buckling one when the relative density is increased. This is associated with the localized deformation mechanism of the 2nd order triangular hierarchy due to the micro-inertia effect.

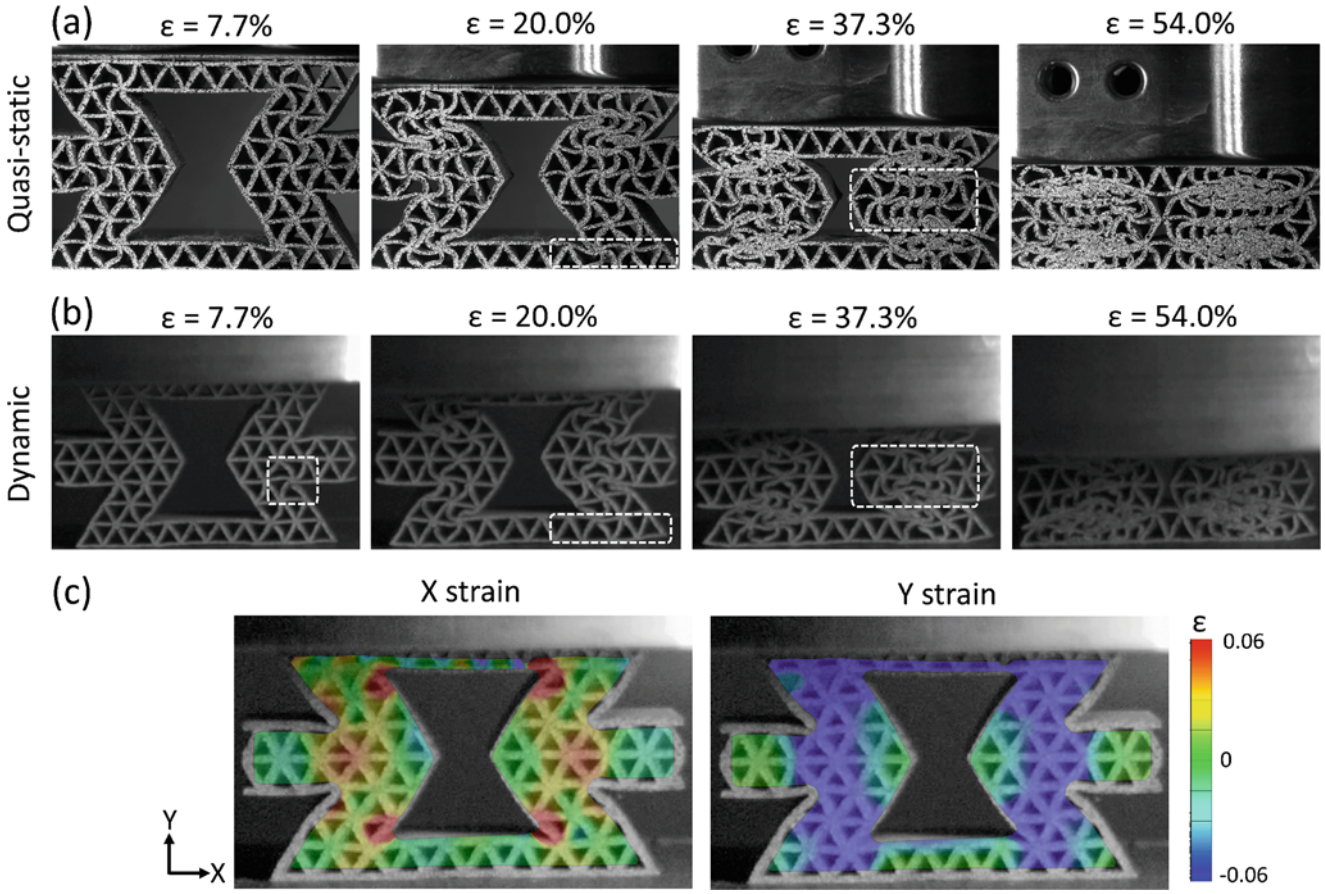


**Fig. 2.5** The deformation of H-ReH ($\overline{\rho} = 0.23$) under (**a**) quasi-static compression, and (**b**) dynamic impact. (**c**) DIC strain contours of H-ReH ($\overline{\rho} = 0.34$) along X and Y direction at $\varepsilon = 10\%$

### *2.3.2 Dynamic Deformation Mechanisms of H-ReHs*

The deformation patterns of H-ReHs under quasi-static and dynamic loading conditions are compared and shown in Fig. 2.5. The deformation patterns correspond to four points on the stress-strain curves shown in Fig. 2.4b. It is observed that at small strains ($\varepsilon = 7.7\%$), the joints and struts of H-ReHs start to deform collectively under quasi-static compression. By contrast, under the dynamic impact, most of the joints and struts are much less deformed. Particularly, localized joints and struts in the corners of H-ReHs are heavily deformed, as highlighted. This is associated with the micro-inertia effect of the 2nd order triangular hierarchy under the dynamic impact, which resists the buckling and rotation of the local struts. Such micro-inertia effect suppresses the compliant buckling of struts under the quasi-static condition [24], thus leading to a much-enhanced elastic strain rate sensitivity of H-ReHs over the post-buckling one, as shown in Figs. 2.3 and 2.4. When the strain further increases to $\varepsilon = 20\%$, the struts in the inclined members are heavily deformed. In addition, the nearby struts in the horizontal member (as highlighted) show much less compression under the dynamic impact. This is also associated with the micro-inertia effect inherited from the linear elastic region. As the strain further increases to 37.3%, the struts in inclined members have been fully compacted, and the struts highlighted in the central region start to be compressed. While a compliant buckling mode of struts is observed under the quasi-static condition, an irregular buckling mode with counterrotation behaviors of certain struts is observed under dynamic impact. This accounts for the two-step post-buckling behavior of H-ReHs under dynamic impact. Lastly, both H-ReHs reach densification with local struts compacted together when $\varepsilon = 54\%$. Figure 2.5c shows the DIC strain contours of the H-ReHs under the dynamic impact. The strain contour in the X direction shows that severe stretching behaviors are localized around the corner of the H-ReH (red region). The stretching behaviors are associated with the inward moving direction of center tips due to the negative Poisson's ratio effect, and the deformation localization around the corner is due to the micro-inertia effect of H-ReHs. The strain contour in the Y direction shows that 2nd order struts within inclined members are compressed heavily in the Y direction (blue region), indicating that these struts carry most of the

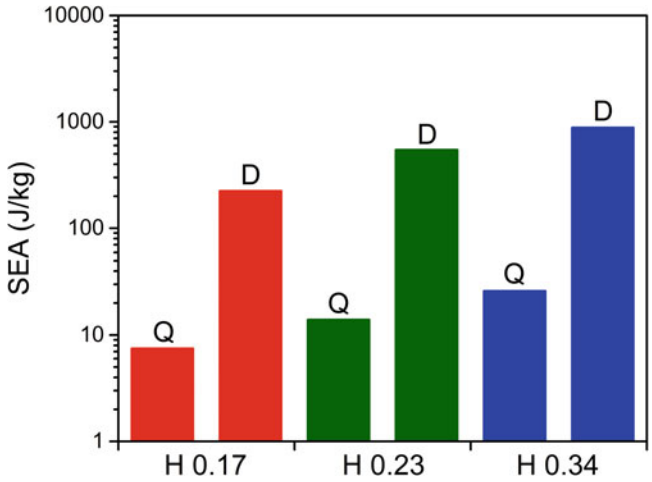


**Fig. 2.6** SEA of H-ReHs with different relative densities under quasi-static and dynamic loading conditions. (Q is denoted for a quasi-static condition and D is denoted for a dynamic condition)

compressive load. By contrast, 2nd order struts in the center tips and the horizontal members are only slightly deformed, which means these regions are less engaged in compressive load bearing.

### *2.3.3 Energy Absorption of H-ReHs*

The specific energy absorption (SEA) of H-ReHs under dynamic and quasi-static loading conditions is shown in Fig. 2.6. It is observed that the SEA of the H-ReHs under dynamic impacts is much higher than the quasi-static loading condition. In addition, such enhancement is further increased by increasing the relative density of H-ReHs. For example, when $\overline{\rho} = 0.17$, there is an order of magnitude enhancement in SEA; when $\overline{\rho} = 0.34$, the dynamic SEA reaches two orders of magnitude higher than the quasi-static one. Such enhancement is attributed to the material strain rate effect together with the micro-inertia effect.

## 2.4 Conclusion

In this study, the mechanical performance of hierarchical reentrant honeycombs (H-ReHs) under dynamic loading conditions is investigated. The stress levels of H-ReHs under dynamic impacts are significantly enhanced with a two-step increment behavior compared to the quasi-static one. Furthermore, it is found that when the relative density is high, the H-ReHs exhibit a different strain rate sensitivity in the linear elastic and the nonlinear post-buckling region. Such difference is due to the micro-inertia effect of the 2nd order triangular hierarchy in H-ReHs, which results in a localized deformation pattern of H-ReHs under the dynamic impact. With the combination of the material strain rate effect and the structural micro-inertia effect, the H-ReHs under dynamic impact reach two orders of magnitude higher specific energy absorption (SEA) than the quasi-static one. These findings can shed light on the design of lightweight but robust materials for crashworthiness applications.

**Acknowledgments** The authors would like to thank the financial support from the Ford-MSU Alliance project.

## References

1. Cole, G.S., Sherman, A.M.: Light weight materials for automotive applications. Mater. Charact. **35**(1), 3–9 (1995)
2. Williams, J.C., Starke Jr., E.A.: Progress in structural materials for aerospace systems. Acta Mater. **51**(19), 5775–5799 (2003)
3. Immarigeon, J.P., Holt, R.T., Koul, A.K., Zhao, L., Wallace, W., Beddoes, J.C.: Lightweight materials for aircraft applications. Mater. Charact. **35**(1), 41–67 (1995)
4. Lu, G., Yu, T.X.: Energy Absorption of Structures and Materials. Elsevier (2003)

5. Schaedler, T.A., Carter, W.B.: Architected cellular materials. Annu. Rev. Mater. Res. **46**, 187–210 (2016)
6. Sun, Y., Li, Q.M.: Dynamic compressive behaviour of cellular materials: a review of phenomenon, mechanism and modelling. Int. J. Impact Eng. **112**, 74–115 (2018)
7. Kader, M.A., Islam, M.A., Saadatfar, M., Hazell, P.J., Brown, A.D., Ahmed, S., Escobedo, J.P.: Macro and micro collapse mechanisms of closed-cell aluminium foams during quasi-static compression. Mater. Des. **118**, 11–21 (2017)
8. Gibson, L.J.: Cellular solids. MRS Bull. **28**(4), 270–274 (2003)
9. Zou, Z., Reid, S.R., Tan, P.J., Li, S., Harrigan, J.J.: Dynamic crushing of honeycombs and features of shock fronts. Int. J. Impact Eng. **36**(1), 165–176 (2009)
10. Tan, P.J., Reid, S.R., Harrigan, J.J., Zou, Z., Li, S.: Dynamic compressive strength properties of aluminium foams. Part I—experimental data and observations. J. Mech. Phys. Solids. **53**(10), 2174–2205 (2005)
11. Hönig, A., Stronge, W.J.: In-plane dynamic crushing of honeycomb. Part I: crush band initiation and wave trapping. Int. J. Mech. Sci. **44**(8), 1665–1696 (2002)
12. Qiu, X.M., Zhang, J., Yu, T.X.: Collapse of periodic planar lattices under uniaxial compression, part II: dynamic crushing based on finite element simulation. Int. J. Impact Eng. **36**(10-11), 1231–1241 (2009)
13. Ashby, M.F., Evans, T., Fleck, N.A., Hutchinson, J.W., Wadley, H.N.G., Gibson, L.J.: Metal Foams: A Design Guide. Elsevier (2000)
14. Evans, K.E., Alderson, K.L.: Auxetic materials: the positive side of being negative. Eng. Sci. Educ. J. **9**(4), 148–154 (2000)
15. Dong, Z., Li, Y., Zhao, T., Wu, W., Xiao, D., Liang, J.: Experimental and numerical studies on the compressive mechanical properties of the metallic auxetic reentrant honeycomb. Mater. Des. **182**, 108036 (2019)
16. Hu, L.L., Zhou, M.Z., Deng, H.: Dynamic indentation of auxetic and non-auxetic honeycombs under large deformation. Compos. Struct. **207**, 323–330 (2019)
17. Yang, L., Harrysson, O., West, H., Cormier, D.: Mechanical properties of 3D re-entrant honeycomb auxetic structures realized via additive manufacturing. Int. J. Solids Struct. **69**, 475–490 (2015)
18. Meza, L.R., Zelhofer, A.J., Clarke, N., Mateos, A.J., Kochmann, D.M., Greer, J.R.: Resilient 3D hierarchical architected metamaterials. Proc. Natl. Acad. Sci. U. S. A. **112**(37), 11502–11507 (2015)
19. Lakes, R.: Materials with structural hierarchy. Nature. **361**(6412), 511–515 (1993)
20. Zheng, X., Smith, W., Jackson, J., Moran, B., Cui, H., Chen, D., Ye, J., Fang, N., Rodriguez, N., Weisgraber, T., Spadaccini, C.M.: Multiscale metallic metamaterials. Nat. Mater. **15**(10), 1100–1106 (2016)
21. Zhan, C., Li, M., McCoy, R., Zhao, L., Lu, W.: 3D-printed hierarchical re-entrant honeycomb with improved structural stability under quasi-static compressive loading. In: ASME International Mechanical Engineering Congress and Exposition, Vol. 85574, p. V003T03A053. American Society of Mechanical Engineers (2021)
22. Zhan, C., Li, M., McCoy, R., Zhao, L., Lu, W.: 3D printed hierarchical re-entrant honeycombs: enhanced mechanical properties and the underlying deformation mechanisms. Compos. Struct. p. 115550 (2022)
23. Li, M., He, B., Barbat, S., Gu, S., Lu, W.: Rate dependent reinforcement of liquid nanofoam on thin-walled tubes. In: ASME International Mechanical Engineering Congress and Exposition, Vol. 58493, p. V014T11A007. American Society of Mechanical Engineers (2017)
24. Wang, Z., Shen, J., Lu, G., Zhao, L.: Compressive behavior of closed-cell aluminum alloy foams at medium strain rates. Mater. Sci. Eng. A. **528**(6), 2326–2330 (2011)

# Chapter 3
# Mechanism of Improving Ballistic Performance of Kevlar through Impregnation of Nanoparticles

**Muhammad Ali Bablu and James M. Manimala**

**Abstract** Treating Kevlar fabric with nanoparticles is found to augment its mechanical properties. This could lead to more lightweight yet flexible armors for specialized applications. In this study, the ballistic performance of neat and silica nanoparticle-treated Kevlar (SNK) fabrics with various percentages by weight of nanoparticle treatment and number of layers is experimentally evaluated. A colloid-based treatment procedure is used to impregnate dry silica nanoparticles into the fabric. The fabric samples are evaluated using a compressed air gun as per a test methodology adapted from NIJ standard 0108.01. Both penetrative and non-penetrative cases are examined. Addition of nanoparticles improved the fabric's ballistic performance by providing about a 17% mass advantage (due to three less layers) for the 40 wt.% SNK vis-à-vis neat Kevlar for the non-penetrative case. SEM imaging reveals that at higher treatment levels, the nanoparticles tend to agglomerate in the interstitial spaces of yarn crossover points, which helps better engage secondary yarns away from the impact location of the projectile. Inspecting the back-face damaged zone areas for penetrative cases shows a strong positive correlation with nanoparticle treatment level, indicating that secondary yarns away from the primary zone are engaged in the impact mitigation mechanism for SNK. A semiempirical model is developed to capture and predict the influence of the treatment level and the number of layers on the kinetic energy dissipated by SNK fabrics. The flexibility of SNK fabrics was evaluated using a fixed cantilever length test. The measured tip deflection angle decreases from 33° for the neat fabric to 19° for the 40 wt.% SNK fabric. Although the addition of nanoparticles does diminish the flexibility of the neat fabric, the SNK fabric retains sufficient flexibility to have significant deflection under its self-weight. Using digital image analysis, the deflection curves for the samples are approximated using those for a cantilevered beam with uniform distributed loading. The educed flexural rigidities range from 48.9 $Nm^2$ for the neat fabric to 113.7 $Nm^2$ for the 40 wt.% SNK. Treating the fabric with nanoparticles tends to restrict the rotational degree of freedom at yarn crossover points to a greater extent, leading to higher flexural rigidity. Further investigations are underway to ascertain the influence of nanoparticle addition on frictional mechanisms using dynamic yarn pullout tests.

**Keywords** Kevlar · Ballistics · Nanoparticle · Modeling

## Nomenclature

| | |
|---|---|
| $\theta$ | Deflection angle of cantilever length |
| $a_j$ | Quadratic fitting coefficients |
| ASTM | American Society for Testing and Materials |
| $b_{jk}$ | Constant for linear interpolants |
| CNT | Carbon nanotubes |
| EI | Flexural rigidity |
| ISO | International Organization for Standardization |
| $KE_{abs}$ | Kinetic energy absorbed |
| $L_c$ | Cantilever length of fabric allowed to flex |
| $L_f$ | Fixed length of fabric sandwiched between plates |
| $m_b$ | Mass of the projectile |
| N | Number of layers |

M. A. Bablu (✉) · J. M. Manimala
School of Mechanical and Aerospace Engineering, Oklahoma State University, Stillwater, OK, USA
e-mail: mbablu@okstate.edu; james.manimala@okstate.edu



S. Mates et al. (eds.), *Dynamic Behavior of Materials, Volume 1*, Conference Proceedings of the Society for Experimental Mechanics Series, https://doi.org/10.1007/978-3-031-17453-7_3

| | |
|---|---|
| NIJ | National Institute of Justice |
| PEG | Polyethylene glycol |
| $q$ | Weight per unit length of the neat or treated fabric |
| SEM | Scanning electron microscopy |
| SNK | Silica nanoparticle-treated Kevlar |
| STF | Shear thickening fluid |
| $v_i$ | Initial velocity of the projectile |
| $v_r$ | Residual velocity of the projectile |
| $w$ | Wt.% of impregnation |
| $x$ | Horizontal distance of the cantilever fabric |
| $y$ | Deflection of the fabric under own loading |

## 3.1 Introduction

Aramid fabrics such as Kevlar® are used in ballistic protection and containment applications, especially where flexibility and low weight are priorities. Depending on the characteristics of the fabrics, Kevlar® can be tailored for specific types of threats and application scenarios. Factors such as fiber type, weave style [1–3], boundary conditions [4, 5], inter-yarn [6, 7] and fabric-projectile [8] friction, and the projectile's characteristics relative to the fabric [9, 10] influence their performance. While on the one hand, new materials can be developed to improve ballistic performance, on the other hand, hybrid structural materials that utilize coactive mechanisms between their constituents could potentially also deliver more adaptable and multifunctional solutions.

There are many types of hybrid structural materials that incorporate fabrics as their primary constituent. The possibility of improving the mechanical properties of Kevlar fabric using different kinds of additives has been investigated previously. Aramid fabrics treated with shear thickening fluids (STF) have been shown to have improved friction between the yarns during impact [11, 12]. The impact performance of STF-Kevlar composites containing 15–45 wt.% of nano-silica in a polyethylene glycol (PEG) solution was studied by Khodadadi et al. [13]. STF-Kevlar is found to better absorb kinetic energy under optimal dynamic loading. Qin et al. [14] demonstrated that the maximum friction between yarns in STF-Kevlar fabrics is "dozens of times" more than that in neat Kevlar fabrics and that optimal stab resistance is attained at about 35 wt.% of STF addition. Using yarn pullout tests, Nilakantan et al. [15] and Hasanzadeh et al. [16] attributed this type of performance enhancement to increased friction between yarns. It has also been found that adding reinforcements such as carbon nanotubes (CNT) [17, 18] or silicon carbide particles [19, 20] to STF improves its rheological behavior even more, which further enhances the impact energy absorption capacity of STF-Kevlar fabrics. Although the addition of STF to Kevlar fabrics clearly improves dynamic performance under impact and stab-type loading, packaging the fabric within a fluid phase [21, 22] could have practical limitations.

The use of surface coatings and nano-additives has also been explored to improve the dynamic performance of aramid fabric composites. Aramid fabrics with ZnO nanowires grown on their surface display an increase in impact resistance by 66% [23] because of the enhancement of inter-yarn friction, as the nanowires limit the mobility of the yarns. Kim et al. [24] investigated a polymeric adhesive coating and STF impregnation applied independently to single layers of Kevlar and Heracron fabrics concluding that the coating's unique method of polymeric anchoring resulted in a significant increase in ballistic performance (59.8% and 90.6% for Kevlar and Heracron, respectively) as compared to moderate improvement by STF impregnation (24.8% and 13% for Kevlar and Heracron, respectively). Caprino et al. [25] used impact zone analysis for the delaminated area to correlate it with the ballistic absorbed energy as a function of the thickness of stitched graphite/epoxy laminates.

On a related note, the change in the flexibility of aramid fabrics such as Kevlar with an increase in the level of treatment or additives could pose consequences for ergonomics and practicality. Kanesalingam et al. [26] demonstrated that treating Kevlar–wool and Kevlar–wool–nylon fabrics with abrasive silica improved their resistance to stab and puncture. However, fabric stiffness values rose, which might have a detrimental effect on wearability due to decreased flexibility.

One promising avenue to enhance the dynamic performance of Kevlar fabrics is via the impregnation of dry silica nanoparticles into the fabric which has been shown to predominantly improve inter-fiber and inter-yarn friction and consequently the shear rigidity of the fabric [27]. It has been found that fabric impregnated with a smaller particle size (100 nm) shows better impact performance [5]. A homogenized continuum constitutive model was also developed [28] using an approach akin to the classical laminated plate theory in order to predict their in-plane and out-of-plane [28] responses.

Characterizing the dynamic mechanic behavior of SNK fabric could enable the further development of reduced-order models for this class of hybrid structural materials.

In this study, the ballistic performance of neat and silica nanoparticle-treated Kevlar (SNK) fabric is evaluated using compressed air gun tests. The underlying mechanisms that result in ballistic performance enhancement are examined. A colloid-based treatment process is used to impregnate the fabric with dry silica nanoparticles. Inferences are drawn regarding the impact mitigation mechanisms of SNK using SEM imaging, high-speed camera footage, and image analysis of damaged zones. Based on a limited set of experiments, a semiempirical model is developed to capture and predict the influence of the percentage by weight of nanoparticle addition and the number of layers on the kinetic energy dissipated by the SNK fabric under ballistic impact. In order to gauge the effect of the treatment on the bending stiffness of SNK, fixed cantilever length flexibility tests are conducted. The deflection curves are approximated using a simple mechanistic model in order to estimate the flexural rigidity of the treated samples. Based on the analysis of the results, quantitative metrics for specific (mass normalized) performance enhancement are extracted. Opportunities for further research and potential application scenarios are also discussed in the conclusion.

## 3.2 Materials and Methods

### *3.2.1 Sample Preparation*

Kevlar 29-based K745 style plain woven fabric is used throughout this study. Plain woven Kevlar fabrics have been shown to provide the best ballistic performance against low-velocity small arms projectiles [29]. The choice of weave style influences performance, especially in the context of adding nanoparticles to the fabric, and is also dependent on the type of impact or ballistic threat to be defeated. K745 is a relatively heavy and coarse weave style. The manufacturer-specified properties of this Kevlar fabric are given in Table 3.1. The steps involved in the sample preparation process are depicted in Fig. 3.1 Firstly, the neat fabric is cut to size, dried, and weighed (steps (i) and (ii)). For the silica nanoparticle treatment, Snowtex® ST-ZL, a commercially available colloidal silica, is used (properties shown in Table 3.2). The aqueous colloid consists of 40 wt.% of 80–100 nm spherical silica particles. For a specific percentage by weight of nanoparticle addition, the appropriate amount of the colloidal silica is measured and diluted with distilled water (steps (iii) and (iv)). The neat fabric swatch is then soaked in this solution in a shallow dish as shown in step (v) of Fig. 3.1. The swatch is turned over periodically while being dried in a convection oven at 80 °C (step (vi)). Once the water has evaporated, the swatch is weighed to ascertain if the targeted percentage by weight of nanoparticle addition has been achieved (step (vii)). If not, the process is repeated with the requisite amount of colloidal solution to make up for the weight addition needed. For the wt.% cases considered in this study, the durability of impregnation/adhesion of the nanoparticles to the woven fabric is found to be excellent if the fabric is not repeatedly deformed or impacted. 0.3 mm thick aluminum tabs are bonded using an epoxy adhesive on all sides of the treated fabric swatch (step (viii)). The samples thus created are attached with all edges clamped to the steel fixture plates that interface with the ballistic containment box using bolts as shown in step (ix) of Fig. 3.1. The tabbed and installed samples have a test face dimension of 101.2 mm × 101.2 mm. This method of installation provides a relatively robust and repeatable boundary condition for the ballistic tests.

Among the 148 fabric swatches prepared, a slight variation from the targeted percentage by weight of nanoparticle addition was observed. For the 10 wt.% swatches, the actual wt.% ranged from 7.3 to 14.3 wt.%; for the 30 wt.% swatches, the actual wt.% ranged from 28.6 to 34.9 wt.%; and for the 40 wt.% swatches, the actual sample wt.% ranged from 38.4 to 44.7 wt.%. Scanning electron microscope (SEM) images of neat and treated samples are shown in Fig. 3.2. For the neat fabric, an estimation of the uniformity and tightness of the weave can be obtained from the SEM images. It is found that the nanoparticles are embedded in the fabric interstices as well as coated on the fabric surface. In the case of the 30 and 40 wt.% treatments, agglomeration of nanoparticles at the yarn crossover points, causing adhesion between parallel and cross yarns,

**Table 3.1** Manufacturer-specified properties for Kevlar K745 fabric

| Property | Value | Unit |
|---|---|---|
| Fiber type | 29 | – |
| Areal density | 0.48 | $kg/m^2$ |
| Thickness | 0.61 | mm |
| Yarn count (Warp and Weft) | 17 | $inch^{-1}$ |
| Yarn size | 3000 | denier |
| Number of filaments per yarn | 1000 | – |

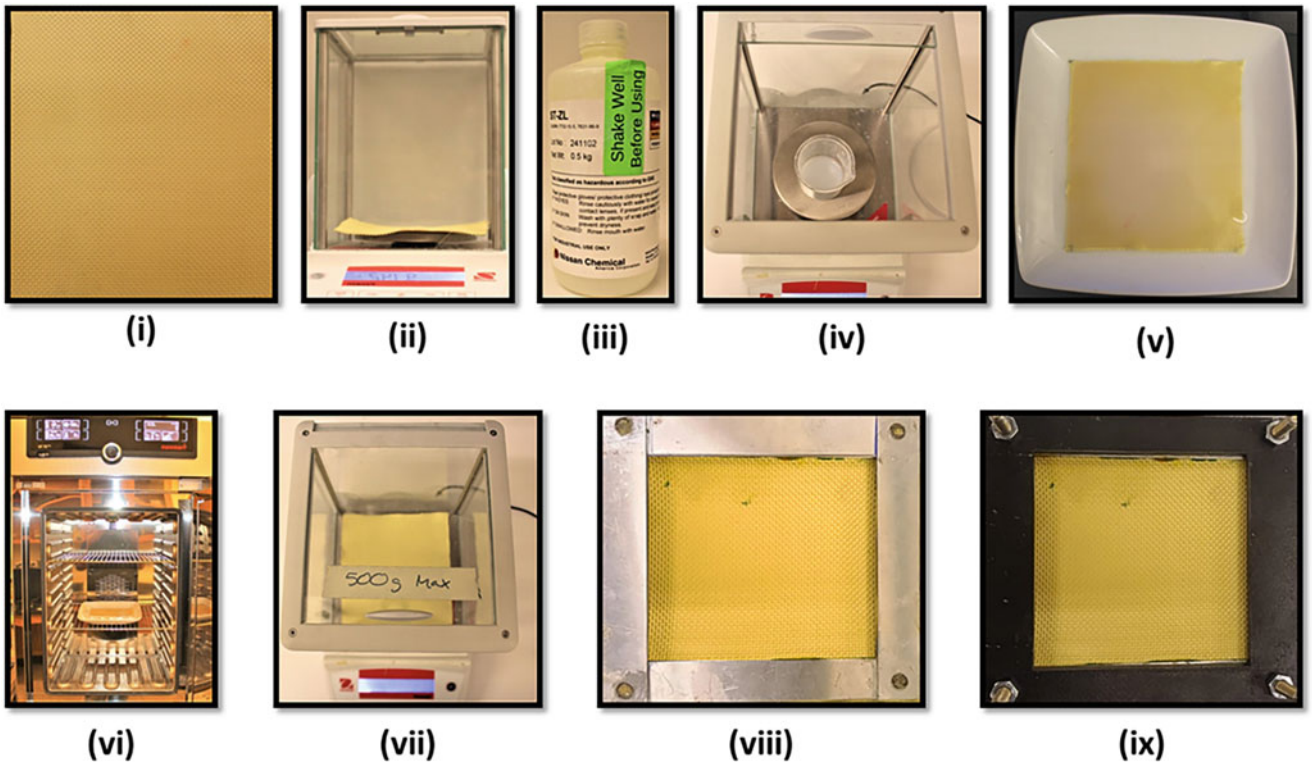


**Fig. 3.1** Steps in the sample preparation process: (i) Neat sample is cut to size, (ii) dried and weighed; (iii) Required amount of colloidal silica is prepared and (iv) weighed; (v) Sample is soaked in the colloid in a shallow dish, (vi) dried in a convection oven at 80 °C for 30 min, flipped and the process is repeated until the water is removed; (vii) Treated SNK sample is weight to ascertain if targeted weight percent addition is achieved; (viii) Aluminum tabs are bonded on to the sample and (ix) the tabbed sample is bolted onto the steel fixture in the ballistic box for testing

**Table 3.2** Manufacturer-specified properties for Snowtex® ST-ZL colloidal silica

| Property | Value | Unit |
|---|---|---|
| $SiO_2$ concentration | 40–41 | wt.% |
| $Na_2O$ concentration | <0.07 | wt.% |
| Particle shape | Spherical | – |
| Particle size | 80–100 | nm |
| Viscosity (at 25 °C) | <5 | mPa.s |
| Specific gravity (at 25 °C) | 1.29–1.32 | – |
| pH | 9.0–10.0 | – |
| Appearance | Opalescent | – |

is observed. For the 40 wt.% case, a layer of nanoparticles is seen to coat the surface of the yarn bundles, including crossover points. This indicates, further increase in the percentage by weight of nanoparticle addition may not augment yarn-yarn interactive mechanisms within the woven fabric. Imaging at different locations on the treated samples reveals that while there is minor nonuniformity, the 40 and 30 wt.% treatments have overall greater coverage of nanoparticles on the fabric surface, especially in the interstitial spaces in comparison to the 10 wt.% treatment and neat cases, as is to be expected.

### *3.2.2 Experimental Setup*

#### Ballistic Tests

The ballistic tests are done using the customized compressed air rifle-based rig shown in Fig. 3.3. It is broadly based on the testing procedure detailed in NIJ Standard 0108.01 [30] and consists of a compressed air rifle (AIR FORCE Texan® Model R1401) that fires a 9.1 mm (0.357″) caliber, 127 grain ($m_b$ = 8.23 g) bullet at up to 950 fps (289.6 m/s) for a maximum

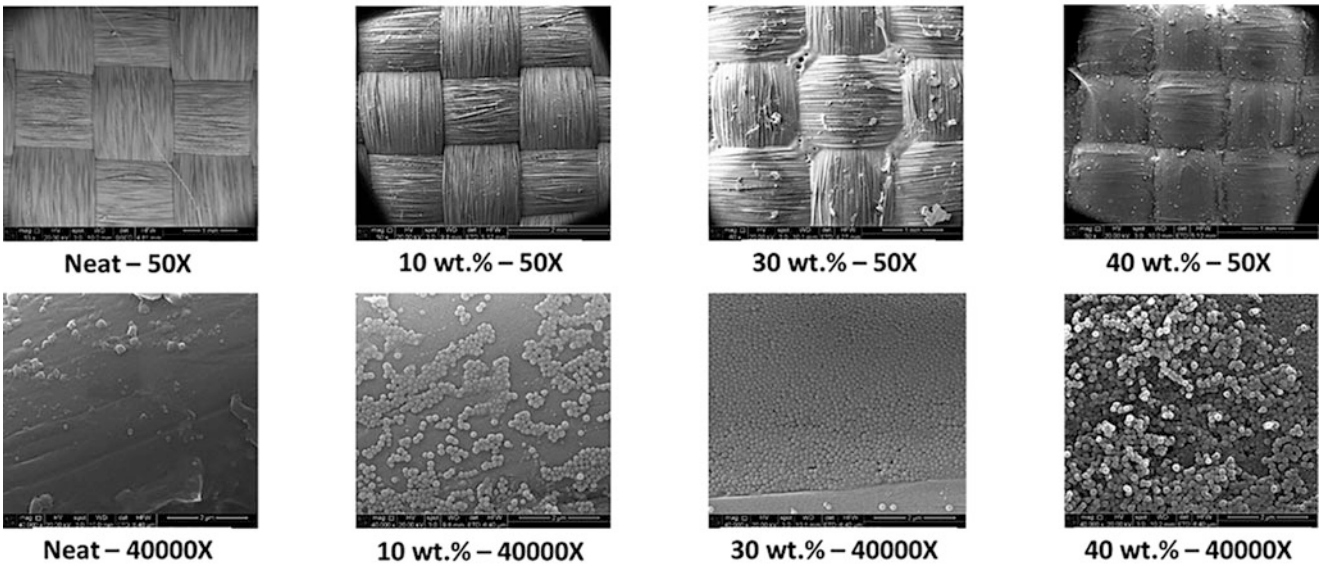


**Fig. 3.2** SEM images of neat and silica nanoparticle-treated Kevlar samples at 50× and 40000× magnifications

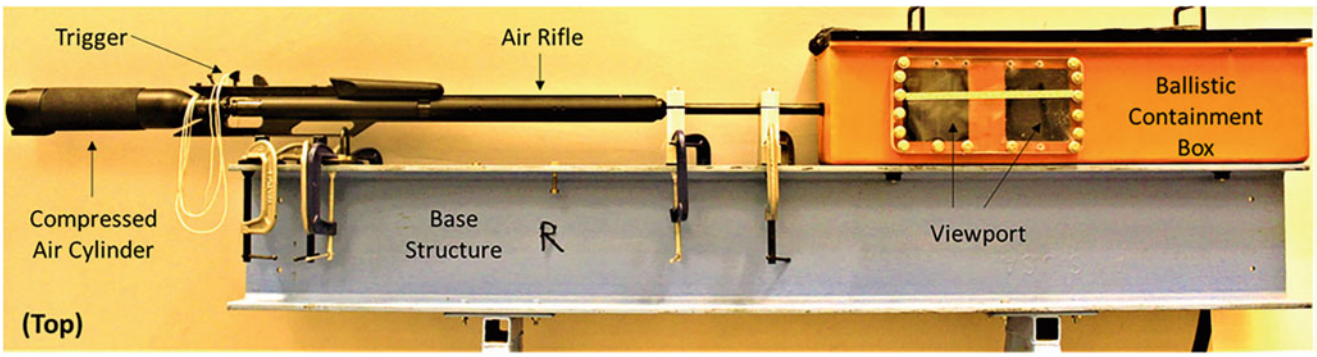


**Fig. 3.3** Experimental setup (top) and its schematic depiction (bottom) for ballistic tests

cylinder pressure of 3000 psi (20.68 MPa). The air rifle is fixed to a base structure and fires into a ballistic containment box which has viewports to observe the ballistic impact. The ballistic box is equipped with fixtures to bolt the test sample in place as well as a rubber backstop. The sample is held in place using steel plates bolted onto the fixtures in the ballistic box. A high-speed camera (Photron® Fastcam Mini UX100) is used to record the impact event, and photographs of the front and back surfaces of the sample are taken after testing. Two samples are considered for each test case, and the incident and residual velocities of the projectile are computed from high-speed camera imagery. The shots are fired at nearly, but not exactly, the same cylinder pressure.

Velocity and energy-based metrics can be used to assess the relative performance of various samples [31]. Once the incident and residual velocities are extracted, the kinetic energy absorbed by the ballistic impact is readily obtained as

$$\mathrm{KE}_{\mathrm{abs}} = \frac{1}{2} m_{\mathrm{b}} \left( v_{\mathrm{r}}^2 - v_{\mathrm{i}}^2 \right) \tag{3.1}$$

where $v_{\mathrm{i}}$ and $v_{\mathrm{r}}$ are the incident and residual velocities of the projectile before and after impact, respectively. For all cases, the front and back face damage zones are photographed and measured.

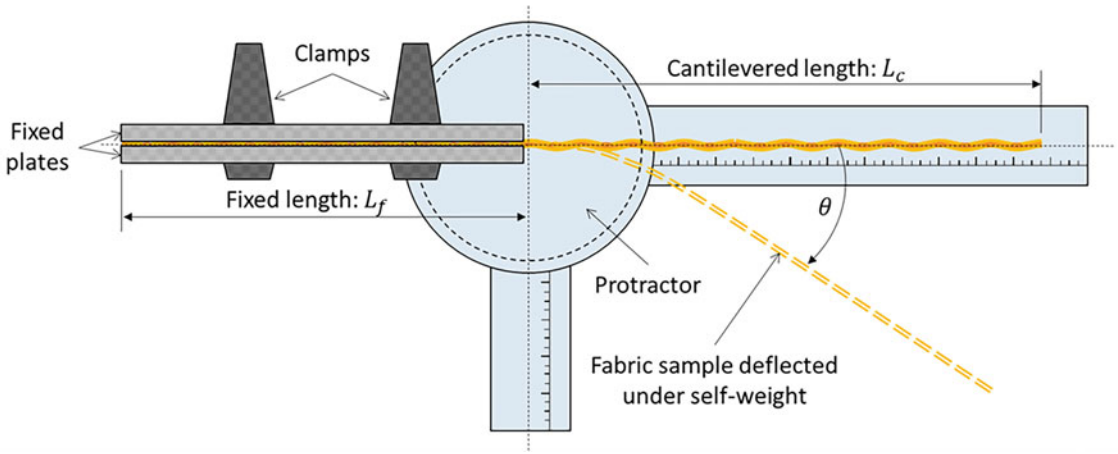


**Fig. 3.4** Schematic depiction of the experimental setup for flexibility tests

### Flexibility Tests

In order to gauge the reduction in the flexibility of the fabric when treated with silica nanoparticles, a set of flexibility tests are performed. Standard testing methods as described in ASTM D1338 [32] or ISO 9073-7 [33] based on Pierce's cantilever test to determine the flexural rigidity of fabrics involve an apparatus consisting of a fabric sample sandwiched between a fixed plate and a sliding plate. In such tests, the sliding plate is moved forward until the unsupported length of the fabric has enough self-weight to flex and touch an inclined plane at a preset angle. Since the fabric samples in this study were treated with dry nanoparticles, it is likely that sliding them between the plates would dislodge the nanoparticles impregnated into the samples and thus adversely affect the tests. Therefore, a modified version of the test termed the fixed cantilever length flexibility test was developed for the nanoparticle-treated Kevlar fabric, as shown in Fig. 3.4. Neat and treated fabric samples having a size of 200 mm × 25 mm are used for the test. A fixed length, $L_f = 70$ mm, is sandwiched between two metal plates and held in place using clamps with a prescribed torque. This leaves a cantilevered length, $L_c = 130$ mm, which is allowed to flex under its self-weight. For all samples, the warp yarn direction was aligned along the cantilevered length. A protractor with a rotatable graduated scale is used to measure the tip deflection angle, $\theta$. The deflected shape of the fabric sample is also recorded using photographs. Obtaining the coordinates of the deflected shape using digital image analysis allows for correlation with mechanistic models in order to extract the flexural rigidity of the neat and treated samples. For each case, a total of nine data sets were collected using three samples with three trials for each sample.

## *3.2.3 Semiempirical Model*

A semiempirical model based on ballistic tests is proposed to predict the performance of SNK within a range of treatment levels and the number of layers that span the test cases. A quadratic polynomial fit is used to calibrate the kinetic energy absorbed as a function of the number of layers for various percentages by weight of nanoparticle addition as defined by

$$\mathrm{KE}_{\mathrm{abs}}(w, \mathrm{N}) = \frac{1}{2} m_{\mathrm{b}} \left[ \{v_r(w, \mathrm{N})\}^2 - \{v_i(w, \mathrm{N})\}^2 \right] = \mathrm{a}_2(w) \cdot \mathrm{N}^2 + \mathrm{a}_1(w) \cdot \mathrm{N} + \mathrm{a}_0(w) \tag{3.2}$$

where $w$ is the percentage by weight of nanoparticle addition, N is the number of layers, $v_{\mathrm{i}}$ is the measured incident velocity, $v_{\mathrm{r}}$ is the measured residual velocity, $m_{\mathrm{b}}$ is the mass of the bullet, and $\mathrm{a}_j$, $j = 0, 1, 2$ are the quadratic fitting coefficients that are expressed as functions of $w$. The choice of the quadratic form with separation of the independent variables, $w$ and N in the fitting function is based on observation of the test data. It is noted that these coefficients are dimensionally akin to energy, with the zeroth order coefficient representing the kinetic energy dissipated due to air damping alone when no sample is present. Next, linear interpolants of the form

$$a_j(w) = b_{j1} \cdot w + b_{j0}, j = 0,1,2 \tag{3.3}$$

are used to determine the fitting coefficients for other treatment levels. Here, $b_{j1}, j = 0, 1, 2$ are constants. This allows for the prediction of the number of layers required for the non-penetrative case for a range of treatment levels apart from the limited set of ballistic tests that are done.

## 3.3 Discussion of Results

### *3.3.1 Ballistic Tests*

Several inferences can be drawn from the ballistic test results. The measurement of the area of the damaged zone is based on a gauge length established in the image by digital analysis. This gauge length in pixels is extracted by matching the yarns per inch in the undistorted region of the sample near the boundary fixity to that specified for the weave style. Inspecting the dimensions of the damaged zone on the back face of the samples shows that there is a clear increase in the area of the damaged zone with the number of layers, but more significantly with an increase in the percentage by weight of nanoparticle addition until the non-penetrative case is achieved for each treatment level (Fig. 3.5a). There is evidence of significantly more yarn breakage at the damaged zone as both the number of layers and treatment level are increased. For the same number of layers, the yarn breakage is noted to be greater at higher treatment levels. It is also seen that for a given number of layers, the area of the damaged zone is, in general, greater when the treatment level is higher. Thus, the influence of the number of layers and the treatment level on the damaged zone area is seen to be co-active in nature, but their individual trends are discernable from limiting cases.

The kinetic energy absorbed in the ballistic tests as a function of the number of layers for various treatment levels is presented in Fig. 3.5b. It is found that the non-penetrative case for all treatment levels is achieved above a threshold value of about 250 J for the kinetic energy absorbed. However, fewer layers are required to attain this threshold when the treatment level is increased. While 7 layers of neat Kevlar are necessary to achieve non-penetrative impact, only 4 are needed for the 40 wt.% SNK. For 4 layers, the 40 wt.% SNK displays about a 130% increase in the kinetic energy absorbed compared to the neat Kevlar.

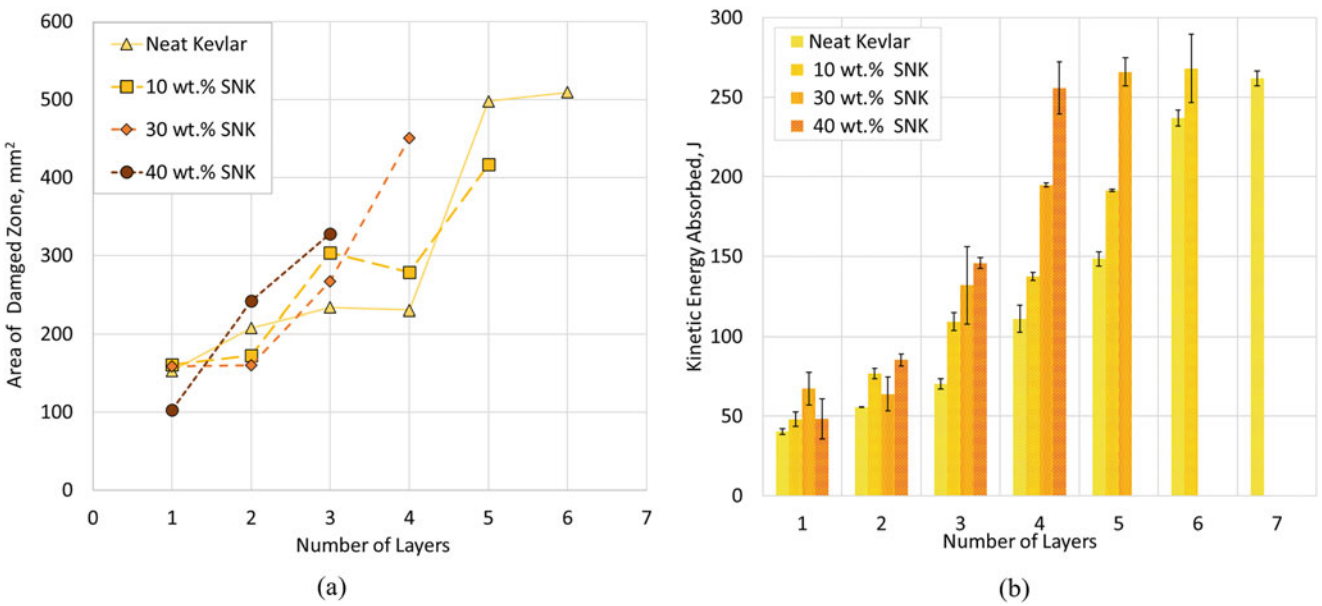


**Fig. 3.5** (**a**) Area of back-face damaged zone for penetrative cases versus the number of layers and (**b**) measured kinetic energy absorbed for neat and SNK samples having various percentages by weight of nanoparticle addition

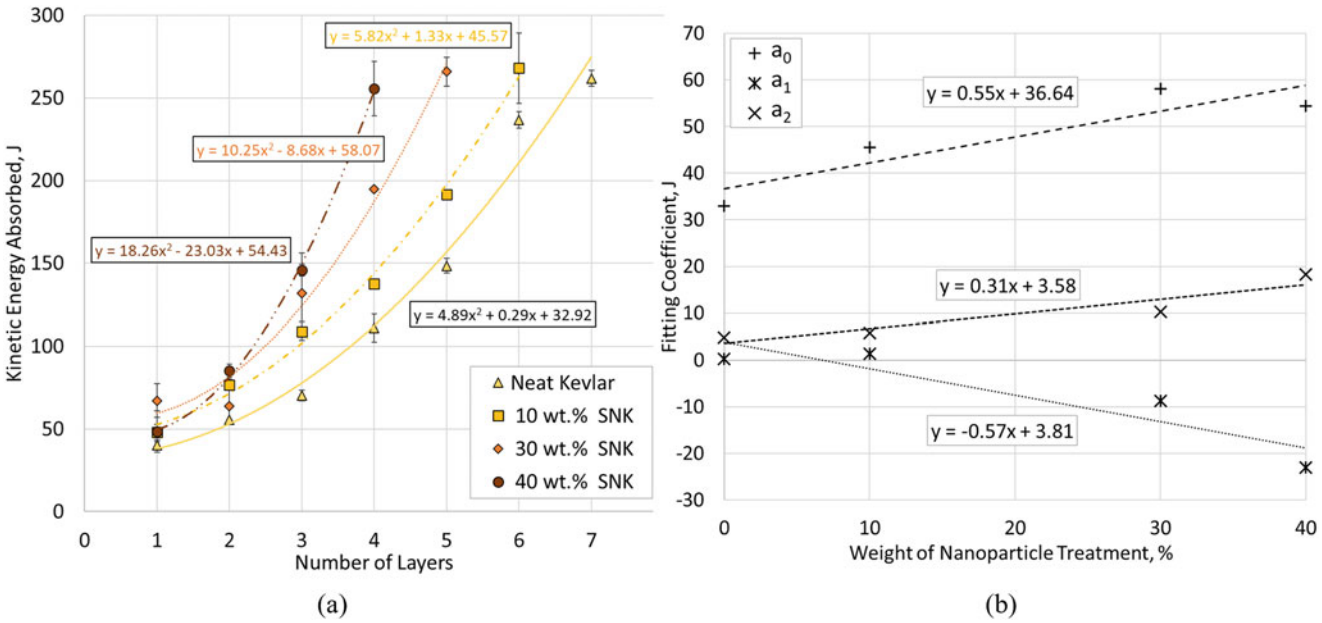


**Fig. 3.6** (**a**) Quadratic curve fits for the kinetic energy absorbed versus the number of layers for neat and SNK samples and (**b**) linear interpolation of the quadratic fitting coefficients for the kinetic energy absorbed versus the number of layers across various percentages by weight of nanoparticle treatment

**Table 3.3** Quadratic fitting coefficients, $a_j(w)$, $j = 0, 1, 2$ extracted from experiments

| $w$, wt.% | $a_2$ | $a_1$ | $a_0$ |
|---|---|---|---|
| 0.00 (neat) | 4.89 | 0.29 | 32.92 |
| 10.00 | 5.82 | 1.33 | 45.57 |
| 30.00 | 10.25 | −8.68 | 58.07 |
| 40.00 | 18.26 | −23.03 | 54.43 |

**Table 3.4** Constants, $b_{jk}$, $j = 0, 1, 2$, $k = 0, 1$ of the linear interpolants for the coefficients of the quadratic fitting functions

| $b_{jk}$ | $k = 0$ | $k = 1$ |
|---|---|---|
| $j = 0$ | 36.64 | 0.55 |
| $j = 1$ | 3.81 | −0.57 |
| $j = 2$ | 3.58 | 0.31 |

### *3.3.2 Semiempirical Model*

The kinetic energy absorbed versus the number of layers from the ballistic tests is approximated using quadratic curve fits as shown in Fig. 3.6a. The quadratic fitting coefficients for the various percentages by weight of nanoparticle treatment are extracted and summarized in Table 3.3. For each treatment level, the zeroth-, first-, and second-order coefficients are approximated using linear fits as shown in Fig. 3.6b. The resulting constants for the linear interpolants are summarized in Table 3.4. Utilizing these constants, the quadratic fitting coefficients for a specific percentage by weight of nanoparticle treatment can be estimated using Eq. 3.3, and using these, the kinetic energy absorbed as a function of the number of layers for that treatment level can be predicted using Eq. 3.2.

Using the parameters obtained for the semiempirical model, the kinetic energy absorbed as a function of the number of layers for new treatment levels (20, 50, and 60 wt.%) is predicted and plotted along with the curve fit for the experimental case (neat, 10, 30, and 40 wt.%) in Fig. 3.7a. The threshold kinetic energy values for the non-penetrative case and the no-sample case as estimated from experiments are also marked. From the predictions, the number of layers required to achieve the non-penetrative case for the new treatment levels can be identified by noting the location at which the predicted curves exceed the threshold value for the kinetic energy absorbed. As the number of layers can only be estimated to integral values, the nearest integral number of layers to the location at which the predicted curves cut the threshold line is chosen.

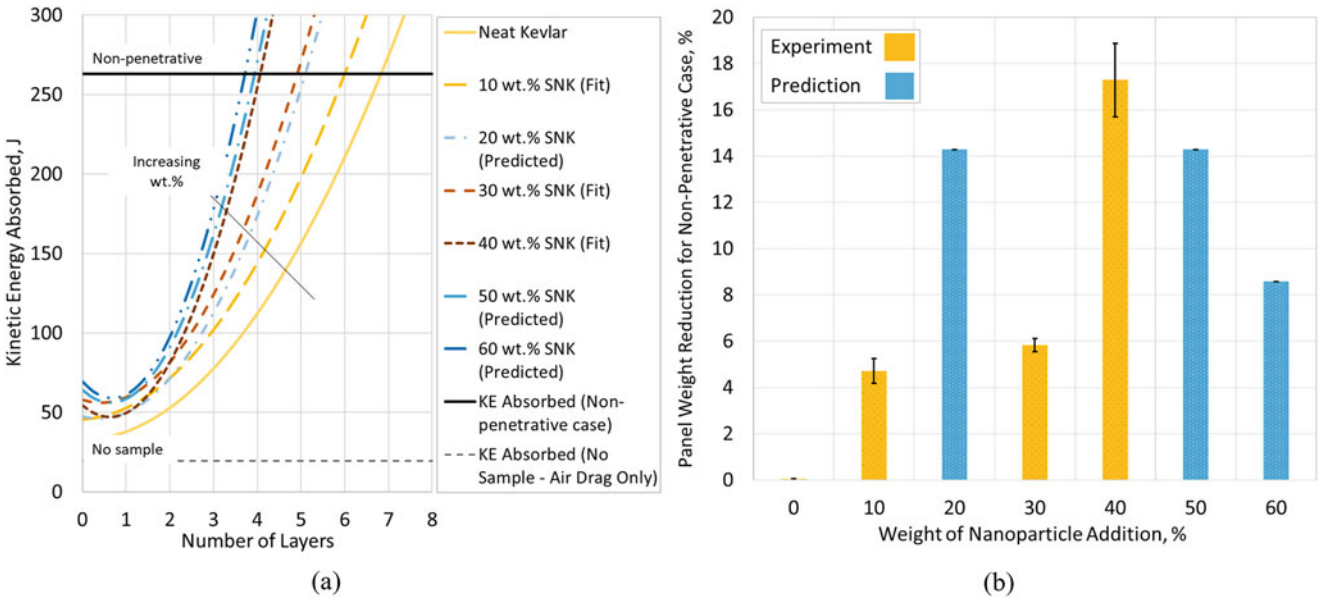


**Fig. 3.7** (**a**) Curve fits and predictions for the kinetic energy absorbed versus number of layers for various percentages by weight of nanoparticle addition and (**b**) measured and predicted overall weight reduction for multilayered SNK versus neat panels for various percentages by weight of nanoparticle addition for the non-penetrative case

Since the addition of nanoparticles to the fabric results in an overall weight increase for the treated fabric in comparison to the neat fabric, it is illustrative to ascertain the relative weight of multilayered samples (or panels) for the non-penetrative case. The percentage weight reduction achieved for the non-penetrative samples versus the percentage by weight of nanoparticle addition is plotted in Fig. 3.7b. Depending on the number of layers required for the non-penetrative case at various treatment levels, the overall weight reduction achieved can fluctuate. It is found that the best overall weight reduction for the non-penetrative case is 17.29% for the 40 wt.% treatment level vis-à-vis the neat case.

### 3.3.3 *Flexibility Tests*

The tip deflection angles (measured clockwise from the horizontal) as obtained from the tests are plotted in Fig. 3.8. A consistent decrement is seen in the tip deflection angle as the percentage by weight of nanoparticle addition is increased. The tip deflection angle decreases from $\theta = 33°$ for the neat fabric to $\theta = 19°$ for the 40 wt.% treated fabric.

Digital image analysis of the photographs from the flexibility tests is used to obtain the deflection curves for the fabric samples. The deflections are measured at approximately 10 mm horizontal spacing for all nine trials across three samples for each treatment level, and the average deflections are plotted in Fig. 3.9a. The measured deflection can be approximated using the theoretical deflection curve for a cantilevered beam under uniform distributed loading given by

$$\mathrm{y} = -\frac{q}{24\mathrm{EI}}\left(6{L_\mathrm{c}}^2x^2 - 4L_\mathrm{c}x^3 + x^4\right) \tag{3.4}$$

where $q$ is the weight per unit length of the neat or treated fabric, $L_\mathrm{c}$ is the length of the cantilever, EI is the flexural rigidity and $(x, \mathrm{y})$ are the measured coordinates on the deflected fabric. The theoretical deflection curve fits obtained using the method of least squares for the measured deflections are plotted in Fig. 3.9a, and the flexural rigidity for each case is educed from the corresponding fitting curve. The educed flexural rigidities range from 48.9 $\mu\mathrm{Nm}^2$ for the neat fabric to 113.7 $\mu\mathrm{Nm}^2$ for the 40 wt.% SNK, as shown in Fig. 3.9b. It is interesting to note that while treating the fabric with nanoparticles does increase both its weight as well as bending stiffness, the influence of stiffness is seen to dominate in the flexibility tests. This is in line with the observation from SEM images that at higher percentages by weight of nanoparticle treatment, the particles are seen to agglomerate in the yarn interstitial and crossover spaces as opposed to along the crests of cross yarns. The impregnation of the nanoparticles into these spaces tends to restrict the rotational degree of freedom at yarn crossover points to a greater extent, leading to higher flexural rigidity.

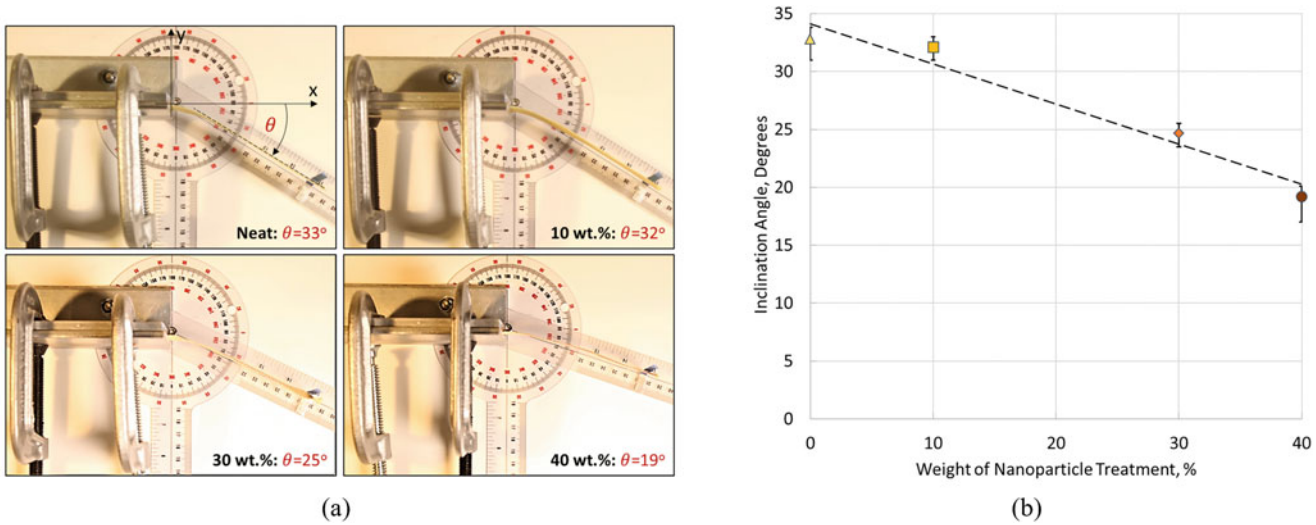


**Fig. 3.8** (**a**) Photographs of neat and SNK flexibility tests and (**b**) measured tip deflection angle versus percentage by weight of nanoparticle treatment from flexibility tests

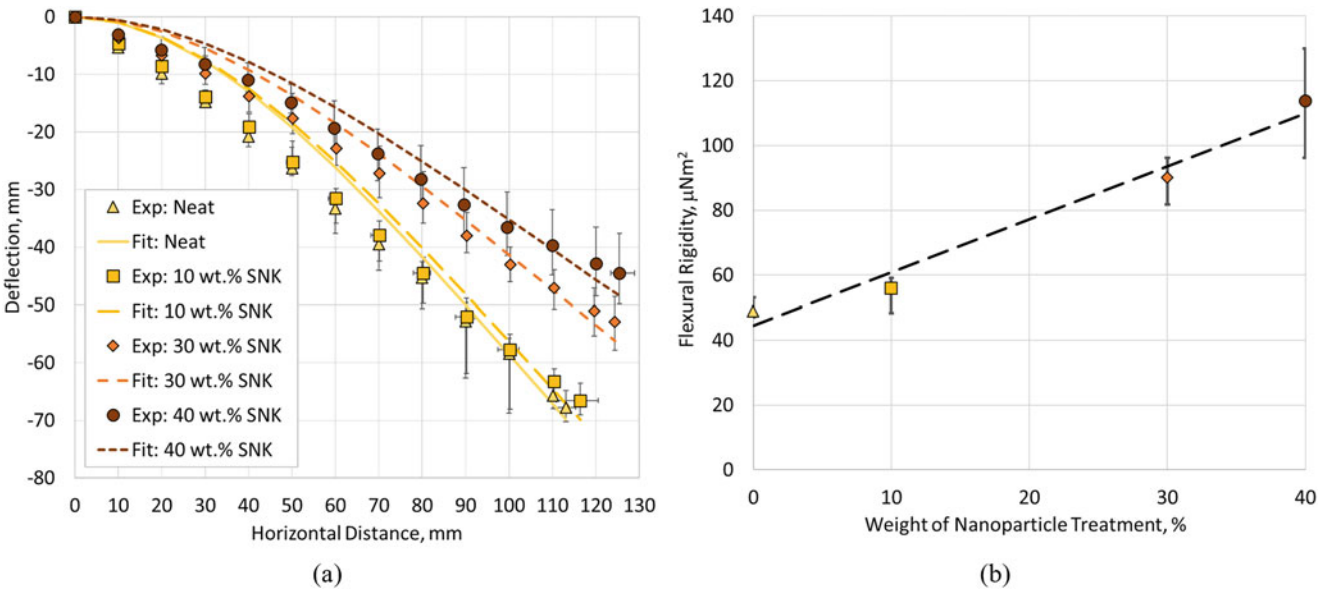


**Fig. 3.9** (**a**) Deflection curve fits for measurements and (**b**) educed flexural rigidity versus percentage by weight of nanoparticle treatment from flexibility tests on neat and treated Kevlar

## 3.4 Conclusion

Ballistic impact tests on SNK fabric indicate superior performance than neat cloth of comparable mass. In the non-penetrative scenario, the 40% SNK has a 17% mass advantage over neat Kevlar (owing to fewer layers). At higher treatment levels, SEM imaging shows nanoparticle infiltration and aggregation in interstitial regions at yarn crossover locations. This reduces yarn mobility and increases inter-yarn friction, allowing secondary yarns to participate in the impact mitigation mechanism. The damaged zone area correlates strongly with the kinetic energy absorbed at higher treatment levels. However, at a threshold treatment level of 40%, nanoparticles coat the fabric surface in several layers, indicating that increasing the percentage by weight of nanoparticle addition may not enhance yarn-yarn interacting mechanisms. Using experimental data, a semiempirical model was validated to incorporate the influence of layer number and treatment level on kinetic energy absorbed. To test SNK without dislodging the impregnated nanoparticles, a customized version of standard fabric flexibility tests was created. The measured tip deflection angle decreases from 33° for the neat fabric to 19° for the 40 wt.% SNK fabric. The flexural rigidity

educed from the deflection curves ranges from 48.9 μNm$^2$ for the neat fabric to 113.7 μNm$^2$ for the 40 wt.% SNK. Further investigations into quasi-static and dynamic yarn pull-out behavior could provide insights into the enhancement in frictional mechanisms due to nanoparticle treatment. The development of a more precise and automated nanoparticle impregnation process could also improve the uniformity of nanoparticle distribution within the fabric. Hybrid structural materials like SNK, along with additive and hybrid fabrication processes reaching critical technical maturity, have the potential to enable multifunctional structural solutions for current and emerging engineering challenges.

**Acknowledgments** Support for this work from the Ray and Linda Booker Fellowship in Aerospace Engineering awarded through the OSU Foundation is gratefully acknowledged. Thanks are due to Oluwafemi Akinmolayan for helping with the flexibility tests.

## References

1. Naveen, J., Jayakrishna, K., Hameed Sultan, M.T.B., Amir, S.M.M.: Ballistic performance of natural fiber based soft and hard body armour-a mini review. Front. Mater. **7**, 440 (2020)
2. Prosser, R.A., Cohen, S.H., Segars, R.A.: Heat as a factor in the penetration of cloth ballistic panels by 0.22 caliber projectiles. Text. Res. J. **70**, 709–722 (2000)
3. Tan, V.B.C., Tay, T.E., Teo, W.K.: Strengthening fabric armour with silica colloidal suspensions. Int. J. Solids Struct. **42**, 1561–1576 (2005)
4. Zeng, X.S., Shim, V.P.W., Tan, V.B.C.: Influence of boundary conditions on the ballistic performance of high-strength fabric targets. Int. J. Impact. Eng. **32**(1-4), 631–642 (2005)
5. Lee, B.W., Kim, I.J., Kim, C.G.: The influence of the particle size of silica on the ballistic performance of fabrics impregnated with silica colloidal suspension. J. Compos. Mater. **43**(23), 2679–2698 (2009)
6. Nadler, B., Steigmann, D.J.: A model for frictional slip in woven fabrics. Comptes Rendus Mecanique. **331**, 797–804 (2003)
7. Zeng, X.S., Tan, V.B.C., Shim, V.P.W.: Modelling inter-yarn friction in woven fabric armour. Int. J. Numer. Methods Eng. **66**, 1309–1330 (2006)
8. Duan, Y., Keefe, M., Bogetti, T.A., Cheeseman, B.A.: Modeling the role of friction during ballistic impact of a high-strength plain-weave fabric. Compos. Struct. **68**, 331–337 (2005)
9. Montgomery, T.G., Grady, P.L.: The effects of projectile geometry on the performance of ballistic fabrics. Text. Res. J. **52**, 442–450 (1982)
10. Tan, V.B.C., Lim, C.T., Cheong, C.H.: Perforation of high-strength fabric by projectiles of different geometry. Int. J. Impact. Eng. **28**, 207–222 (2003)
11. Bender, J., Wagner, N.J.: Reversible shear thickening in monodisperse and bidisperse colloidal dispersions. J. Rheol. **40**, 899–916 (1996)
12. Lee, Y.S., Wagner, N.J.: Dynamic properties of shear thickening colloidal suspensions. Rheol. Acta. **42**, 199–208 (2003)
13. Khodadadi, A., Liaghat, G., Vahid, S., Sabet, A.R., Hadavinia, H.: Ballistic performance of Kevlar fabric impregnated with nanosilica/PEG shear thickening fluid. Compos. B. Eng. **162**, 643–652 (2019)
14. Qin, J., Guo, B., Zhang, L., Wang, T., Zhang, G., Shi, X.: Soft armor materials constructed with Kevlar fabric and a novel shear thickening fluid. Compos. B Eng. **183**, 107686 (2020)
15. Nilakantan, G., Merrill, R.L., Keefe, M., Gillespie, J.W., Wetzel, E.D.: Experimental investigation of the role of frictional yarn pull-out and windowing on the probabilistic impact response of kevlar fabrics. Compos. B. Eng. **68**, 215–229 (2015)
16. Hasanzadeh, M., Mottaghitalab, V., Babaei, H., Rezaei, M.: The influence of carbon nanotubes on quasi-static puncture resistance and yarn pull-out behavior of shear-thickening fluids (STFs) impregnated woven fabrics. Compos. Part A Appl. Sci. Manuf. **88**, 263–271 (2016)
17. Mittal, G., Nešović, K., Rhee, K.Y., Mišković-Stanković, V.: Investigation of corrosion behaviour of carbon nanotubes coated basalt fabric as a reinforcement material. Compos. B. Eng. **178**, 107493 (2019)
18. Gürgen, S., Kuşhan, M.C.: The ballistic performance of aramid based fabrics impregnated with multi-phase shear thickening fluids. Polym. Test. **64**, 296–306 (2017)
19. Yadav, B.N., Muchhala, D., Singh, P., Venkat, A.N.C., Mondal, D.P.: Synergic effect of MWCNTs and SiC addition on microstructure and mechanical properties of closed-cell Al–SiC-MWCNTs HCFs. Compos. B. Eng. **172**, 458–471 (2019)
20. Gürgen, S., Kuşhan, M.C., Li, W.: Shear thickening fluids in protective applications: a review. Prog. Polym. Sci. **75**, 48–72 (2017)
21. Egres Jr, R.G., Lee, Y.S., Kirkwood, J.E., Kirkwood, K.M., Wetzl, E.D., Wagner, N.J.: "Liquid armor": protective fabrics utilizing shear thickening fluids. In: IFAI 4th International Conference on Safety and Protective Fabrics, October 26–27, Pittsburgh, PA (2004)
22. Abtew, M.A., Boussu, F., Bruniaux, P.: Dynamic impact protective body armour: a comprehensive appraisal on panel engineering design and its prospective materials. Def. Technol. **17**(6), 2027–2049 (2021)
23. Malakooti, M.H., Hwang, H.S., Goulbourne, N.C., Sodano, H.A.: Role of ZnO nanowire arrays on the impact response of aramid fabrics. Compos. B Eng. **127**, 222–231 (2017)
24. Kim, Y.H., Sathish Kumar, S.K., Park, Y., Kwon, H., Kim, C.G.: High-velocity impact onto a high-frictional fabric treated with adhesive spray coating and shear thickening fluid impregnation. Compos. B Eng. **185**, 107742 (2020)
25. Caprino, G., Lopresto, V., Santoro, D.: Ballistic impact behaviour of stitched graphite/epoxy Compos. Sci. Technol. **67**, 325–335 (2007)
26. Kanesalingam, S., Nayak, R., Wang, L., Padhye, R., Arnold, L.: Stab and puncture resistance of silica-coated Kevlar–wool and Kevlar–wool–nylon fabrics in quasistatic conditions. Text. Res. J. **89**, 2219–2235 (2019)
27. Dong, Z., Sun, C.T.: Testing and modeling of yarn pull-out in plain woven Kevlar fabrics. Compos. Part A Appl. Sci. Manuf. **40**, 1863–1869 (2009)
28. Manimala, J.M., Sun, C.: Investigation of failure in Kevlar fabric under transverse indentation using a homogenized continuum constitutive model. Text. Res. J. **84**, 388–398 (2014)

29. Chu, C.K., Chen, Y.L.: Ballistic-proof effects of various woven constructions. Fibres Text. East. Eur. **18-6**(83), 63–67 (2010)
30. NIJ Standard 0108.01 – Ballistic Resistant Protective Materials. NIJ Standard 0108.01 (1985)
31. Randjbaran, E., Zahari, R., Abdul Jalil, N.A., Abang Abdul Majid, D.L.: Hybrid composite laminates reinforced with Kevlar/carbon/glass woven fabrics for ballistic impact testing. Sci. World J. **413753** (2014)
32. ASTM D1388-18 Standard Test Method for Stiffness of Fabrics. ASTM International (2018)
33. ISO Standard – Textiles-Test methods for nonwovens-Part 7: determination of bending length. BS EN ISO 9073-7 (1998)

# Chapter 4
# Mixed-Mode Dynamic Fracture Behavior of Soda-Lime Glass Studied using Digital Gradient Sensing Method


**S. Dondeti and H. V. Tippur**

**Abstract** Structures often fail under combined tension and shear loads, and hence, it is critical to understand the mixed-mode fracture behavior of materials. In this work, the dynamic mixed-mode fracture of soda-lime glass (SLG) was experimentally investigated using the full-field optical method—digital gradient sensing (DGS). Freestanding single-edge notched specimens were subjected to reverse impact loading using a modified Hopkinson pressure bar. By eccentrically loading the specimens parallel to the initial notch, various mode mixities, from pure mode-I to nearly pure mode-II conditions, were achieved by changing the amount of eccentricity. Ultrahigh-speed photography was utilized in conjunction with DGS methodology to measure the angular deflection of light rays that are proportional to in-plane stress gradients in two orthogonal directions. In this ongoing research, mode-I and mode-II stress intensity factor histories prior to and at crack initiation will be evaluated in the next phase by performing an over-deterministic least squares analysis on optically measured full-field data. From the critical stress intensity factors at crack initiation, a fracture envelope for SLG encompassing different mode mixities will be developed. From the fractured samples, kink angles will be measured and compared with established fracture criteria.

**Keywords** Dynamic fracture · Mixed-mode fracture · Optical measurements · Fracture envelope · Transparent materials

## 4.1 Introduction

Soda-lime glass (SLG) is a commonly used structural material in many civilian and military structural applications due to its optical transparency, hardness, corrosive resistance, and low cost. Despite its ubiquity, the dynamic fracture behavior of SLG under mixed-mode loading conditions is not yet reported in the literature. Most mixed-mode investigations to date are limited to brittle polymers. Some examples include the works of Kirugulige and Tippur [1], who have studied mixed-mode dynamic fracture in polymeric Functionally graded materials (FGM) using optical interferometry—CGS. Sundaram and Tippur [2] have investigated mixed-mode dynamic fracture behaviors of PMMA and polycarbonate using DGS. Investigating the dynamic fracture in SLG using full-field optical methods, however, poses unique challenges due to its high stiffness and low toughness. Furthermore, crack speeds in this material exceed 1500 m/s, accompanied by highly localized crack tip deformations. Sundaram and Tippur [3] were the first to successfully study dynamic fracture in SLG by extending DGS to this difficult material. Recently, Dondeti and Tippur [4] performed a comparative study to investigate dynamic fracture in SLG using full-field optical methods, photoelasticity, DIC, and DGS methods. Their results show that the DGS method allowed both visualization and quantification of dynamic fracture parameters, whereas the other two methods could not. This led Dondeti and Tippur [5] to use DGS to investigate cascading crack branching in SLG and identify a few fracture mechanics-based precursors of the crack branching phenomenon. The focus of this study is to examine mixed-mode dynamic fracture using DGS in conjunction with ultrahigh-speed photography and gather relevant data for SLG.

S. Dondeti (✉) · H. V. Tippur
Department of Mechanical Engineering, Auburn University, Auburn, AL, USA
e-mail: szd0057@auburn.edu; tippuhv@auburn.edu



S. Mates et al. (eds.), *Dynamic Behavior of Materials, Volume 1*, Conference Proceedings of the Society for Experimental Mechanics Series, https://doi.org/10.1007/978-3-031-17453-7_4

## 4.2 Experimental

Planar SLG specimens of geometry 50 mm × 100 mm were cut from a 5.7 mm thick sheet and a 12 mm long notch was machined into a 100 mm edge, Fig. 4.1a. To achieve crack initiation and growth over a range of mode mixities, loading eccentricity ($e$)—the distance between the notch and load application point on the opposite 100 mm edge—was varied. Five different mixed-mode specimens were studied using eccentricity, $e = 0$, 6, 12, 18, and 24 mm while maintaining a constant notch length of $a = 12$ mm in all specimens. These SLG specimens were subjected to reverse impact loading as shown in Fig. 4.1b. A modified Hopkinson pressure bar was used to dynamically load the specimen via stress waves and schematic representation of the experimental setup is shown in Fig. 4.2. A steel striker (305 mm long, 25.4 mm diameter) was made to impact a steel long-bar (1830 mm long, 25.4 mm diameter) to generate a compressive stress wave that loaded the specimens. A trigger pulse was generated at impact, which in turn initiated the camera and flash lamps. An ultrahigh speed Kirana-05M single sensor (924 × 768 pixels; capable of recording up to 180 full resolution images and at up to 5 million fps) camera, positioned 4 m in front of the specimen, was used for recording images. A random black and white speckle pattern created on a planar surface (speckle target) was positioned at a distance of 1 m behind the SLG specimen and recorded through the region of interest in the specimen. A pair of high-energy flash lamps was used to illuminate the speckles at 1 Mfps in these experiments.

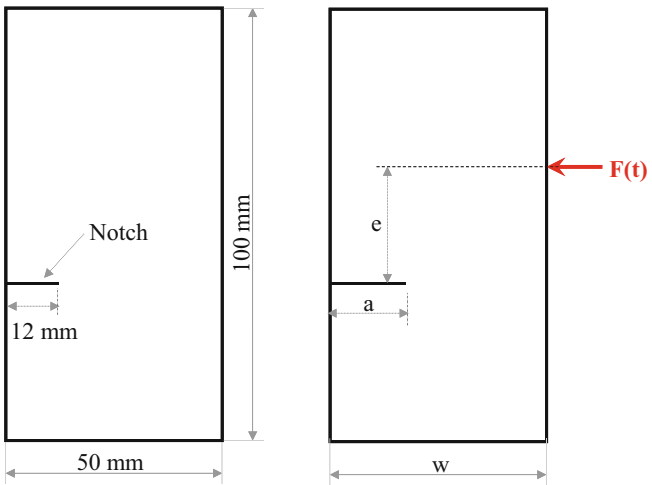


**Fig. 4.1** (**a**) 50 mm × 100 mm mixed-mode soda-lime glass specimen geometry along with (**b**) eccentric reverse impact loading configuration

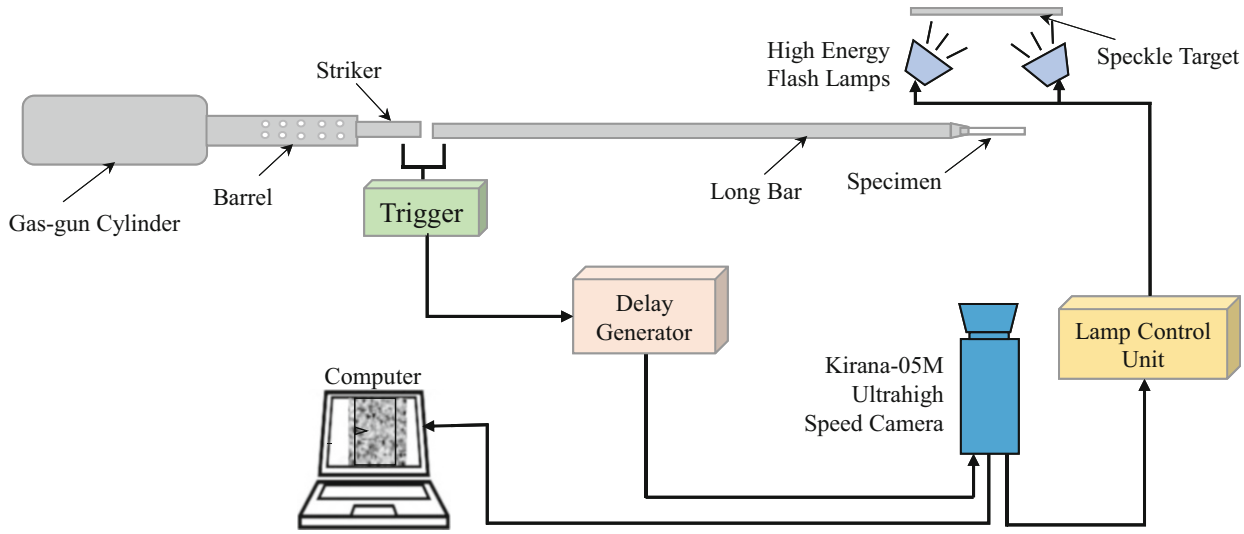


**Fig. 4.2** Experimental setup to study dynamic fracture of glass using DGS

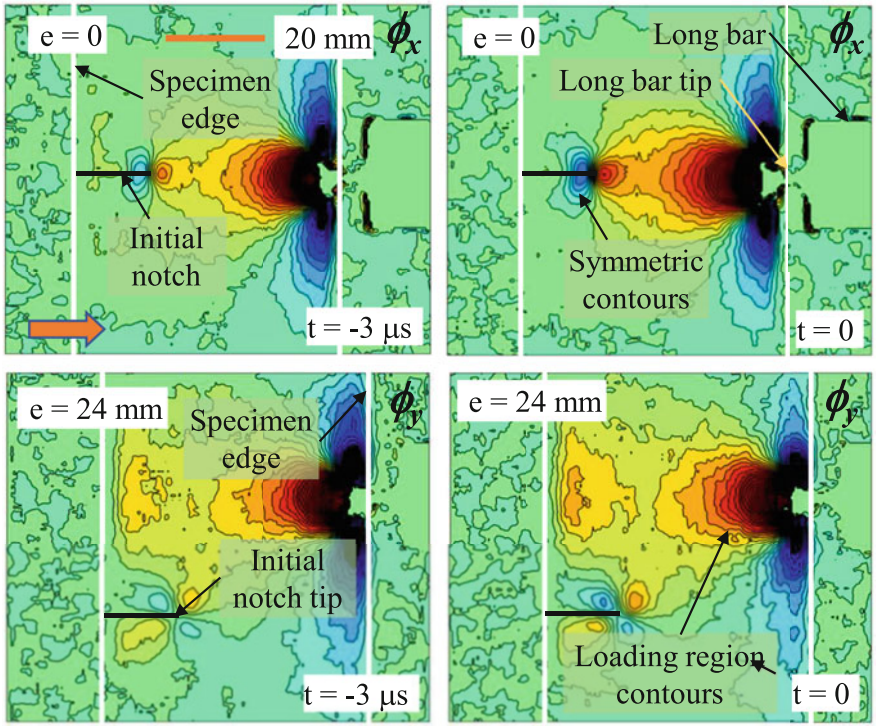


**Fig. 4.3** Angular deflection contours proportional to stress gradients in the $x$- and $y$-directions (time, $\tau = 0$ corresponds to crack branching). Top and bottom rows correspond to mode-$I$ ($e = 0$) and mixed-mode ($e = 24$ mm) fracture initiation

## 4.3 Optical Measurements

Transmission mode DGS measures the angular deflection of light rays in two mutually perpendicular planes ($x$-$z$ and $y$-$z$ planes, $z$ being the optical axis), caused by combined refractive index and specimen thickness changes due to the local state of stress. Those angular deflections $\phi_x$ and $\phi_y$ are proportional to gradients of the sum of in-plane normal stresses ($\sigma_x + \sigma_y$) in the $x$- and $y$-directions, respectively. The angular deflections are quantified by correlating speckle images in the deformed and the reference state of the SLG specimen. The details of the working principle of the method are avoided here for brevity but can be found in Ref. [6]. Figure 4.3 shows representative angular deflection contours in the pre-initiation and initiation stages of fracture events, at time instants of $t = -3$ μs and $-0$. Here, time, $t = 0$, corresponds to crack initiation at the notch tip. The contours have a closed lobe structure converging to a point, as shown in Fig. 4.3, due to the singular nature of stress gradients at the crack tip location. This allows easy detection of the crack tip location from post-processed images.

## 4.4 Work-in-Progress

In the next phase of this research, the mode-I and mode-II stress intensity factor histories, $K_I(t)$ and $K_{II}(t)$, will be evaluated using over-deterministic least-squares analyses of optical measurements (stress gradients $\frac{\partial}{\partial x}(\sigma_x + \sigma_y)$, $\frac{\partial}{\partial y}(\sigma_x + \sigma_y)$ ) in conjunction with the elasto-dynamic crack tip fields. Currently, the evaluation of fracture parameters from optical measurements is underway. Next, a dynamic fracture envelope for SLG under mixed-mode loading conditions will be obtained. The existing fracture criteria will be compared with the empirical fracture envelope. Additional crack branching features, if any, will be identified and studied.

## 4.5 Summary

Mixed-mode dynamic fracture of SLG is being investigated using the full-field optical method DGS. Ultrahigh-speed photography used in conjunction with DGS was used to map contours of angular deflections in the pre-initiation and post-initiation stages. The dynamic fracture parameters are currently being evaluated under various mode-mixity conditions. Generation of a dynamic fracture envelope during mixed-mode loading will provide an insight into SLG fracture behavior. Finally, kink angles will be measured, and the fracture envelope will be compared with existing fracture criteria.

## References

1. Kirugulige, M.S., Tippur, H.V.: Mixed-mode dynamic crack growth in functionally graded glass-filled epoxy. Exp. Mech. **46**(2), 269–281 (2006)
2. Sundaram, B.M., Tippur, H.V.: Dynamic mixed-mode fracture behaviors of PMMA and polycarbonate. Eng. Fract. Mech. **176**, 186–212 (2017)
3. Sundaram, B.M., Tippur, H.V.: Full-field measurement of contact-point and crack-tip deformations in soda-lime glass. Part-II: stress wave loading. Int. J. Appl. Glas. Sci. **9**(1), 123–136 (2018)
4. Dondeti, S., Tippur, H.V.: A comparative study of dynamic fracture of soda-lime glass using photoelasticity, digital image correlation and digital gradient sensing techniques. Exp. Mech. **60**(2), 217–233 (2020)
5. Dondeti, S., Tippur, H.V.: Cascading crack bifurcations in soda-lime glass: quantification of fracture mechanics-based precursors using Digital Gradient Sensing. Int. J. Solids Struct. **234**, 111252 (2022)
6. Periasamy, C., Tippur, H.V.: Full-field digital gradient sensing method for evaluating stress gradients in transparent solids. Appl. Opt. **51**(12), 2088–2097 (2012)

# Chapter 5
# Measurement of Cone-Cylinder Deceleration in Sand


**Stephan Bless, Sophia R. Mercurio, Magued Iskander, and James Mathis**

**Abstract** Cone cylinders measuring 25 mm in diameter and weighing 108 g were shot into dense silica sand beds, mostly at 200 m/s, using a vertical-firing 75-mm diameter compressed-air gun. Velocity-time records were obtained with a multichannel homodyne photon Doppler velocimeter (PDV). Good values for deceleration were obtained below about 150 m/s. In terms of Poncelet parameters, the Poncelet drag coefficient for dense sand was bivalued, being 2.0 above about 80 m/s and 1.5 below that, and was unaffected by saturation. It was about 1.0 for medium dense sand. Values of the R term were 250–450 kPa.

**Keywords** Sand · Poncelet · PDV · Vertical impact · Drag

## 5.1 Introduction

Investigations of impact-driven penetration into soils have a long history. Research has been motivated by many engineering applications, including military and civilian. In addition, soils are a common example of granular material, and the response of granular materials to impact loading is a subject of scientific interest for its own sake.

"Deep" penetration is defined as cases in which free surface effects can be ignored, and local geostatic pressure continuously increases with distance. To study deep penetration, we have developed and employed a relatively vertical impact facility.

A review of impact and penetration into sand has recently appeared in [1]. An important theme that emerges from that review is that for deep penetration, the initial penetration resistance is due to target inertia, and it is very high, proportional to velocity squared, and it, therefore, is of relatively short duration. As the projectile slows down, the resisting stress is eventually due to strength and friction. In that way, it resembles conventional bearing stress, and it is expected to increase with depth. In many cases of practical interest, late-stage resistance has a relatively large effect on the final depth of penetration (DOP).

The observations summarized in [1] have been augmented by several more recent studies, [2] measured deceleration of spheres in sand, [3] measured the force on bullets penetrating sand, [4] measured deceleration of rods penetrating sand, [5] measured resisting force on rods moving through sand at high speeds, and [6] studied bullets penetrating sand and other granular materials and paid particular attention to the instabilities that occur near the end of the penetration channel. Only [2] and [4] examined vertical trajectories.

## 5.2 Launcher and Projectiles

A vertical impact facility was designed and constructed at the Southwest Research Institute (SwRI) in San Antonio, Tx. Projectiles were launched with a vertically mounted compressed gas gun positioned on-center above a soil specimen prepared in a standard 55-gal steel target drum, as shown in Fig. 5.1. The projectiles were launched down the barrel and

S. Bless (✉) · S. R. Mercurio · M. Iskander
Department of Civil and Urban Engineering, Tandon School of Engineering at New York University, Brooklyn, NY, USA
e-mail: sbless@nyu.edu; SRM392@nyu.edu; Iskander@nyu.edu

J. Mathis
Southwest Research Institute, San Antonio, TX, USA
e-mail: james.mathis@swri.org



S. Mates et al. (eds.), *Dynamic Behavior of Materials, Volume 1*, Conference Proceedings of the Society for Experimental Mechanics Series, https://doi.org/10.1007/978-3-031-17453-7_5

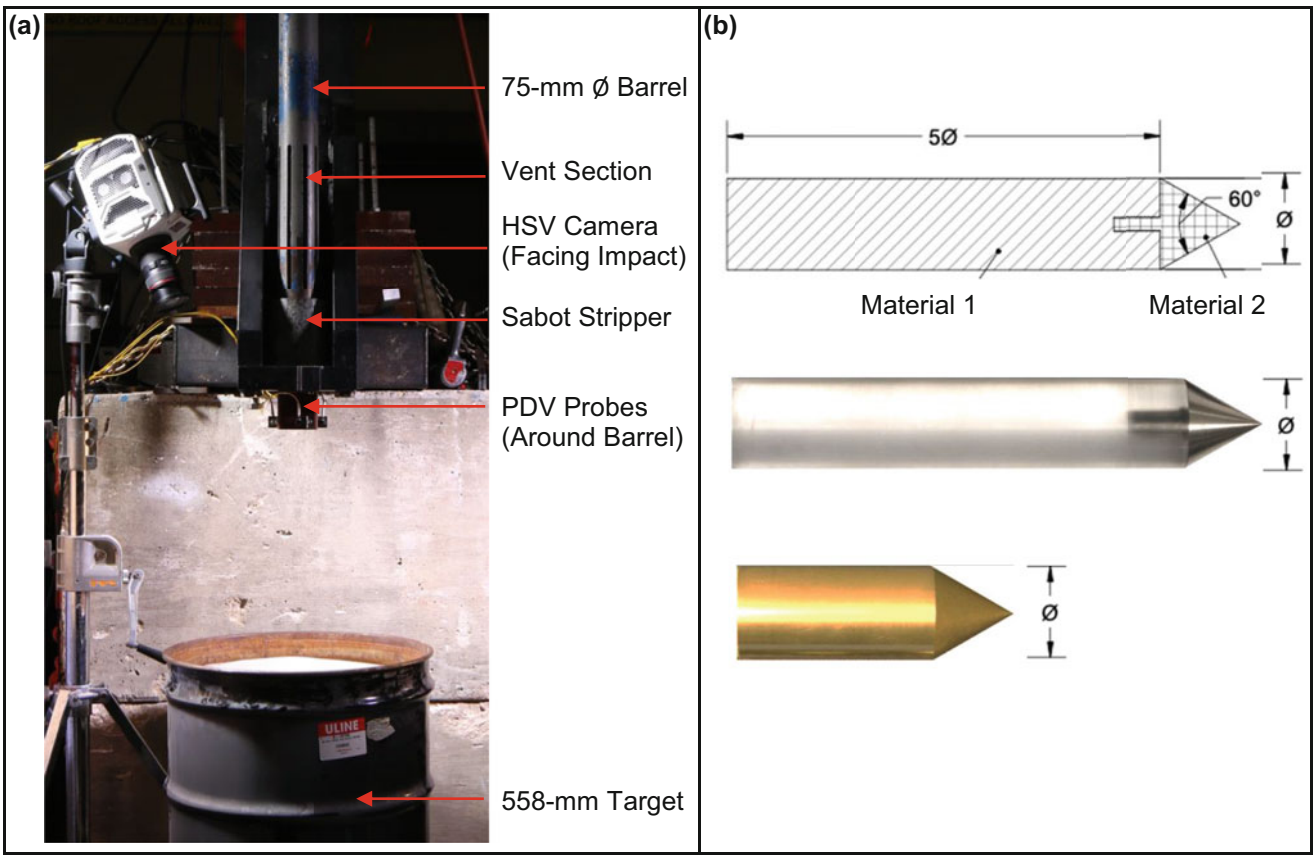


**Fig. 5.1** (**a**) Launcher and target configuration; (**b**) projectile design

through a vented section using a sabot. The sabot was separated by a hard stop against an aperture plate (sabot stripper) to release the 25-mm-diameter conical projectile. Impact speed was measured with a video camera (see below).

The designed projectile consisted of a conical nose (material one) threaded into a lighter shank (material two) as shown in Fig. 5.1a. Material one was HRC30 steel for both projectiles, while material two was polycarbonate for the standard projectile and 6061-T6 aluminum for the short projectile. The standard shank was 5 diameters long (125 mm) with a 60° conical nose, resulting in a total length of 149 mm and a total mass of 108 g. The length of the short projectile's shank was calculated to mimic the mass of the standard shank.

The projectiles were launched with one-piece polyethylene sabots with an intended velocity of 200 m/s, varying for some tests. The rear face of the projectile was covered with retroreflective tape to facilitate PDV measurements. The projectiles were reused as no visible deformation was noticed.

The compressed gas gun is mounted on a rail and hoisted above the target drum to shoot vertically downward. The gun uses either nitrogen or helium as the driving gas. It has a launch tube with a 75 mm inner diameter (ID) and a 3000-psi breech. In test firings, it was found that 490 psi nitrogen was sufficient to achieve the intended velocity.

## 5.3 Instrumentation

Independent measurements of impact velocity were recorded by the individual components of the instrumentation system. All instrumentation was triggered synchronously, before the projectile impacted the target. High-speed video (HSV) captured impact and early-time penetration from different views. A multichannel PDV system recorded the velocity-time history during projectile penetration.

Two high-speed video (HSV) cameras recorded the projectile to estimate the angle of attack and obtain an independent measurement of impact velocity. One HSV camera recorded the projectile at 22,000 frames per second (fps), looking

downward. It was positioned above the target drum with an offset of 20° from the impact point. The second HSV camera recorded the projectile at 37,000 fps from a horizontal view.

PDV obtains frequency measurements of Doppler-shifted light waves reflected from a target. The Doppler shift is computed from the beat frequency produced by the interference of two light beams, a reference beam, and a target beam. In a traditional homodyne system, one laser is used and the light beam is split to produce both the reference and target signals. For a stationary object, the reference and target signals are the same frequency, and there is no beat frequency. For a moving object, the frequency of the reflected beam is shifted by the Doppler effect.

A homodyne configuration was used for the PDV system. A single 3W IPG Photonics 1550 nm fiber laser source and a NSTec PDV with four channels were used. The light beam was split across the four channels and four reference beams. Each channel required a fiber optic probe to collect the reflected light from the back of the projectile. Each probe was mounted on the sabot stripper, and each probe was independently aligned along the penetration depth and ideally observed the reflection from the tail of the projectile at different time intervals. The target signal is mixed with the reference signal to produce a beat frequency, which is recorded by the oscilloscope. A beat frequency of 1 GHz corresponds to an instantaneous velocity of 775 m/s. Since the record length of the oscilloscope was relatively short, a delay generator was used to postpone the trigger to the scope for a predetermined time, when the projectile was expected to exit the gun barrel. SIRHEN software was employed to process the data to obtain the time history [7].

## 5.4 Sand Targets

Preparation of soil targets with uniform and repeatable densities was a major challenge in this program. Ottawa sand was used to prepare the targets in standard steel 55-gallon drums, with internal dimensions of 571 mm in diameter and 876 mm in height. This is fine siliceous sand consisting of rounded grains with a particle diameter typically between 0.3 mm and 0.15 mm. The maximum and minimum densities of this sand were found to be 1420 kg/m$^3$ and 1800 kg/m$^3$, respectively.

Sand targets were prepared by dry pluviation. A pluviator is a sand raining machine designed to prepare sand samples of uniform relative densities. Typically, a pluviator is composed of a reservoir, a shutter, and diffuser screens [8].

The pluviator used for the tests discussed in this paper consisted of a hopper drum, a shutter, and two diffuser screens (Fig. 5.2c). A standard 55-gallon drum housed the pluviator components. The shutter was created using the bottom of the steel hopper drum and a wooden plate (Fig. 5.2a). A porosity of 4% was specified by the hole pattern. The top diffuser was spaced 25.5 cm below the shutter, and the bottom diffuser was 18 cm below it. The diffusers were both composed of the same 1.6 mm-diameter steel wire mesh that were offset 45° from each other (Fig. 5.2b). A plastic shroud was used to constrain the sand falling from the hopper so it would all end up in the drum. The final density was achieved by controlling the falling speed by means of reverse airflow. The average densities were 1650 and 1740 kg/m$^3$, with an uncertainty of about 1%.

For some tests, the dense sand was then saturated. In soil mechanics, saturation is defined as the condition in which void spaces, which are filled with air during dry conditions, are replaced by water. For this condition, a second step was performed to hydrate the dry, uniformly prepared sand specimen. Uniformly dense packed silica grains were prepared in target drums, and a hydration drum was used to contain the water. A tap was machined into both the target and hydration drums at the same elevation, specified as a minimum height from the bottom of the sand target. To begin the soil saturation, the hydration drum was filled with water to a maximum height of about 5 mm above the bottom of the tap inlet. The estimated infusion rate was approximately 18 mL/s. This procedure was employed to avoid damage to the soil skeleton, which is defined as the solid matrix within the granular media. Saturation, defined as the fraction of voids that are water-filled, is estimated to be 98%.

## 5.5 Experiments

Six tests were selected for analysis because they provide good PDV records for nearly all of the penetration history (Table 5.1). Other tests provided only partial records which were consistent with the complete $V(t)$ histories in these six.

Qualitatively the penetration process is revealed in the vertical-looking HSC. Figure 5.3 shows an image. A crater forms at touchdown, continues to expand after touchdown, narrows with penetration depth, often shows an imprint where the rear of the projectile struck the crater wall, and, unless there is too much deflection, remains open until the projectile has stopped. For dense dry sand, in the baseline configuration, the crater diameter at the surface at the time of the penetration one length is between 80 and 100 mm.

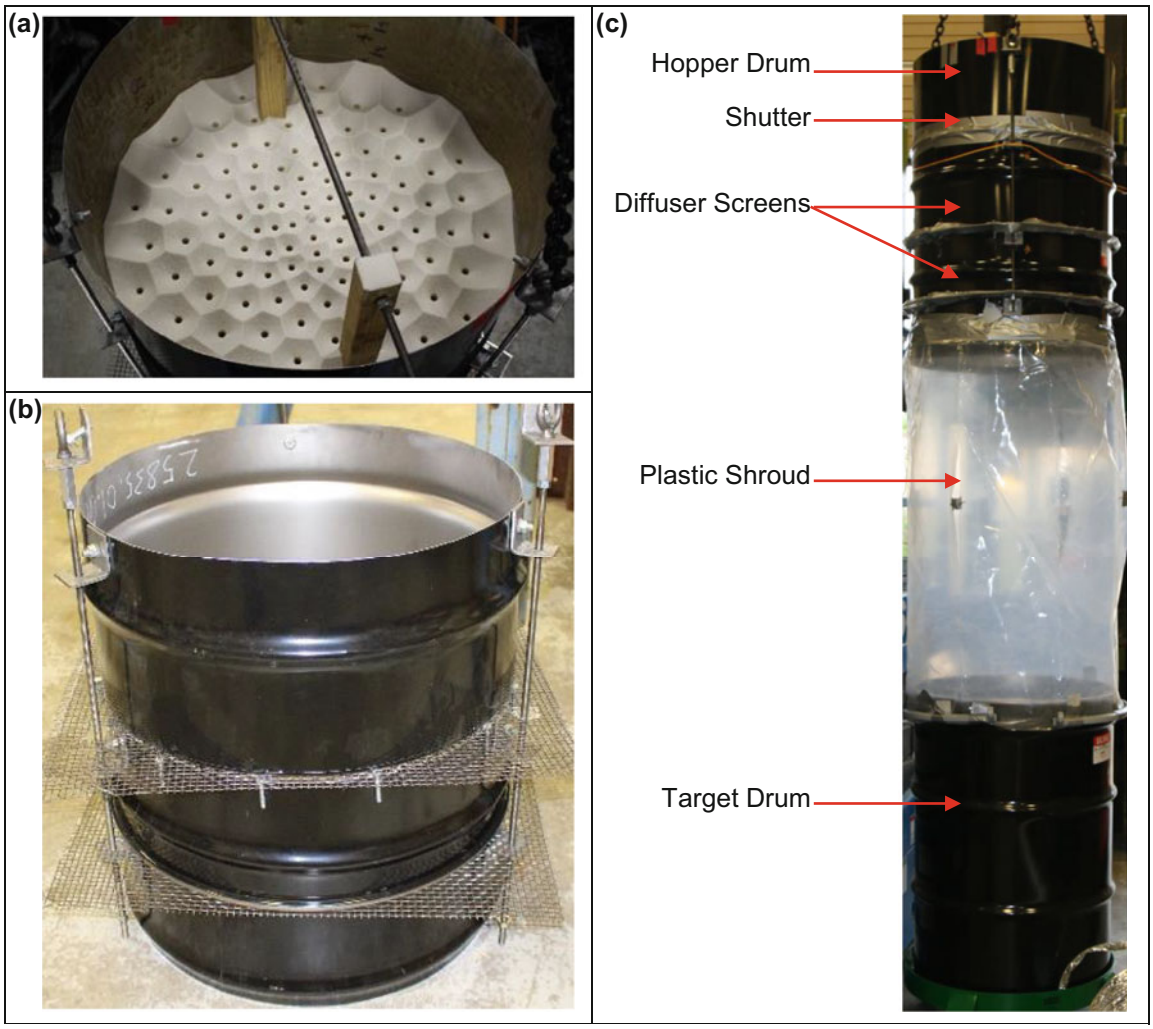


**Fig. 5.2** (**a**) Hopper drum with an open shutter. (**b**) Diffuser assembly with two screens. (**c**) Pluviator assembly

**Table 5.1** Experiments used for PDV Analysis

| Test ID | Projectile | Velocity | Density | Test ID | Projectile. | Velocity | Density |
|---|---|---|---|---|---|---|---|
| T13 | Standard | 204 | 1650 | T18 | Short | 181 | 1740 |
| T15 | Standard | 208 | 1740 | T19 | Standard | 96 | 1740 |
| T17 | Standard | 190 | 2110 (wet) | T21 | Standard | 203 | 1740 |

PDV data for the three baseline conditions—dry dense sand (1740 kg/m$^3$), medium dense sand (1650 kg/m$^3$), and wet sand—are shown in Fig. 5.4. For most of the record, the greatest deceleration occurs for DWS, the least for MDS. However, as the projectiles slow to below about 20 m/s, the deceleration for saturated sand seems to increase faster than for the other cases. All records have the same trend: a region where deceleration is a decreasing function of velocity followed by a region where the deceleration is almost constant. For dry sand, higher density significantly increases the penetration resistance, and water saturation decreases it.

There were two methods to confirm the reliability of the PDV data, and both suggested high confidence in test results. First, there were several cases where PDV records can be compared for the same impact conditions. Reproducibility was excellent, as shown for the dense case in Fig. 5.4. Second, the horizontal viewing camera provides (x,t) data during penetration and also provides a check on the PDV, although only at higher velocities because the view of the projectile is blocked eventually as it dips below the drum rim. Although of lower precision than the PDV, the data from this camera were wholly consistent with the PDV results. An example is shown in Fig. 5.5.

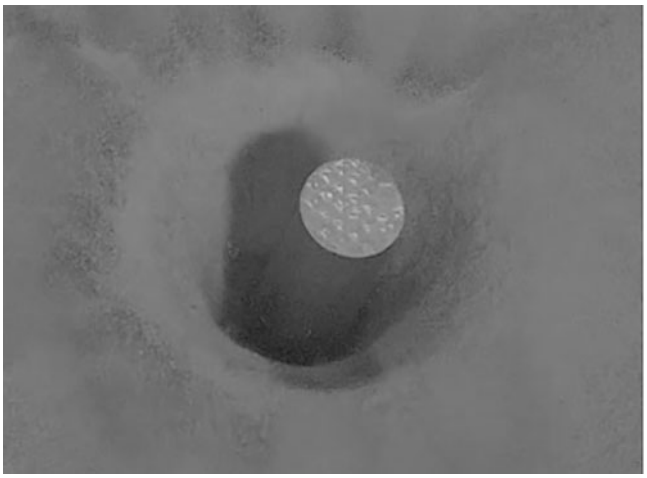

**Fig. 5.3** View of impact in shot 21, at about half penetration

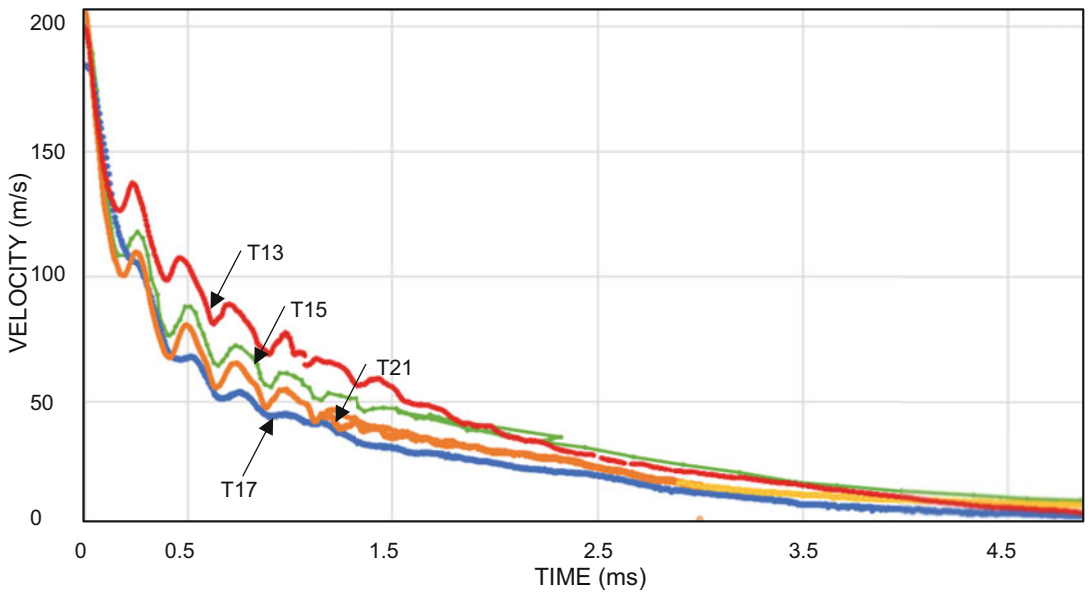


**Fig. 5.4** PDV data for sand types: T13 (medium dense), T15 and T21 (dense), and T17 (saturated)

A problem was encountered with oscillations at early times, examples of which are shown in Fig. 5.5. These are due to acoustic vibrations in the projectile shaft. The reverberation time for a simple longitudinal wave traveling at the sound speed in polycarbonate (2300 m/s) gives an oscillation frequency of 0.1 ms. The observed frequency is a little longer than this, probably because the wave is not purely longitudinal and it is spread out by the nose impact embedment time. The strain in this wave would be about $u/c$, where $u$ is the vibration amplitude (in velocity) and $c$ is sound speed – this gives 0.005, which is reasonable for an elastic wave in the projectile. The vibrations made it difficult to resolve any irregularities in deceleration for the first half of the penetration depth for the baseline projectile and also introduced ambiguity into the precise touchdown time. Oscillations were almost entirely eliminated in excursions with a lower velocity (T19) and with a shorter projectile (T18). However, for the baseline case, it is not possible to precisely compute depth from the PDV records because of the ambiguity in velocity at early times. When DOP is measured by excavation, it is usually 15–25 mm deeper than estimated from integration. We refer to the penetration obtained by integrating the PDV record as the "integrated depth."

Critical angle of attack, defined as when the crater rim is marred by impact from the back of the projectile, was about 10°. This happened in about a quarter of the shots. For the baseline projectile, the AoA does not have a discernable effect on the (v, t) record. It has only a small effect on the final DOP, even though in most cases the projectile is recovered at an angle of 20–40°. Rotation of the projectile apparently happens as it is brought to rest because even for impacts above the critical AoA, the projectile rear surface remains visible until the velocity has dropped below a few m/s. Thus, in sand, for this moderate

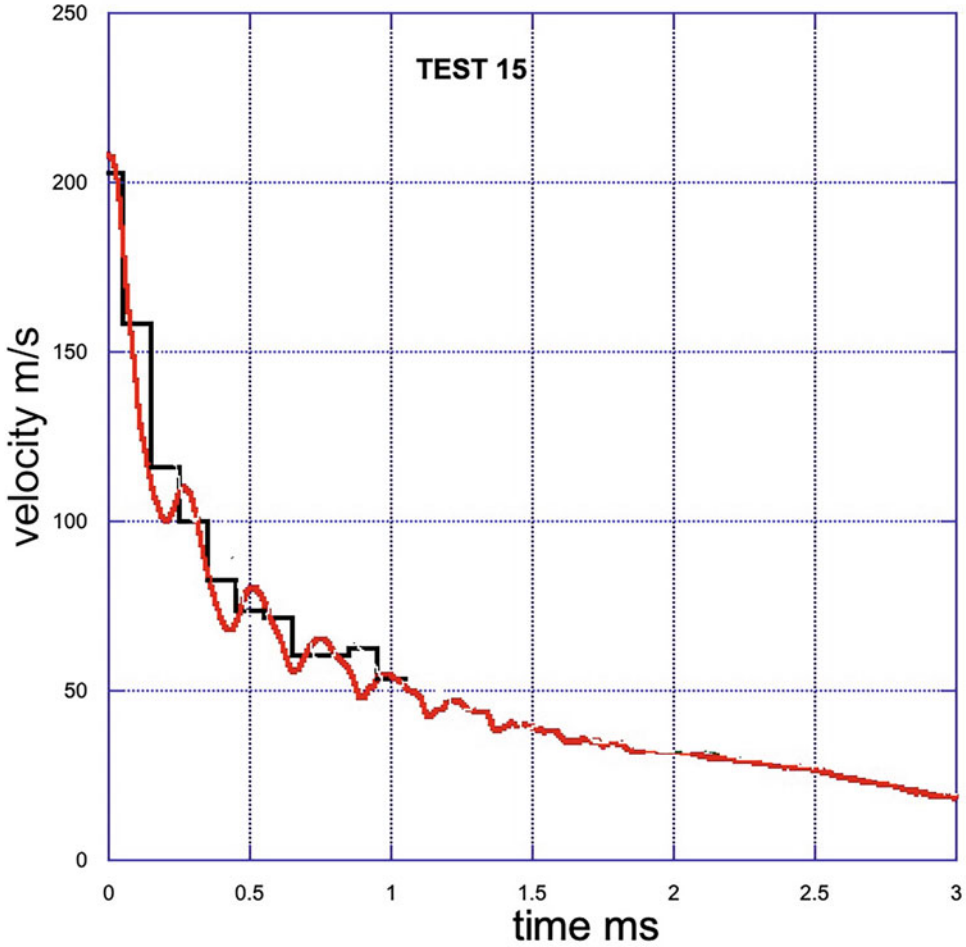


**Fig. 5.5** Velocity vs time for T15, comparison of PDV and high-speed video

slenderness ratio projectile, contact with the crater wall only results in destabilization once the velocity is so low that there is little additional penetration.

## 5.6 Penetration Resistance

The physical quantity of most interest in these experiments is force. Penetration resistance is, defined as the force that resists penetration divided by the cross-sectional area.

$$Q = \frac{F}{A} = -\frac{M\frac{\mathrm{d}V}{\mathrm{d}t}}{A} \tag{5.1}$$

Penetration resistance is proportional to d$V$/d$t$, and as is evident from Fig. 5.6, it decays rapidly with depth. A surprising consequence is that total penetration is not very sensitive to velocity for relatively high velocities. From Fig. 5.6, for impact at 200 m/s, more than three-quarters of the penetration takes place after V has decreased by half.

This was consistent with our measurements of post-test DOP; the final depth of penetration in test 19 (at 96 m/s) was 235 mm, whereas the average of tests 15 and 21, at 208 m/s, was 256 mm.

We discuss penetration resistance in the geo-Poncelet framework [9], according to which

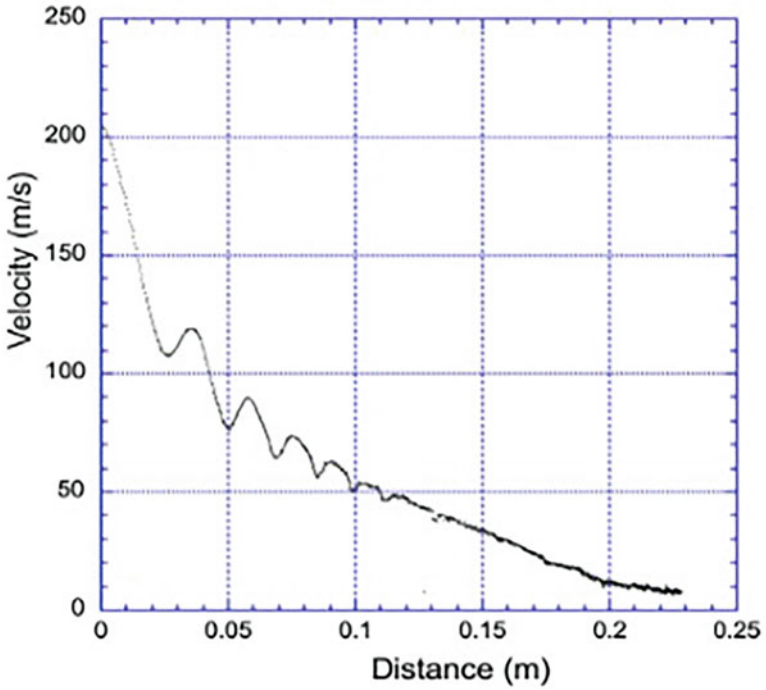


**Fig. 5.6** Velocity as a function of integrated depth in T15

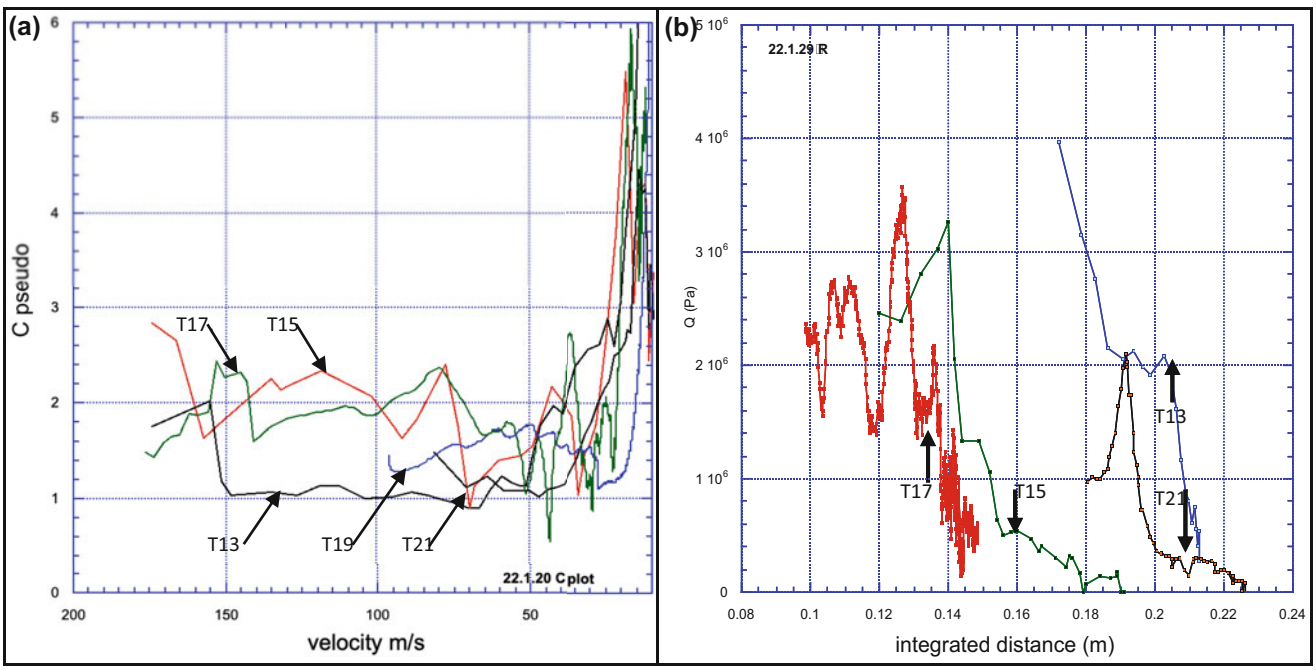


**Fig. 5.7** (**a**) Effective Poncelet drag, from (5.3a); (**b**) stress on a penetrator, from (5.3b)

$$F = \rho C A V^2 + R(z)A \tag{5.2}$$

Where $\rho$ is soil density, $C$ is the Poncelet drag coefficient, and $R(z)$ is the depth-dependent bearing resistance. Working in the context, we plot the $C$ vs velocity and $Q$ vs z in Fig. 5.7.

$$C_{\text{psuedo}} = -\frac{M\left(\frac{dV}{dt}\right)}{\rho A V^2} \text{ and } Q = -\frac{M\left(\frac{dV}{dt}\right)}{A} \quad (5.3a, b)$$

At high velocity, where the first term dominates, $C_{\text{peudo}} = C$. When we fit data using (5.3a), $C_{\text{pseudo}}$ will grow as the second term in (5.2) becomes important and the first term in (5.2) falls as $V^2$. To the extent that (5.2) is correct, eventually, as the projectile sufficiently slows, $Q = R$; *e.g.*, we can evaluate $R$ in (5.2) from the asymptote of $Q$ as $V \rightarrow 0$.

Values of $C_{\text{pseudo}}$ at high velocity and $Q$ at low velocity are plotted in Fig 5.7. Because of the initial oscillations, computing $C_{\text{pseudo}}$ was only possible after considerable smoothing of $V(t)$. Different data sets required somewhat different approaches: these included cubic splines, polynomial fits, and even in some cases using Bézier curves, with the criteria of maximizing fidelity but assuring that the value of $dV/dt$ was never positive. Although $V(t)$ starts at nominally 200 m/s, it is not possible to determine with adequate confidence $dV/dt$ above about 150 m/s due to both the initial oscillation and the possible invalidness of (1) if there be large stress gradients within the projectile. In addition, since we measure $\rho C$, the small uncertainty in density produces a small uncertainty in the values of Poncelet drag.

In Fig. 5.7a, the dense sand experiments all display a jump in values of $C$, similar to what was pointed out in [9] and [10]. The values are about 2 above about 80 m/s and about 1.5 below that. The value of $C$ for saturated is not distinguishable from DDS; hence the greater penetration resistance for wet sand is due primarily to its greater density, not its drag coefficient. Medium dense sand has a significantly lower drag coefficient, close to 1. Drag is more sensitive to density than any other variable tested. This sensitivity probably accounts for slight variations among DDS tests and probably some of the relatively small variation of drag with depth that emerges from the data.

Values of $Q$ are plotted in Fig. 5.7b. $Q$ approaches $R$ as the ratio of the second to the first term in (1) becomes sufficiently large. The homodyne resolution for low velocity is relatively poor, thus $dV/dt$, which is expected to be constant, dissolves into noise as the projectile comes to rest. Assuming $C$ is equal to 2.5, the largest reasonable value in Fig. 5.7a, then for dense sand, the ratio is about 2.3 at 20 m/s and about 10 at 10 m/s. Thus, it is only reasonable to take $Q$ as an approximation to $R$ below about 10 m/s. This point is indicated by vertical arrows in Fig. 5.7b. For dense sand, values of $R$ vary from about 250 to 450 kPa. For medium dense sand, the data for low velocity are imprecise, and R is between 400 and 600 kPa. Likewise, for wet sand, there is quite a lot of jitter, but $R$ is between 100 and 600 kPa. The fact that $Q$ does not decrease monotonically with distance might mean that (2) does not adequately represent the velocity and distance dependence of penetration resistance. Alternatively, it has been suggested that fluctuations in $Q$ are due to force chain buckling [10, 11]. In these impacts, the effect of fluctuations in stress at low velocity has a relatively small effect on the total DOP.

## 5.7 Comparisons to Other Measurements

Deceleration of $L/D = 10$ low-mass 10-mm diameter conical-nose rods penetrating a different dense silica sand (1830 kg/m$^3$) was measured in one test by [4]. They double-differentiated $z(t)$ data and found an effectively constant value of $C = 1.3$ between 55 and 25 m/s, with fluctuations of about 0.1. $Q$ fluctuates for $10 > V > 1.5$ m/s with a mean value of 2.17 MPa and a standard deviation of 1.3 MPa. This behavior is qualitatively similar to what we observe here, but $C$ is about 15% less and $R$ three times higher. Total penetration in those experiments was only about a third of that in the present work – therefore, whether the differences between $C$ and $R$ are due to the shallower depths, shot-to-shot variations, diameter effects, or difference in the source material is yet to be determined. The differences between $C$ and $R$ for silica sand between these tests probably have little engineering consequence for predicting maximum inertial loads on a penetrator or predicting DOP.

**Acknowledgments** The authors appreciate many helpful discussions about experiment design and data interpretation with Prof. Mehdi Omidvar at Manhattan College and Messrs. Don Grosch and Tom Moore at SwRI. This work was supported by the Strategic Environmental Research and Development Program (SERDP grant MR19-1277).

## References

1. Omidvar, M., Bless, S., Iskander, M.: Recent Insights into Penetration of Sand and Similar Granular Materials, pp. 1–37 (2019). https://doi.org/10.1007/978-3-030-23002-9_5
2. Peden, R., Omidvar, M., Bless, S., Iskander, M.: Photonic doppler velocimetry for study of rapid penetration into sand. Geotech. Test. J. **37**(1) (2014). https://doi.org/10.1520/GTJ20130037

3. Glößner, C., et al.: Instrumented projectile penetration testing of granular materials. Exp. Mech. **57**(2), 261–272 (2017). https://doi.org/10.1007/s11340-016-0228-0
4. Omidvar, M., Malioche, J.D., Chen, Z., Iskander, M., Bless, S.: Visualizing kinematics of dynamic penetration in granular media using transparent soils. Geotech. Test. J. **38**(5), 656–672 (2015). https://doi.org/10.1520/GTJ20140206
5. Bragov, V., Balandin, V., Igumnov, L., Kotov, V.L., Kruszka, L., Lomunov, K.: Impact and penetration of cylindrical bodies into dry and water-saturated sand. Int. J. Impact Eng. **122**(July), 197–208 (2018). https://doi.org/10.1016/j.ijimpeng.2018.08.012
6. Børvik, T., Dey, S., Olovsson, L.: Penetration of granular materials by small-arms bullets. Int. J. Impact Eng. **75**, 123–139 (2015). https://doi.org/10.1016/j.ijimpeng.2014.07.016
7. Ao, T., Dolan, D.H.: SANDIA REPORT SIRHEN: a data reduction program for photonic Doppler velocimetry measurements (2010). [Online]. Available: http://www.ntis.gov/help/ordermethods.asp?loc=7-4-0#online
8. Rad, N.S., Tumay, M.T.: Factors affecting sand specimen preparation by raining. Geotech. Test. J. **10**(1), 31–37 (1987). https://doi.org/10.1520/GTJ10136J
9. Kenneally, B., Omidvar, M., Bless, S., Iskander, M.: Observations of velocity-dependent drag and bearing stress in sand penetration. Dyn. Behav. Mater. **1**, 29–35 (2021)
10. Allen, W.A., Mayfield, E.B., Morrison, H.L.: Dynamics of a projectile penetrating sand. J. Appl. Phys. **28**(3), 370–376 (1957). https://doi.org/10.1063/1.1722750
11. Omidvar, M., Bless, S., Iskander, M.: Global Observations & post mortem analysis of penetration in sand. In: Rapid Penetration into Granular Media: Visualizing the Fundamental Physics of Rapid Earth Penetration (2015). https://doi.org/10.1016/B978-0-12-800868-3.00005-5
12. Clark, A.H., Petersen, A., Kondic, L., O'Hern, C., Behringer, R.P.: Granular impact: a grain-scale approach. In: Rapid Penetration into Granular Media: Visualizing the Fundamental Physics of Rapid Earth Penetration, pp.319–351. Elsevier (2015). https://doi.org/10.1016/B978-0-12-800868-3.00010-9

# Chapter 6
# High Strain Rate Compressive Behavior of 3D Printed Liquid Crystal Elastomers

**Brett Sanborn, Devesh Mistry, Bo Song, Kai Yu, Kevin Long, and Christopher M. Yakacki**

**Abstract** Polymers are widely used as damping materials in vibration and impact applications. Liquid crystal elastomers (LCEs) are a unique class of polymers that may offer the potential for enhanced energy absorption capacity under impact conditions over conventional polymers due to their ability to align the nematic phase during loading. Being a relatively new material, the high rate compressive properties of LCEs have been minimally studied. Here, we investigated the high strain rate compression behavior of different solid LCEs, including cast polydomain and 3D-printed, preferentially oriented monodomain samples. Direct ink write (DIW) 3D printed samples allow unique sample designs, namely, a specific orientation of mesogens with respect to the loading direction. Loading the sample in different orientations can induce mesogen rotation during mechanical loading and subsequently different stress-strain responses under impact. We also used a reference polymer, bisphenol-A (BPA) cross-linked resin, to contrast LCE behavior with conventional elastomer behavior.

**Keywords** Kolsky compression bar · Liquid crystal elastomer · LCE · Polymer

## 6.1 Introduction

Polymers are a broad class of materials regularly used in the protection of valuable assets from mechanical insults such as impact or vibration. Polymers are often manufactured in a foamed state, which allows energy absorption of the material via induced changes in the mesostructure. The mechanical performance of polymer foams can be further enhanced through careful selection of the base polymer to allow energy dissipation from both microstructure and mesostructure effects. Many widely used polymers have amorphous microstructure and isotropic material behavior.

Liquid crystal elastomers (LCE) may offer enhanced strain-rate-dependent impact absorbing capability due to their ability to undergo an alignment phase transition, wherein the nematic liquid crystal domains are oriented during finite straining. This alignment phase transition has the potential to offer a new energy dissipation mechanism for shock and vibration applications compared to standard polymers. LCE lattices have been shown to exhibit such dissipative mechanical properties in the vibratory loading regime (dynamic mechanical analysis) [1] and in drop tests [2] compared to conventional polymer lattices. Advances in 3D printing technology have allowed the printing of LCEs with different mesogen orientations and, by extension, differences in mechanical response for this unique class of polymer. Yet, the behavior of LCEs has not been studied in detail at elevated strain rates in compression.

B. Sanborn · B. Song · K. Long
Sandia National Laboratories, Albuquerque, NM, USA
e-mail: bsanbor@sandia.gov; bsong@sandia.gov; knlong@sandia.gov

D. Mistry
School of Physics and Astronomy, University of Leeds, Leeds, UK
e-mail: D.A.Mistry@leeds.ac.uk

K. Yu
Department of Mechanical Engineering, University of Colorado, Denver, Denver, CO, USA
e-mail: KAI.2.YU@UCDENVER.EDU

C. M. Yakacki (✉)
Department of Mechanical Engineering, University of Colorado, Denver, Denver, CO, USA

Impressio Inc., Aurora, CO, USA
e-mail: CHRIS.YAKACKI@UCDENVER.EDU



S. Mates et al. (eds.), *Dynamic Behavior of Materials, Volume 1*, Conference Proceedings of the Society for Experimental Mechanics Series, https://doi.org/10.1007/978-3-031-17453-7_6

In this investigation, we studied the mechanical behavior of solid LCEs and a reference polymer, bisphenol-A (BPA), at high strain rates. Both materials have glass transition temperatures near 0 °C and have similar storage moduli near 80 °C, where the LCE is well above its nematic-to-isotropic transition temperature (about 45 °C). At room temperature, the LCE materials are in their nematic state and exhibit the enhanced dissipation behavior seen in standard dynamic mechanical analysis data [3]. Direct ink write (DIW) 3D printing was used to produce LCEs with (aligned) monodomain 0 and 90° mesogen orientations with respect to the loading direction. The BPA reference polymer was printed in the same way. As an additional reference, a cast polydomain LCE was produced which had no preferential mesogen orientation. Using Kolsky compression bar up to a strain rate of 3000 $s^{-1}$, the compressive behavior of the LCE was evaluated to understand the effect of mesogen rotation during dynamic loading.

## 6.2 Results and Discussion

Figure 6.1 shows the compressive mechanical response of BPA and LCE at the highest tested strain rate of 3000 $s^{-1}$. The BPA reference material printed in the 0 and 90° orientations shows an insignificant difference in compressive response, which is expected given the isotropic nature of BPA. The LCEs in polydomain and monodomain 90° orientation exhibit a similar response, which is most likely attributable to the lack of mesogen rotation induced during compression. The mesogens of the monodomain LCE 90° are oriented perpendicular to the direction of loading and are effectively loaded transversely, resulting in the mesogens being subjected to tension as the overall material sample is compressed. The LCE monodomain 0° samples exhibit an initially higher stiffness before flattening to a plateau at an engineering strain of approximately 5%, indicating that mesogen rotation occurred. The polydomain LCE response is similar to the LCE 90° orientation with some additional compliance as only a fraction of the nematic domains can reorient along the loading direction. Of the five tested materials, the soft elasticity observed in the LCE monodomain 0° behaves most like an ideal absorber.

Figure 6.2a shows the strain rate dependence of the LCE monodomain 0° material over a strain rate range of 760–2880 $s^{-1}$. The initial stiffness of the material increases with an increasing strain rate. The plateau stress of the material also increases with increasing strain rate, indicating that the mesogen rotation process may be rate dependent. By contrast, the entire curve of the BPA 0° reference polymer (Fig. 6.2b) increases with increasing strain rate. This is expected given the amorphous nature of the BPA.

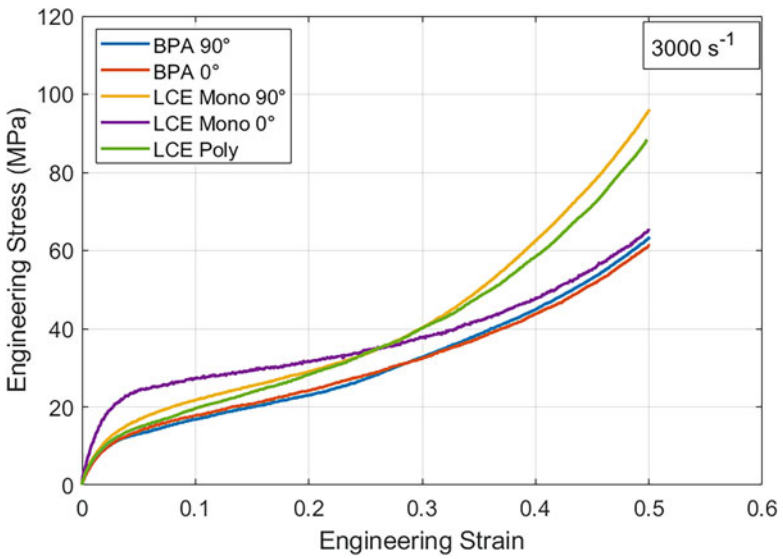


**Fig. 6.1** High strain rate compressive response of LCE and BPA polymers 3D printed with different orientations

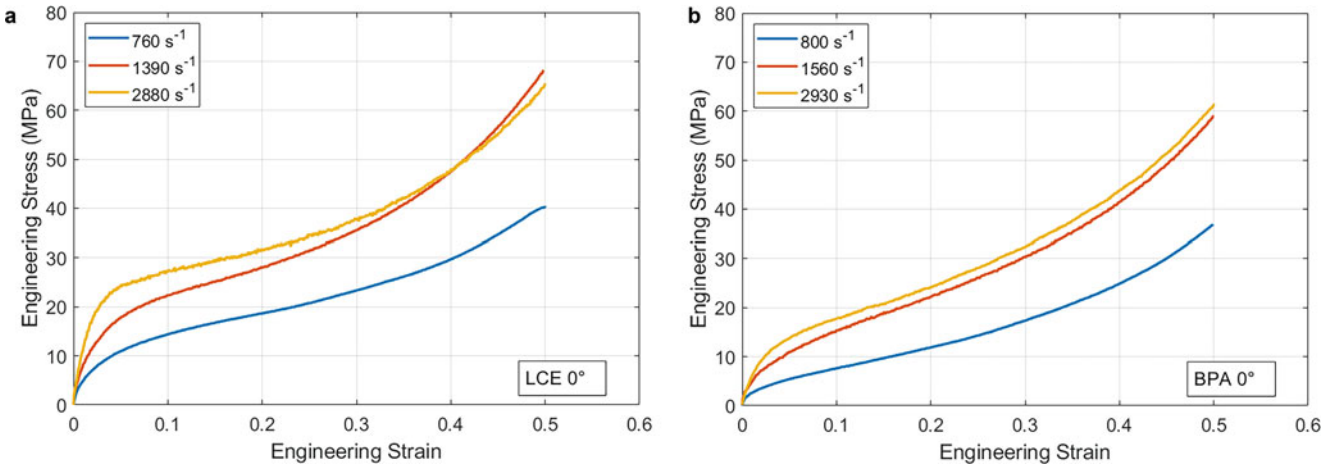


**Fig. 6.2** Compressive stress-strain curves of (**a**) LCE monodomain 0° and (**b**) BPA 0° over a strain rate range of ~800–3000 $s^{-1}$

## 6.3 Conclusion

The dynamic compressive response of 3D-printed solid BPA and LCE polymers was studied as a function of strain rate. LCEs printed with mesogens oriented parallel to the direction of loading displayed soft elasticity and behaved like an ideal absorber compared to either the reference polymer (BPA) or LCE with perpendicularly aligned mesogens (90°) even though all materials studied are solid, incompressible polymers. This information can be exploited to enhance the energy absorption capacity of foams or 3D printed lattices to increase their protective capability for impact applications.

**Acknowledgments** Sandia National Laboratories is a multimission laboratory managed and operated by National Technology and Engineering Solutions of Sandia, LLC, a wholly owned subsidiary of Honeywell International, Inc., for the US Department of Energy's National Nuclear Security Administration under contract DE-NA0003525. The views expressed in the article do not necessarily represent the views of the US Department of Energy or the United States Government.

## References

1. Traugutt, N.A., Mistry, D., Luo, C., Yu, K., Ge, Q., Yakacki, C.M.: Liquid-crystal-elastomer-based dissipative structures by digital light processing 3D printing. Adv. Mater. **32**, 2000797 (2020)
2. Luo, C., Chung, C., Taugutt, N.A., Yakacki, C.M., Long, K.N., Yu, K.: 3D printing of liquid crystal elastomer foams for enhanced energy dissipation under mechanical insult. ACS Appl. Mater. Interfaces, 12698–12708 (2021)
3. Mistry, D., Traugutt, N.A., Sanborn, B., Volpe, R.H., Chatham, L.S., Zhou, R., Song, B., Yu, K., Long, K.N.: Soft elasticity optimises dissipation in 3D-printed liquid crystal elastomers. Nat. Commun. **12**, 6677 (2021)

# Chapter 7
# A Novel Method for Development of Constitutive Models Under Simultaneous Extreme Strains and Strain Rates


**Homar Lopez-Hawa, Viswanathan Madhavan, and Wilfredo Moscoso-Kingsley**

**Abstract** This work presents a new experimental configuration for studying material behavior under extreme thermomechanical conditions. Deformation strains up to 10, strain rates up to $10^6$ 1/s, and temperatures close to melting are achievable. The new configuration makes a rigid and hard tool strike a specimen that protrudes from the surface of a substrate. The fin-like specimen is deformed in simple shear by the fast-moving tool. The particular geometry of the specimen creates a shear band that travels nearly one-dimensionally across the fin, from the point of impact. The one-dimensional shear band is characterized by uniform stress, strain, strain rate, and temperature. The configuration is an attractive platform for the accurate development of constitutive models, under simultaneous extreme strain and strain rate. The deformation force can be measured with simple devices. This paper presents a proof of concept for the platform. The deformation is modeled using high-resolution finite element analysis. Deformation force, stress, strain, strain rate, and temperature are obtained from this numerical experiment. Simple analytical models are fitted to the data to infer the constitutive model of the material. The inferred constitutive model is compared to the one given as input to the finite element experiment. The comparisons show minimal deviations, which indicate that real experiments should produce highly accurate flow stress measurements, if the shear band propagates one-dimensionally. The numerical experiments were performed using the Johnson-Cook model for AISI 4340. It is important to note that the numerical experiments resulted in adiabatic shear bands without material damage criteria.

**Keywords** FEA · Constitutive models · Dynamic behavior · High strain rate · High strain

## 7.1 Introduction

The study of material behavior under dynamic loading has been an area of interest to the materials performance community since the beginning of the twentieth century. Many studies have shown that the mechanical response of materials under static or quasi-static conditions is different from the response under dynamic conditions [1]. For instance, Scapin and Manes [2] and Manes et al. [3] reported that the flow stress of aluminum 6061-T6 remains fairly constant for strain rates between $10^{-3}$ 1/s and $10^3$ 1/s, increases 10% when the strain rate exceeds $10^3$ 1/s, and increases 40% when the strain rate exceeds $10^4$ 1/s. Other materials such as Ti-6Al-4V, micarta, and lucite are also known to have strain rate sensitivity [4]. Several testing methods have been used to study the effects of loading conditions, i.e., strain and strain rate on flow stress. The Cam plastometer [5] has been used to obtain material behavior under compressive strains up to ~50%, at strain rates up to $10^2$ 1/s. This test imposes uniform strain and strain rate; however, it demands high power drives, typically 40 kW or more. For experiments where a higher load capacity is required, the drop-tower compression test may be implemented. This test has the capacity to apply loads of 900 kN in a time interval as short as 20 μs [6]. However, since the load is driven by gravity, the strain rate is not constant. Another test known as the Kolsky bar compression test has been widely adopted due to its ability to impose uniform compressive stains up to 50%, at high strain rates up to $10^4$ 1/s [7]. The Kolsky bar compression setup has been modified in various ways to induce deformation by shear. One of these modifications incorporates hat-shaped specimens to induce shear bands at the intersection between the brim and the crown [8]. While this configuration leads to strains higher than 50% at strain rates higher than $10^4$ 1/s, the specimen preparation is complicated, and the shear zone is not observable directly.

There is a need for testing under conditions of very high strain and strain rates (strains >200%, strain rates $>10^5$ 1/s), in order to obtain the mechanical response of materials under the extreme conditions encountered in machining [9] and many

H. Lopez-Hawa (✉) · V. Madhavan · W. Moscoso-Kingsley
Department of Industrial, Systems and Manufacturing Engineering, College of Engineering, Wichita State University, Wichita, KS, USA
e-mail: hxlopezhawa@shockers.wichita.edu; vis.madhava@wichita.edu; wilfredo.moscoso@wichita.edu



S. Mates et al. (eds.), *Dynamic Behavior of Materials, Volume 1*, Conference Proceedings of the Society for Experimental Mechanics Series, https://doi.org/10.1007/978-3-031-17453-7_7

other manufacturing processes. A test capable of imposing such high strains and strain rates, after simple specimen preparation steps, and having a directly observable shear zone is highly desirable. This work introduces such a new dynamic test. The new test is validated numerically using high-resolution finite element analysis (FEA). The modeling predicts the formation of adiabatic shear bands of deterministic geometry that, if confirmed experimentally, would result in strains up to 1000% (strains up to 10), strain rates up to $10^6$ 1/s, and temperatures from ambient to above 50% of the melting point. The new test makes a hard tool strike, at high speed, a specimen that protrudes from the surface of a substrate. The fin-like specimen is deformed in a simple shear by the tool. The FEA simulations are used as numerical experiments from which the tool force is calculated and in turn used to infer the material flow stress, following the same procedure to be applied after actual tool force measurement.

## 7.2 Experimental

In the typical arrangement, a rectangular piece of material protrudes from a substrate, as shown schematically in Fig. 7.1. Several geometric configurations were tested numerically using FEA to obtain a thin, straight shear zone having a deterministic orientation. The configuration in Fig. 7.1 is one possibility leading to one such deterministic shear plane. A key parameter is the fin height-to-width ratio. The FEA showed that a fin height-to-width ratio of 0.3 would lead to deterministic shear planes, albeit in the presence of a constraint tool, as shown in Fig. 7.1. Other configurations that avoid the constraint tool, not discussed herein, have been found. The fillet radius (25 μm) on the right of the fin is needed to reduce the stress concentration in the initial region of contact between tool and fin, thereby allowing the deformation to propagate along the shear plane. A tool edge radius of 10 μm has been used herein. However, this radius has been found to have negligible effect on tool force. The tool starts in contact with the specimen and accelerates to a speed of 15 m/s, moving in the negative-X direction. Full speed is reached after 6.5 μs or tool displacement of 46.5 μm. There is no friction between the tools and the fin.

The numerical experiments were modeled using 2D plane strain shell elements with the commercially available software LS-DYNA®. For accurate modeling of the severe deformation, an adaptive remeshing algorithm is implemented in the specimen. The element characteristic size after remeshing is set to be 0.5 μm. The workpiece is divided into two different parts, to facilitate the modeling. They are the main body of the fin (WP1) and the right side of the substrate (WP2). The contact between WP1 and WP2 is set to be automatic surface-to-surface, with thermal conduction enabled between them. This workpiece separation results in the expected fin displacement. That is, the fin slides over WP2, naturally, without having to recur to element deletion or other artificial material failure criteria to cause the sliding. Both of these parts are modeled following the Johnson-Cook [10] constitutive model for AISI 4340 with constants as reported in Table 7.1. Other physical properties of the material are presented in Table 7.2. The tools are modeled as rigid bodies. The cutting tool is only allowed to move in the X direction, while the workpiece is restrained in place by constraining all the degrees of freedom of the bottom nodes. The initial temperature for all nodes is set to be the same as the ambient temperature (293 K). It is assumed that 100% of the work done by plastic deformation is converted into heat energy. The model is thermo-mechanically coupled. Thermal conduction between the tools and the specimen is allowed.

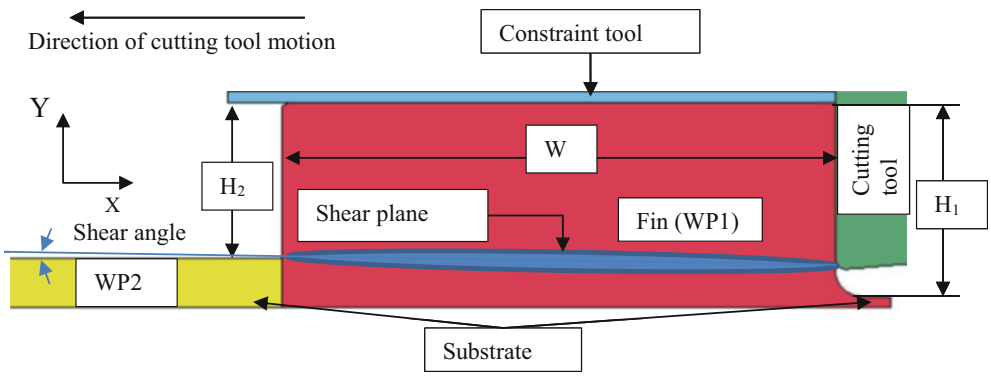


**Fig. 7.1** Fin cutting experimental configuration. Overall fin dimension are $H_1 = 175$ μm, $W = 500$ μm and $H_2 = 140$ μm. The fillet radius on the right of the fin is of 25 μm. WP1 and WP2 are both set for adaptive remeshing, with automatic surface to surface contact between them. The cutting and constraint tools are set with automatic contact against WP1. There is no friction between WP1 and the tools. The cutting tool edge radius is 10 μm

**Table 7.1** Johnson-Cook material parameters used in the simulations

| Material | $A$ (MPa) | $B$ (MPa) | $n$ | $c$ | $M$ | $\dot{\varepsilon}_0\ (s^{-1})$ |
|---|---|---|---|---|---|---|
| AISI 4340 | 792 | 510 | 0.26 | 0.014 | 1.03 | 1 |

**Table 7.2** Other physical material properties used in the simulations

| Material | $E$ (GPa) | $G$ (GPa) | $\rho\ \left(\frac{\text{kg}}{\text{m}^3}\right)$ | $C_p$ (J/kgK) | $T_m$ | $\lambda$ (W/mK) |
|---|---|---|---|---|---|---|
| AISI 4340 | 200 | 77 | 7830 | 477 | 1793 | 44.5 |

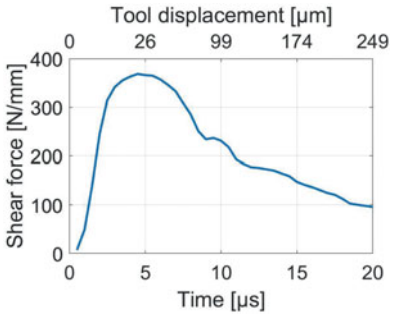


**Fig. 7.2** Evolution of horizontal force for numerical experiment using AISI 4340 steel material model at 15 m\s with tool radius of 10 μm. The bottom abscissa shows the numerical experiment time, while the top abscissa shows the tool displacement

The cutting forces acting on the cutting tool, along the X and Y directions, are obtained by integrating, respectively, the normal and friction forces acting on the contact nodes at the cutting tool-fin interface. To decrease spurious noise from the contact algorithm and from remeshing, the forces are obtained at a high sampling rate of 1 GHz and smoothed by a moving average of over 15 points.

The cutting forces along the X and Y directions, $F_x$ and $F_y$, respectively, are then used to calculate the shear force acting on the shear plane $Fs$, with the help of Merchant's model [11], which results in Eq. (7.1), where $\phi$ is the shear angle (Fig. 7.1). This angle was found to be very close to 0°. The flow stress is then calculated using Eq. (7.2). In Eq. (7.2), the length of the shear plane $L_s$ is the distance, along the shear plane direction, measured from the initial location of the left corner point common to the red WP1 and the yellow WP2 in Fig. 7.1 to the current location of the tool cutting edge. The workpiece thickness $b$, in the FEA simulations and in Eq. (7.2), is 1 mm.

$$Fs = F_x * \cos\phi - F_y * \sin\phi \tag{7.1}$$

$$\sigma = \sqrt{3} * \frac{Fs}{L_s b} \tag{7.2}$$

The numerically calculated flow stress obtained from the numerically calculated cutting forces is compared with the mean von Mises stress acting along the shear plane, extracted directly from the FEA results.

## 7.3 Results

Figure 7.2 illustrates an FEA fin cutting simulation cycle, and shows the shear force $Fs$ exerted by the tool on the fin as a function of time (and tool displacement). Upon the start of the shearing, the shear force increases to about 5 μs and then decreases monotonically, presumably, until the fin is cut off from the substrate. Since the FEA model does not incorporate material failure, the fin is cut off when the tool reaches WP 2. The simulation shown in Fig. 7.2 was arbitrarily stopped at time = 20 μs. The sudden drop in force is due to adiabatic shear banding, wherein the rate of thermal softening is larger than the rate of strain hardening [12]. The simulation indicates the potential of fin cutting to produce severe deformation by causing adiabatic shear banding to form under very large strains and strain rates.

Figures 7.3 and 7.4 show the deformation fields after the tool has sheared the fin for a total of 3 μs and 15 μs, respectively. The first instance (3 μs, Fig. 7.3) corresponds to an early stage of deformation where the mean strain along the shear zone is

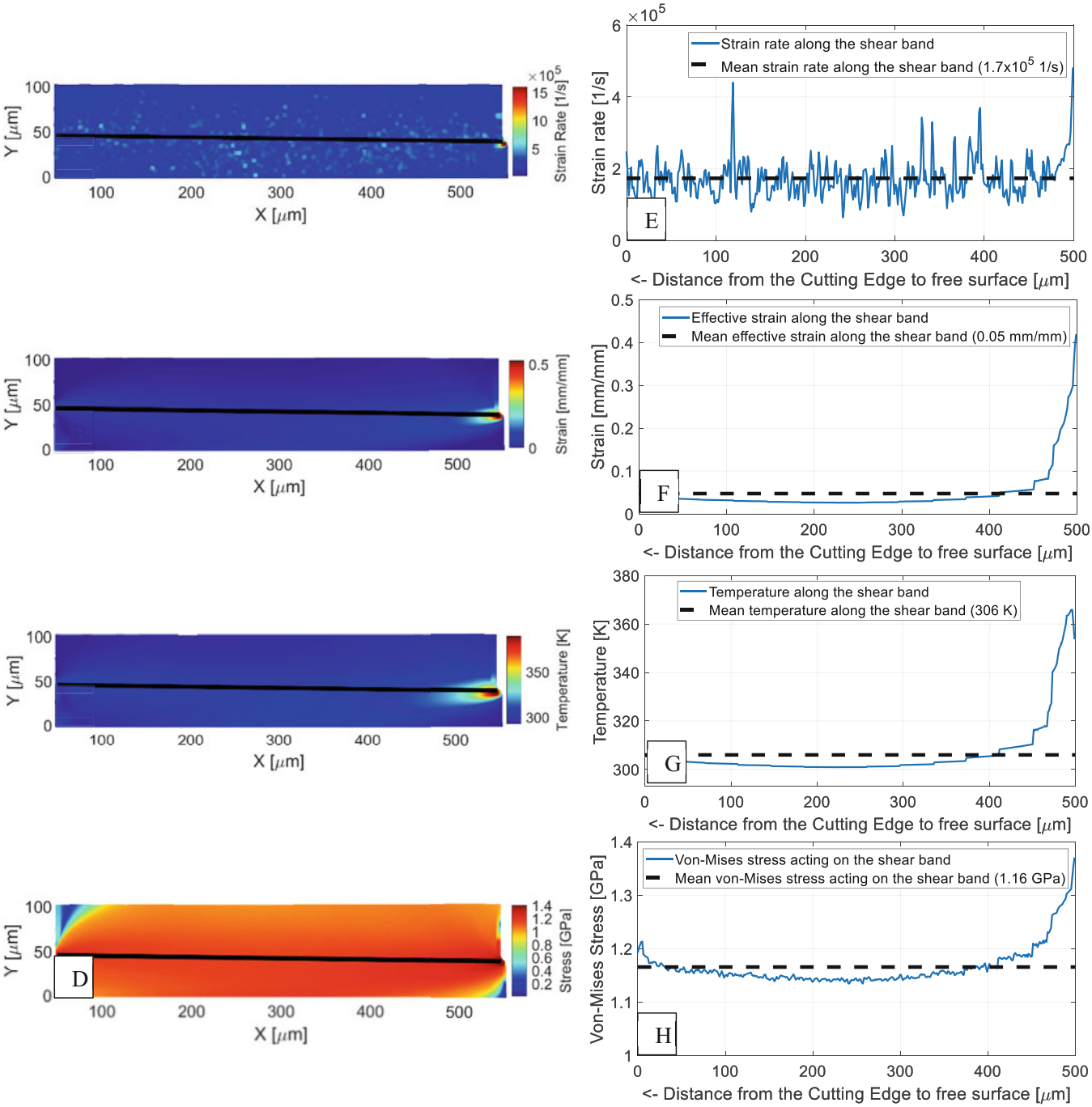


**Fig. 7.3** Results for AISI 4340, at time = 3 μs. The figures on the left, from **a** to **d**, show the different field variables strain rate, strain, temperature, and von Mises stress, respectively. The solid black lines represent the approximate location of the center of the shear plane, defined by the maximum strain rate. The figures on the right, from **e** to **h**, represent the values of strain rate, strain, temperature, and von Mises stress along the approximate center of the shear plane, respectively

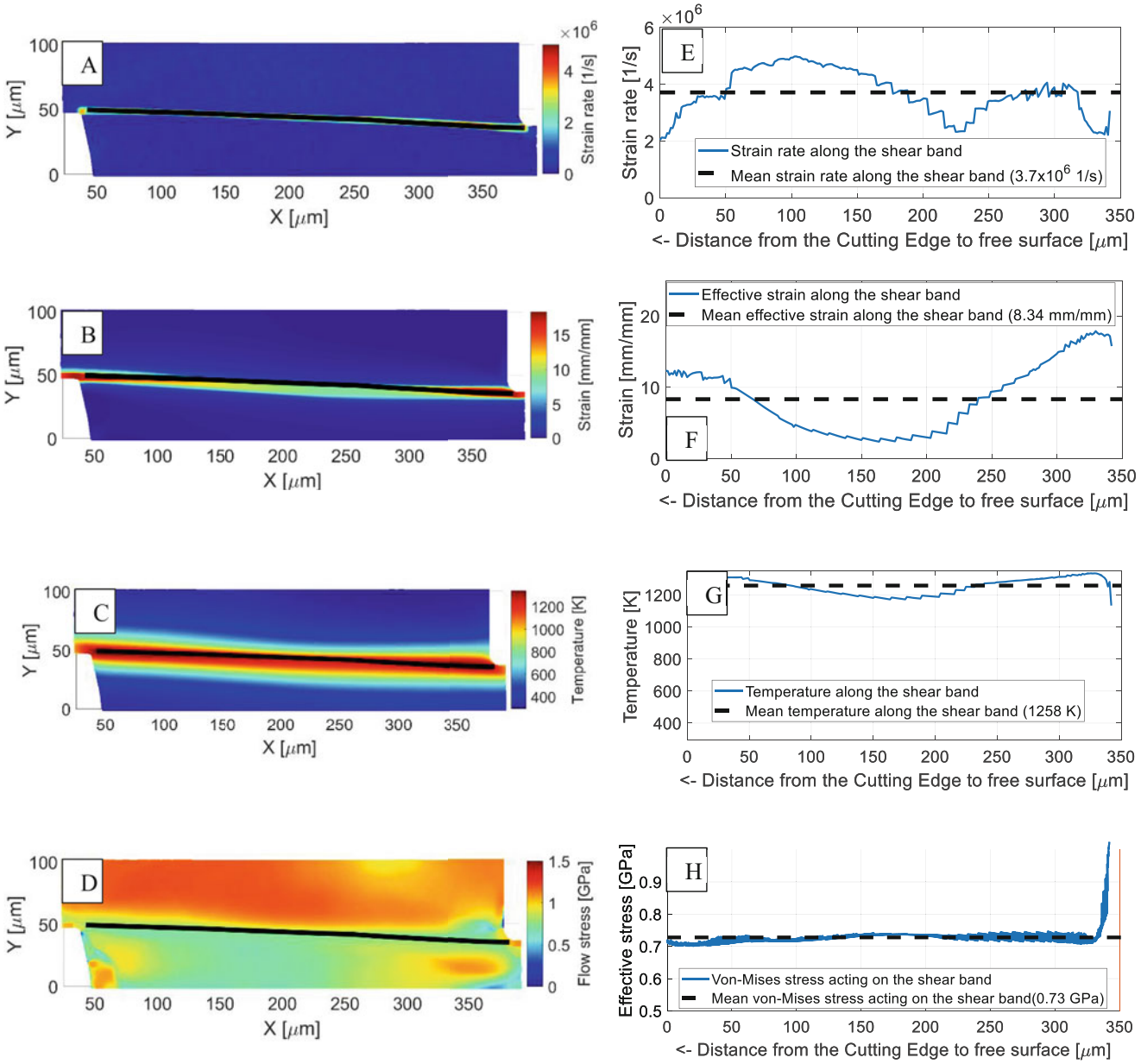


**Fig. 7.4** Results for AISI 4340, at time = 15 μs. The figures on the left, from **a** to **d**, show the different field variables strain rate, strain, temperature and von Mises stress, respectively. The solid black lines represent the approximate location of the center of the shear plane, defined by the maximum strain rate. The figures on the right, from **e** to **h**, represent the values of strain rate, strain, temperature, and von Mises stress along the approximate center of the shear plane, respectively

small (~5%) and the shear zone is not fully developed. The second instance (15 μs, Fig. 7.4) corresponds to a late stage of deformation where the shear zone has fully evolved into a planar, adiabatic shear zone, with a very large mean strain along the shear zone (~800%).

The shear plane can be readily identified from the strain rate field, since it is, among the different field quantities, the one that displays the largest gradients across the thickness of the shear zone. The large strain rate gradients are especially observed after an adiabatic shear band starts to form. The process to identify the shear plane from the strain rate is best illustrated using Fig. 7.4a. The center of the shear plane is the line connecting the locations of maximum strain rate along vertical cross sections drawn from the cutting tool to the fin's free side. The shear plane is the black line in Fig. 7.4a–d. Field variable values at the nodes intersected by the shear plane are then extracted. During the early deformation stage, even the strain rate is diffuse. For

this special case, Fig. 7.3a, the shear plane is taken as the line connecting the tool cutting edge and the initial point of intersection between the fin's left side and the substrate. The shear plane is the black line in Fig. 7.3a–d.

Figures 7.3e–h, and 7.4e–h show the field variables as functions of distance from the tool face, for time = 3 μs and 15 μs, respectively. In the plots, the abscissa represents distance $X$ along the shear plane, with $X = 0$ being the initial location of the point of intersection between the fin's left side and the substrate. For time = 3 μs, the tool cutting edge is located at $X = 493$ μm. For time = 15 μs, the tool cutting edge is located at $X = 325$ μm.

From Fig. 7.2, the shear force and tool displacement for cutting times of 3 μs and 15 μs are, respectively, 342 N and 6.6 μm and 147 N and 175 μm. Converting tool displacement into shear plane length and using Eqs. (7.1) and (7.2), the numerically calculated flow stresses for cutting times of 3 μs and 15 μs are, respectively, 1.21 GPa and 0.78 GPa. These numerically calculated flow stresses are within 4.3% and 6.8%, respectively, of the mean von Mises stresses acting on the shear plane, which are 1.16 GPa and 0.73 GPa, respectively (see Figs. 7.3h and 7.4h). The numerically calculated flow stress and the mean von Mises stress acting on the shear plane are found to be remarkably close to each other, in spite of the spike in von Mises stress in the vicinity of the tool cutting edge. The mean von Mises stress is also virtually the same as the flow stress obtained from inserting the mean strain, strain rate, and temperature on the shear plane into the JC model, with parameters equal to those used in the FEA simulations. The JC flow stresses are 1.19 GPa and 0.75 GPa for cutting times of 3 μs and 15 μs, respectively.

The numerically calculated flow stress, obtained from numerically calculated forces, following the formulation to be implemented after actual tool force measurements, matches the mean von Mises stress acting on the shear plane and the JC flow stress for corresponding mean shear-plane strain, strain rate, and temperature. This demonstrates, in principle, the validity of fin cutting as a test for the measurement of flow stress.

From the results presented in Figs. 7.3 and 7.4, a single fin cutting test performed at a constant cutting speed may be used to produce a wide range of strain, strain rate, and temperature, from which the material flow stress may be derived. Additional control over the strain rate and temperature may be achieved by changing the cutting speed. The strain path may be altered by subjecting the material to plastic deformation prior to fin cutting. The temperature may be altered by heating or cooling the fin during the cutting. Moreover, since the test may impose severe strain, it may be used to find the fracture limit of materials with limited ductility.

## 7.4 Conclusion

A proof of concept was presented for a new experimental configuration, called fin cutting, to obtain material flow stress under conditions of high strains, strain rates, and temperatures. Strains up to 800%, strain rates of the order of $10^6$ 1/s, and temperatures about 70% of the melting point were obtained by finite element simulations of the deformation. The distribution of stress along the shear plane is expected to be uniform. The modeling showed a good correlation between the numerically obtained flow stress, mean von Mises stress acting on the shear plane, and the JC flow stress for corresponding mean shear-plane strain, strain rate, and temperature. These stresses are within 6% of each other.

**Acknowledgments** This material is based upon work supported by the Department of Energy, National Nuclear Security Administration under Award Number DE-NA0003222.



## References

1. Meyers, M.A.: Dynamic Behavior of Materials. Wiley, New York (1994)
2. Scapin, M., Manes, A.: Behaviour of Al6061-T6 alloy at different temperatures and strain-rates: experimental characterization and material modeling. Mater. Sci. Eng. A. **734**, 318–328 (2018)

3. Manes, A., Peroni, L., Scapin, M., Giglio, M.: Analysis of strain rate behavior of an Al 6061 T6 alloy. Proc. Eng. **10**, 3477–3482 (2011)
4. Maiden, C.J., Green, S.J.: Compressive strain-rate tests on six selected materials at strain rates from $10^{-3}$ to $10^{4}$ in/in/sec. In: Transactions of the ASME, pp. 496–504 (1966)
5. Bailey, J.A., Singer, R.E.: Plane-strain cam plastometer for use in metal-working studies. J. Inst. Met. **92**(9), 288 (1964)
6. Adler, W.F., James, T.W., Kukuchek, P.E.: Development of a Dynamic Compression Fixture for Brittle Materials. Effects Technology, Santa Barbara (1981)
7. Kolsky, H.: An investigation of the mechanical properties of materials at very high rates of loading. Proc. Phys. Soc. Sect. B. **62**, 676–700 (1949)
8. Hartmann, K., Kunze, H., Meyer, L.: Metallurgical effects on impact loaded. In: Shock Waves and High-Strain Rate Phenomena in Metals, pp. 325–337 (1981)
9. Shaw, M.: Metal Cutting Principles. Oxford University Press, New York (1984)
10. Johnson, G.R., Cook, W.H.: Fracture characteristics of three metals subjected to various strains, strain rates, temperatures and pressure. Eng. Fract. Mech. **21**(1), 31–48 (1985)
11. Merchant, M.E.: Mechanics of the metal cutting process. I. Orthogonal cutting and a type 2 chip. J. Appl. Phys. **16**(5), 267–275 (1945)
12. Recht, R.F.: Catastrophic thermoplastic shear. J. Appl. Mech. **31**(2), 189–193 (1964)

# Chapter 8
# Temperature- and Strain-Rate-Dependent Mechanical Response of a 316 Stainless Steel


**Angela Y. Ku and Bo Song**

**Abstract** A comprehensive study of the mechanical response of a 316 stainless steel is presented. The split-Hopkinson bar technique was used to evaluate the mechanical behavior at dynamic strain rates of 500 $s^{-1}$, 1500 $s^{-1}$, and 3000 $s^{-1}$ and temperatures of 22 °C and 300 °C under tension and compression loading, while the Drop-Hopkinson bar was used to characterize the tension behavior at an intermediate strain rate of 200 $s^{-1}$. The experimental results show that the tension and compression flow stress are reasonably symmetric, exhibit positive strain rate sensitivity, and are inversely dependent on temperature. The true failure strain was determined by measuring the minimum diameter of the post-test tension specimen. The 316 stainless steel exhibited a ductile response, and the true failure strain increased with increasing temperature and decreased with increasing strain rate.

**Keywords** Stainless steel · Strain rate effect · Temperature sensitivity · Intermediate strain rate

## 8.1 Introduction

Stainless steels have been of great interest to the automotive, aerospace, defense, medical, and nuclear power industries for their excellent corrosion resistance, machinability, and mechanical properties. In these applications, it is desirable for stainless steels to be resistant against external impact from low-speed accidental crash to explosion, and this requires understanding of the mechanical response under different loading environments. The 300 series austenitic stainless steels are nonmagnetic when annealed and can only be strengthened through cold working. They have a face-centered cubic (FCC) crystal structure that is attained through alloying elements such as nickel, manganese, and nitrogen [1]. This allows them to exhibit excellent strength and ductility at both cryogenic and elevated temperatures.

The mechanical response of austenitic stainless steels under different loading conditions has been investigated by several research groups over the years [2–4]. Byun et al. [2] studied the tension response of several annealed and cold-worked austenitic stainless steels at a quasi-static strain rate of $10^{-3}$ $s^{-1}$ and over a temperature range of −150 °C to 450 °C. They found the material deformation became increasingly more localized as the temperature increased from −100 °C to 200 °C. Lee et al. [3] investigated the compression response of 316L stainless steel over a dynamic strain rate range of 1000 $s^{-1}$ to 5000 $s^{-1}$ and a temperature range of 25 °C to 800 °C. The specimens were more liable to fracture at higher strain rates (i.e., 5000 $s^{-1}$) and lower temperatures (i.e., 25 °C and 200 °C), and the failure behavior was dominated by the formation of adiabatic shear bands. Jin et al. [4] studied the tension behavior of a 304L-VAR stainless steel at ambient temperature and at every order of magnitude of strain rate from $10^{-3}$ $s^{-1}$ to 3500 $s^{-1}$. They were able to bridge the gap between the quasi-static and dynamic loading regimes by performing experiments at intermediate strain rates using the fast MTS and Drop-Hopkinson bar.

The objective of the current work is to characterize the tension and compression behavior of a 316 stainless steel at temperatures of 22 °C and 300 °C and at intermediate and dynamic strain rates using the Drop-Hopkinson bar and split-Hopkinson bar technique, respectively. The effects of strain rate and temperature on the mechanical response of a 316 stainless steel are determined. The experimental data obtained from this study will be used to develop, calibrate, and validate a material model that can be used for various applications in the automotive, aerospace, defense, medical, and nuclear power industries.

A. Y. Ku (✉) · B. Song
Sandia National Laboratories, Albuquerque, NM, USA
e-mail: ayku@sandia.gov; bsong@sandia.gov



S. Mates et al. (eds.), *Dynamic Behavior of Materials, Volume 1*, Conference Proceedings of the Society for Experimental Mechanics Series, https://doi.org/10.1007/978-3-031-17453-7_8

**Table 8.1** Reported chemical composition of 316 stainless steel

| C | Co | Cr | Cu | Mn | Mo | N | Ni | P | S | Si | Fe |
|---|---|---|---|---|---|---|---|---|---|---|---|
| 0.015 | 0.41 | 16.53 | 0.36 | 1.29 | 2.024 | 0.030 | 10.51 | 0.031 | 0.026 | 0.27 | Remainder |

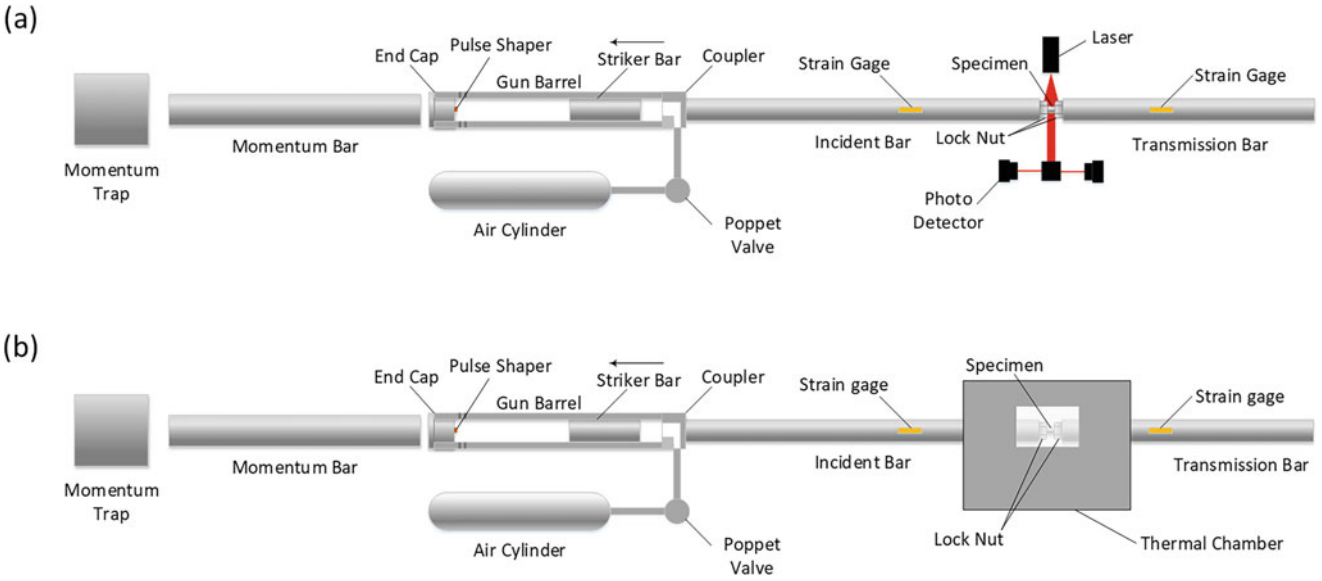


**Fig. 8.1** Schematic view of the tension split-Hopkinson pressure bar setup for experiments at (**a**) 22 °C and (**b**) 300 °C

## 8.2 Experimental Details

An annealed 316 stainless steel was investigated in this study. The alloy was obtained from Marco Steel and Aluminum and the chemical composition from the supplier is listed in Table 8.1. The tension and compression specimens were obtained from a cold-drawn round bar with a diameter of 25.4 mm. The tension specimens had a diameter of 3.18 mm and a gage length of 6.35 mm for an L/D ratio of 2. The compression specimens had a diameter of 6.35 mm and a length of 3.18 mm for an L/D ratio of 0.5. The specimen was designed to ensure uniform deformation and to reduce the longitudinal and radial inertia effects during a dynamic experiment.

The split-Hopkinson pressure bar was used to perform dynamic uniaxial tension and compression experiments at nominal strain rates of 500 $s^{-1}$, 1500 $s^{-1}$, and 3000 $s^{-1}$. A schematic of the tension and compression setups is shown in Figs. 8.1 and 8.2 and presented in detail in [5] and [6], respectively. The tension setup at 22 °C includes a high-speed laser extensometer, as shown in Fig. 8.1a. The laser beam was split into two separate high-speed photodetectors to measure the displacement histories of the incident and transmission bar ends, respectively [7]. The tension experiments at 300 °C were performed using a thermal chamber, and a thermocouple was placed on the surface of the specimen to measure the temperature, as shown in Fig. 8.1b. The deformation over the gage section for all tension specimens was corrected using the procedures presented in [8].

Uniaxial tension experiments in the intermediate strain rate range were conducted at 22 °C using the Drop-Hopkinson bar, as shown in Fig. 8.3. The procedures for the Drop-Hopkinson bar are presented in detail in [9]. The same methods were used to measure the displacement histories of the bars and to correct the specimen deformation over the gage section.

## 8.3 Results and Discussion

The mechanical behavior of a 316 stainless steel is characterized under uniaxial tension and compression loading at 22 °C and 300 °C and at various strain rates. At least three specimens were tested at each experimental condition and the average engineering and true stress-strain curves are presented in Figs. 8.4 and 8.5, respectively. It is noted that, due to the limited

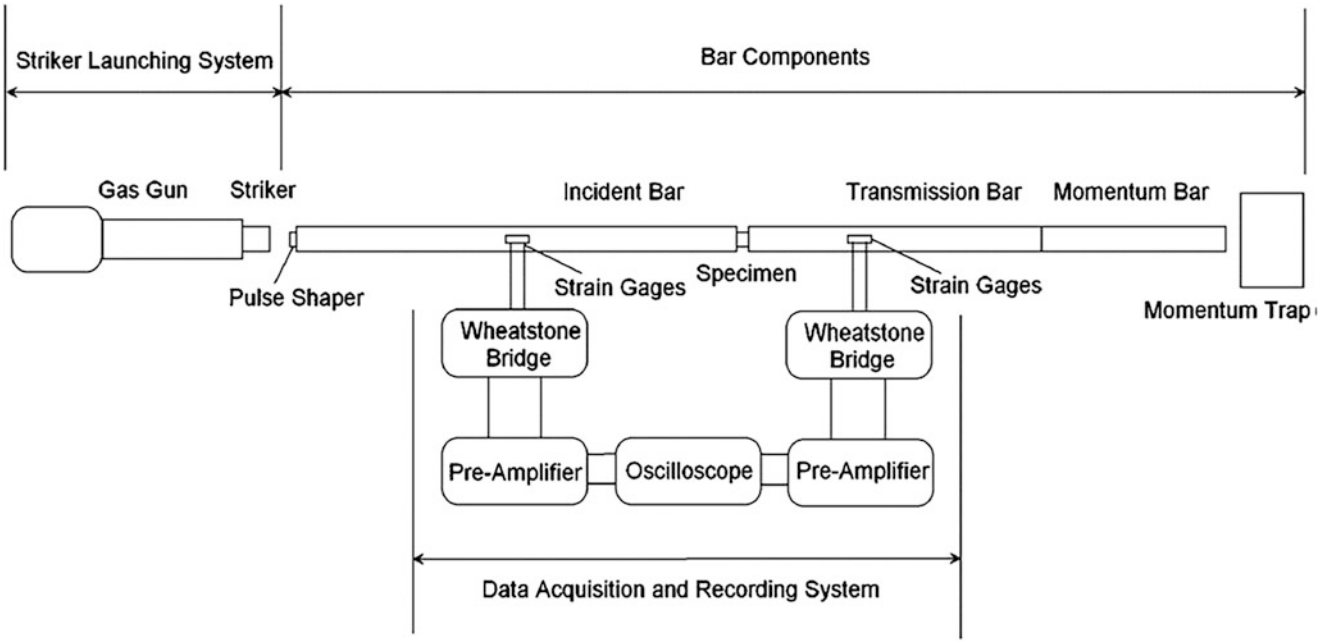


**Fig. 8.2** Schematic view of the compression split-Hopkinson pressure bar setup [6]

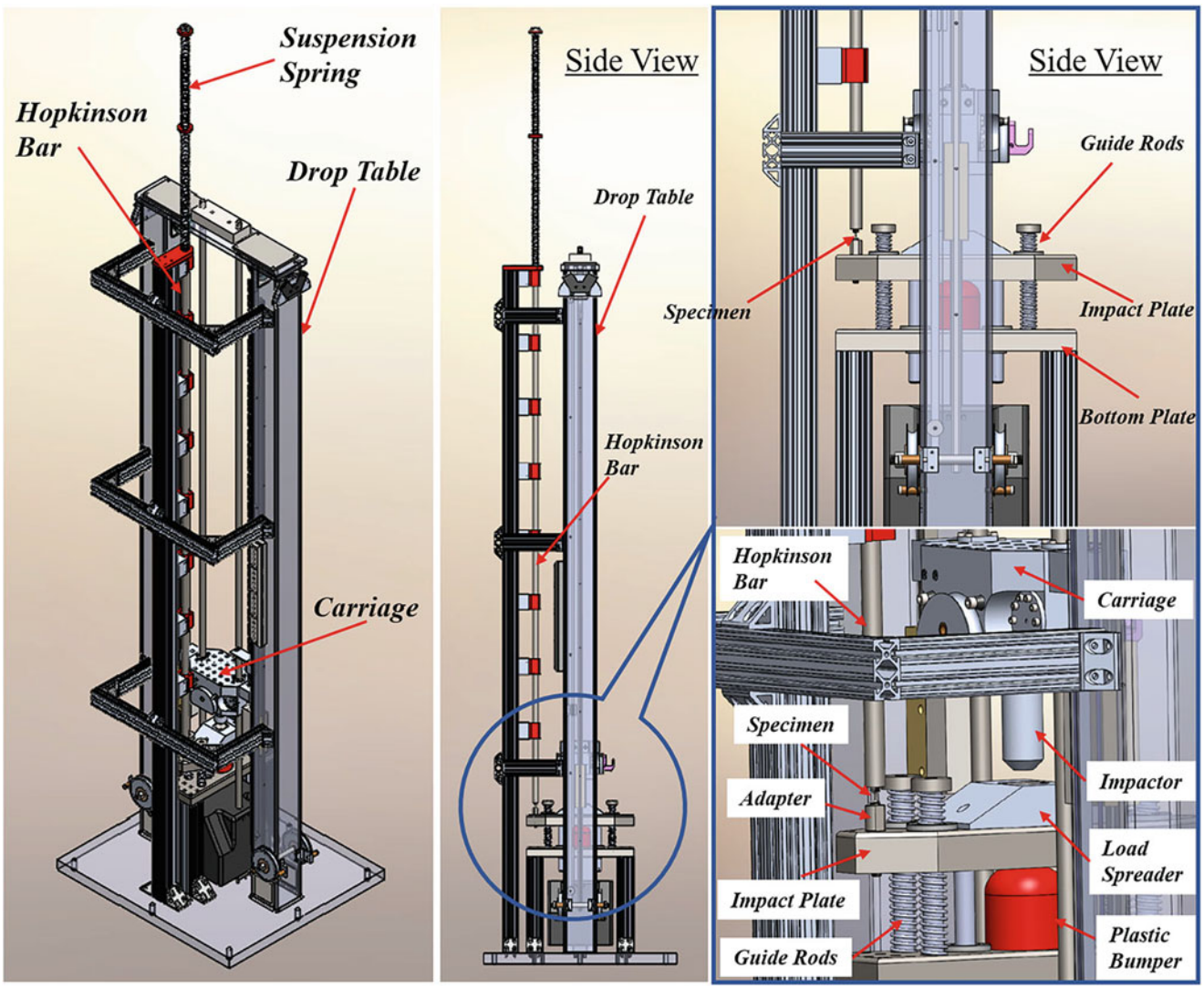


**Fig. 8.3** Schematic view of the Drop-Hopkinson bar setup [9]

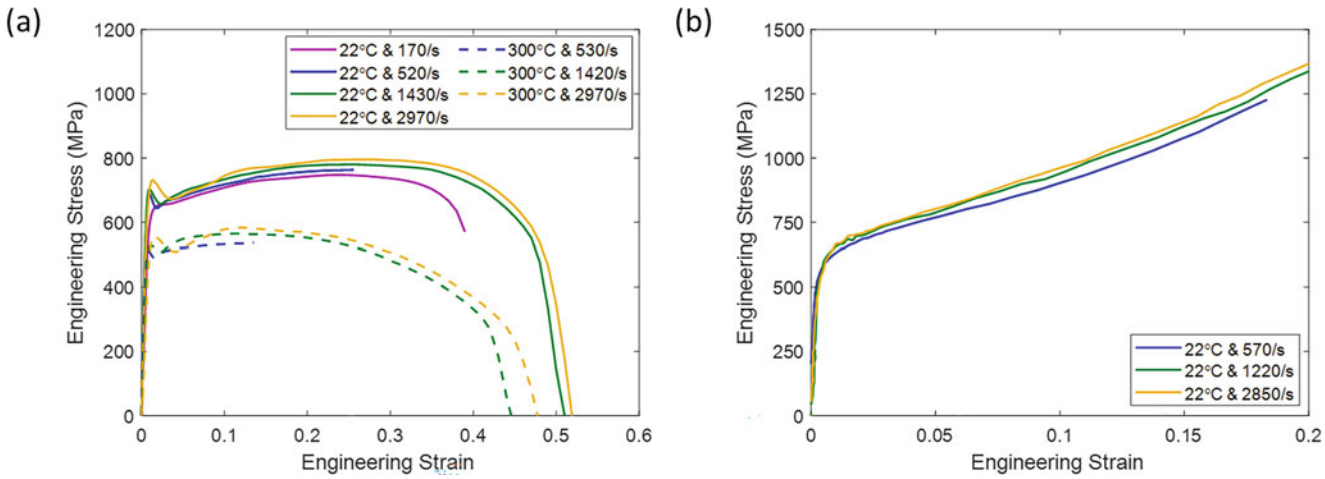


**Fig. 8.4** Engineering stress-strain behavior of 316 stainless steel at various temperatures and strain rates under (**a**) tension and (**b**) compression loadings

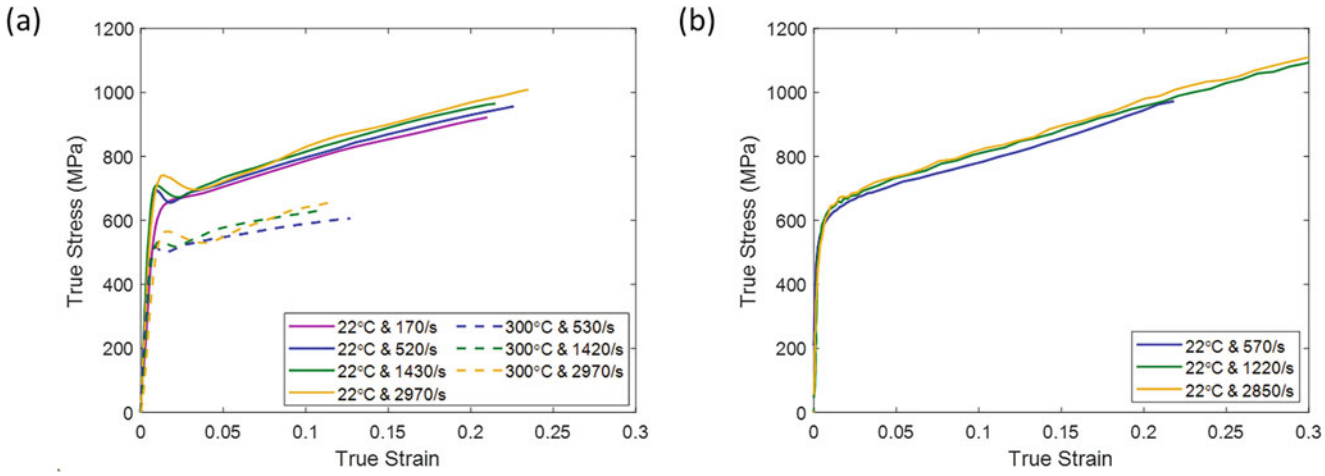


**Fig. 8.5** True stress-strain behavior of 316 stainless steel at various temperatures and strain rates under (**a**) tension and (**b**) compression loadings

duration of loading, the stress-strain curves at 22 °C/520 $s^{-1}$ and 300 °C/530 $s^{-1}$ shown in Fig. 8.4a do not represent specimen failure. The true stress-strain curves in tension, as shown in Fig. 8.5a, are plotted up to the onset of necking.

The tension and compression flow stress exhibit positive strain rate sensitivity that varies with strain and are inversely dependent on temperature. At 22 °C, increasing strain rate results in a ~10% increase in the 0.2% tensile yield stress and a ~7% increase in ultimate tensile stress. At 300 °C, deformation becomes more localized, as indicated by a decrease in engineering strain to failure, and material behaviors such as yield stress, ultimate tensile stress, and strain hardening rate are reduced. Figure 8.6 compares the tension and compression response at 22 °C under dynamic loading at the same strain rates. The results show reasonable symmetry in flow stress.

Figure 8.7 shows the effect of strain rate on the true failure and strain at onset of necking. The true failure strain is determined by measuring the minimum diameter of the post-test specimen. The strain at onset of necking is determined from the engineering strain at the ultimate tensile stress, which is then converted to true strain. Increasing temperature from 22 °C to 300 °C results in an increase in failure strain and decrease in strain at onset of necking. In addition, the true failure strain decreases with increasing strain rate, though the strain at onset of necking remains somewhat constant.

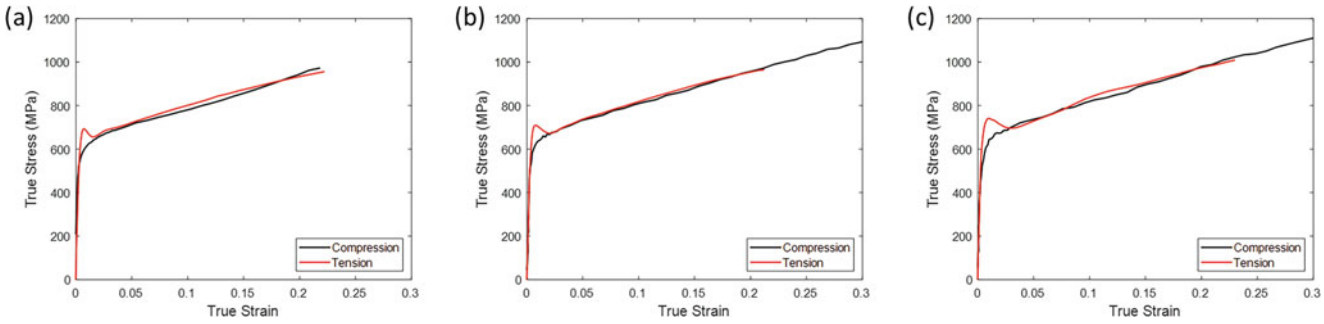


**Fig. 8.6** Comparison of the true tension and compression behavior of 316 stainless steel at 22 °C and at nominal strain rates of (**a**) 500 $s^{-1}$, (**b**) 1500 $s^{-1}$, (**c**) 3000 $s^{-1}$

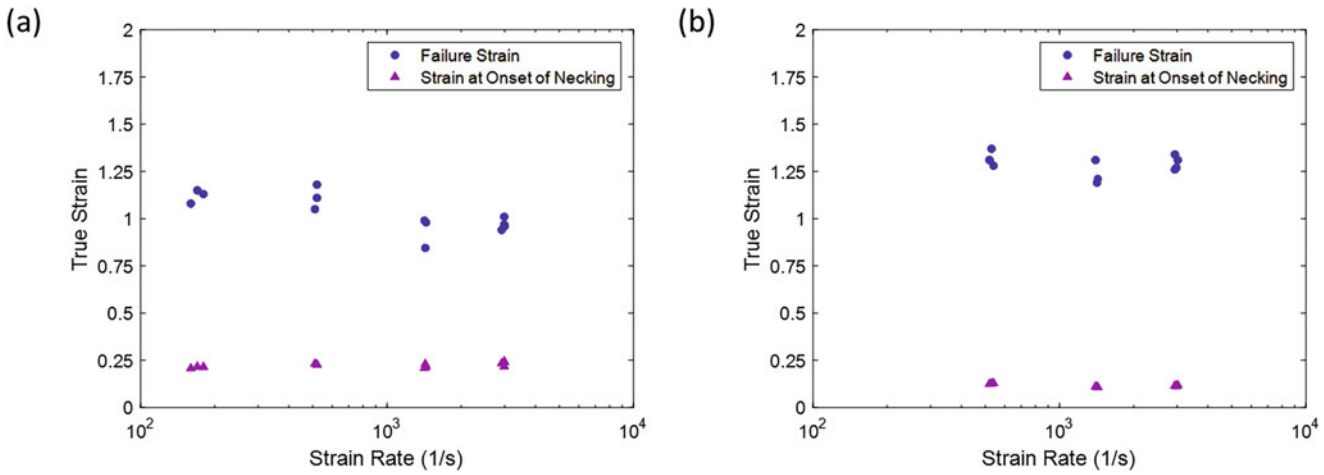


**Fig. 8.7** Strain rate effect on the failure strain and strain at onset of necking at (**a**) 22 °C and (**b**) 300 °C

## 8.4 Conclusion

In this study, the mechanical response of a 316 stainless steel is characterized at 22 °C and 300 °C and at various strain rates between 200 $s^{-1}$ and 3000 $s^{-1}$. The experimental results show that the tension and compression flow stress are reasonably symmetric, exhibit positive strain rate sensitivity, and are inversely dependent on temperature. The true failure strain in tension is determined by measuring the minimum diameter of the post-test specimen. The 316 stainless steel is very ductile, and the true failure strain increased with increasing temperature and decreased with increasing strain rate.

**Acknowledgments** Sandia National Laboratories is a multimission laboratory managed and operated by National Technology and Engineering Solutions of Sandia, LLC, a wholly owned subsidiary of Honeywell International, Inc., for the US Department of Energy's National Nuclear Security Administration under contract DE-NA0003525. The views expressed in the article do not necessarily represent the views of the US Department of Energy or the United States Government.

## References

1. Washko, S.D., Aggen, G.: Wrought stainless steels, properties and selection: irons, steels, and high-performance alloys. In: ASM Handbook, vol. 1, pp. 841–907. ASM International (1990)
2. Byun, T.S., Hashimoto, N., Farrell, K.: Temperature dependence of strain hardening and plastic instability behaviors in austenitic stainless steels. Acta Mater. **52**(13), 3889–3899 (2004)

3. Lee, W.S., Lin, C.F., Chen, T.H., Luo, W.Z.: High temperature deformation and fracture behaviour of 316L stainless steel under high strain rate loading. J. Nucl. Mater. **420**(1–3), 226–234 (2012)
4. Jin, H., Sanborn, B., Lu, W.Y., Song, B.: Mechanical characterization of 304L-VAR stainless steel in tension with a full coverage of low, intermediate, and high strain rates. Mech. Mater. **152**, 103654 (2021)
5. Song, B., Antoun, B.R., Connelly, K., Korellis, J., Lu, W.Y.: Improved Kolsky tension bar for high-rate tensile characterization of materials. Meas. Sci. Technol. **22**(4), 045704 (2011)
6. Song, B., Connelly, K., Korellis, J., Lu, W.Y., Antoun, B.R.: Improved Kolsky-bar design for mechanical characterization of materials at high strain rates. Meas. Sci. Technol. **20**(11), 115701 (2009)
7. Nie, X., Song, B., Loeffler, C.M.: A novel splitting-beam laser extensometer technique for Kolsky tension bar experiment. J. Dyn. Behav. Mater. **1**(1), 70–74 (2015)
8. Song, B., Sanborn, B., Susan, D., Johnson, K., Dabling, J., Carroll, J., Brink, A., Grutik, S., Kustas, A.: Correction of specimen strain measurement in Kolsky tension bar experiments on work-hardening materials. Int. J. Impact Eng. **132**, 103328 (2019)
9. Song, B., Sanborn, B., Heister, J.D., Everett, R.L., Martinez, T.L., Groves, G., Johnson, E., Kenney, D., Knight, M., Spletzer, M., Haulenbeek, K., McConnell, C.: An apparatus for tensile characterization of materials within the upper intermediate strain rate regime. Exp. Mech. **59**(7), 941–951 (2019)

# Chapter 9
# Experimental Investigation of the Nonlocal Dynamic Damage Mechanism in Shale

**Ali F. Fahem, Achyuth Thumbalam Guthai, and Raman P. Singh**

**Abstract** Understanding the dynamic failure mechanisms of shale is critical for optimizing oil and gas extraction from unconventional resources. This work presents the experimental investigation of the mechanism of nonlocal damage distribution in shale material under dynamic loading conditions. A circular disk specimen is subjected to local biaxial loading conditions and tested under two different experimental configurations. First, dynamic damage is investigated when the material is under tensile load along the bedding direction and compressive load perpendicular to the bedding direction. Second, the disk is rotated 90°, and the damage is investigated when a compressive load is applied in the bedding direction and a tensile load in the perpendicular direction. The specimens are dynamically loaded using a split Hopkinson pressure bar (SHPB). A noncontact optical technique, digital image correlation, is utilized to monitor the full-field strain and nonlocal damage initiation. As a result, two different dynamic damages are observed and discussed. The experimental setup and the nonlocal damage as a function of the bedding direction are also discussed.

**Keywords** Digital image correlation · Full-field data · Nonlocal damage · Shale · SHPB · Micro- and macro-damage

## 9.1 Introduction

Many researchers have investigated the topic of the damage mechanism of shale with the intent to increase the damaged area, which directly affects the production of oil and gas, particularly when the oil price moves more than $75. In general, three different approaches are used to solve the damage model: (i) total strain approach, Costin, 1983 [1, 2]; (ii) stress at damage initiation approach, Ashby, 1990 [3]; and (iii) the local kinetic energy of motion approach [4]. Some of the literature reported on damage mechanics of shale is, for example, in 2018, Zhu et al. studied the dynamic rock behavior numerically and observed that the dynamic damage of rock is a function of rheological condition, dynamic load disturbance, and time [5]. Jin and Arson, in 2018, proposed a numerical solution to evaluate the nonlocal damage mechanism of shale using empirical equations [6]. The results show that the damaged area simultaneously depends on the tension and compression load. Xu et al., 2016 [7] reviewed damage in shale and classified it into two main categories, namely, chemical and physical damage. Chemical damage includes the reaction between the structure of rocks and stored fluids, whereas physical damage includes phase confine damage and stress damage. Kong et al., 2019, worked on characterizing dynamic damage in brittle materials (coal) [8].

A. F. Fahem (✉)
Department of Materials Science and Engineering, College of Engineering, Architecture, and Technology, Oklahoma State University, Tulsa, OK, USA

Department of Mechanical Engineering, University of Al-Qadisiyah, Al-Qadisiyah, Iraq
e-mail: ali.fahem@qu.edu.iq

A. T. Guthai
Department of Mechanical and Aerospace Engineering, College of Engineering, Architecture, and Technology, Oklahoma State University, Tulsa, OK, USA

R. P. Singh
Department of Materials Science and Engineering, College of Engineering, Architecture, and Technology, Oklahoma State University, Tulsa, OK, USA

Department of Mechanical and Aerospace Engineering, College of Engineering, Architecture, and Technology, Oklahoma State University, Tulsa, OK, USA



S. Mates et al. (eds.), *Dynamic Behavior of Materials, Volume 1*, Conference Proceedings of the Society for Experimental Mechanics Series, https://doi.org/10.1007/978-3-031-17453-7_9

Wang et al., 2020, studied the shale failure mechanism experimentally [9]. They subjected the specimen to a uniaxial compressive load and deployed acoustic emissions devised to collect the cumulative damage. They showed that the size of the initial crack affects the compressive strength and reduces the elastic modulus of shale. Also, the dynamic damage is related to the crack density and the stress-strain change. Furthermore, the results showed that the specimen with a wing crack is damaged and more sensitive under shear stress than compressive stress. Most experimental works were done using far-field load and total damage responses to build a theoretical prediction model. In this work, 3D-digital image correlations are used to predict the nonlocal damage mechanism of shale under biaxial loading conditions.

## 9.2 Experimental Approach

A standard split Hopkinson pressure bar, SHPB [9], was used to test Oklahoma shale circular disk specimens under radial compressive load [10]. The specimens were prepared by drilling and cutting with a low-speed metallographic saw (Buehler IsoMet 1000, Lake Bluff, IL, USA) to final dimensions of 12 mm in diameter and 3 mm in thickness. The Hopkinson bars used were made from aluminum with 25.4 mm in diameter and 1750 mm in length, and two-linear strain gauges were attached at points M and N, as shown in Fig. 9.1. The high-speed camera, Hyper Vision (HPV-X2) from Shimadzu (Kyoto, Kyoto, Japan) [11], was employed with a frame rate of one million frames per second to record the specimen deformation during loading. The camera was triggered by an incident wave maser at gauge A with a time delay of around 200 μsec. The MDO model from Tektronix (Beaverton, OR, USA) oscilloscope is used to record the incident, reflected, and transmitted waves and trigger the camera and light. The images recording the deformation were transferred from the RAM of the cameras and saved to a PC for further analysis and to find the full-field deformation and strain using the Vic-2D program developed by Correlated Solution [12]. The far-field load applied is uniaxial. However, the specimen is deformed in biaxial directions. This unique setup can provide the properties of the specimen in two directions, as well as the damage mechanism and fracture development. The test procedure is repeated for 90° and 0° orientations.

## 9.3 Results and Discussion

Shale material's damage parameter is affected by the microstructure component and macro load conditions. Also, damage has to be evaluated along two dimensions, longitudinal (L) and transverse (T) to the bedding orientation. So, two models of dynamic damage factors can be used: the total damage and the local damage model. The total dynamic damage, $D(t)$, is a function of the initial elastic modulus $E_o$ and cumulative elastic modulus $E(t)$, [3, 10]. This model is strongly affected by the volume and mass of the testing specimens, Eq. 9.1.

The nonlocal damage model [1, 2] is a function of local stress components, crack density, and other factors, Eq. 9.2. The nonlocal damage or random damage can be calculated using a modified Costin formula for damage that includes the effect of microstructural features and degree of anisotropy [13].

$$D_i(t) = \sqrt[3]{1 - \frac{E_i(t)}{E_{io}}}\, c_i \tag{9.1}$$

$$\varepsilon_i(t) = \sigma_i(t)\left(\frac{1}{E_{io}\left[1 - \left(D_i^3/c_i\right)\right]} + \frac{v_o}{E_{io}}\right) + \frac{T_i}{k_i} D_i^3 \tag{9.2}$$

where:

$E_i$, Cumulative elastic modulus
$E_{i0}$, Initial elastic modulus
$\sigma_i$, Far-field stress
$\varepsilon_i$, Local strain
$c_i$, Crack distribution
$v_o$, Poisson's ratio
$T_i$, Local stress
$k_i$, The elastic modulus related to stiffness around the crack zone
$i = L, T$, L and T are longitudinal and transverse directions related to the shale's layer orientations.

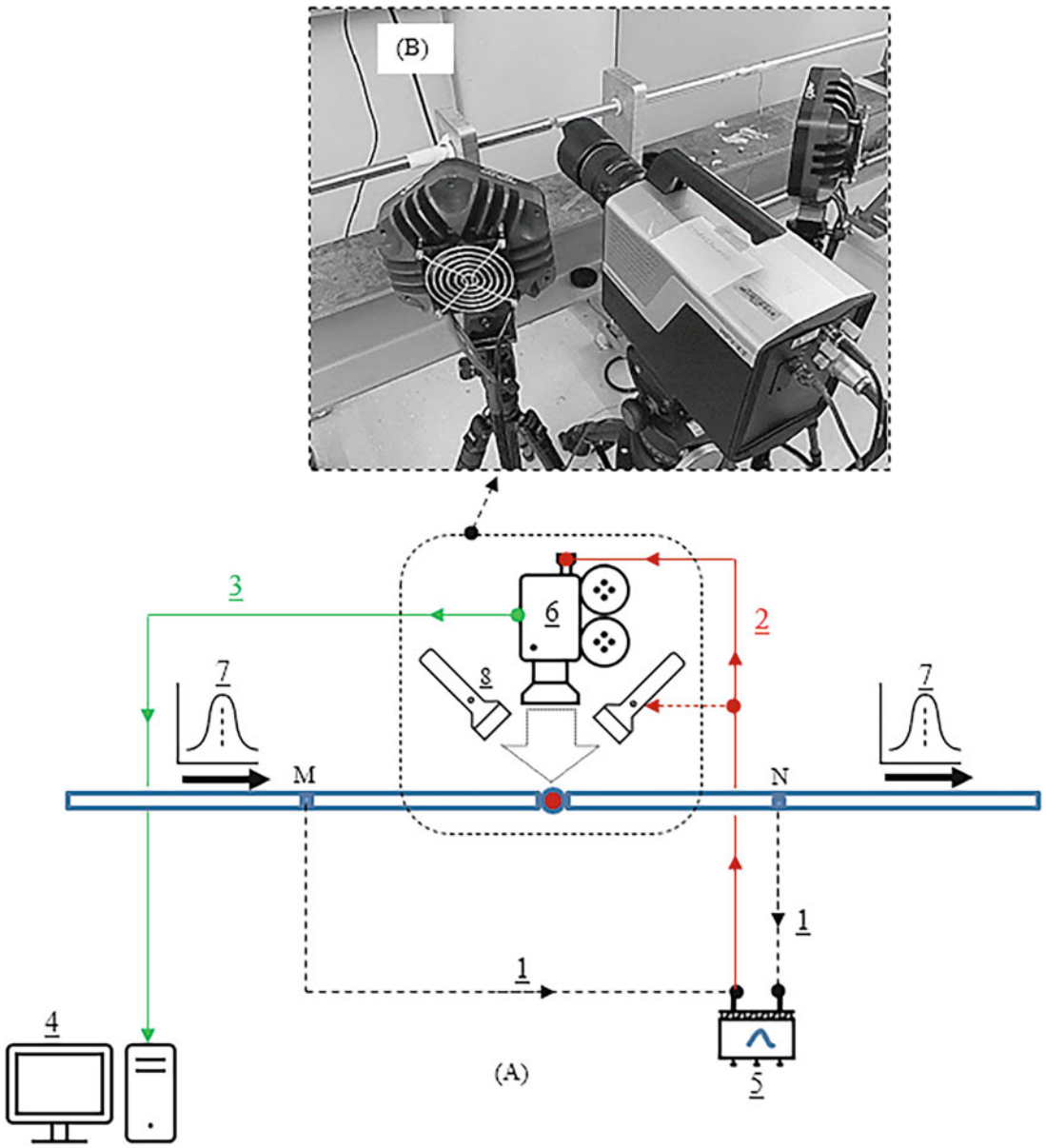


**Fig. 9.1** SHPB setup. Part A shows the overall schematic of the setup, and Part B shows the actual image of this configuration around the specimen, where connection 1 is for transferring the strain gauge signals to the oscilloscope. Path 2 is used to trigger the high-speed camera and the lights. Line 3 transfers and saves the selected images from the camera's RAM to the PC hard drive. 4 is the PC used to run the Vic2D program from correlated solution. Item 5 is an oscilloscope that is used to record the incident and transmitted wave and trigger the camera. The high-speed camera, HPV-X2, is number 6. The incident and transmuted waves are 7. Finally, the pair of lights are 8

The deformation of a circular disk was captured using an HPV-X2 camera with a frame rate of 1,000,000 fps, as shown in Fig. 9.2, with the shale specimen reaching a visual crack at $\approx 10 \mu sec$ as shown at the center of the disk. However, after that, the specimen fragments into many pieces from different locations, *random location*. Thus, there are two observation points from this test. First, at the macroscale level, the specimen was deformed, and the maximum strain was developed at the center. This behavior matches with the theoretical solution of a circular disk under the radial compressive load [14]. This deformation and fragmentation are geometry dependent, i.e., the shape of the specimen is forcing the shale to start damage and failure at that location, and it might not be the weakest point.

Secondly, using an optical method, 2D-DIC, the full-field strain at the surface shows more pre-damage, related to microcrack, which is growing faster than the one at the center points. At the microscale, the damage develops randomly and depends on the strength between the particles. Tracking the loading time at that is shown in Fig. 9.3. The specimen was

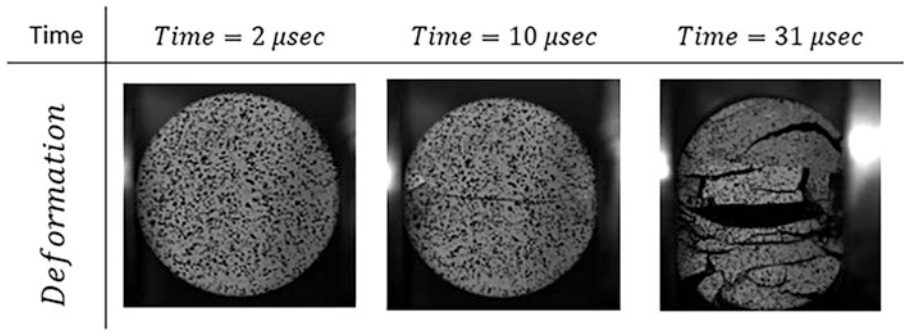


**Fig. 9.2** Typical images of circular disk deformation at different stages starting from initial loading up to full fragments

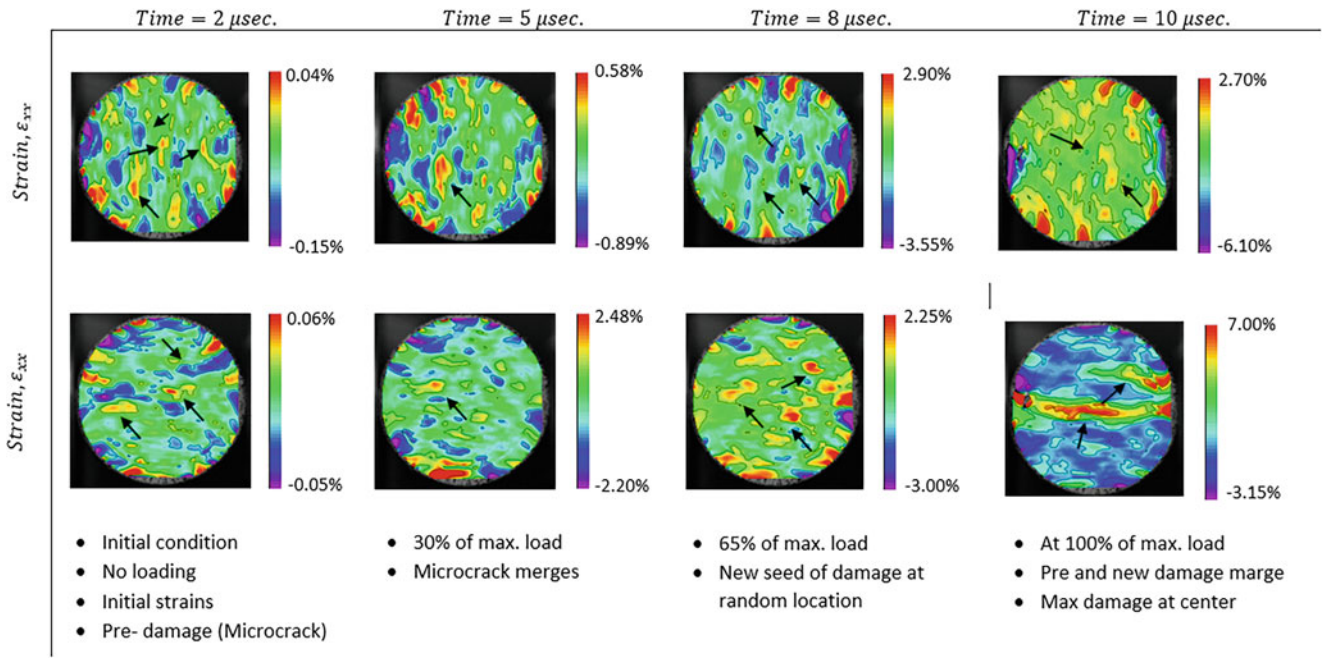


**Fig. 9.3** Typical Nonlocal damage progress of shale under impulse loading when compressive load propagates along the bedding directions and tensile load in the perpendicular direction

initially not loaded, but it still has some pre-damage or microcracks. When the loading reaches almost 30% of the maximum load, the pre-damage is moving and merging at random locations. With more load, at almost 65% of maximum load, the new seeds of damage show up. These seeds are integrated with the pre-cracks and made high concentrated strain locations at random locations. At this point, the specimen starts cracking at random locations; however, the geometry effect is forcing the stress flow to concentrate on the center of the disk. After the crack starts at the center, nonlocal damages are developed to fragment the disk into many pieces. The circular dick specimen shows two different damage behaviors. First, at the center of the disk due to the circular geometry and, second, at random points due to the microdamage behavior of shale. This behavior was observed for both $90^{\circ}$ and $0^{\circ}$ test loading orientations.

## 9.4 Conclusion

The dynamic damage mechanism of shale was investigated using SHBP and digital image correlation. On-local dynamic damage distribution in shale material is observed during the test; however, the maximum and initiation damage is developed at the center due to the disk geometry effect. The main points of this work are listed as follows:

- The circular disk shows both global and local damage mechanism.
- The circular disk specimen data can be used to estimate the dynamic strength of shale.
- For dynamic damage mechanism investigation, the full-field data must be used and cumulative data from zero up to 70% of maximum load.

## References


1. Costin, L.S.: A microcrack model for the deformation and failure of brittle rock. J. Geophys. Res. **88**(B11), 9485–9492 (1983). https://doi.org/10.1029/JB088iB11p09485
2. Costin, L.S., Duffy, J., Freund, L.B.: Fracture initiation in metals under stress wave loading conditions. Fast Fract. Crack Arrest (ASTM STP). **627**, 301–318 (1977)
3. Ashby, C.G., Sammis, M.F.: The damag mechanics of brittle solids in compression. Pure Appl. Geophys. PAGEOPH. **133**(3), 489–521 (1990)
4. Grady, D.E., Kipp, M.E.: Continuum modelling of explosive fracture in oil shale. Int. J. Rock Mech. Min. Sci. **17**(3), 147–157 (1980). https://doi.org/10.1016/0148-9062(80)91361-3
5. Zhu, W., Wei, J., Niu, L., Li, S., Li, S.: Numerical simulation on damage and failure mechanism of rock under combined multiple strain rates. Shock. Vib. **2018**, 1 (2018). https://doi.org/10.1155/2018/4534250
6. Jin, W., Arson, C.: Anisotropic nonlocal damage model for materials with intrinsic transverse isotropy. Int. J. Solids Struct. **139–140**, 29–42 (2018). https://doi.org/10.1016/j.ijsolstr.2018.01.020
7. Xu, C., Kang, Y., You, Z., Chen, M.: Review on formation damage mechanisms and processes in shale gas reservoir: known and to be known. J. Nat. Gas Sci. Eng. **36**, 1208–1219 (2016). https://doi.org/10.1016/j.jngse.2016.03.096
8. Kong, X., Wang, E., He, X., Zhao, E., Zhao, C.: Mechanical characteristics and dynamic damage evolution mechanism of coal samples in compressive loading experiments. Eng. Fract. Mech. **210**(April), 160–169 (2018). https://doi.org/10.1016/j.engfracmech.2018.04.005
9. Fahem, A., Kidane, A., Sutton, M.A.: A novel method to determine the mixed mode (I/III) dynamic fracture initiation toughness of materials. Inernational Fract. Mechincs. **224**(May), 47–65 (2020). https://doi.org/10.1007/s10704-020-00445-3
10. Fahem, A., Singh, R.: Dynamic damage evolution in shale in the presence of pre-existing microcracks. SEM Annu. Conf. June 14–17, 2021. **1**(1), 1–10 (2021). https://doi.org/10.1007/978-3-030-86562-7_7
11. Shimadzu, "Hyper Vision HPV-X2," 2020. https://www.shimadzu.com
12. Correlated Solution Inc., "Vic-2D Digital Image Correlation," *Armo, SC, USA*. www.correlatedsolutions.com
13. Parisio, F., Samat, S., Laloui, L.: Constitutive analysis of shale: a coupled damage plasticity approach. Int. J. Solids Struct. **75–76**, 88–98 (2015). https://doi.org/10.1016/j.ijsolstr.2015.08.003
14. Muskhelishvili, N.I.: Some Basic Problems of the Mathematical Theory of Elasticity, fourth. Springer Science and Business Media Dordrecht, Moscow (1977)

# Chapter 10
# Effects of Internal Particle Damper Thickness and Location on Damping Sustainability of Additively Manufactured Nickel Alloy Beams


**John P. Hollkamp and Onome Scott-Emuakpor**

**Abstract** In recent studies, laser powder bed fusion (LPBF) additive manufacturing has created structural beam components possessing internal pockets containing unfused metallic powder. Compared to fully fused beams, these pocketed beams have demonstrated a remarkable improvement in damping performance, suppressing vibrations by as much as 95%. This suggests that internal geometries containing unfused powder can be a significant design feature to reduce vibration and extend the life of structural components. However, additional studies and improvements are needed before these designs can become widespread. For example, it has been observed that the unfused powder begins to fuse to the walls of the pockets when subjected to high strain loading, reducing their damping abilities. This study investigates the effects of the thickness of the beams and the pocket's axial location in LPBF nickel-based alloy 718 beams on their damping sustainability after being subjected to high strain loads. The beams are subjected to successive resonance dwells with increasing strain amplitude. After each dwell, the damping performance is assessed via frequency sweeps. Results from this study indicate that the decrease in damping performance follows the same relative trend regardless of the beam thickness. The axial location of the pockets affects the initial damping and also influences when the powder begins to fuse.

**Keywords** Structural dynamics · Particle damping · Vibration analysis · Additive manufacturing · Quality factor

## 10.1 Introduction

Damping technologies have long been researched to reduce vibration, extend the lifetime, and reduce the maintenance frequency and costs of structural components. Damping technologies include but are not limited to hard coatings, viscoelastic layers, and impact and friction dampers [1–9]. A much-researched damping treatment is particle damping, which dissipates kinetic energy through the inelastic collisions and friction between vibrating masses and the walls of their enclosure [7–9]. The dynamics of particle dampers are typically nonlinear due to the complexities of the Hertz collisions and loss mechanisms. Recent particle damper research conducted by Scott-Emuakpor et al. [10–15] has been motivated by gas turbine engines and the ever-persisting need to improve their performance. For instance, despite the beneficial lightweight design of integrally bladed turbine rotors, they are more susceptible to vibratory loads and high cycle fatigue. In order to improve the damping of structural beams representative of turbine blades without adding additional weight, Scott-Emuakpor et al. [10–15] leveraged the manufacturing capabilities of laser powder bed fusion (LPBF) additive manufacturing to create particle dampers internal to the structure. These internal particle dampers are pockets within Inconel (IN) 718 structural beams that are completely full of the unfused powder feedstock used in LPBF. The first study conducted by Scott-Emuakpor et al. [10] reduced the vibrations of the beams by as much as 95% compared to a corresponding fully fused beam even though the volume of the unfused powder pockets was as low as 1–4% of the total beam volume. Further studies [11–15] examined the placement of the unfused powder pockets, the excited bending mode, the amplitude of the excitations, and other manufacturing parameters such as material and laser scanning sequence. Additionally, Refs. [12, 13] proposed a simplified model that related the vibratory shear load and displacement to the damping performance of the particle-damped beams.

Despite the encouraging results of the internal particle damper research conducted in Refs. [10–15], more research is needed before this technology can be regularly incorporated into structural components such as gas turbine engine blades. For example, the effects of other variables on the operating environments of gas turbine engines, including high temperatures, rotational speeds, and centrifugal forces, must be examined. Moreover, the ability to accurately model the physics of the

J. P. Hollkamp (✉) · O. Scott-Emuakpor
United States Air Force Research Laboratory, Wright-Patterson AFB, OH, USA
e-mail: john.hollkamp.1.ctr@us.af.mil; onome.scott-emuakpor.1@us.af.mil



S. Mates et al. (eds.), *Dynamic Behavior of Materials, Volume 1*, Conference Proceedings of the Society for Experimental Mechanics Series, https://doi.org/10.1007/978-3-031-17453-7_10

powder particles across a wide spectrum of operating conditions and frequency excitations would be instrumental in reliably predicting the damping performance and optimizing the particle damper design. To this endeavor, Kiracofe et al. [16] developed a discrete element method numerical simulation of particle-damped beams that has shown promise but is still computationally expensive. On the other hand, the challenge that will be studied in this paper is the ability to maintain the damping performance of the particle dampers at high strain amplitudes. We call this the damping sustainability of the particle damper. Scott-Emuakpor et al. [11] found that the superb initial damping performance of the particle-damped beams began to degrade after subjection to thousands of cycles at high strain amplitudes due to high-impact loads fusing portions of the unfused powder to the walls of the pocket. When some of the powder fused to the walls, there was less unfused powder capable of energy-dissipating motion, leading to a decrease in damping performance. Two additional studies investigated the decrease in damping sustainability due to powder fusion. In the first, Scott-Emuakpor et al. [15] manufactured six LPBF IN 718 beams with differing pocket shapes. Reference [15] concluded that curved non-wavelike internal surface features were the optimal shape for damping sustainability. Still, all the specimens eventually experienced damping degradation due to powder fusion. In a follow-up study, Hollkamp et al. [17] analyzed the role that the axial locations of the unfused powder pockets had on damping sustainability. They found that the axial location of the beams affected the initial damping performance and damping sustainability. A model based on the location of the pockets with respect to the deflection shape of the excited bending mode could accurately determine the initial damping behavior. Regarding damping sustainability, Hollkamp et al. [17] concluded that the beams that exhibited the best initial damping performance were also the first to experience damping degradation. However, they concluded that the axial location of the pockets was not the optimal variable to maintain damping sustainability.

This paper serves as a follow-up study to Ref. [17]. Like in Ref. [17], the axial location of the pockets will be varied. However, the chief variable studied here will be the thickness of the beam specimens. The damping sustainability of beams of different thicknesses will be measured and compared. In addition, experimentation and analysis of the damping performance of corresponding fully fused beam specimens (i.e., beams containing no pockets of unfused powder) will be examined. The goal of the study is to examine the role that the thickness of the beams has on its damping sustainability and to identify additional parameter variations and experiments that will continue to improve internal particle damping technologies and maintain damping sustainability.

## 10.2 Beam Designs and Manufacturing

The design and dimensions of the IN 718 beams are given in Fig. 10.1. The beams contain two internal pockets of unfused powder. In Ref. [17], the thickness of the beams was kept constant at 3.18 mm (0.25 in.). In this study, two additional thicknesses are studied: 6.35 mm and 9.53 mm. The thickness of the pockets was chosen to be 20% of the overall beam thickness, while the combined length of the two pockets was chosen to be 20% of the total beam length (10% each). As seen in Fig. 10.1, the manufactured beam was 229 mm long, although 51 mm of the beam is clamped between stainless steel blocks. Thus, the test portion of the IN 718 beams is 178 mm long. For each of the beam thicknesses, 4 beams with different axial pocket locations were tested, for a total of 12 beams. We call the four 3.18 mm-thick beams "*Series A*," the 6.35 mm-thick beams "*Series B*," and the 9.53 mm-thick beams "*Series C*," as stated in Table 10.1 for reference. For each beam series, one of the tested beams contained no pockets of unfused powder. These fully fused (FF) beams served as a basis to compare the damped beams. The axial locations of the other three beams for each series are given in Table 10.2 below.

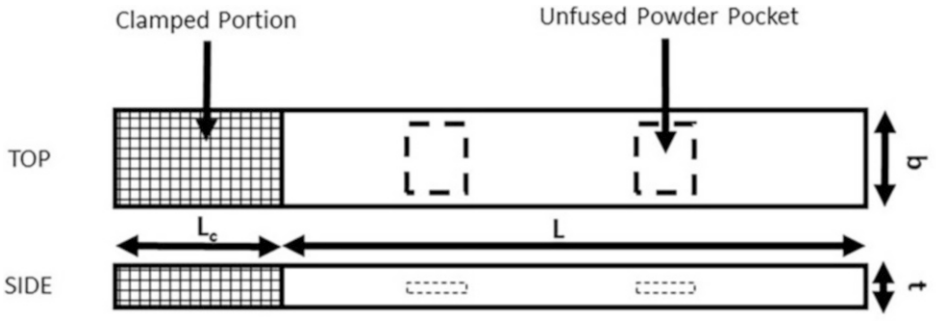


| Variable | Value (mm) |
|---|---|
| L | 178 |
| $L_c$ | 50.8 |
| b | 25.4 |
| t | 3.18, 6.35, or 9.53 |

**Fig. 10.1** Illustration of the beam specimen design containing two pockets of unfused powder

**Table 10.1** Series names for the three different beam thicknesses studied

| Beam series name | Beam thickness (mm) |
|---|---|
| A | 3.18 |
| B | 6.35 |
| C | 9.53 |

**Table 10.2** Axial start and end location of the particle-damped beams as measured from the end of the clamped portion

| Beam # | First pocket start location (mm) | First pocket end location (mm) | Second pocket start location (mm) | Second pocket start location (mm) |
|---|---|---|---|---|
| 1 | 36.5 | 54.3 | 116.5 | 134.3 |
| 2 | 73.7 | 91.4 | 153.7 | 171.5 |
| 3 | 23.9 | 41.6 | 103.9 | 121.7 |

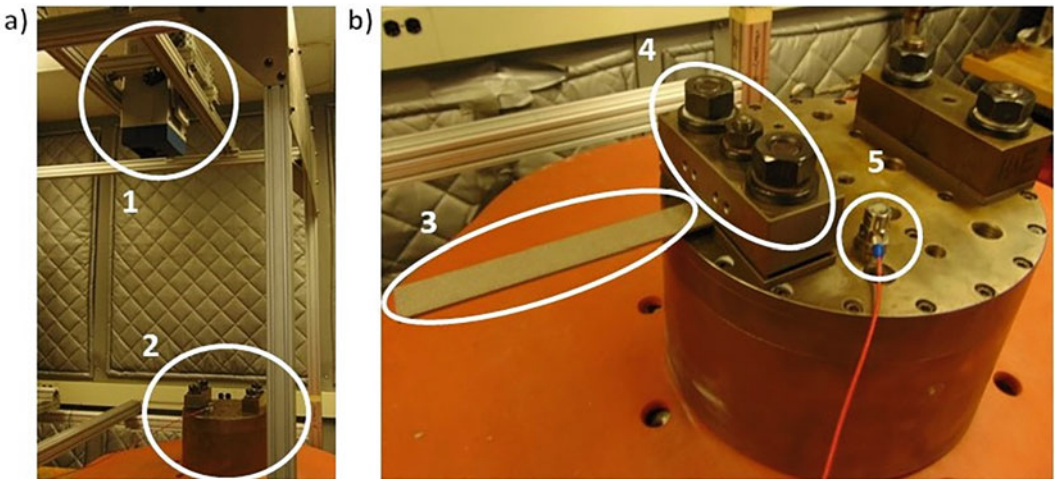


**Fig. 10.2** (**a**) The shaker experimental test configuration with (1) the laser vibrometer and (2) the shaker head. (**b**) A close-up view of the shaker head depicting (3) the mounted beam specimen, (4) the clamping blocks, bolts, and nuts, and (5) an accelerometer

The beam specimens were manufactured by LPBF additive manufacturing using a Concept Laser M2 cusing machine whose IN 718 powder feedstock was gas atomized with an average diameter of 27 µm. The scan strategy of the Concept Laser M2 varied the machine parameters for the core, skin, and contours of the specimen and can be found in more detail in Ref. [15]. To summarize, the laser power for the contour, skin, and core scan strategies was, respectively, 120 W, 180 W, and 370 W. Likewise, the raster speeds for the contour, skin, and core, respectively, were 280 mm/s, 800 mm/s, and 700 mm/s. The laser spot size was 50 µm, 130 µm, and 180 µm for the contour, skin, and core. Lastly, the skin strategy had a hatch distance of 105 µm, while the core strategy had a hatch distance of 130 µm. While the pockets were desired to be totally full of the unfused powder, Refs. [10–15] estimated that the pockets were between 88% dense and 100% full.

## 10.3 Experimental Procedure

The experimental configuration and procedure are nearly the same as that in Ref. [17]. The setup is shown in Fig. 10.2. The clamped beam specimen was mounted to a 27 kN Unholtz-Dickie electrodynamic shaker. The nuts on the bolts of the clamping blocks were tightened using an English unit torque wrench: 120 ft-lb torque on 1 1/16 in. nuts with 5/8 in. studs and 100 ft-lb on a 7/8 in. nut with a 3/8 in. center stud. A Vibration Research VR9500 controller and an Endevco 2271A charge-type accelerometer controlled the excitation amplitude and frequency of the shaker. A Polytec OFV-5000 (OFV-505 head) single-point laser vibrometer was mounted overhead as seen in Fig. 10.2a to measure the velocity response of the tip of the cantilever specimen as well as the phase relative to the shaker. The laser point measured the flexural velocity of the specimen at approximately 4 mm from the cantilever's tip. The experimental procedure can be summarized as follows:

1. Determine the location of the desired resonance frequency of the specimens by conducting a low-amplitude broadband sweep. For *Series A* (i.e., the 3.18 mm-thick beams), the desired resonance frequency was the third natural frequency. However, the natural frequencies of the thicker beams from *Series B* and *Series C* were larger. The shaker was not capable of capturing the higher third resonance frequencies of *Series B* and *Series C*. Thus, the second resonance frequency was instead analyzed for *Series B* and *C*. This is further discussed in the results section below.
2. After identifying the desired resonance frequency, narrow the window of the frequency sweep to approximately 3 bandwidths around the resonance peak. Use a frequency sweep rate of 30 s or more per half power bandwidth to cleanly capture the frequency response function (FRF) of the velocity at and near resonance.
3. Repeat Step #2 for three or more different shaker accelerations. This is done to ensure that the FRFs' amplitudes scale linearly. This study measured the velocity FRFs for shaker head accelerations of 1 G, 1.5 G, and 2 G.
4. Measure the quality factor $Q$ by applying the half-power bandwidth method [18] to the three FRFs before conducting a resonance dwell. Recall that $Q$ is the inverse of the damping loss factor η.
5. Perform a sinusoidal resonance dwell around the resonance frequency lasting 750,000 cycles. The amplitude of this dwell is chosen to correspond to a maximum axial strain of 100 μm/m at the clamped end of the specimen (see below for details on how to specify the amplitude of the resonance dwell accordingly).
6. After the dwell is complete, obtain the FRFs corresponding to shaker head accelerations of 1 G, 1.5 G, and 2 G and measure the quality factor $Q$ by applying the half-power bandwidth method.
7. Repeat Steps #5 and #6, increasing the amplitude of the strain resonance dwell by 50 μm/m until the specimen cracks.

In setting the amplitude of the resonance strain dwells in Steps #5 and #7, the shaker input was controlled by setting the velocity amplitude measured by the laser vibrometer. To determine the relationship between the measured velocity at the tip of the beam and the maximum axial strain at the clamped end, the Euler-Bernoulli beam theory was applied [18]. According to the Euler-Bernoulli beam theory, the axial strain $\epsilon_{xx}$ in the beam is

$$\epsilon_{xx} = -z\frac{\partial^2 w}{\partial x^2} \tag{10.1}$$

where $x$ is the axial coordinate, $z$ is the distance from the neutral axis along the beam's thickness, and $w$ is the flexural displacement. Using Eq. (10.1), it is possible to derive the desired velocity-strain relationship. For the sake of brevity, the details of the derivation are left to Ref. [17], while the final equation is given here as

$$v = \frac{Ac\varepsilon}{h} \tag{10.2}$$

where $v$ is the velocity near the beam tip measured by the laser, $c$ is the wave speed constant ($c = \sqrt{EI/\rho A}$ where $E$ is Young's modulus, $I$ is the area moment of inertia, ρ is density, and $A$ is the cross-sectional area), $h$ is the beam thickness, and $\varepsilon$ is the maximum strain at the clamped end. The constant $A$ is defined as

$$A = \cos\beta X - \cosh\beta X - \frac{\cos\beta L + \cosh\beta L}{\sin\beta L + \sinh\beta L}(\sin\beta X - \sinh\beta X) \tag{10.3}$$

where $\beta^2 = \omega/c$, $\omega$ is the natural frequency of the dwell, and $X = L$-4 mm (the location of the laser point). By using Eq. (10.2), the laser velocity amplitude corresponding to the maximum axial strain can be determined and set as the constant amplitude of the laser measurement during the resonance dwell.

## 10.4 Results and Discussion

Following the experimental procedure, the frequency response functions of the flexural velocity near the beam tip were measured by the laser vibrometer. As mentioned in Step #6, three FRFs were obtained for each specimen corresponding to shaker head accelerations of 1 G, 1.5 G, and 2 G. Example plots of the FRFs taken from *Series B*'s Beam #3 are depicted in Fig. 10.3. Figure 10.3a shows the FRFs obtained after the 100 μm/m resonance dwell. The FRFs show a resonance frequency of 840 Hz. Moreover, the FRFs are linear, as evidenced by the fact that the amplitude of the 2 G FRF is double that of the 1 G FRF, and so forth. On the other hand, Fig. 10.3b depicts the FRFs obtained after the 250 μm/m resonance dwell. As will be discussed in Fig. 10.4, this dwell corresponds to a region during which powder fusion is occurring. Analyzing each FRF in Fig. 10.3b individually would convey the notion that the system is perhaps still linear. However, it is obvious that the

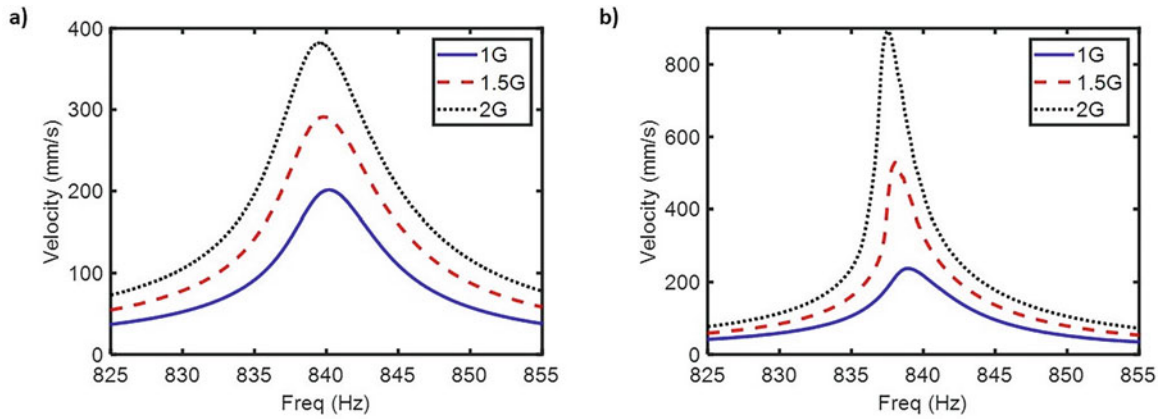


**Fig. 10.3** (**a**) An example of the three frequency response functions taken after the initial resonance dwell where the response is linear. (**b**) An example of FRFs taken during the dwells in which powder fusion occurs, resulting in a nonlinear dynamic response

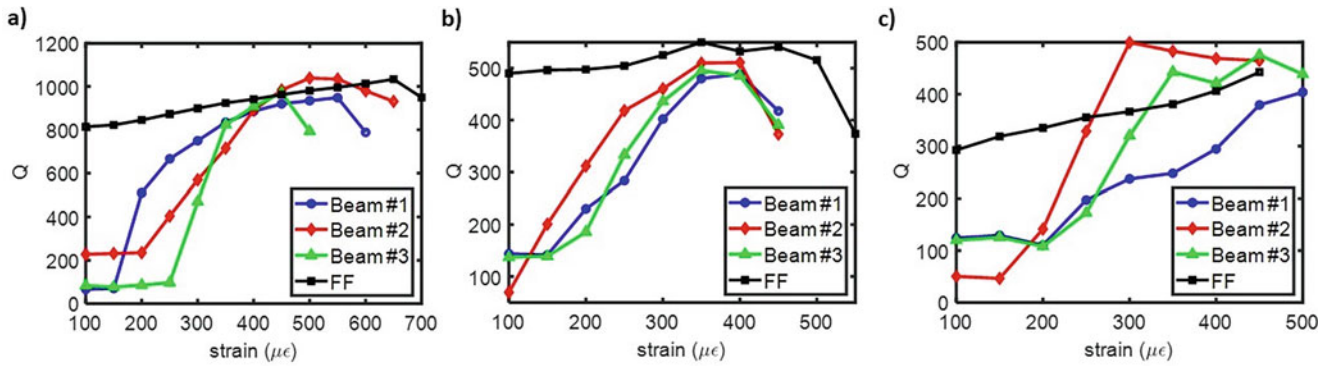


**Fig. 10.4** (**a**) The damping sustainability curves for *Series A*. Note that the data for Beam #1 and #2 of *Series A* were taken from Ref. [17]. (**b**) The damping sustainability curves for *Series B*. (**c**) The damping sustainability curves for *Series C*

dynamics are nonlinear during this powder fusion region since the amplitudes of the FRFs did not increase in a linear fashion (for instance, the 2 G FRF peak amplitude in Fig. 10.3b is approximately four times that of the 1 G FRF peak amplitude). Additionally, it is seen in Fig. 10.3b that the resonance frequency begins to shift slightly to the left as the shaker head excitation increases. Although these nonlinearities are not necessarily surprising given that particle dampers can behave nonlinearly, the application of the half-power bandwidth method to calculate $Q$ now possesses a greater dependency on the amplitude of the shaker excitation. To allow for consistent comparisons between the specimens, the average value of $Q$ obtained by applying the half-power bandwidth method to the three FRFs is taken.

The average quality factors obtained from Step #6 after each dwell are plotted in Fig. 10.4 for each beam series given in Table 10.1. The data from Beam #1 and #2 from *Series A* was taken directly from Ref. [17]. The experimental data for Beam #3 is original to this work since Beam #3 in Ref. [17] was seen to be anomalous. Before comparing the results between the three beam series, first consider Fig. 10.4a individually. In Fig. 10.4a, the initial $Q$ values after the 100 μm/m strain dwell of the particle-damped beams were between 8% and 25% of that of the fully fused beam, indicative of significant amounts of damping added by the presence of the unfused powder pockets. The differences between the initial $Q$ values are directly related to the axial location of the unfused powder pockets with respect to the flexural displacement of the excited mode, detailed further in Ref. [17]. Pockets located near the antinodes of the flexural displacement shape function demonstrated better initial damping performance in comparison to unfused powder pocket locations located near the nodes [17]. In Fig. 10.4a, Beams #1 and #3 had pocket locations closer to the antinodes of the third bending mode (recall that *Series A* was conducted around the third bending resonance frequency) than Beam #2. However, for all three beams, the $Q$ values begin to increase after the higher amplitude strain dwells. The increase in the quality factors (hence, the decrease in damping performance) occurred as portions of the unfused powder began to fuse to the pocket walls. This powder fusion process where the quality factors increase is seen in Fig. 10.4, beginning as early as after the 150 μm/m dwell in some specimens. The powder fusion process and increase in $Q$ continue to occur at higher strain amplitudes in Fig. 10.4a until all three particle-damped beam curves appear to level out around the 450 μm/m strain dwell. This is where the powder fusion process has terminated. It

is seen that the final $Q$ values for each specimen decrease. These $Q$ values were obtained after cracking formed at the clamped end of the specimen. The improvement in damping performance here results from the high cycle fatigue cracking rather than the particle damping. What is interesting to note in Fig. 10.4a is the trend of the fully fused beam specimen. The initial $Q$ value of the fully fused beam was approximately 800. It was anticipated that the $Q$ value would remain approximately this constant value after each dwell since there were no pockets that would experience powder fusion. However, the values of $Q$ did increase slightly after each dwell, with $Q$ approximately equal to 1000 when cracks formed. Even more curiously, the $Q$ values after the higher strain dwells of the particle-damped beams were approximately the same as (or even greater) than the fully fused beam. Although powder fusion does in fact decrease the damping sustainability of the particle-damped beams, their $Q$ values should not be this comparable to the fully fused beam since there is still unfused powder present capable of damping. We believe that the most likely reason is due to imperfect clamping. It is hypothesized that the top clamp in Fig. 10.2 likely exhibited some bowing during the shaking of the fully fused beam, leading to additional losses via the imperfect clamp. While the particle-damped beams likely also experienced this imperfect clamping, its effects would not be as drastic since the amplitudes of the vibration (as seen when comparing the velocity FRFs of all the specimens) for the damped beams were smaller than that of the fully fused beams. Thus, the damping losses from the imperfect clamp would be more pronounced on the fully fused specimen, meaning that its true $Q$ values would be greater than reported. Naturally, additional experiments to prove this hypothesis are planned to be performed in the near future.

Consider now the damping sustainability plots for *Series B* and *Series C* given respectively in Fig. 10.4b and c. First, note that the fully fused beams in these beam thickness series had even lower $Q$ values than those of the fully fused beams in *Series A*. In fact, the initial $Q$ value for the fully fused beam of *Series C* was approximately 300. This is certainly too low of a $Q$ value for a fully fused beam. In theory, the thickness of the fully fused beam should not alter the damping capabilities. We again believe that the imperfect clamp is the most likely reason for this. The clamping losses increased as the thickness of the fully fused beam increased. Additionally, the fact that the initial damping values of the particle-damped beams of *Series B* and *C* were in the same neighborhood as that of *Series A* further supports the notion that the clamping losses did not affect the $Q$ measurements of the particle-damped beams as much as that of the fully fused beams. When comparing the damping behavior after the initial resonance dwell of a maximum strain amplitude of 100 μm/m in the three plots of Fig. 10.4, it is seen that the initial damping of Beam #2 in *Series B* and *Series C* was the best among the three particle-damped beams, while the initial damping behavior of Beam #2 in *Series A* was the worst of the three particle-damped beams. This is due to the fact that the resonance dwells conducted in *Series B* and *Series C* were around the second resonance frequency, while the dwells were conducted around the third resonance frequency for *Series A*. In carefully examining the flexural mode shapes, the locations of the unfused powder pockets in Beam #2 were located closest to the antinodes of the second mode shape among the beam specimens, while it was located the farthest from the antinodes of the third bending mode shape. In retrospect, the resonance dwells of *Series A* should have been conducted around the second bending mode to allow for a more direct comparison of the initial damping among the three beam thickness series of Table 10.1. However, with regard to damping sustainability, the similar curve shapes in the three plots of Fig. 10.4 indicate that the damping decreases regardless of which resonance frequency the strain dwells occur. In Fig. 10.4b, the powder fusion process begins almost immediately as evidenced by the early increase in the slope of the curves. In both Fig. 10.4b and Fig. 10.4c, the $Q$ values of Beam #2 increase before those of Beams #1 and #3. This supports the claim in Ref. [17] that a tradeoff occurs between the initial damping abilities and the damping sustainability. This is due to the fact that the larger vibratory loads experienced by pockets located closer to the antinodes of the beam bending mode shape cause powder fusion to occur earlier. The final $Q$ values of the damped beams in Fig. 10.4b and c were around 400–500 while those in Fig. 10.4a were approximately 800. This is again difficult to compare since the dwells occurred around different bending modes. Since *Series B* and *Series C* were both conducted about the second bending mode, their damping sustainability plots are directly compared in Fig. 10.5.

The comparisons of the particle-damped beams in Fig. 10.5 show that the powder fusion process for the beams in *Series B* began during strain dwells 50 μm/m less than their counterparts in *Series C*. This may be due to the fact that the distance between the top and bottom of the beam specimens to the pockets' locations was greater in the thicker *Series C*. However, the pocket thickness was chosen as 20% of the overall beam thickness for all beam specimens so that the axial strain profile across the pocket thickness would remain consistent according to Eq. (10.1) regardless of the beam thickness. In fact, this is the reason why the slopes of the curves of each beam in *Series B* during the initial portion of the powder fusion phase were approximately equivalent to those of their counterpart beams in *Series C*. Additionally, all the specimens in *Series B* and *Series C* began to experience high cycle fatigue cracking around the same time after the 450 μm/m or 500 μm/m strain dwell.

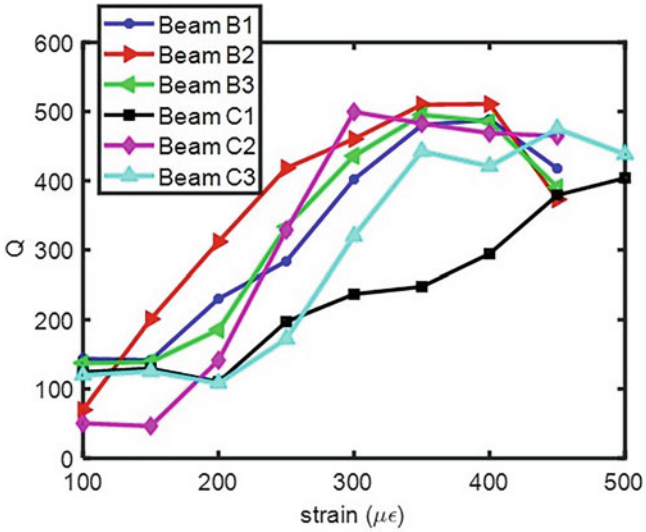


**Fig. 10.5** Direct comparison of the damping sustainability curves of the damped beam specimens from *Series B* and *Series C*

## 10.5 Conclusion and Future Work

This study explored the role that the thickness and axial location of two-pocketed beams containing unfused powder had on their damping sustainability. Three different series of beam thicknesses, as given in Table 10.1, were explored. Each beam series consisted of four beams, three of which were particle-damped beams with differing internal pocket axial locations and the last beam was a fully fused specimen. In examining the variation of the axial location of the pockets, the study confirmed the findings of Ref. [17] that beams containing pockets located near or at the antinodes of the bending mode possessed better damping ability. However, there was a tradeoff between the initial damping performance and the damping sustainability, with the beams possessing the best initial damping being the ones to first experience powder fusion. In addition, the fully fused beam specimens, while possessing initial damping greater than those of the damped beams, experienced losses from imperfect clamping. As a result, the fully fused beam data should have possessed larger quality factors and should not have varied between beam series. Varying the thickness of the beams did not prevent the damping degradation at higher strain amplitudes from occurring. The same trend of the damping sustainability curves remained consistent where the initial damping performance is maintained until powder fusion begins. Once the powder within the pockets begins to fuse to the walls, all beam specimens in every thickness series see large increases in their $Q$ values before leveling out immediately before high cycle fatigue failure. Direct comparisons between *Series B* and *Series C* to *Series A* were difficult since they were conducted around different bending modes. However, comparing *Series B* to *Series C* demonstrated that the beam thickness did not change how powder fusion within the pockets occurred. The specimen thickness may play a minor role in when powder fusion begins, with thicker beams experiencing the beginning of powder fusion at slightly larger strain amplitudes.

Future research activities will focus on how to measure the effect of imperfect clamping and minimize its losses, especially for fully fused beam specimens. Once these clamping losses are minimized, it is anticipated that the $Q$ values of the fully fused beams will remain constant and will be greater than those found in this study. In addition, while it was concluded that the degradation of damping at higher strain amplitudes was independent of which resonance frequency the strain dwell was conducted and at which the quality factor was measured, an open question is whether these trends hold true if the dwell is conducted at one resonance frequency and the damping is measured at a different resonance. For example, does the damping performance measured at the second bending resonance frequency decrease if the strain amplitude dwells are conducted around the third bending mode? Future work will examine this question.

**Acknowledgments** We acknowledge the National Academies of Sciences, Engineering, and Medicine for their funding through the National Research Council Research Associateship Program. We thank the Turbine Engine Fatigue Facility of the US Air Force Research Laboratory and Universal Technology Corporation (UTC), particularly UTC contractor Philip Johnson, for their aid. Lastly, we acknowledge Dr. Ryan Kemnitz from the Air Force Institute of Technology for assisting in manufacturing the beam specimens on the Concept Laser M2 LBPF machine.

## References


1. Nashif, A., Jones, D., Henderson, J.: Vibration Damping. John Wily & Sons, New York (1991)
2. Jones, D., Parin, M.: Technique for measuring damping properties of thin viscoelastic layers. J. Sound Vib. **24**(2), 201–210 (1972)
3. López, I., Busturia, J., Nijmeijer, H.: Energy dissipation of a friction damper. J. Sound Vib. **278**(3), 539–561 (2004)
4. Petrov, E., Zachariadis, Z., Beretta, A., Elliott, R.: A study of nonlinear vibrations in a frictionally damped turbine disk with comprehensive modeling of aerodynamic effects. J. Eng. Gas Turbines Power. **135**(3) (2013)
5. Torvik, P.: On estimating system damping from frequency response bandwidths. J. Sound Vib. **330**(25), 6088–6097 (2011)
6. Torvik, P., Langley, B.: Material properties of hard coatings developed for high damping. In: 51st AIAA/SAE/ASEE Joint Propulsion Conference Proceedings. AIAA Paper 2015-4195 (2015)
7. Gagnon, L., Morandini, M., Ghiringhelli, G.: A review of particle damping modeling and testing. J. Sound Vib. **459**, #114865 (2019)
8. Lu, Z., Wang, Z., Masri, S., Lu, X.: Particle impact dampers: past, present, and future. Struct. Control. Health Monit. **25**(1) (2018)
9. Olson, S.: An analytical particle damping model. J. Sound Vib. **264**(5), 1155–1166 (2003)
10. Scott-Emuakpor, O., George, T., Runyon, B., Holycross, C., Langley, B., Sheridan, L., O'Hara, R., Johnson, P., Beck, J.: Investigating damping performance of laser powder bed fused components with unique internal structures. In: Proceeding of TurboExpo: Power for Land, Sea, and Air. Paper GT2018-75977 (2018)
11. Scott-Emuakpor, O., George, T., Runyon, B., Beck, J., Sheridan, L., Holycross, C., O'Hara, R.: Sustainability study of inherent damping in additively manufactured nickel alloy. AIAA J. **57**(1), 456–461 (2019)
12. Scott-Emuakpor, O., George, T., Runyon, B., Holycross, C., Sheridan, L., O'Hara, R.: Assessing additive manufacturing repeatability of inherently damper nickel alloy components. J. Eng. Gas Turbines Power. **142**(3) (2020)
13. Scott-Emuakpor, O., Beck, J., Runyon, B., George, T.: Validating a multifactor model for damping performance of additively manufactured components. AIAA J. **58**(12), 5440–5447 (2020)
14. Scott-Emuakpor, O., Sheridan, L., Runyon, B., George, T.: Vibration fatigue assessment of additively manufactured nickel alloy with inherent damping. In: *Proceeding of TurboExpo: Power for Land, Sea, and Air*. Paper GT2020-14122 (2020)
15. Scott-Emuakpor, O., Schoening, A., Goldin, A., Beck, J., Runyon, B., George, T.: Internal geometry effects on inherent damping performance of additively manufactured components. AIAA J. **59**(1), 379–385 (2021)
16. Kiracofe, D., Postell, M., Scott-Emuakpor, O., Runyon, B., George, T.: Discrete element method simulations of additively manufactured components with integrated particle dampers. In: *Proceeding of TurboExpo: Power for Land, Sea, and Air*. Paper GT2021-58462 (2021)
17. Hollkamp, J., Scott-Emuakpor, O., Celli, D.: Analyses of damping sustainability of additively manufactured nickel alloy components subjected to high strain loading cycles. In: *Proceeding of TurboExpo: Power for Land, Sea, and Air*. Paper GT2022-81207 (2022)
18. Rao, S.: Mechanical vibrations. Pearson Education, Upper Saddle River, NJ (2017)

# Chapter 11
# A Study on the Influence of Concrete Saturation Ratio for Depth of Penetration Experiments

**George H. Vankirk, Jean C. Santiago-Padilla, Jesse A. Sherburn, and William F. Heard**

**Abstract** Concrete is a widely used building material and is integral in the construction of protective structures used by the U.S. Army. These protective structures are designed to resist extreme loading such as blast and penetration, which requires an accurate assessment of concrete strength. The curing and subsequent drying process of massive concrete structures is a slow phenomenon. This leads to the assumption that massive concrete structures, such as personnel bunkers, may remain saturated at their core throughout their lifetime, long after the exterior has dried. Preliminary data exists concerning saturation ratio effects on high-pressure triaxial loading of conventional strength concrete (CSC), which showed that increasing the degree of saturation of CSC lowered the proportional strength of the material at high confining pressures. In order to further expand on this area of research, depth of penetration experiments were performed using CSC targets at three highly controlled saturation ratios: ambient cured, saturated, and oven-dried. The depth of penetration experiments are ideal experiments for probing the saturation effects on the concrete due to the high pressures induced by impact. Spherical projectiles will be fired at velocities ranging between 343 m/s and 6.8 km/s, and trends will be identified between the degree of saturation and the depth of penetration and overall crater size.

**Keywords** Concrete · High-velocity impact · Two-stage light gas gun · Saturation · Impact

## 11.1 Introduction

The design of hardened structures relies on an understanding of both the quasi-static and dynamic responses of materials. Since World War II, there has been an increasing evolution of building materials used in hardened construction, as well as the introduction of advanced weapon threats. The curing and subsequent drying of concrete structures is known to be a slow phenomenon. Therefore, it is a safe assumption that concrete structures used in hardened construction may retain a saturated core throughout their lifespan but experience a decrease in relative moisture concrete at their faces. This research includes the study of a concrete material subjected to various levels of controlled saturation. There is extensive literature published documenting penetration data into concrete material at various velocities [1–6]. Additionally, there is supporting literature detailing the saturation effects on the quasi-static material properties of concretes [7–10]. The US Army Engineer Research and Development Center (ERDC) is engaged in studying the response of concrete material subjected to shock and penetration loading produced by impacts ranging from conventional velocities and extending through hypervelocities. The purpose of this work is to perform both quasi-static and dynamic experiments on concrete materials with controlled levels of saturation to quantify the effects of the degree of saturation on the material properties. This data set will be critical for understanding how the in situ variable of saturation influences the response of concrete subjected to impacts at a wide range of velocities. This study also provides a complimentary computational modeling effort that seeks to challenge current numerical methods and material models by predicting saturation effects in high-velocity impact.

G. H. Vankirk (✉) · J. C. Santiago-Padilla
Geotechnical Structures Laboratory, Survivability Engineering Branch, U.S. Army Engineer Research and Development Center, Vicksburg, MS, USA
e-mail: george.h.vankirk@erdc.dren.mil; Jean.C.SantiagoPadilla@erdc.dren.mil

J. A. Sherburn · W. F. Heard
Geosciences and Structures Division, U.S. Army Engineer Research and Development Center, Vicksburg, MS, USA
e-mail: jesse.a.sherburn@erdc.dren.mil; william.f.heard@erdc.dren.mil



S. Mates et al. (eds.), *Dynamic Behavior of Materials, Volume 1*, Conference Proceedings of the Society for Experimental Mechanics Series, https://doi.org/10.1007/978-3-031-17453-7_11

## 11.2 Background

Extreme dynamic loading of concrete structures produced by an explosive blast or penetration can produce a differential triaxial stress state within the material. During these types of loading events, the concrete material withstands various kinds of loading paths, which manifest in varying degrees of damage and failure modes [11]. The complex loading paths observed during these extreme events have traditionally been simulated in a controlled laboratory environment using simplified mechanical loading paths [12–14]. Specifically, the triaxial loading paths observed included uniaxial strain in compression, hydrostatic compression, and triaxial compression at varying degrees of confining pressure. Through many previous studies, it has been shown that under confinement, geomaterials such as rock and concrete exhibit brittle failure at low confining pressures, and ductile failure at higher confining pressures, with a transitional region between the two [7]. Additionally, previous studies have indicated that the degree of saturation of concrete material plays a strong influence on the mechanical behavior of the material [10]. As the saturation ratio of the material is increased, the ultimate stress is decreased. Saturated specimens exhibit increased ductile behavior under high conferment, and the apparent concrete strength increases under high confinement as concrete dries. At higher levels of confinement, a more pronounced effect is produced in terms of observed resistance between dried and saturated concrete, with the drier concrete displaying a much higher load-carrying capacity. Material models have been developed which include the addition of allowing for variance in the degree of saturation to quantify the complex behavior [15]. These material models have been used in conjunction with numerical methods to simulate dynamic events such as high-velocity penetration. Numerous studies have been conducted regarding the penetration of concrete and concrete-like materials at conventional velocities [7–10]. Little research exists in the literature regarding the impacts of concrete and concrete-like materials above conventional velocities, and a brief overview of the relevant literature concerning this topic was previously documented in [16]. As impact velocity increases, both the penetrator and the target material experience higher pressures. These elevated impact conditions may result in different damage states of a concrete target in terms of depth of penetration and impact crater diameter. The resultant damage from impacts over a wide range of velocities may be further pronounced when the degree of saturation of the concrete target is varied.

## 11.3 Analysis

To ensure that the degree of saturation within the material could be controlled, a conventional strength concrete (CSC) was chosen for this study. The specific concrete material used in this study, conventional strength portland cement (CSPC), had been previously characterized by ERDC and has associated material models in the Elastic-Plastic Impact Computation (EPIC) code [17]. Baseline modeling efforts were performed in EPIC using a modified version of the Advanced Fundamental Concrete (AFC) material model [15], fitted to previously captured laboratory characterization data for CSPC. The fitted CSPC material had an unconfined compressive strength of 38 MPa and a density of 2275 kg/m$^3$; the porosity was held at the experimental average of 15%; and the saturation percentage was varied between 30 and 95%. Axisymmetric penetration models were simulated to make initial predictions of crater size and guide the design of the concrete targets for depth of penetration experiments, determining a target thickness that achieved the semi-infinite condition by avoiding back-surface interactions during projectile impact. A 12.7 mm sphere modeled with an S-2 tool steel Johnson-Cook (JC) fit [18, 19] was chosen as the penetrator for the simulations. For each saturation ratio, three impact velocities were numerically investigated: 2 km/s, 3.5 km/s, and 7 km/s. Results from the baseline modeling effort indicated that crater depth steadily increases with the degree of saturation. For targets with higher saturation, the target depth needed to be increased to account for the saturation effects. Based on the model predictions, it was determined that the diameter of the targets used in the experimental study would be 40 cm and the depth of the targets for oven-dried, ambient cured, and saturated curing conditions would be 45 cm, 50 cm, and 55 cm, respectively. The predicted crater depth as a function of saturation percentage for the various impact velocities is shown in Fig. 11.1.

In an attempt to control the degree of saturation of relatively large concrete specimens to be used in penetration experiments, the curing methods outlined in [10] will be followed when producing the concrete targets for this study. All concrete materials will be initially wet cured for a period of 28 days. After the initial 28-day period, the curing protocols used to produce the specimens with varying degrees of saturation will deviate. For the initial wet cure, after placement, the concrete material will be allowed to harden and covered with burlap and plastic sheeting. Soaker hoses and an automatic timer will be used to wet the concrete for one hour every 12 h for the duration of the 28 days. After 28 days, the concrete forms will be stripped and the saturated specimens will be weighed and placed in water storage tanks, which were prepared in accordance with [20]. Oven-drying specimens will be prepared in waves of six specimens at a time due to oven space constraints. Oven

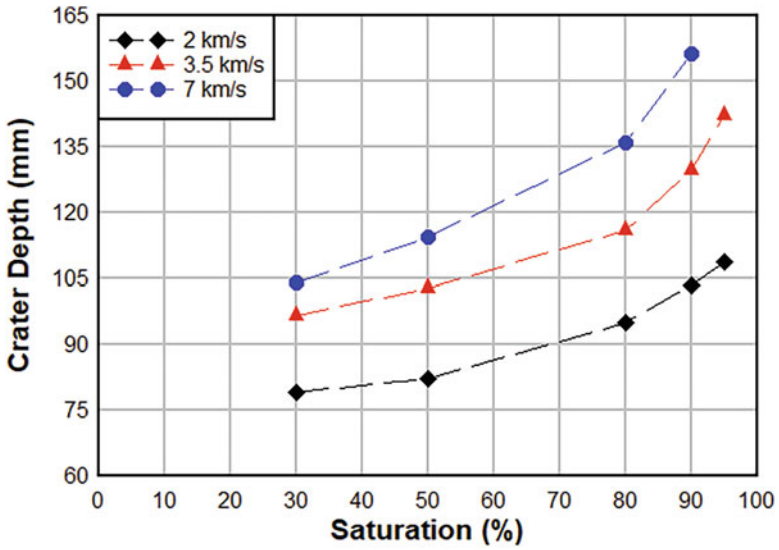


**Fig. 11.1** Numerical predictions of crater depth as a function of the concrete degree of saturation for a 12.7 mm steel sphere

**Fig. 11.2** Concrete curing protocols for saturated specimens (left) and oven-dried specimens (right)

drying will be accomplished until the specimens reach a steady state (no longer showing a reduction in weight) in accordance with [21]. Curing protocols for the saturated and oven-dried specimens are shown in Fig. 11.2. After the curing protocols are complete, quasi-static characterization experiments involving triaxial compression stress paths will be performed on cored specimens of the CSPC targets. The recorded quasi-static test data can then be used for future material model fitting and validation.

For this study, a 12.7-mm S2 tool steel sphere with an approximate mass of 8.4 g will be used as the projectile. Two laboratory gun systems will be used to launch the projectiles at velocities ranging from 343 m/s (Mach 1) to 6860 m/s (Mach 20). For conventional velocities up to 2058 m/s (Mach 6), a traditional fixed bore powder gun will be used. Data capture for the conventional velocity experiments will utilize two Model 35 Oehler chronographs to measure projectile velocity and a pair of Phantom V710 high-speed cameras to record the event. For impact experiments above conventional velocities, a 25-mm bore two-stage light gas gun (2SLGG) will be used. The ERDC 25-mm bore 2SLGG is shown in Fig. 11.3. A pair of laser curtains will capture the velocity of impacts produced by the 2SLGG, and the impact face will be recorded using a Specialized Imaging Kirana 5 M ultra-high-speed video camera. The proposed test matrix in Table 11.1 was developed in order to investigate the effect of varying degrees of saturation in terms of depth of penetration using a conventional strength concrete material. The experimental results will be presented at the conference.

**Fig. 11.3** ERDC 25-mm two-stage light gas gun (2LSGG)

**Table 11.1** Proposed parametric study for depth of penetration experiments on CSPC concrete

| Concrete curing condition | Impact velocity | Testing method |
|---|---|---|
| Oven-dried | 343 m/s (Mach 1) to 6860 m/s (Mach 20) | Powder gun/ 2SLGG |
| Ambient cured | 343 m/s (Mach 1) to 6860 m/s (Mach 20) | Powder gun/ 2SLGG |
| Saturated | 343 m/s (Mach 1) to 6860 m/s (Mach 20) | Powder gun/ 2SLGG |

## 11.4 Conclusion

The study of ballistic impact against concrete with varying degrees of saturation is of great importance to the U.S. Army. This effort focuses on the quantification of concrete damage at elevated velocities that have had few previous numerical and experimental excursions in open literature. The experimental data set provided by this study is expected to influence the design of protective structures that may be exposed to extreme loading conditions such as penetration and blast, as well as provide a valuable challenge to current numerical methods and material models.

**Acknowledgments** Permission to publish was granted by the Director of the Geotechnical and Structures Laboratory.

## References

1. White, M.P.: Effects of Impact and Explosion. Office of Scientific Research and Development, Washington, DC (1946)
2. Forrestal, M.J.: Penetration into dry porous rock. Int. J. Solids Struct. **22**(12), 1485–1500 (1985)
3. Warren, T.L., Fossum, A.F., Frew, D.J.: Penetration into low strength (23 MPa) concrete: target characterization and simulation. International Journal of Impact Engineering. **30**, 477–503 (2004)
4. Forrestal, M.J., Altman, B.S., Cargile, J.D., Hanchak, S.J.: An empirical equation for penetration depth of ogive-nose projectiles into concrete targets. International Journal of Impact Engineering. **15**(4), 395–405 (1994)
5. Hanchak, S.J., Forrestal, M.J., Young, E.R., Ehrgott, J.Q.: Perforation of concrete slabs with 48 and 140 MPa unconfined compressive strength. Int. J. of Impact Eng. **121**, 1–7 (1992)
6. Gran, J.K., Frew, D.J.: In-target radial stress measurements from penetration experiments into concrete by ogive-nose steel projectiles. Int. J. of Impact Engng. **19**(8), 715–726 (1996)
7. Imran, I., Pantazopoulou, S.J.: Experimental study of plain concrete under triaxial stress. ACI Mater. J. **93**(6), 589–601 (1996)
8. Malecot, Y., Vu, X.H., Daudeville, L.: Unconfined compressive strength is a poor indicator of the high-pressure mechanical response of concrete. DYMAT. **2009**, 1325–1331 (2009)
9. Forquin, P., Piotroska, E.: Experimental investigation of the confined behavior of dry and wet high-strength concrete: quasi static versus dynamic loading. Journal of dynamic behavior of materials. **2015**(1), 191–200 (2015)
10. Vu, X.H., Malecot, Y., Daudeville, L., Buzaud, E.: Experimental analysis of concrete behavior under high confinement: effect on saturation ratio. Int. J. Solids Struct. **46**(2009), 1105–1120 (2008)
11. Vankirk, G.H.: Residual Strength of a High Strength Concrete Subjected to Triaxial Pre-Stress. Mississippi State University (2020)
12. Akers, S.A., Reed, P.A., Ehrgott, J.Q.: High-Pressure Uniaxial Strain and Triaxial Shear Test Equipment, p. 1986. U.S. Army Engineer Research and Development Center, Vicksburg, MS (1986)

13. Williams, E.M., Akers, S.A., Reed, P.A.: Laboratory Characterization of Sam-35 Concrete. U.S. Army Engineer Research and Development Center, Vicksburg, MS (2006)
14. Williams, E.M., Graham, S.S., Reed, P.A., Rushing, T.S.: Characterization of Cor-Tuf Concrete with and without Steel Fibers. U.S. Army Engineer Research and Development Center, Vicksburg, MS (2009)
15. Adley, M., Frank, A., Danielson, K., Akers, S., O'Daniel, J.: *The Advanced Fundamental Concrete (AFC) Model*: Technical Report ERDC/GSL TR-10-51. U.S. Army Engineer Research and Development Center, Vicksburg, MS (2010)
16. Vankirk, G.H., Sherburn, J.A., Heard, W.F., Chappell, E.M.: An initial study of ultraordnance impact experiments on concrete. In: Mates, S., Eliasson, V. (eds.) Dynamic Behavior of Materials, vol. 1. Conference Proceedings of the Society for Experimental Mechanics Series. Springer, Cham (2022). https://doi.org/10.1007/978-3-030-86562-7_6
17. Johnson, G.R., Beissel, S.R., Gelach, C.A., Holmquist, T.J.: User Instructions for the 2020 Version of the EPIC Code. Southwest Research Institute, Minneapolis, MN (2020)
18. Johnson, G.R., Cook, W.H.: A Constitutive Model and Data for Metals Subjected to Large Strains, High Strain Rates and High Temperatures. Proceedings of the 7th International Symposium on Ballistics, The Hague (1983)
19. Johnson, G.R., Cook, W.H.: Fracture characteristics of three metals subjected to various strains, strain rates, temperatures and pressures. Eng. Fract. Mech. **21**(1) (1958)
20. C01 Committee: Standard Specification for Mixing Rooms, Moist Cabinets, Moist Rooms, and Water Storage Tanks Used in the Testing of Hydraulic Cements and Concretes, 2019th edn. ASTM International, West Conshohocken, PA. (2019)
21. C09 Committee: Standard Test Method Total Evaporable Moisture Content of Aggregate by Drying, 2019th edn. ASTM International, West Conshohocken, PA. (2019)

# Chapter 12
# Effect of Crystal Size on the Failure Mechanics of Polymer-Bonded Explosives

**Chizoba Onwuka, Vijendra Gupta, Michael Sutton, and Addis Kidane**

**Abstract** Polymer-bonded explosives (PBXs) contain explosive crystals bonded together by a polymeric binder and are widely used in extreme loading conditions such as rocket propellants and explosive munitions because of their high performance and low sensitivity. PBXs typically constitute 80–95% of energetic crystals and 5–20% of a soft polymer binder. The particle size of crystals has a significant effect on the mechanical properties of most polymer particulate composites. In this paper, the effect of particle size on the deformation behavior of PBX under dynamic loading is investigated. This study involves testing polymer-bonded sugar (PBS) samples, a well-known mechanical simulant of PBXs, with four different crystal sizes – coarse, intermediate, fine, and superfine – with corresponding crystal sizes of 600–850 μm, 425–600 μm, 212–425 μm, and 100–212 μm, respectively. A dynamic compression load is applied to these samples using a split Hopkinson pressure bar (SHPB). The macroscale and local dynamic deformation of the samples are captured by taking a series of images of the samples as they deform using a high-speed camera. From the macroscale experiment, it was observed that as the crystal size increases from superfine crystal size to coarse crystal size, the ultimate compressive stress of the PBS decreases. The mesoscale experiment shows that the local von Mises strain field of PBS for different crystal size specimens is different. The von Mises strain field in higher crystal size specimens such as coarse crystal size specimens is highly localized in the polymer-rich regions while more dispersed across the specimens with lower crystal size, particularly superfine crystal size. This study would give an in-depth knowledge and understanding of how the crystal size affects the deformation mechanics of energetic and other particulate polymer composites.

**Keywords** Crystal size · Polymer-bonded explosives · Polymer-bonded sugar · Macroscale · Mesoscale

## 12.1 Introduction

Polymer-bonded explosives (PBXs) belong to a class of particulate composites that contain energetic crystals that adhere to a polymeric binder [1–3]. The energetic crystal is usually 75–96% of the total mass of the PBXs, while the remaining part constitutes a small amount of polymer binder [4, 5]. The main function of the polymer binder is to desensitize the high explosive to unwanted external stimuli and provide structural integrity to the composite material [6]. PBXs are used in a wide variety of applications, particularly in military and civilian fields, to develop products such as rocket propellants, weapons, etc. [6, 8, 9].

Several studies have been carried out on the mechanical behavior of polymer-bonded explosives under dynamic loading using the typical split Hopkinson pressure bar setup [5, 10, 11]. Ravindran et al. found out that polymer-bonded sugar (PBS) – a simulant of polymer-bonded explosives – does not exhibit significant strain hardening after yielding, however shows a long plateau region which is caused by the presence of a polymeric binder [10]. Further, the global deformation behavior of PBS is affected by the mass fraction of the individual constituent elements such that an increase in the mass fraction of the explosive particles causes the deformation behavior of PBS to shift from one being controlled by the polymeric binder to one controlled by the explosive particles [5].

The mechanical behavior of PBXs also depends on the crystal size; increasing the crystal size decreases the strength of PBXs because the failure paths of fracture for a larger crystal size are longer than those of a lower crystal size [11].

In this study, the effect of crystal size on the deformation mechanics of polymer-bonded sugar – a mock explosive of PBXs – is investigated. Dynamic compression load is applied to the various crystal size specimens using a split Hopkinson

C. Onwuka · V. Gupta · M. Sutton · A. Kidane (✉)
Department of Mechanical Engineering, College of Engineering and Computing, University of South Carolina, Columbia, SC, USA
e-mail: conwuka@email.sc.edu; vijendra@email.sc.edu; sutton@sc.edu; kidanea@cec.sc.edu



S. Mates et al. (eds.), *Dynamic Behavior of Materials, Volume 1*, Conference Proceedings of the Society for Experimental Mechanics Series, https://doi.org/10.1007/978-3-031-17453-7_12

pressure bar (SHPB). The global and local dynamic deformation behaviors of the samples are studied, and the global stress-strain curve for each crystal size as a function of strain rate is obtained and compared. Also, the full-field strain data is measured through 2D digital image correlation.

## 12.2 Materials and Methods

The material used in this study is polymer-bonded sugar (PBS), which is a known simulant of polymer-bonded explosives. PBS contains sugar crystals of different crystal sizes: coarse, intermediate, fine, and superfine mixed with plasticized hydroxyl-terminated polybutadiene (HTPB) binder – a composition of hydroxyl-terminated polybutadiene (HTPB)/dioctyl sebacate (DOS)/toluene diisocyanate (TDI). The details of the composition of the sample are shown in Table 12.1.

The detailed sample preparation process is discussed as follows: first, the sugar is separated into different crystal sizes – coarse, intermediate, fine, and superfine – using a sieve and poured inside a container and labeled accordingly. Then HTPB was mixed with dioctyl sebacate and toluene diisocynate, which are the plasticizer and the curing agent, respectively, to obtain a plasticized HTPB solution. Thereafter, the solution is added to the individual sugar crystal sizes obtained earlier and mixed thoroughly for about 15–20 min to coat the surface of the sugar crystals with the polymer binder. Then, the resulting mixture was kept in an oven for 4 h at 80 °C. This process is regarded as partial curing, and it helps in enhancing the binding properties of the coated polymers. The partially cured mixture was pressed at 90 MPa in a steel mold of 25.4 mm in diameter at room temperature using an MTS machine and placed in an oven at 80 °C for 48 h to completely cure the samples. Finally, the cured samples were machined to form a cube geometry of side 14 mm using a milling machine. The specimen dimension is shown in Fig. 12.1a.

To enhance DIC measurement, two different methods of speckling were adopted for the macroscale and mesoscale experiments, respectively. For the macroscale experiment, a high-contrast, random, and isotropic speckle is applied to the surface of the specimen. The detailed process of choosing the right speckle can be seen in [12]. To apply speckles on the surface of the specimen, first, the specimen is clamped vertically on a tripod stand, and a thin coat of white paint was applied to the surface of the specimen, followed by black paint. The selected speckle size is between 500 and 600 μm. The specimen dimensions with speckle pattern for the macroscale DIC measurement and the actual image of the specimen after speckling are shown in Fig. 12.1a, b, respectively.

For the mesoscale digital image correlation, three major steps are followed: polishing, marking, and speckling. These are done in order to relate the strain fields at the grain scale level with the underlying microstructure. The processes are discussed below.

First, the specimen was dry polished with silicon carbide paper of a grid size of 800–1200 μm attached to a polishing machine as shown in Fig. 12.1c.

Second, the area of interest (AOI) on the specimen was marked using an HB pencil. Thereafter, the left and top part of the specimen is covered with scotch tape in an L shape, leaving the microstructure of the right bottom side of the specimen for imaging and speckling.

Finally, the AOI is speckled; to speckle the specimen, white paint is applied to the specimen using an airbrush and a black toner powder is deposited immediately on the partially dried white paint using an air gun and allowed to dry completely. Thereafter, the scotch tape was removed to give an average speckle size of 60–90 μm. The dimension of the sample showing the speckle patterns of AOI is shown in Fig. 12.1d.

**Table 12.1** Compositions of different crystal size samples

| Type | Crystal size (μm) | Sugar (% wt.) | HTPB (% wt.) (monomer) | DOS ((% wt.) (plasticizer) | TDI (% wt.) (curing agent) |
|---|---|---|---|---|---|
| Coarse | 600–850 | 95.00 | 3.60 | 0.96 | 0.44 |
| Intermediate | 425–600 | 95.00 | 3.60 | 0.96 | 0.44 |
| Fine | 212–425 | 95.00 | 3.60 | 0.96 | 0.44 |
| Superfine | 100–200 | 95.00 | 3.60 | 0.96 | 0.44 |

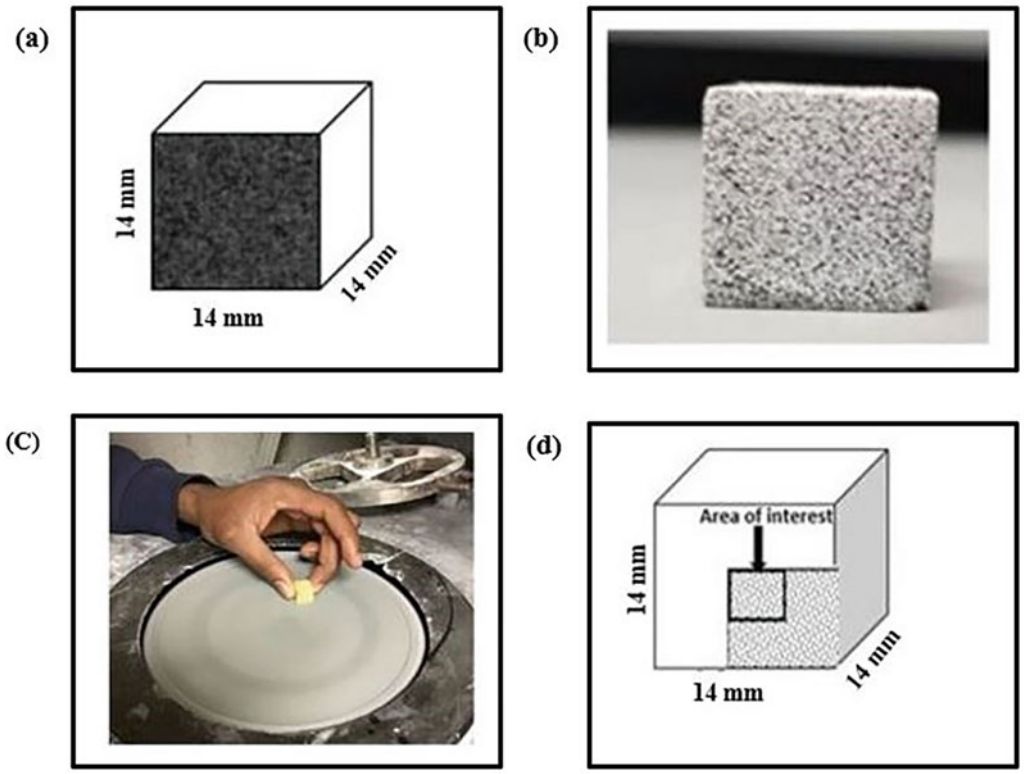


**Fig. 12.1** (**a**) Dimension of the specimen for macroscale experiment. (**b**) Original image of the specimen with speckle pattern for macroscale experiment. (**c**) Specimen being polished with a carbide paper. (**d**) Specimen dimension for the mesoscale experiment with AOI = 4.28 mm × 2.40 mm

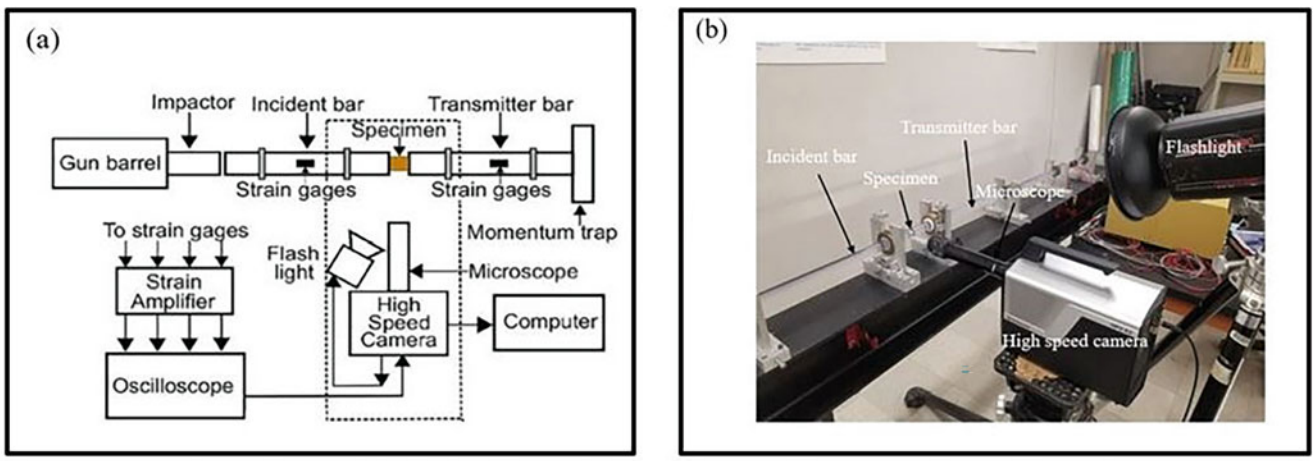


**Fig. 12.2** (**a**) Schematic description of the experimental setup. Diagram was extracted from [5] (**b**). The actual image of the experimental setup

## 12.3 Experimental Setup and Data Analysis

The specimen was dynamically compressed via a split Hopkinson pressure bar (SHPB) setup consisting of an incident and a transmitter bar of length and diameter of 1830 mm and 25.4 mm, respectively. The schematic description and the actual photograph of the experimental setup are shown in Fig. 12.2a, b, respectively. To reduce friction between the bars and the specimen, a thin layer of grease is applied gently at the interface between the bar and the specimen. Since the specimen is made of low impedance material, polymeric bars are used as the incident and transmitter bars to prevent impedance mismatch between the specimen and the bars [13]. Thereafter, the strains in the bars are measured with the help of the strain gauges

attached at the middle of the incident and transmitter bars and used to calculate the average strain rate, strain, and stress in the specimen using Eqs. 12.1, 12.2 and 12.3 below.

$$\text{Specimen strain rate; } \dot{\varepsilon}_s(t) = \frac{-2C_b}{l_s}\varepsilon_{R(t)} \tag{12.1}$$

=

$$\text{Strain in the specimen; } \varepsilon_s(t) = \int_0^t \frac{-2C_b}{l_s}\varepsilon_{R(t)}dt \tag{12.2}$$

=

$$\text{Stress in the specimen; } \sigma_s(t) = \frac{E_b A_b}{A_s}\varepsilon_{T(t)} \tag{12.3}$$

where '$l_s$' is the length of the specimen, '$\varepsilon_{R(t)}$ 'is the reflected strain signal. '$\varepsilon_{T(t)}$ 'is the transmitted strain signal. $C_b = 1470$ m/s' is the speed of the wave in the polymeric bar, and '$E_b = 2.5$ GPa' is the modulus of elasticity of the bar material. '$A_b$ 'is the cross-sectional area of the bar, and '$A_s$ 'is the cross-sectional area of the specimen.

To measure the macroscale and mesoscale full-field strain using DIC, an ultra-high-speed imaging camera HPVX2 by Shimadzu was used. The camera has the capability of capturing ten million images per second; however, the image-acquiring rates selected for the study were 100,000 frames/seconds and 1,000,000 frames/seconds for the macroscale and mesoscale experiments, respectively, and it was able to capture the total durations of the dynamic events. For the macroscale experiment, a 100 mm Tokina lens that yielded a field of view of 27.20 mm × 17.00 mm at a resolution of 100.00 μm/px was used, while for the mesoscale experiment, a high magnification far-field microscope was attached to the camera. The high magnification microscope yielded a field of view of 4.28 mm × 2.40 mm at a resolution of 10.73 μm/px. Since high illumination is needed for dynamic experiments at a high frame rate, a photogenic flash lamp was used to illuminate the sample.

The images acquired during the experiments were post-processed in VIC-2D, a commercial software by correlated solutions. Subset sizes of 21 × 21 and 9 × 9 were used for the macroscale and mesoscale experiments, respectively, which considers at least 3 × 3 speckles in a subset. The step size and filter size selected for the macroscale experiment were 4 pixels and 15, respectively, while a step size of 2 pixels where chosen for coarse, intermediate and fine crystal size specimens and 1 pixel for superfine crystal size for the mesoscale experiment. A filter size of 9 was chosen for all the crystal size specimens for the mesoscale experiments. The matching algorithm chosen for both the macroscale and mesoscale experiments is zero normalized squared difference (ZNSD). To convert the digital signal into continuous data, an optimized 8-tap interpolation function was selected. The complete information about the imaging and postprocessing parameters for both the macroscale and mesoscale experiments can be seen in Tables 12.2 and 12.3, respectively.

## 12.4 Result and Discussion

### *12.4.1 Macroscale Deformation Behavior*

Figure 12.3 shows the global stress-strain curves for coarse, intermediate, fine, and superfine crystal size specimens of polymer-bonded sugar. The coarse crystal size specimen corresponding to a 600–850 μm crystal size reached an ultimate

**Table 12.2** Image parameters used in the study

| Parameter | Macroscale | Mesoscale |
|---|---|---|
| Imaging lens | 100 mm Tokina lens | Navitar extension tube |
| Field of view | 27.20 mm × 17.00 mm | 4.28 mm × 2.40 mm |
| Imaging frame rate | 100,000 fps | 1,000,000 fps |
| Pixel-to-length ratio | 100.00 μm/px | 10.73 μm/px |

**Table 12.3** Postprocessing parameters used in the study

| Parameter | Macroscale | Mesoscale |
|---|---|---|
| Correlation criteria | ZNSD | ZNSD |
| Interpolation | Optimized 8-tap | Optimized 8-tap |
| Subset size | 21 × 21 pixel$^2$ | 9 × 9 pixel$^2$ |
| Step size | 4 pixels | Superfine crystal size specimen = 1 pixel, Coarse, intermediate and fine crystal size specimens = 2 pixels |
| Filter size | 15 | 9 |

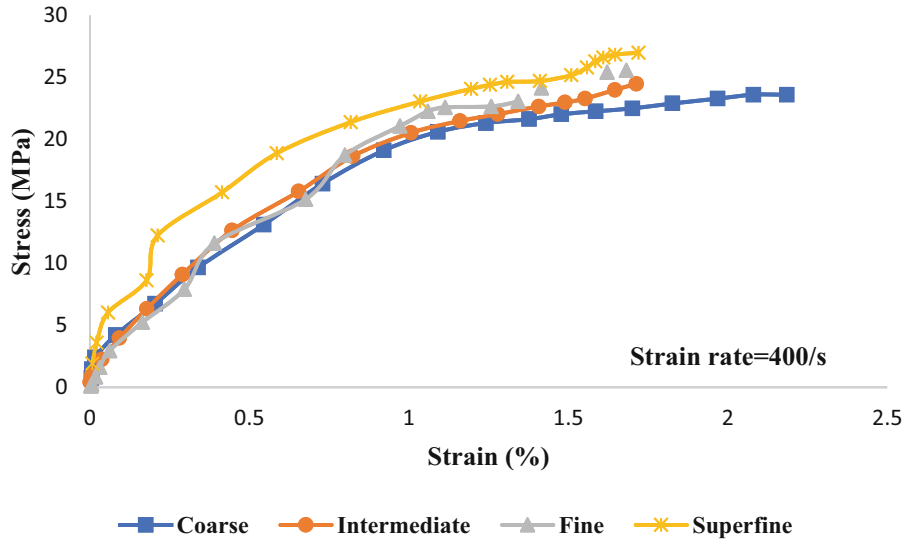


**Fig. 12.3** Global stress-strain curves for different crystal sizes of polymer-bonded sugar

**Table 12.4** The ultimate compressive stress and its corresponding strain for different crystal sizes

| Type | Crystal size (μm) | Average density (g/cm$^3$) | Ultimate compressive stress (MPa) | Strain (%) |
|---|---|---|---|---|
| Coarse | 600–850 | 1.44 | 23.61 | 2.18 |
| Intermediate | 425–600 | 1.44 | 24.47 | 1.71 |
| Fine | 212–425 | 1.47 | 25.58 | 1.68 |
| Superfine | 100–200 | 1.52 | 27.00 | 1.72 |

compressive stress of 23.61 MPa at around 2.18% global axial strain, while the ultimate compressive stress and corresponding strain of the superfine crystal size specimen corresponding to 100–212 μm crystal sizes are 27.00 MPa and 1.72%, respectively. The ultimate compressive stress and the corresponding strains for the remaining crystal size specimens are shown in Table 12.4.

From the result, it was observed that as the crystal size increases from superfine crystal size to coarse crystal size, the ultimate compressive stress of the PBS decreases. A similar behavior was observed for RF 38-22(159 μm) and RF 38-09 (710 μm), polymer-bonded explosives prepared with a mixture of cyclotrimethylene trinitramine (RDX) and hydroxyl-terminated polybutadiene (HTPB) binder where the higher crystal size deforms at a lower stress than the lower crystal size [7].

To explain this phenomenon, the average number of interparticle contacts is considered. Accordingly, superfine crystal size has a higher ultimate compressive stress than coarse crystal size, and this could be due to the average number of interparticle contacts being higher in a superfine crystal size specimen than in a coarse crystal size specimen. A high number of contacts between the crystals would enhance interparticle interactions and reduce the average stress between the particles [7]. Since high interparticle contacts correspond inversely to the stresses arising between the particles [14]. Thus, the specimen corresponding to the superfine crystal size would have a higher ultimate compressive stress. Similarly, coarse crystal size with a lower average number of contacts would crush at a lower axial load. A similar trend is also observed for intermediate and fine crystal size specimens.

### *12.4.2 Mesoscale Deformation Behavior*

The local von Mises strain at 1.42% global axial strains for coarse, intermediate, fine, and superfine crystal size specimens is shown in Fig. 12.4. It was found that the local von Mises strain field developed during the deformation of PBS for all the crystal size specimens is highly heterogenous. A similar observation was discovered in [15]. The von Mises strain field in higher crystal size specimens such as coarse crystal size specimens is highly localized in the polymer-rich regions, while the von Misses strain field is more dispersed across the specimens with lower crystal sizes, particularly superfine crystal size specimens, as seen in Fig. 12.4. The main reason for this phenomenon can be explained by considering two crystal size

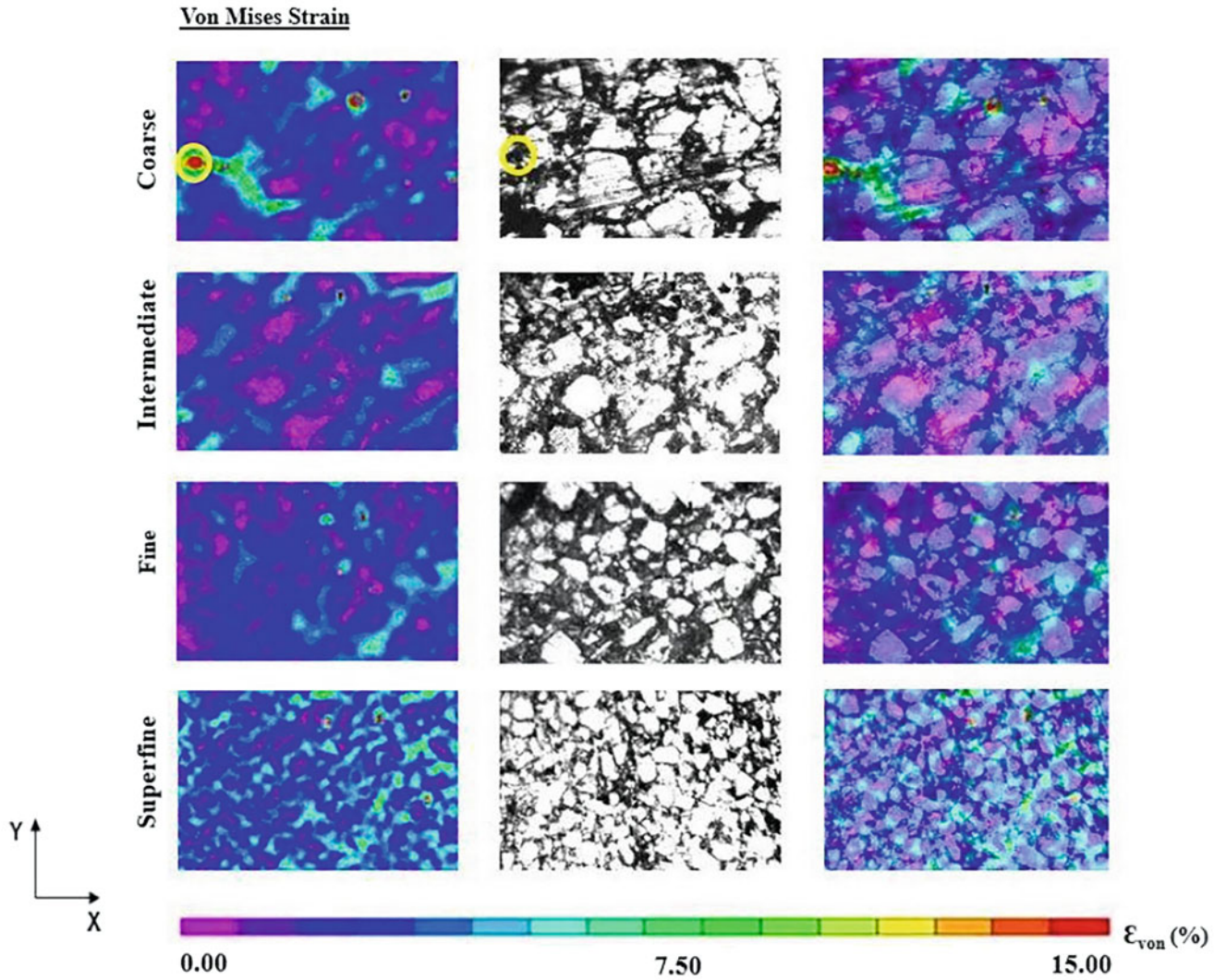


**Fig. 12.4** The local von Mises strain for coarse, intermediate, fine and superfine crystal size specimens along with the underlying microstructure at a global axial strain of 1.42% (Specific locations are marked)

specimens: the coarse and superfine crystal size specimens. The coarse crystal size specimen has a lower number of particles as well as greater average spacing between the crystals than the superfine crystal size specimen. The space between the crystals in the coarse specimen is mostly filled with the polymeric binder. Upon application of the same external load to both coarse and superfine crystal size specimens, a lower number of force chain paths would be developed in the coarse crystal size specimen than in the superfine crystal size specimen. Consequently, causing stress concentration and strain localization at some areas in the coarse crystal size specimen, particularly the polymer-rich regions as shown in the marked region in Fig. 12.4. This behavior is likely to cause damage to be initiated early in the coarse crystal size specimen, hence decreasing the material strength.

On the other hand, the superfine crystal size specimen has a higher number of crystal-to-crystal contact points than the coarse crystal size specimen. An increase in the number of contact points between the crystals would result in a larger contact area across the specimen [16]. Consequently, the superfine crystal size specimen would have less strain localization and more uniform strain distribution than the coarse crystal size specimen. Hence, the superfine crystal size specimen is less likely to fracture early because of reduced strain localization, thereby making it have a higher ultimate compressive stress than the coarse crystal size specimen. A similar explanation can be attributed to intermediate and fine crystal size specimens.

## 12.5 Conclusion

In summary, we studied the effect of crystal size on the deformation behavior of polymer-bonded sugar under dynamic load. Four different crystal sizes of PBS: coarse, intermediate, fine, and superfine crystals corresponding to crystal sizes of 600–850 μm, 425–600 μm, 212–425 μm, and 100–212 μm, respectively, are used for the study. A high-speed camera along with a high-magnification tube is employed to study the local and global deformation behavior of the different crystal sizes. The macroscale experiment shows that as the crystal size increases from superfine crystal size to coarse crystal size, the ultimate compressive stress of the PBS decreases, while the mesoscale experiment shows that the local von Mises strain field of PBS for all the crystal size specimens is highly heterogenous. The von Misses strain field in higher crystal size specimens, such as coarse crystal size specimens, is highly localized, occurring in the polymer-rich regions, but becomes evenly distributed as the crystal size decreases.

**Acknowledgment** The financial support of the Air Force Office of Scientific Research (AFOSR) under Grant No. FA9550-14-1-0209 is gratefully acknowledged.

## References

1. Goldrein, H., Rae, P., Palmer, S., Lewis, A.: Ageing effects on the mechanical properties of a polymer bonded explosive. In: Mallinson, L.G. (ed.) Ageing Studies and Lifetime Extension of Materials. Springer, Boston MA (2001). https://doi.org/10.1007/978-1-4615-1215-8_13
2. Youcai, X., Xiangdong, X., Yanyi, X., et al.: Mechanical behavior of a typical polymer bonded explosive under compressive loads. J Energ Mater. (2001). https://doi.org/10.1080/07370652.2021.1980151
3. Catzin, C.: Manufacturing and characterization of energetic materials. ETD Collection for University of Texas, El Paso. AAI10118239 (2016). https://scholarworks.utep.edu/dissertations/AAI10118239
4. Ravindran, S., Tessema, A., Kidane, A.: Local deformation and failure mechanisms of polymer bonded energetic materials subjected to high strain rate loading. J. Dyn Behav Mater. **2**, 146–156 (2016). https://doi.org/10.1007/s40870-016-0051-9
5. Ravindran, S., Gupta, V., Tessema, A., et al.: Effect of particle mass fraction on the multiscale dynamic failure behavior of particulate polymer composites. Exp. Mech. **59**, 599–609 (2019). https://doi.org/10.1007/s11340-019-00493-4
6. Palmer, S., Field, J., Huntley, J.: Deformation Strengths and Strains to Failure of Polymer Bonded Explosives Proc R Soc Lond A440399 419 (1993). https://doi.org/10.1098/rspa.1993.0023
7. Siviour, C., Laity, P., Proud, W., et al.: High strain rate properties of a polymer-bonded sugar their dependence on applied and internal constraints. Proc R Soc a Math. Phys Eng Sci. **464**(2093), 1229–1255 (2008). https://doi.org/10.1098/rspa.2007.0214
8. Yuliang, L., Binbin, X., Rong, C., et al.: Dynamic Mechanical Properties and Constitutive Relation of an Aluminized Polymer Bonded Explosive at Low Temperatures. Shock Vib. **2014**, 918103 (2014). https://doi.org/10.1155/2014/918103. Article ID 918103, 6 pages
9. Li, S., Xiao, J.: Molecular dynamics simulations for effects of fluoropolymer binder content in CL-20/TNT based polymer-bonded explosives. Molecules. **26**, 4876 (2021). https://doi.org/10.3390/molecules26164876
10. Ravindran, S., Tessema, A., Kidane, A.: Multiscale damage evolution in polymer bonded sugar under dynamic loading. Mech. Mater. **114**, 97–106 (2017). https://doi.org/10.1016/j.mechmat.2017.07.016
11. Siviour, C., Gifford, M., Walley, S., et al.: Particle size effects on the mechanical properties of a polymer bonded explosive. J. Mater. Sci. **39**, 1255–1258 (2004). https://doi.org/10.1023/B:JMSC.0000013883.45092.45
12. Sutton, M.A, Orteu, J.J., Schreier, H.: Image Correlation for Shape, Motion and Deformation Measurements: Basic Concepts, Theory and Applications. Springer Science & Business Media; ISBN: 978-0-387-78746-6. (2009). https://link.springer.com/content/pdf/10.1007%2F978-0-387-78747-3.pdf
13. Zhao, H., Gary, G., Klepaczko, J.: On the use of a viscoelastic split hopkinson pressure bar. Int J Impact Eng. **19**, 319–330 (1997). https://doi.org/10.1016/S0734-743X(96)00038-3
14. Sankaye, S.: Dynamic Testing to Determine some Mechanical Properties of Aluminum, Copper, and Dry Eglin Sand Using Split Hopkinson Pressure Bar (SHPB), High Speed Photography and Digital Image Correlation (DIC). Master's Thesis Oklahoma State University (2011) https://shareok.org/bitstream/handle/11244/10054/Sankaye_okstate_0664M_11522.pdf?sequence=1
15. Ravindran, S.M.: Multiscale Deformation and Failure Behavior of Polymer Bonded Explosives Subjected to High-Rate Loading. Doctoral Dissertation University of South Carolina (2018) https://scholarcommons.sc.edu/cgi/viewcontent.cgi?article=5964&context=etd
16. Rumchik, C.G., Jordan, J.L., Elert, M., et al.: Effect of aluminum particle size on the high strain rate properties of pressed aluminized explosives. AIP Conf Proc. **955**, 795–798 (2007). https://doi.org/10.1063/1.2833243

# Chapter 13
# High-Strain-Rate Behavior of 3D-Printed CuCrZr

**Marco Sasso, Edoardo Mancini, Mattia Utzeri, Gianluca Chiappini, Daniele Cortis, Donato Orlandi, and Luca Di Angelo**

**Abstract** CuCrZr alloys achieve high mechanical properties by thermal (e.g., supersaturated temper and aging), mechanical (e.g., ECAP), or thermomechanical treatments (solution annealing, cold working, and aging). This alloy can be considered a functional material, and it can be exploited in different application fields, thanks to a combination of thermal, electrical, and strength properties. In this work, tensile tests at different strain rates have been conducted on CuCrZr specimens produced by additive manufacturing. As-built and heat-treated conditions have been considered. The quasi-static tests have been performed by an electromechanical testing machine, while the high strain rate tests have been performed by a direct-tension split Hopkinson bar. The geometry of the samples has been selected based on the requirements of the dynamic tests, and the same geometry was used in quasi-static tests for the sake of comparison. High-speed imaging has been used to capture the real strain of the specimens. The results showed a limited positive strain rate sensitivity in terms of flow stress for as-built conditions, whereas negative strain rate sensitivity was observed for the heat-treated samples, but positive sensitivity in terms of ductility was observed for as-built, whereas uncertain results occurred in the case of heat-treated material.

**Keywords** High strain rate · CuCrZr alloy · Additive manufacturing · SLM · Hopkinson bar

## 13.1 Introduction

CuCrZr alloys reach high mechanical properties by thermal (e.g., supersaturated temper [1] and aging [2]), mechanical (e.g., ECAP, [3, 4]), or thermomechanical treatments (solution annealing, cold working, and aging) [5]. This alloy can be considered a functional material, and it can be exploited in different application fields, thanks to a combination of thermal, electrical, and strength properties [6, 7]. For instance, in the field of high electrical power, CuCrZr is used as material for the trolley contact wire of high-speed trains or as material for electronic commutators [8], while in the welding field as material for resistance electrodes [9] and in the high heat flux field as material for rocket chambers or several components in fusion reactor experiments [10]. Recently, CuCrZr has been used also as a material for additively manufactured parts by laser powder bed fusion [11]; this may further extend the application of such material in fields where its strain rate dependency plays a role, such as in the case of the plasma-facing components used as a heat sink in the ITER reactor [12]. The study of the dynamic behavior of additively manufactured materials is growing rapidly in the last years [13–16]; nevertheless, literature on the high strain rate properties of CuCrZr is limited [17, 18].

In this work, tensile tests at different strain rates have been conducted on CuCrZr specimens produced by additive manufacturing. As-built and heat-treated conditions have been considered. The quasi-static tests have been performed by an

M. Sasso (✉) · M. Utzeri
Dipartimento di Ingegneria Industriale e Scienze Matematiche, Università Politecnica delle Marche, Ancona, Italy
e-mail: m.sasso@univpm.it; m.utzeri@pm.univpm.it

E. Mancini · L. Di Angelo
Dipartimento di Ingegneria Industriale e dell'Informazione e di Economia, Università degli Studi dell'Aquila, L'Aquila, Italy
e-mail: edoardo.mancini@univaq.it; luca.diangelo@univaq.it

G. Chiappini
Università Telematica eCampus, Como, Italy
e-mail: gianluca.chiappini@uniecampus.it

D. Cortis · D. Orlandi
Laboratori Nazionali del Gran Sasso, Istituto Nazionale di Fisica Nucleare, L'Aquila, Italy
e-mail: daniele.cortis@lngs.infn.it; donato.orlandi@lngs.infn.it



S. Mates et al. (eds.), *Dynamic Behavior of Materials, Volume 1*, Conference Proceedings of the Society for Experimental Mechanics Series, https://doi.org/10.1007/978-3-031-17453-7_13

electromechanical testing machine, while the high strain rate tests have been performed by a direct-tension split Hopkinson bar. The geometry of the samples has been selected based on the requirements of the dynamic tests, and the same geometry was used in quasi-static tests for the sake of comparison. High-speed imaging has been used to capture the real strain of the specimens. The results were analyzed in terms of material strength and ductility.

## 13.2 Material

CuCrZr alloys usually contain 0.5 ÷ 1.5 wt% Cr and 0.03 ÷ 0.3 wt% Zr; however, alloys with a chemical composition significantly exceeding the above range are also made, e.g., Cu0.3wt%Cr0.5wt%Zr. The alloy here considered is the ASTM C18400, commercial name Hovadur® CCZ, by Schmelzmetall. The chemical composition, according to the supplier datasheet, is reported in Table 13.1. The powder size is in the range of 15–45 μm.

The specimens have been manufactured by Selective Laser Melting (SLM) with the SISMA MySint100® 3D printer (Fig. 13.1). The building volume is 100 × 100 mm, and the working chamber is inerted by nitrogen; the system uses a 200 W fiber laser, which produces a laser spot of 30 μm diameter with a typical layer thickness of 20–40 μm.

Round bars of 14 mm diameter have been produced using process parameters developed by the LNGS Design Department and Additive Manufacture Laboratory; in particular, a volumetric energy density of 260 J/mm$^3$ was adopted. Some of the produced specimens were subjected to heat treatment (5 h at 580 °C, followed by air cooling). The threads were obtained from successive lathe machining; no further finishing operations were carried out. Figure 13.2 shows a photo of the raw bars and (partially) machined samples.

**Table 13.1** Chemical composition of the tested material (in % of weight)

| Cr | Zr | Fe | Si | Others total | Cu |
|---|---|---|---|---|---|
| 0.5–1.2 | 0.03–0.3 | Max 0.08 | 0.1 | 0.2 | 98.1–99.4 |


**Fig. 13.1** SLM 3D printer used for specimen manufacturing

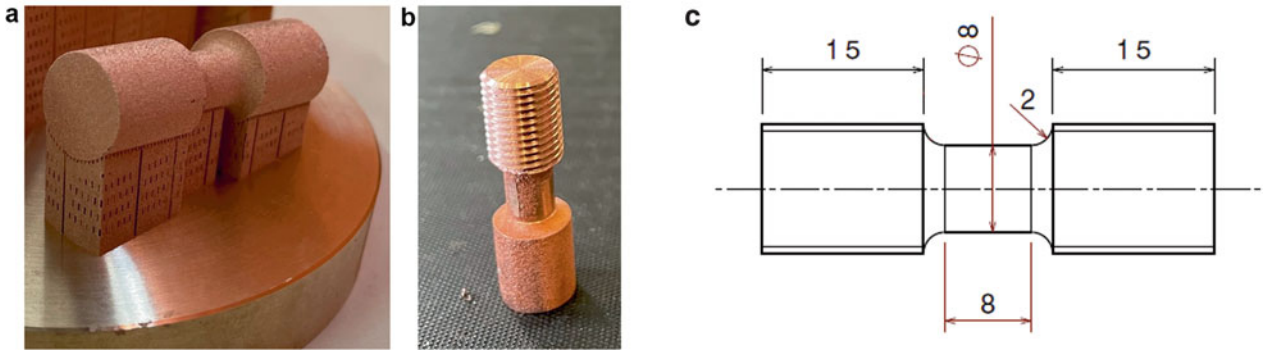


**Fig. 13.2** Manufactured samples: (**a**) raw bar with supports, (**b**) sample partially machined at the lathe, (**c**) sample dimensions


**Fig. 13.3** Direct-tension split Hopkinson bar used for the tests [19]

## 13.3 Experimental Methods

The quasi-static tensile tests were carried out utilizing an electromechanical testing machine (model Zwick Z050®) in displacement control. An engineering strain rate of $10^{-3}$ $s^{-1}$ was adopted. Pictures of the sample during the deformation are acquired by means of a high-resolution digital camera (model Blackfly BFS-U3-88S6M-C) at a frame rate of 32 fps with a resolution of 2162 × 4098 pixels.

The dynamic tensile tests were carried out by the direct-tension split Hopkinson bar shown in Fig. 13.3 [19, 20]. It consists of three aligned bars: a 3.0 m long prestressed bar, a 7.5 m long input bar, and a 4.0 m long output bar. All bars are made of 17-4 PH steel and have a diameter of 18 mm; the CuCrZr samples are connected between the input and output bars' threaded extremities. The brittle failure of a thin disc occurring at the loading end of the statically compressed bar generates a tensile input wave that starts travelling at sound speed along the prestressed bar itself and then in the input bar. When the input tensile ($\varepsilon_i$) wave reaches the sample, it is partially transmitted into the output bar ($\varepsilon_t$), and partially reflected ($\varepsilon_r$) into the input bar.

Resistance strain gauges in full Wheatstone bridge configuration are used to measure these strain waves. In the hypotheses of uniaxial wave propagation, elastic behavior of the bars, and force equilibrium in the sample, the engineering strain rate, strain, and stress are computed with the classical Hopkinson bar theory:

$$\dot{\varepsilon}(t) = -\frac{2C_0}{L_S}\varepsilon_R(t) \tag{13.1}$$

$$\varepsilon(t) = -\frac{2C_0}{L_s}\int_0^t \varepsilon_R(\tau)\cdot d\tau \tag{13.2}$$

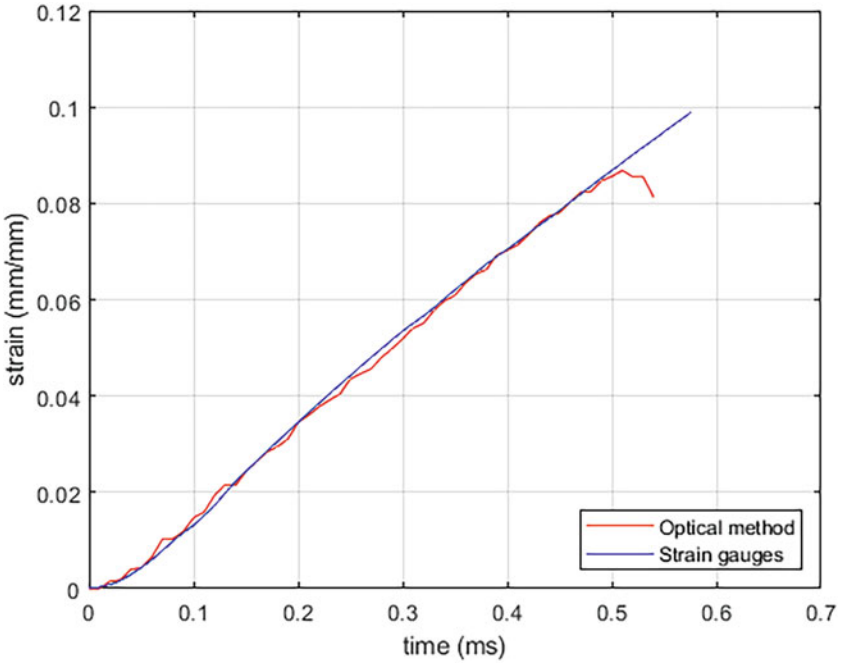


**Fig. 13.4** Comparison of engineering strain as computed by Eq. 13.2 and by image analysis

$$\sigma(t) = \frac{A_b \cdot E_b}{A_s} \varepsilon_T(t) \tag{13.3}$$

Synchronizing the waves at the rising edge of $\varepsilon_r$ and $\varepsilon_t$, and eliminating time from Eqs. (13.1), (13.2) and (13.3), the engineering stress-strain curves are obtained. Optical methods are almost routinely used today to have accurate local deformation measurements, to be used for assessing the true stress-strain curves of materials [20–22]. Therefore, pictures of the deforming samples were acquired during the tests by means of a high-speed camera (model Photron SA4) at a frame rate of 100,000 fps and a resolution of 192 × 128 pixels. These pictures have been used to assess directly the deformation by tracking the displacements of suitable markers applied onto the surface of the sample, thus validating the measurement given by Eq. (13.2). An example of correspondence between the strain measured by the optical method and by the processing of strain gauge signal is reported in Fig. 13.4.

## 13.4 Results and Discussion

Pictures of the samples deformed during the tests are reported in Fig. 13.5. The first column refers to a quasi-static on the as-built condition, whereas the second and third columns refer to dynamic tests on as-built and heat-treated conditions, respectively; on the dark metal background, lighter vertical stripes are visible, which have been applied to the surface, acting as markers to measure the deformation by analyzing the image.

The engineering stress-strain curves are reported in Fig. 13.6. Figure 13.6a shows the results in the as-built condition, whereas Fig. 13.6b shows the results for the heat-treated condition. For easier comparison, the two graphs have the same axis limits. All tests, both in static and dynamic loading conditions, resulted in the failure of the specimen; the curves of the dynamic tests are interrupted at the last significant point, and the stress drop is not reported. The legends report the average of the engineering strain rate, computed by Eq. (13.2) considering only the points after material yield stress.

Analyzing the curves given in Fig. 13.6 of the previous section, a quite distinctive behavior of the material is observed. As far as the heat treatment is considered, it is clear that it had a beneficial effect on the material performance, in terms of yield and ultimate stress; in fact, the curves in Fig. 13.6b are significantly higher than those in Fig. 13.6a.

On the other hand, it appears that while the material in the as-built condition has a slight positive strain rate sensitivity, the material in the heat-treated condition has a strongly negative strain rate sensitivity. In fact, in the heat-treated samples, a

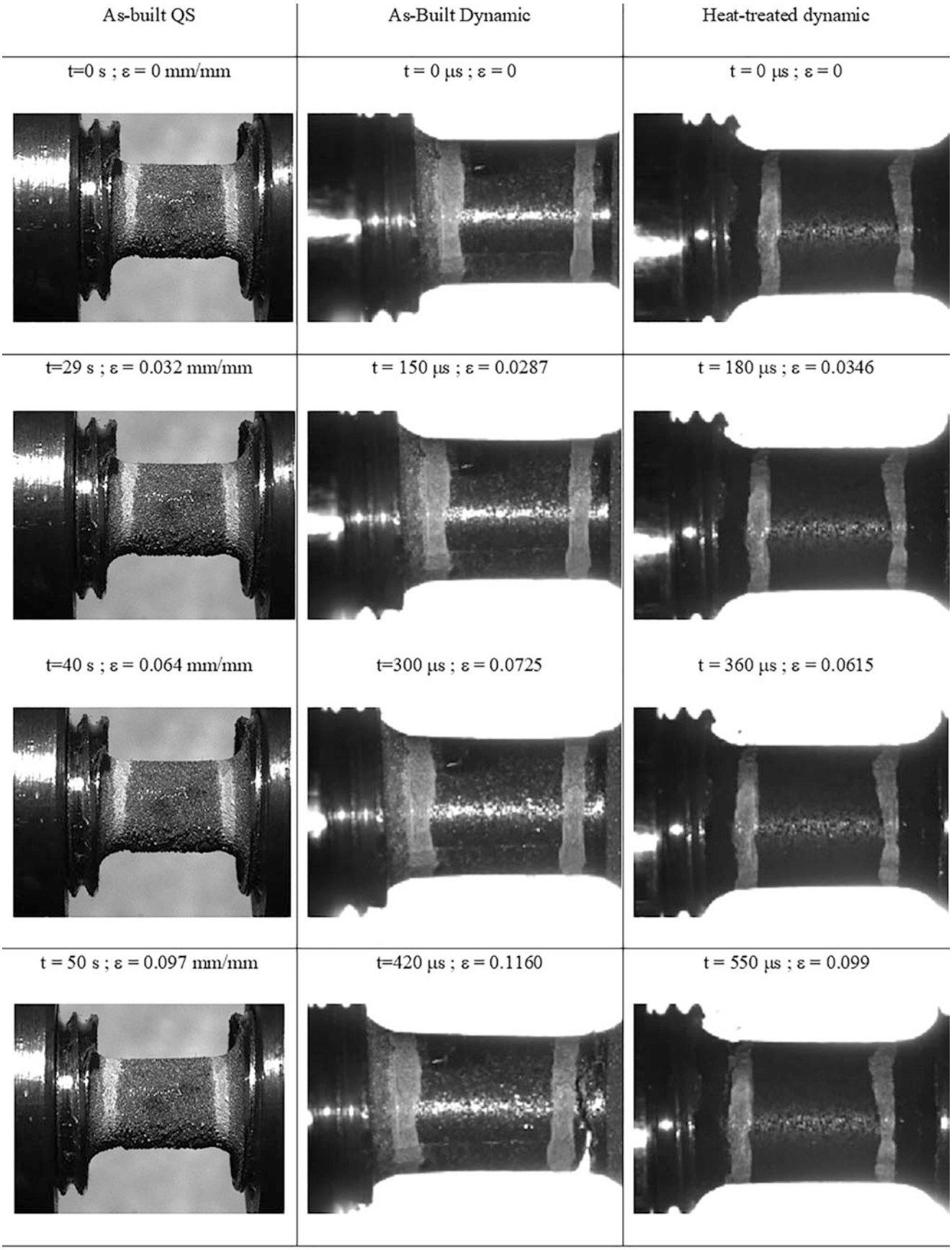


**Fig. 13.5** Pictures of deformed samples acquired during the dynamic tests

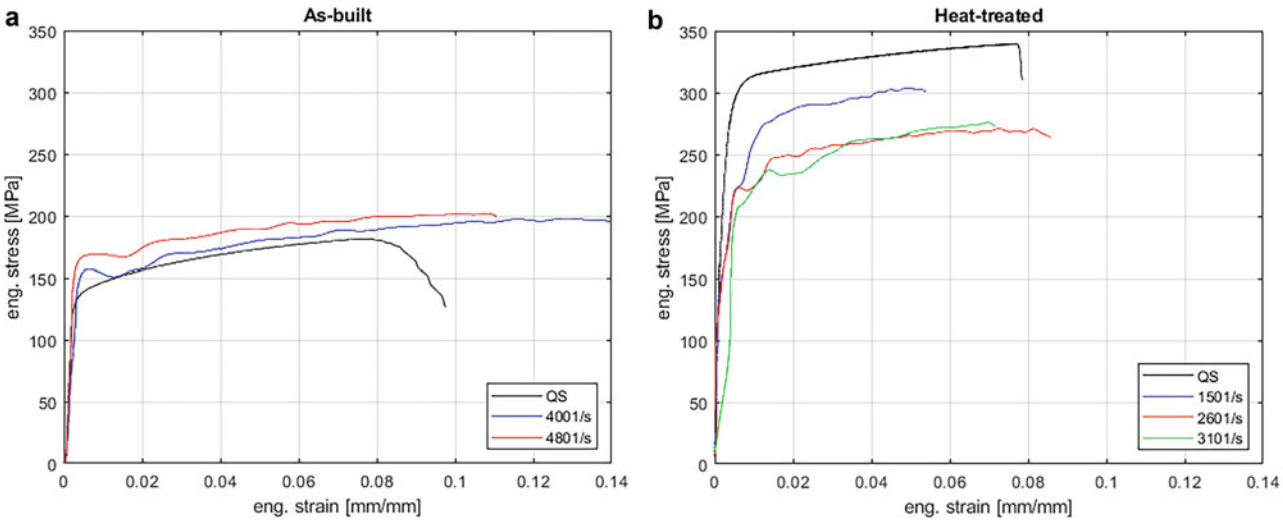


**Fig. 13.6** Engineering stress-strain curves at different strain rates: (**a**) as-built, (**b**) heat-treated

relevant decrease in the flow stress curve is observed, in the order of 20%, even if the maximum strain rate was only about 300 $s^{-1}$. In as-built samples, the increase in flow stress is of the order of 10% with a strain rate of approximately 500 $s^{-1}$.

The ductility of the material showed a behavior that is even more peculiar. In fact, considering the quasi-static results, the same strain to failure is observed for as-built and heat-treated conditions. If the dynamic curves are considered, it is noted a clear increase in ductility for the as-built samples; on the other hand, controversial results are found for the heat-treated samples, where a negligible change in strain to failure is noted for the tests at about 300 $s^{-1}$, whereas a decrease is noted in the test at 150 $s^{-1}$. It must be admitted that caution is needed in considering these results, since they could be affected by eventual inhomogeneities; an analysis of the presence of voids and defects and their correlation with ductility is underway.

## 13.5 Conclusion

The paper describes the results of dynamic tensile tests on CuCrZr samples manufactured by Selective Laser Melting; both as-built and heat-treated conditions have been investigated. Quasi-static tests have also been performed for comparison purposes. The heat treatment has a clear beneficial effect on the material strength in quasi-static conditions. On the other hand, the flow stress curves highlighted a limited or slight positive strain rate sensitivity of the as-built material, whereas a negative strain rate sensitivity was observed in the heat-treated samples. The strain to failure appears to increase with strain rate in the as-built conditions, whereas wavering results were obtained in the heat-treated condition; however, caution is required in considering the ductility results, and a thorough analysis of the presence of any inhomogeneities is desirable.

## References

1. Ostachowski, P., Bochniak, W., Lagoda, M., Ziólkiewicz, S.: Strength properties and structure of CuCrZr alloy subjected to low-temperature KOBO extrusion and heat treatment. Int. J. Adv. Manuf. Technol. **105**, 5023–5044 (2019)
2. Kalinin, G.M., Ivanov, A.D., Obushev, A.N., Rodchenkov, B.S., Rodin, M.E., Strebkov, Y.S.: Ageing effect on the properties of CuCrZr alloy used for the ITER HHF components. J. Nucl. Mater. **367–370**(B), 920–924 (2007)
3. Mishnev, R., Shakhova, I., Belyakov, A., Kaibyshev, R.: Deformation microstructures, strengthening mechanisms, and electrical conductivity in a Cu-Cr-Zr alloy. Mater. Sci. Eng. **A629**, 29–40 (2015)
4. Zhilyaev, A.P., Shakhova, I., Morozova, A., Belyakov, A., Kaibyshev, R.: Grain refinement kinetics and strengthening mechanisms in Cu-0.3Cr-0.5Zr alloy subjected to intense plastic deformation. Mater. Sci. Eng. **A654**, 131–142 (2016)
5. Barabash, V.R., Kalinin, G.M., Fabritsiev, S.A., Zinkle, S.J.: Specification of CuCrZr alloy properties after various thermomechanical treatments and design allowables including neutron irradiation effects. J. Nucl. Mater. **417**(1-3), 904–907 (2011)

6. Barabash, V., Peacock, A., Fabritsiev, S., Kalinin, G., Zinkle, S., et al.: Materials challenges for ITER – current status and future activities. J. Nucl. Mater. **367–370**, 21–32 (2007)
7. Zinkle, S.J., Fabritsiev, S.A.: Copper alloys for high heat flux structure applications. Nucl. Fusion Suppl. **5**, 163–192 (1994)
8. Choi, H.L., Lee, K.Y., Kwun, S.L.: Fabrication of high strength and high conductivity copper alloys by rod milling. J. Mater. Sci. Lett. **16**(19), 1600–1602 (1997)
9. Heyduk, F., Ziółkiewicz, S., Bochniak, W., Korbel, A.: Manufacturing rods for production of spot welding electrodes using the KOBO extrusion method. Metal Form. **26**(4), 325–334 (2015)
10. Fabritsiev, S.A., Zinkle, S.J., Singh, B.N.: Evaluation of copper alloys for fusion reactor divertor and first wall components. J. Nucl. Mater. **233–237**(1), 127–137 (1996)
11. Jahns, K., Bappert, R., Bohlke, P., Krupp, U.: Additive manufacturing of CuCr1Zr by development of a gas atomization and laser powder bed fusion routine. Int. J. Adv. Manuf. Technol. **107**, 2151–2161 (2020)
12. Holzwarth, U., Stamm, H.: The precipitation behaviour of ITER-grade Cu–Cr–Zr alloy after simulating the thermal cycle of hot isostatic pressing. J. Nucl. Mater. **279**(1), 31–45 (2000)
13. Utzeri, M., Bhagavatam, A., Mancini, E., Dinda, G., Sasso, M., et al.: Quasi-static and dynamic behavior of inconel 625 obtained by laser metal deposition: experimental characterization and constitutive modeling. J. Eng. Mater. Technol. **143**, 041007–041001 (2021)
14. Utzeri, M., Farotti, E., Coccia, M., Mancini, E., Sasso, M.: High strain rate compression behaviour of 3D printed carbon-PA. J. Mater. Res. **36**(10), 2083–2093 (2021)
15. Mirone, G., Barbagallo, R., Giudice, F., Di Bella, S.: Analysis and modelling of tensile and torsional behaviour at different strain rates of Ti6Al4V alloy additive manufactured by electron beam melting (EBM). Mater. Sci. Eng. A. **793**, 139916 (2020)
16. Jakkula, P., Ganzenmüller, G., Gutmann, F., Plaff, A., Mermagen, J., et al.: Strain rate sensitivity of the additive manufacturing material Scalmalloy®. J. Dyn. Behav. Mater. **7**, 518–525 (2021)
17. Qian, X., Peng, X., Song, Y., Huang, J., Wei, Y., et al.: Dynamic constitutive relationship of CuCrZr alloy based on Johnson-Cook model. Nucl. Mater. Energy. **24**, 100768 (2020)
18. Wang, Y., Mohamed, O., Dunn, K., Sui, T., Bashir, M., et al.: Effects of stress triaxiality and strain rate on the fracture of a CuCrZr alloy. J. Nucl. Mater. **543**(1), 152546 (2021)
19. Mancini, E., Sasso, M., Rossi, M., Chiappini, G., Newaz, G., et al.: Design of an innovative system for wave generation in direct tension–compression split Hopkinson Bar. J. Dyn. Behav. Mater. **1**(2), 201–213 (2015)
20. Peroni, L., Scapin, M., Fichera, C.: An advanced identification procedure for material model parameters based on image analysis. In: Proceedings of 10th European LS-DYNA conference, Würzburg, Germany (2015)
21. Sasso, M., Fardmoshiri, M., Mancini, E., Rossi, M., Cortese, L.: High speed imaging for material parameters calibration at high strain rate. Eur. Phys. J. Spec. Topic. **225**(2), 295–309 (2016)
22. Sasso, M., Mancini, E., Chiappini, G., Sarasin, F., Tirillò, J.: Application of DIC to static and dynamic testing of agglomerated cork material. Exp. Mech. **58**(7), 1017–1033 (2018)

# Chapter 14
# A Vertical Ballistics Range with Photon Doppler Velocimeter Instrumentation for Projectile Penetration Testing in Soils

**D. Grace, S. Mercurio, M. Omidvar, S. Bless, and M. Iskander**

**Abstract** The operation of a vertical-firing ballistic range is described, along with instrumentation to produce high-resolution velocity-time measurements of projectile penetration in sand targets. The range comprises a single-stage gas gun with a 14.45-mm-inner-diameter smooth-bore barrel and a maximum operating pressure of 300 bar. The launch mechanism is a combination of an electropneumatic solenoid valve and a fast-acting shuttle valve. The gun loading curve is determined for projectiles having a mass of approximately 35 g. The launcher efficiency, defined as the ratio of the actual muzzle velocity to the theoretical prediction, assuming the isentropic expansion of the compressed helium gas, is calculated as a function of the reservoir pressure. A conventional photon Doppler velocimeter (PDV) was designed and assembled on the range to directly measure the projectile velocity-time history during flight and penetration into soil targets. Magnetic sensors were used to trigger the data acquisition system. Additional magnetic sensors were assembled to measure the projectile muzzle velocity when steel projectiles were used. Loose- and Densely-packed soil targets were prepared by means of pluviation. Results from shots into loose and dense sand were analyzed, demonstrating the significance of the soil target packing in the penetration resistance of sand.

**Keywords** Projectile · Sand · Gun · Photon Doppler velocimeter · Penetration

## 14.1 Introduction

Penetration in soils is a widely investigated topic that has been subject to extensive experimental, numerical, and analytical research. Insights from projectile penetration tests in soils can be used in various applications, such as the determination of terminal penetration depth of torpedo anchors used for mooring offshore oil platforms in deep sea soils [1], planetary impact [2] design of underground facilities for military installations, and prediction of the depth of burial (DoB) of unexploded ordnances (UxO) at formerly used defense sites (FUDS), among others. The latter application is the motivation for this study.

There are several models available for the prediction of the terminal depth of burial of munitions in the ground. These models generally rely on experimental data for calibration of parameters or validation of predictions. This necessitates collecting high-fidelity data of projectile penetration in various soils under a range of impact velocities. Some models such as purely empirical penetration models [3] require only the terminal penetration depth, while others such as the Poncelet model [4–6] rely on a complete description of the velocity-time history. There are several methods to measure the velocity of a projectile during penetration in a soil sample, including time of arrival screens [7], high-speed imaging [5, 8] embedded accelerometers [9], flash X-ray [10, 11], refractive index matching techniques [12, 13], and photon Doppler velocimetry [14, 15]. Each of the above methods has advantages and disadvantages and is suited for a particular experimental configuration. The present study focuses on the use of a photon Doppler velocimeter for obtaining velocity-time histories of projectiles penetrating sands.

D. Grace · M. Omidvar (✉)
Department of Civil and Environmental Engineering, Manhattan College, Riverdale, NY, USA
e-mail: dgrace01@manhattan.edu; omidvar@manhattan.edu

S. Mercurio · S. Bless · M. Iskander
Civil and Urban Engineering Department, Tandon School of Engineering, New York University, Brooklyn, NY, USA
e-mail: mercurio@nyu.edu; sbless@nyu.edu; iskander@nyu.edu



S. Mates et al. (eds.), *Dynamic Behavior of Materials, Volume 1*, Conference Proceedings of the Society for Experimental Mechanics Series, https://doi.org/10.1007/978-3-031-17453-7_14

## 14.2 Experimental Setup

A state-of-the-art experimental setup was constructed to conduct impact and penetration tests on soil targets (Fig. 14.1). The electropneumatic compressed-gas gun (Sydor Technologies) was vertically mounted to a rigid steel and aluminum frame. Ballistic testing was carried out on loose and dense 50–80 Ottawa sand targets, which were prepared by dry pluviation. The single-stage, high-performance launcher can deliver up to a maximum pressure of 300 bar, corresponding to a maximum velocity of 1000 m/s. High-purity helium was used in this study. A free-floating shuttle valve is used to deliver reservoir pressure to projectiles and requires a minimum of 30 bar for operation. When the pressure is accumulated in the reservoir chamber, the shuttle valve is pushed up against the bottom of the cylinder. Once the solenoid valve is opened, the gas in the solenoid is released from the exhaust pipe, and the shuttle valve flies backward, resulting in the release of the pressurized gas to the gun breech, thereby firing the projectile. The shuttle valve requires a pressure of at least 25 bar in order to push the seal against the cylinder; lower pressures may not produce a tight seal, and will result in some gas leakage.

A fine-tuned regulator allows the required pressure from the helium source into the launcher reservoir, using a ball valve. When closed, the valve prevents gas leakage from the cylinder, and the launcher is ready to be fired. The ball valve is equipped with two limit switches that serve as a safety interlock system. The limit switches are equipped with two rollers that move in and out of notches in the ball valve. When the ball valve is in the load position, the limit switches are activated; therefore, the launcher is not capable of being fired. When in the fire position, the rollers of the switch are not in contact with the ball valve; therefore, they are not activated, thereby allowing for the launcher to be trigerred. A shuttle valve is operated inside the reservoir, which allows the launcher to be fired when the solenoid is triggered. When the pressure chamber is pressurized, the shuttle valve is pushed against the pressure reservoir breech opening, thereby sealing the breech opening between the pressure reservoir and the gun barrel. Small leaks in the shuttle valve resulted in pressure drops prior to firing. A pressure drop of 1.25 bar/min and 5.25 bar/min was observed at reservoir pressures of 50 bar and 150 bar, respectively. The breech is located at the end of the barrel and is used to load the projectile. A two-step clamp setup, comprising a safety clamp and a barrel clamp, is used to lock the barrel in place. The launcher is fired electrically by the solenoid, which is located at the back end of the pressure reservoir, as shown in Fig. 14.1. The solenoid is connected to dry compressed air, regulated to a max pressure of approximately 8 bar. When the gun is triggered, a signal is sent to the solenoid valve, which releases the compressed gas through the back end of the pressure reservoir. This generates a pressure differential in the front and back end of the shuttle valve located within the pressure reservoir. As a result, the shuttle valve abruptly moves away from the breech, thereby releasing compressed gas into the gun barrel.

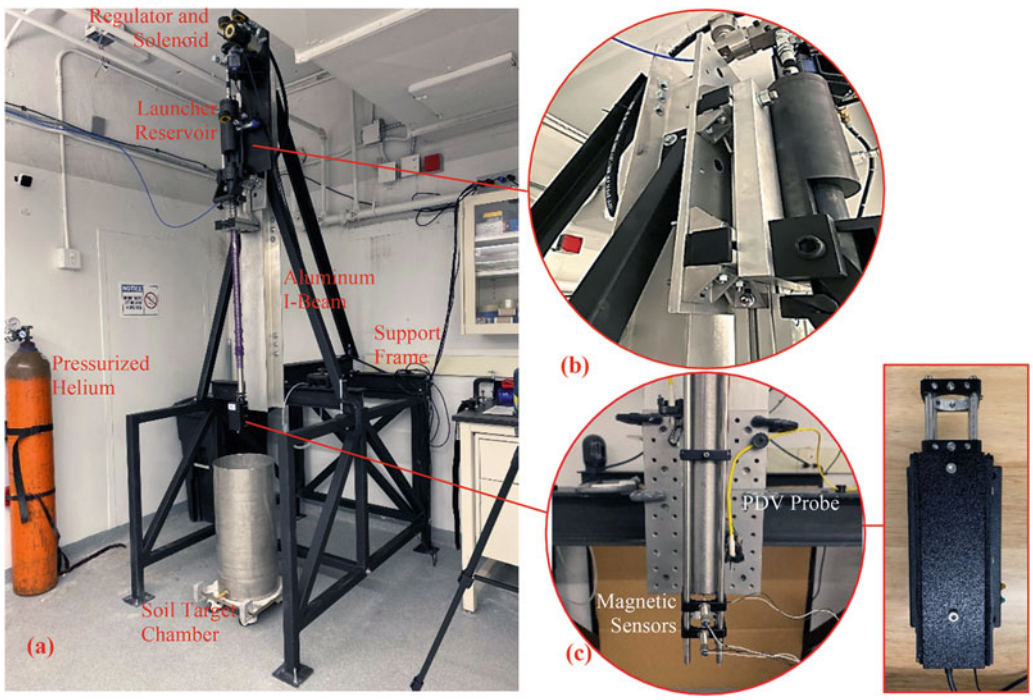


**Fig. 14.1** Vertical launcher and speed sensors. (**a**) launcher, support frame, and soil target chamber; (**b**) mounting of the launcher chamber onto the aluminum I-bream; (**c**) two instrumentation systems to measure muzzle velocity, including magnetic sensors (left) and photogate arrays (right)

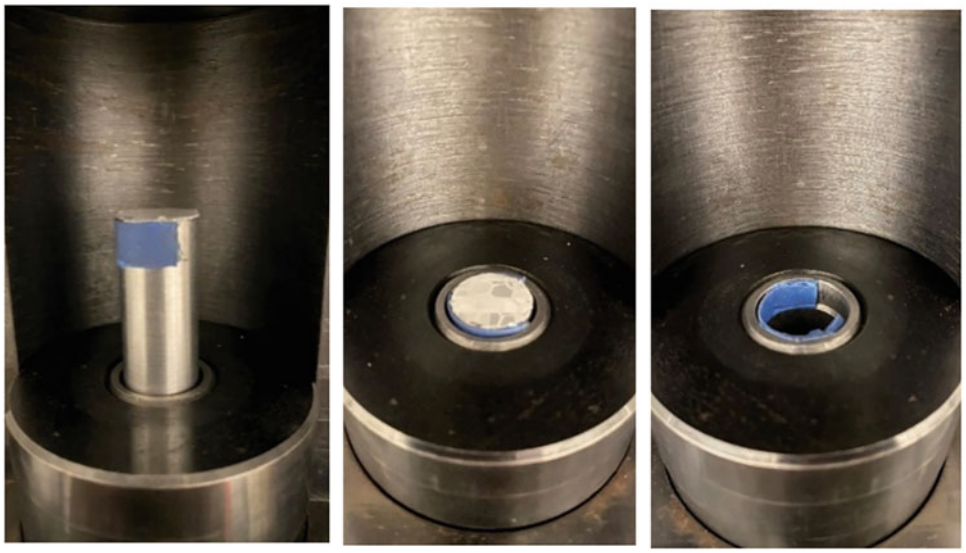

**Fig. 14.2** Projectile mounting in the breech using double-sided tape

The theoretical muzzle velocity was compared to velocity readings independently determined from instrumented sensors. Two magnetic sensors (Honeywell 3050A13) were spaced 25.4 mm apart directly below the muzzle. When launched, ferrous projectiles create an electric current to produce a magnetic signal measured by the sensors. The time delay between signals is recorded by the oscilloscope (PicoScope 5444D), and the muzzle velocity can be determined. In the case of the aluminum projectile reported herein, photogates were employed as a means of measuring the muzzle velocity. Three equidistance photogates were linearly mounted below the muzzle. In this configuration, when launched, the projectile disrupts the light signal as it passes through each of the photogates. The time delay between the disrupted signals is recorded, from which the muzzle velocity can be calculated.

Long rod projectiles were loaded into the gun breech using double-sided mounting tape (Fig. 14.2). The inner bore of the barrel is precision-machined to a diameter of 14.45 mm. The projectile tested in this study was a cylindrical rod having a diameter of 14.30 mm and a length of 76 mm. The mass of the projectile was 34.5 g. Retroreflective tape was mounted on the back of the projectile to facilitate measurements of the photon Doppler velocimeter since the incident and reflected beam are measured by a single fiber optic probe.

A rigid, passively isolated frame was designed in-house for vertical mounting of the launcher. The frame was designed to support the 300-lb launcher mass and anticipate the effects of kickback and resulting vibrations caused by firing. The frame is fabricated primarily from steel. A 7-foot-long aluminum I-beam was mounted on the frame to support the launcher and to provide adequate space and mounting options for optical and magnetic instrumentation. The launcher was mounted on an aluminum plate, which was bolted through the flanges of the aluminum I-beam.

The theoretical muzzle velocity was derived from energy equilibrium for the isentropic expansion of gas in the barrel. The principle states that the projectile potential energy and the energy required for the expansion of gas behind the projectile are equal to the projectile kinetic energy. An efficiency, $\eta$, is introduced to account for losses. The theoretical muzzle velocity, $v$, is calculated for the projectile as:

$$v = \eta \sqrt{\frac{2}{m} \frac{P_0 V_0}{\gamma - 1} \left[ 1 - \left( \frac{V_0}{V_0 + A l_b} \right)^{\gamma - 1} \right] + 2 g l_b} \tag{14.1}$$

where $m$ is the mass, $g$ is the acceleration due to gravity, $l_b$ is the length of the barrel, $V_0$ is the reservoir volume, $P_0$ is the reservoir pressure, and $\gamma$ is the specific heat ratio of heat capacity at constant pressure to heat capacity at constant volume (1.66 for helium), and $A$ is the cross-sectional area. Theoretical velocities were calculated at different pressures for the aluminum projectile used in this study, as shown in Fig. 14.3, and were compared to the experimental measurements found using the magnetic sensors and photogates. It can be seen that (1) the launcher velocity increases nonlinearly with an increase in reservoir pressure and (2) the efficiency of the launcher is inversely related to the reservoir pressure, i.e., higher reservoir pressures result in lower efficiency. The launcher efficiency varied between 70% and 90% and was most efficient with a pressure of 70 bar.

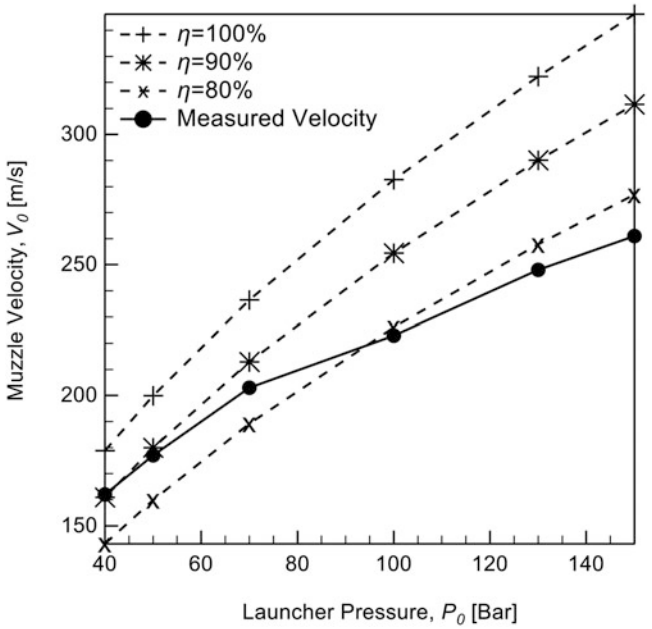


**Fig. 14.3** Muzzle velocity as a function of launcher reservoir pressure from experiments and theoretical calculations

## 14.3 PDV Measurements

The PDV system was designed as a conventional configuration using a single light source. The laser beam is used for both the target and reference beams. Approximately 90% of the light is distributed to the target beam, and 10% of the light is reserved as the unshifted reference beam. The target beam travels through a fiber optic cable leading to an optical probe which is aligned with the penetration path of the projectile. Light reflected from the back of the projectile is collected into the same probe, known as the target signal. The source frequency of an optical signal is shifted when reflected from a moving target, known as a Doppler shift. These two frequencies combine to produce a beat frequency, as follows:

$$f_b = |f_D - f_0| \tag{14.2}$$

where $f_b$ is the beat frequency, $f_D$ is the Doppler shifted frequency, and $f_0$ is the original source frequency. The frequency of the beat signal is related to the instantaneous velocity of the moving projectile, $v(t)$ [15, 16]:

$$f_b(t) = 2\left[\frac{v(t)}{c}\right] f_0 = 2\left[\frac{v(t)}{\lambda_0}\right] \tag{14.3}$$

$$v(t) = \frac{1}{2}\lambda_0 f_b(t) \tag{14.4}$$

where $c$ is the speed of light and $\lambda_0$ is the wavelength of the laser light source used. The beat signal can be transferred through an optical-to-electrical converter, which converts the optical beat signal into an electric signal. The electric signal can then be transferred to an oscilloscope to quantify the frequency of the beat signal and therefore measure the projectile velocity. An oscilloscope with the capability to resolve shifts in the frequency of the projectile at a high temporal resolution is needed to produce a velocity-time history of the penetration of the projectile during an experiment. A coherent tunable light with a wavelength of 1550 nm was used. Early PDV applications used high-power laser light with up to 2 W of power, high-power lasers are not necessarily needed for most applications. A laser with a maximum power of 42 mW was used in this study.

The PDV system used in this study was acquired from Quantifi Photonics and housed in a PXIe-1078 chassis (National Instruments), which controls the PDV setup and sends signals to the optical-to-electrical converter, which in turn sends a digital signal to the oscilloscope (Tektronix 6-Series mixed signal oscilloscope). The chassis is connected to a computer. The PXI Platform Services software MAX and the PDV are controlled using the Cohesion UI. A collimated probe was used to aim light at the back of the projectile (Fig. 14.4).

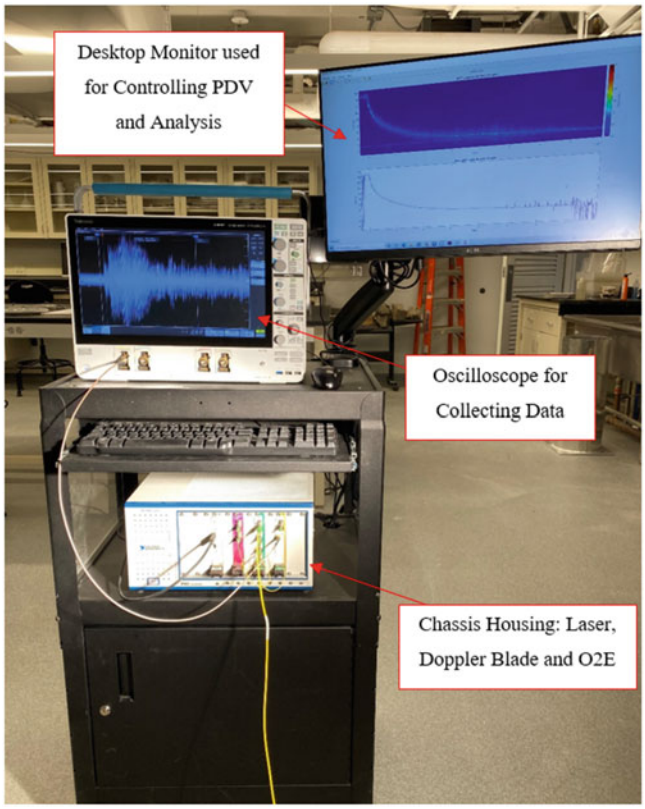


**Fig. 14.4** Photon Doppler velocimetry measurement system used in this study

**Fig. 14.5** Trial velocity measuring system used (left) and a screenshot from oscilloscope measurements of the setup (right)

## 14.4 Results

Measurements from the PDV system described above were first validated in trial experiments. A metal cutting blade was mounted on a hand drill, and retroreflective tape was placed on angles near the outer edge of the cutting blade. The hand drill was mounted firmly on a level surface and was then operated at a speed of 2000 rpm. The PDV probe was aligned such that the laser light beam crossed the center of the angle when it was at a horizontal position. The angular velocity of the rotating angles, which is the velocity that the PDV probe should measure, was calculated as 18.8 m/s. Measurements from the PDV system, shown in the oscilloscope screenshot in Fig. 14.5, revealed a time delay of approximately 30.1 ms between two successive

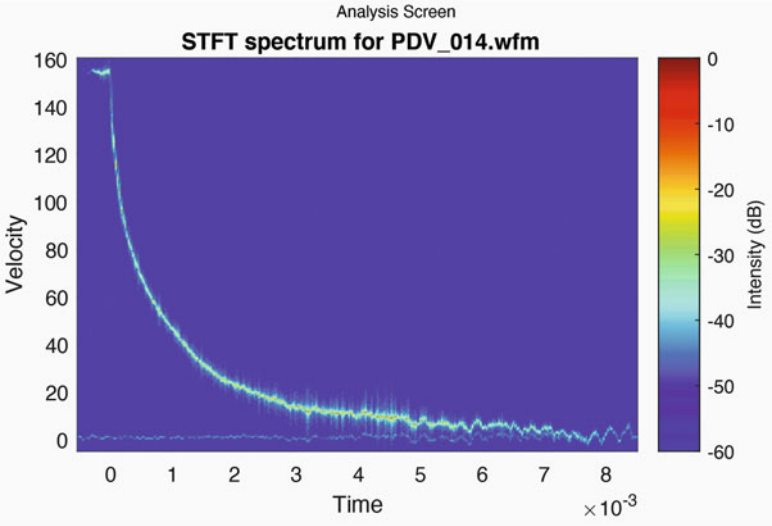


**Fig. 14.6** Spectrogram of the PDV signal from a projectile penetrating dense sand at an impact velocity of 155 m/s

signals returned from the same mounted angle. This corresponded to a measured velocity of 18.1 m/s, which approximately matches the expected velocity. The difference between the measurement and the predicted velocity can be attributed to the actual operating efficiency of the hand drill and minor misalignments in the trial setup.

Projectile penetration tests were carried out on soil targets prepared under loose and dense packing. The loose and dense dry sand samples had a density of 1520 kg/m$^3$ and 1760 kg/m$^3$, respectively. The sand consisted of Ottawa Sand with all the soil particles retained between the number 50 and 80 sieves. A pluviator was designed and built for preparing dry samples at precise densities, the details of which can be found in [14]. The laser wavelength and power used in the experiments were 1550.000710 nm and 10 dbmW, respectively. The signals were analyzed in the open-source code SIRHEN [17]. The spectrogram in Fig. 14.6 shows a spectrogram of a projectile launched at an impact velocity of 155 m/s into dense dry sand. The projectile velocity was captured during pre-impact and impacted the soil at a velocity of approximately 155 m/s. Upon impact, soil resistance caused a deceleration in the projectile and a resulting velocity decay until the projectile came to rest at the terminal penetration depth. The signal shows the trace of the velocity decay from impact to the terminal penetration depth. Shots into loose sand typically produced a signal that extended from impact to a penetration velocity of approximately 0.2 $V_0$, where $V_0$ is the impact velocity. The loss of signal in these experiments was attributed to projectile tilt in deep penetration.

The signal shown in Fig. 14.6 was obtained at a sampling rate of 6.25 Gs/s, resulting in a signal with a very high temporal resolution. Even after a short time Fourier Transform (STFT) on 2048-point windows, the resulting velocity time history had a very high temporal resolution. The small noise inherent to the velocity calculations at such high fidelity would then be magnified in the differentiation process to obtain a deceleration time history of penetration. In order to reduce some of the noise resulting from numerical calculations, the velocity-time data obtained from the PDV signal was smoothed prior to differentiation. Raw signals were used for integration purposes, since the integration effectively removes high frequencies. The velocity-time history was smoothed using a Savitsky-Golay filter, which operates as a piecewise polynomial fit to the data [12]. A trapezoidal integration was used to integrate the velocity-time history and obtain the penetration-time history. The calculated terminal depth of penetration was compared to the measured depth of penetration. The deceleration vs. time history was further smoothed using a Savitsky-Golay filter.

A comparison of ballistic experiments in dense and loose dry sand at an impact velocity of approximately 155 m/s is shown in Fig. 14.7. The results suggest that packing density plays a major role in the terminal penetration depth in sand. In loose sand, there is an initial high deceleration as the projectile nose is embedded in the soil target. Beyond this initial impact deceleration, the velocity-time curve exhibits an approximate quadratic shape, and the velocity-penetration depth curve is approximately linear. The signal is lost at a penetration velocity of approximately 40 m/s. The terminal penetration depth in the loose soil target from post-mortem analysis was 331 mm. In contrast, penetration into dense sand results in several regimes. There is an initial high deceleration at impact and embedment into the soil target, similar to the loose sand. However, this initial zone extends deeper into dense sand and results in a significant reduction in penetration velocity, from impact to approximately 120 m/s. Following this initial deceleration, the projectile penetrates the soil target at a constant high deceleration until a penetration velocity of approximately 80 m/s. There appears to be a transition in the velocity-time data,

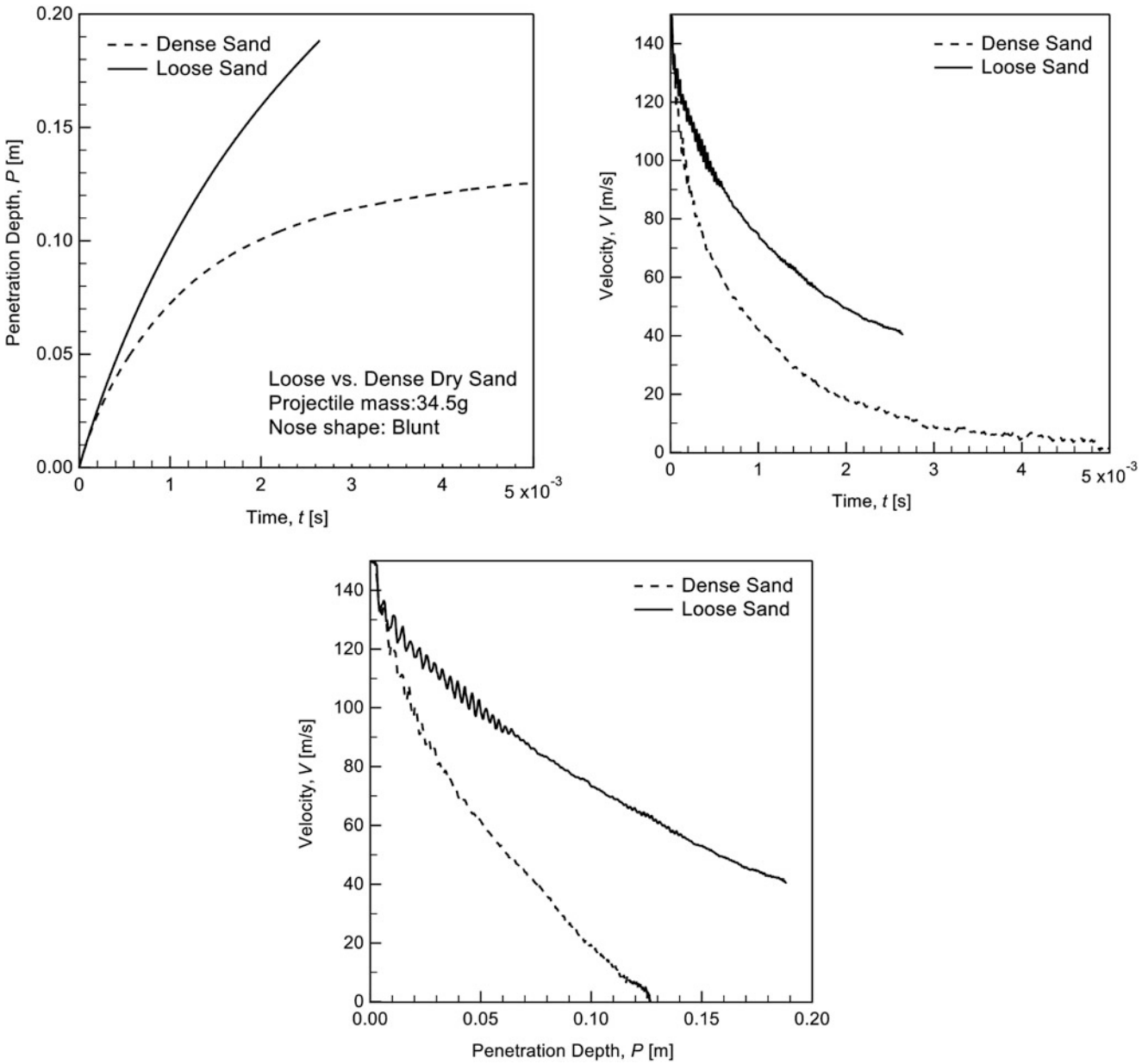


**Fig. 14.7** Comparison of ballistic shots into loose and dense dry Ottawa sand

marking a change in resistance to penetration at this depth. This penetration velocity approximately matches the acoustic wave propagation velocity in dense dry sand and could mark the transition from supersonic to subsonic penetration. A second transition can be identified at lower velocities of approximately 40 m/s, which could mark the transition from inertial-dominated resistance to frictional bearing resistance, below which shear localization occurs in the soil ahead of the projectile [18]. Finally, at a penetration velocity of approximately 10 m/s, the projectile experiences an abrupt deceleration as it comes to rest. The terminal penetration depth of the blunt aluminum projectile in dense sand was 141 mm, which is 58% lower than the terminal penetration depth in loose sand, pointing to the importance of packing density in predicting the depth of burial of ordnances in sandy soils.

## 14.5 Conclusions

A vertical-firing ballistic range was used to launch projectiles into loose and dense sand targets. A PDV setup was used to measure the projectile velocity in flight and during penetration in the soil target. 14.3-mm diameter cylindrical rod projectiles were launched at an impact velocity of 155 m/s. Loose and dense sand targets were prepared by means of dry pluviation. The launcher efficiency, defined as the ratio of the actual muzzle velocity to the theoretical prediction, was found to vary with the reservoir pressure. An optimal efficiency of 87% was found at a reservoir pressure of 70 bar. Comparison of shots into dry loose and dense sand targets revealed the significance of packing density in penetration resistance. There appeared to be two transitions in the velocity-time history, at approximately 80 m/s and 40 m/s. The transitions were more pronounced in dense sand compared to loose sand. In dense sand, the projectile came to an abrupt stop when its velocity reached approximately 10 m/s. The terminal penetration depth of the blunt aluminum projectile in dense sand was 141 mm, which was 58% lower than that in loose sand, pointing to the importance of packing density in predicting the depth of burial of ordnances in sandy soils.

**Acknowledgement** The authors gratefully acknowledge the support of the Strategic Environmental Research and Development Program (SERDP) of the United States of America, Grant No: MR19-1277.

## References

1. O'Loughlin, C.D., Richardson, M.D., Randolph, M.F., Gaudin, C.: Penetration of dynamically installed anchors in clay. Geotechnique. **63**(11), 137 (2013)
2. Ruiz-Suárez, J.C.: Penetration of projectiles into granular targets. Rep. Prog. Phys. **76**(6), 066601 (2013)
3. Young, C.W.: Depth prediction for earth-penetrating projectiles. J. Soil Mech. Found. Div. Proc. Am. Soc. Civil Eng. **95**(SM3), 803–817 (1969)
4. Allen, W.A., Mayfield, E.B., Morrison, H.L.: Dynamics of a projectile penetrating sand. J. Appl. Phys. **28**(3), 370–376 (1957). https://doi.org/10.1063/1.1722750
5. Omidvar, M., Bless, S., Iskander, M.: Global observations & post mortem analysis of penetration in sand. In: Rapid Penetration into Granular Media: Visualizing the Fundamental Physics of Rapid Earth Penetration (2015). https://doi.org/10.1016/B978-0-12-800868-3.00005-5
6. Dayal, U., Allen, J.H., Jones, J.M.: Use of an impact penetrometer for the evaluation of the in-situ strength of marine sediments. Mar. Geotechnol. **1**(2), 73–89 (1975)
7. Bless, S.J., Berry, D.T., Pedersen, B., Lawhorn, W.: Sand penetration by high-speed projectiles. AIP Conf. Proc. **1195**, 1361–1364 (2009). https://doi.org/10.1063/1.3295061
8. Borg, J.P., van Vooren, A., Morrissey, M.: In situ characterization of projectile penetration into sand. In: Rapid Penetration into Granular Media: Visualizing the Fundamental Physics of Rapid Earth Penetration, pp. 187–227. Elsevier (2015). https://doi.org/10.1016/B978-0-12-800868-3.00006-7
9. Glößner, C., et al.: Instrumented projectile penetration testing of granular materials. Exp. Mech. **57**(2), 261–272 (2017). https://doi.org/10.1007/s11340-016-0228-0
10. Collins, A.L., et al.: The effect of rod nose shape on the internal flow fields during the ballistic penetration of sand. Int. J. Impact Eng. **38**(12), 951–963 (2011). https://doi.org/10.1016/j.ijimpeng.2011.08.002
11. Cooper, W.L., Breaux, B.A.: Grain fracture in rapid particulate media deformation and a particulate media research roadmap from the PMEE workshops. Int. J. Fract. **162**(1–2), 137–150 (Mar. 2010). https://doi.org/10.1007/s10704-010-9467-8
12. Omidvar, M., Iskander, M., Bless, S.: Mesoscale observations of dynamic penetration in granular media using transparent soils. In: Rapid Penetration into Granular Media: Visualizing the Fundamental Physics of Rapid Earth Penetration (2015). https://doi.org/10.1016/B978-0-12-800868-3.00012-2
13. Nordstrom, K., Losert, W.: Refractive index matching: microstructure evolution during impact using refractive index-matched granular matter. In: Iskander, M., Bless, S., Omidvar, M. (eds.) Rapid Penetration into Granular Media: Visualizing the Fundamental Physics of Rapid Earth Penetration, pp. 353–376. Elsevier, Oxford (2015). https://doi.org/10.1016/B978-0-12-800868-3.00009-2
14. Kenneally, B., Omidvar, M., Bless, S., Iskander, M.: Observations of velocity-dependent drag and bearing stress in sand penetration. Dyn. Behav. Mater. **1**, 29–35 (2021)
15. Peden, R., Omidvar, M., Bless, S., Iskander, M.: Photonic Doppler velocimetry for study of rapid penetration into sand. Geotech. Test. J. **37**(1) (2014). https://doi.org/10.1520/GTJ20130037
16. Dolan, D.H.: Extreme measurements with Photonic Doppler Velocimetry (PDV). Rev. Sci. Instrum. **91**(5) (2020). https://doi.org/10.1063/5.0004363. American Institute of Physics
17. Ao, T., Dolan, D.H.: Sandia Report SIRHEN: a data reduction program for photonic Doppler velocimetry measurements (2010). [Online]. Available: http://www.ntis.gov/help/ordermethods.asp?loc=7-4-0#online
18. Bless, S., Omidvar, M., Iskander, M.: High-speed penetration of granular geomaterials. In: Iskander, M., Bless, S., Omidvar, M. (eds.) Rapid Penetration into Granular Media: Visualizing the Fundamental Physics of Rapid Earth Penetration, pp. 93–144. Elsevier, Oxford (2015). https://doi.org/10.1016/B978-0-12-800868-3.00004-3

# Chapter 15
# Large Deformation Explicit Finite Element Simulations of Drop Tower Experiments on Clay

**R. White, M. Omidvar, A. Ads, S. Bless, and M. Iskander**

**Abstract** Results of a high strain rate unconfined compression test on a clay soil sample and corresponding finite element simulations are presented. A drop tower was adapted to drop weights onto a saturated cylindrical kaolin clay soil sample. The engineering stress-strain response was found using piezoelectric load cells and a high-speed camera. Remolded cylindrical clay samples were prepared by the static compaction of hydrated clay in a cylindrical mold. The drop tower experiment featured a mass of 13.4 kg dropped from a height of 1.5 m, resulting in an impact velocity of 4.15 m/s and a constant strain rate of 56/s on the soil sample. Results of the high strain rate experiments revealed that the saturated kaolin clay strength, as quantified using the unconfined compressive strength, exhibited significant strain-rate dependence. An approximately 100% increase in the unconfined compressive strength was observed at a strain rate of 56/s compared to the quasi-static strength. Three-dimensional finite element simulations of the drop tower setup were then used to replicate the observed response. A penalty contact algorithm, available in the commercial finite element code Abaqus/Explicit, was used to simulate the soil-loading ram interactions. Elastic-purely plastic extended Tresca constitutive equations with strain rate and strain softening inclusions were used to capture the strain rate dependence of clay. A comparison of the experiments and the simulations revealed that the modeling procedures and the constitutive model used were able to capture the salient features of the response observed from the drop tower experiments.

**Keywords** Clay · Rate · Impact · Finite element · Drop tower

## 15.1 Introduction

The high strain rate (HSR) response of soils is of interest in a number of civilian and defense engineering applications [1–6]. Soils exhibit various degrees of strain rate dependence, related to particle size, degree of saturation, relative packing density, particle mineralogy and morphology, and stress level, among others. The majority of studies on the strain rate dependence of soils focus on the response of granular materials such as sand and gravel [7]. While early studies on the strain rate dependence of clay can be dated back to Casagrande and Shannon [8], experimental data on the response of clayey soils is sparse. This scarcity of data can be attributed to a number of factors. Sample preparation for material characterization and scaled model testing is far more challenging in clayey soils compared to granular soils. The response of clayey soils under HSR loading is expected to be undrained. Measuring pore water pressures in laboratory tests for the derivation of constitutive properties is extremely difficult. Moreover, the large strain response of clayey soils can exhibit significant strain softening, which is difficult to capture in conventional laboratory compression and shear tests. Nevertheless, many engineering applications of high strain loading involve clayey soils, thereby necessitating a better understanding of the high strain rate response of these soils.

R. White · M. Omidvar (✉)
Department of Civil and Environmental Engineering, Manhattan College, Riverdale, NY, USA
e-mail: omidvar@manhattan.edu

A. Ads
Civil and Urban Engineering Department, Tandon School of Engineering, New York University, Brooklyn, NY, USA

Structural Engineering Department, Faculty of Engineering, Tanta University, Tanta, Egypt

S. Bless · M. Iskander
Civil and Urban Engineering Department, Tandon School of Engineering, New York University, Brooklyn, NY, USA



S. Mates et al. (eds.), *Dynamic Behavior of Materials, Volume 1*, Conference Proceedings of the Society for Experimental Mechanics Series, https://doi.org/10.1007/978-3-031-17453-7_15

The use of high strain rate compression tests to characterize soils under dynamic impact is widely documented in the literature. High strain rates are achieved through various impact methods, including drop-weight systems, gas- or hydraulic-driven pistons, and explosive-loaded pistons, among others. Drop tower experiments are routinely used to determine the impact resistance of solids [9, 10]. In a drop-weight setup, a material specimen is impacted by a weight released from a predetermined height. The weight falls freely under gravity to reach a specified impact velocity. A standard drop-weight apparatus features four main components: a frame and guide for the drop weight, the drop weight, a weight release mechanism, and the loading base. Strain rates achieved using a drop tower setup are dependent on the maximum drop height achievable by the setup. Drop-weight tests are commonly used in characterizing the impact response of materials including steel, concrete, glass, and composites, among others. Drop-weight experiments can provide insight into the dynamic properties of materials such as energy absorption, fracture toughness, failure mechanisms, and strength reduction. Drop towers can be modified for HSR testing of soils to investigate uniaxial compression and triaxial compression and extension response in soils.

Impact stress applied to a soil mass during drop-weight testing introduces complex stress waves which propagate in the soil. The acceleration of the heavy weight during drop-weight impact tests often introduces ringing in the force-time response of the material. These oscillations can lead to uncertainties when characterizing the dynamic response of soil. Stress wave reflection effects are additionally prevalent when using drop-weight impact tests and are further complicated by a severe impedance mismatch generated between the soft soil sample and rigid steel drop tower apparatus. The results of experimental drop-weight impact tests on soil can thus be challenging to interpret. Studies on the interpretation of the high strain rate soil response from impact tests are commonly based on experimental approaches. While essential information on HSR soil response can be obtained through experimental studies, a comprehensive understanding can require an expensive and time-consuming testing campaign. Numerical models can be used to further inform drop tower experiments and the HSR response of soil in a time and cost-efficient manner. Numerical simulations of soil under monotonic impact are largely limited to SHPB tests and dynamic compaction of soil. Using carefully designed numerical simulations, a better understanding of the HSR response of soil under drop-weight loading can be achieved, particularly in clayey soils.

In this study, a drop tower was adapted for high strain rate testing of soil samples. A high strain rate unconfined compression test was carried out on clay. Numerical simulations were carried out in the commercially available finite element code Abaqus/Explicit to inform both the design and analysis of drop tower impact tests on soil. In the next sections, first, a brief description of the experimental setup and sample preparation is presented. Next, the numerical simulations used to capture the experimental testing procedure are described, including the geometry and mesh, contact interactions, loading, and soil constitutive response. The large deformation finite element simulations are then validated using the described drop tower experiments on unconfined clay samples.

## 15.2 Drop Tower Experiments

A drop tower apparatus was adapted to achieve high strain rate loading conditions on clay samples. The drop tower consisted of two vertical guide rails, a weight box having a mass of 13.4 kg, a loading ram having a mass of 1.80 kg, a braking system, and a sample holding area. The test setup is schematically shown in Fig. 15.1. The weight and attached ram were released from various drop heights using an electronic system attached to the top of the tower. A braking system was used along with dampers to control the impact and prevent multiple impacts. The damper was made of a vinyl material commercially known as Isodamp. A 6 mm-thick damper was attached to both the top and bottom load cells.

Piezoelectric button load cells were used to record the load at the top and bottom of the sample. The load cells had a capacity of 1000 lb. The top load cell was attached to the end of the ram, and a second load cell was attached to the loading base. The load cells were attached to the ram or sample loading base using a stainless steel base. The load cell was covered by a rigid lid attached to the ram and load cell base using two horizontal screws. The rigid lid was not fixed and could move vertically a maximum of 1 mm. Data from the top and bottom load cells were recorded at a sampling rate that resulted in samples at 10-μs intervals. Strain in the clay sample during testing was measured using a high-speed camera. The high-speed camera was operated at a frame rate of 10 kHz during testing.

The clay samples tested were prepared from kaolin clay powder. A series of tests were conducted to determine the Atterberg limits. Liquid and plastic limits were determined as 53% and 28%, respectively. Cylindrical soil samples were prepared at a dry density of 1.45 g/cm$^3$ using a water content of 32%. Static compaction was used to prepare the soil sample. A stainless-steel cylindrical mold with an internal diameter of 3.8 cm and a height of 15.2 cm was used to prepare a sample with 3.8 cm diameter and a height of 7.6 cm. Samples were prepared in three stages. First, kaolin powder was mixed with 35% water content by weight, 3% higher than the required water content, and kept for 24 h to ensure full hydration. Second, the hydrated mix was cycled through a pug mill three times to ensure uniformity and wrapped firmly for 24 h. Lastly, the weight

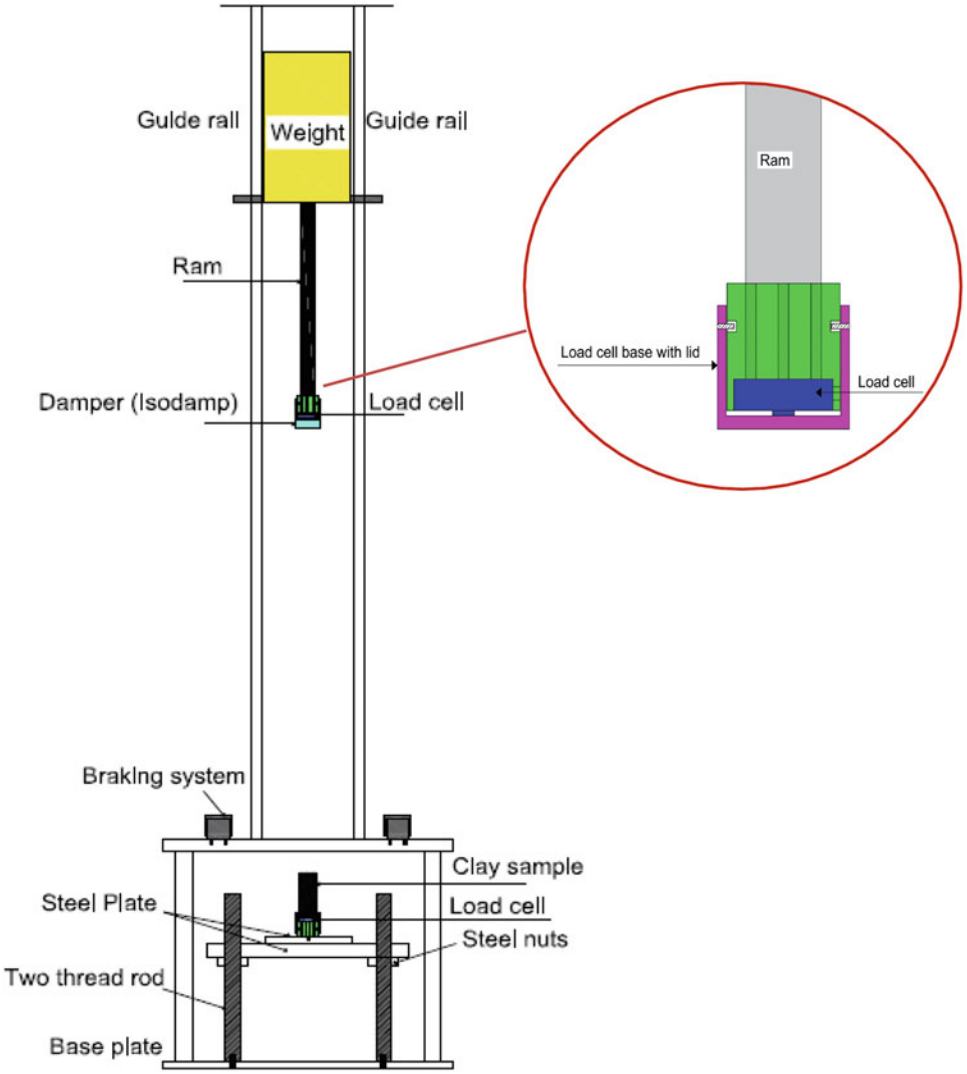


**Fig. 15.1** Schematic representation of the drop tower setup, along with details of the load cap and load cell assembly

**Fig. 15.2** Longitudinal cross-section of kaolin clay sample

required for a sample with a dry density of 1.45 g/cm$^3$ was added to the mold and compacted with an automated system at a rate of 1 mm/min. The dry density and water content of the sample were recorded after preparation as 1.41 g/cm$^3$ and 33%, respectively. The uniformity of samples prepared using the described method was examined after preparation by taking vertical and horizontal sections as shown in Fig. 15.2. The quasi-static response of the clay was determined using static unconfined compression tests. Tests were conducted at a rate of 1%/min. The results are shown in Fig. 15.3. The unconfined compressive strength of the clay was found to be 98 kPa at a strain of 15%. Given that the sample was unconfined, the undrained shear strength was half the unconfined compressive strength, i.e., 49 kPa.

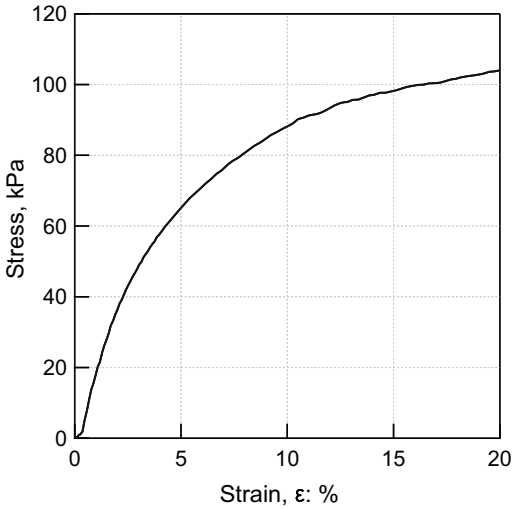


**Fig. 15.3** Quasi-static unconfined compression test results

An HSR unconfined compression test was performed on a cylindrical clay sample to investigate the strain rate dependence of the undrained shear strength. The clay sample in consideration featured a diameter of 3.8 cm and a height of 7.5 cm, resulting in a sample length-to-width ratio of two. The dry unit weight of the sample was 1.41 g/cm$^3$. The drop tower described above was used to drop a mass of 13.4 kg from a drop height of 1.5 m, resulting in an impact velocity of 4.15 m/s and a constant strain rate of 56/s on the clay sample. The decrease in sample height during testing was recorded using images obtained from a high-speed camera to quantify axial strain in the sample.

## 15.3 Numerical Simulations

A multibody dynamic large deformation explicit three-dimensional (3D) finite element model was produced to replicate the experimental setup. Multibody dynamic simulations of the soil sample, the drop tower apparatus, and the supporting frame were carried out using the commercial code Abaqus/Explicit. The experimental apparatus was modeled using a combination of deformable parts and rigid bodies to maximize computational efficiency. Components of the drop tower experiment that were of interest in the multibody dynamic simulations were modeled as deformable parts, including the drop weight, load cell caps, soil sample, base, and braking system. The drop tower guide rails and supporting base plates were simulated using rigid display bodies. Initial sensitivity analysis with the inclusion of these parts as deformable bodies revealed that the simplified approach had negligible effect on the overall response of the soil sample and the multibody drop tower setup. The dimensions of each part were identical to those reported above for the high strain rate drop tower experiment.

All parts were assembled to replicate the experimental setup as accurately as possible. The drop weight was composed of the weight, ram, load cell, and load cell cap. The load cell cap was assembled on the ram by modeling a screw connection such that the movement of the cap accurately replicated the experiments. The soil sample was assembled on the loading base, which included the base load cell and load cell cap connected with a screw connection, similar to the top load cell cap. The base rested on the tower frame, represented by rigid body parts mimicking the geometry of the experimental setup. The weight was allowed to fall freely along the guide rails of the tower frame to impact and compress the soil sample. The brake mechanism was engaged once the soil sample reached an engineering strain of approximately 30%.

All deformable parts in the simulation were meshed with 8-node linear brick elements with reduced integration and hourglass controls. Reduced integration elements feature fewer integration points compared to fully integrated elements, thereby reducing the runtime of simulations. Hourglass stiffness controls limit zero-energy deformation modes in reduced integration elements, which can otherwise lead to unrealistic results and numerical instabilities. Linear reduced-integration elements with hourglass controls provide reasonable accuracy if a sufficiently fine mesh is used. A minimum of 10 nodes per wavelength is recommended in soil elements with a time step no larger than the time required for the wave to pass one element [11]. A fine mesh was additionally required to ensure an accurate representation of the contact between surfaces during ram impact and separation. The mesh used in the simulation was ultimately selected based on sensitivity analysis and a mesh convergence study, with consideration of computational efficiency. The soil mesh selected for the simulations presented herein comprised 1 mm long elements along the height of the soil samples with radial structured elements also having a

dimension of 1 mm. Damper mesh dimensions were identical to ensure contact was enforced appropriately at the soil-damper interface. The stable time increment in Abaqus/Explicit analyses was estimated as the time required for the dilatational wave to pass one element. The dilatational wave speed was calculated as 202 m/s. The maximum stable time increment for the soil was therefore 4.95e-6 s. A time increment of 7e-8 s, smaller than the time required for the wave to pass one element, was used in the analysis to ensure stability.

The general contact algorithm in Abaqus/Explicit was used to describe the interaction of the various components in the experimental setup. The general contact algorithm captures complex contact through advanced tracking to ensure interactions are enforced efficiently. All contact interface properties were described using the coulomb friction model. Frictional sliding and normal behaviors were defined using a friction coefficient and hard contact, respectively. Contact interactions were defined for three cases of material contact: (i) steel on steel, (ii) steel on damper, and (iii) clay on damper. Steel-on-steel contact was defined with a coulomb friction coefficient $\mu = 0.1$ to represent a lubricated contact surface. Steel contact with the damper was modeled with a coulomb coefficient of $\mu = 0.64$. Contact between the clay and damper was modeled as lubricated with a friction coefficient of $\mu = 0.1$.

The drop-weight experiments were simulated in two steps. The first step captured the free falling of the weight along the guide rails until impact. In order to reduce computation time, the fall height of the drop weight was reduced from 1.5 m to 0.004. An initial velocity of 4.14 m/s was applied to the drop weight, which was then allowed to fall under gravity to impact the soil sample. The initial velocity was chosen such that the impact velocity on the soil sample matched that of the experiments, *i.e.*, 4.15 m/s. The total time for the step was 1 ms. Initial stresses resulting from the self-weight of the soil were also prescribed to the soil sample in this step to ensure the computation time in this step was sufficient to allow for the soil stresses to equilibrate. The second step of the analysis was initiated at impact and extended for an additional 5.5 ms. During this step, the impactor was in contact with the soil and compressed the soil sample as it continued to fall under gravity. Near the end of this step, the brakes engaged, and further compression of the soil sample was prevented. The brakes engaged at an engineering strain of 30%, corresponding to a compression of 22.5 mm in the soil sample. Boundary conditions restricting movement in all directions were applied to the loading base, drop weight, and brakes. The loading base and brakes were fixed to the tower frame while the drop weight was restricted from motion in the x and y directions during free fall and impact.

In addition to replicating their geometries accurately in the simulations, the parts were assigned physical and mechanical constitutive properties to closely match those of the experimental setup. The simulated setup included three materials: steel, damper, and clay. The steel members were modeled using a linear elastic material model with a mass density of 7344 kg/m$^3$, a Young's modulus of 200GPa, and a Poisson's ratio of 0.3. The mass density of the steel was reduced for the drop-weight geometry to ensure the mass was identical to that used in the experimental setup. The total mass of the simulated drop weight was approximately 15.25 kg, commensurate with the weights used in the experiments. The damper in the experimental setup, commercially identified as Isodamp, was modeled as a viscoelastic material. The material properties of Isodamp were obtained from [12]. Mass density and Poisson's ratio were defined as 1289 kg/m$^3$ and 0.432, respectively. A Young's modulus was approximated by identifying the relationship between strain rate and stiffness from the stress-strain response of Isodamp at various loading rates. Strain rates expected in this simulation range between 50/s and 750/s for the soil and damper, respectively. These strain rates correspond to a Young's modulus between 10 MPa and 100 MPa. Young's modulus was thus specified as the approximate average of the range at 55 MPa. Viscoelastic parameters were obtained from experimental data for a damper material provided by [13]. Prony series parameters for the Maxwell model were obtained from the Levenburg-Marquardt algorithm. Prony series parameters were defined following Dassault Systems Simulia [14] documentation.

The clay was modeled as an elastic, perfectly plastic material with extensions to incorporate strain rate and strain softening effects on undrained strength. The undrained strength of clay is both strain rate- and strain level dependent [15]. Under rapid loading conditions, the undrained shear strength of clay can increase by approximately 5–20% for every tenfold increase in strain rate. Depending on the soil sensitivity, undrained strength can also see a 20–50% reduction at large strains [16]. The two aforementioned behaviors were incorporated into an elastic-perfectly plastic Tresca Yield surface. This was achieved by the implementation of a vectorized user-defined field (VUSDFLD) in Abaqus/Explicit, which updated the undrained shear strength in every time step as a function of the elemental strain rate and plastic shear strain, as follows [17]:

$$s_u = \left[1 + \eta\left(\frac{\max\left(\gamma, \dot{\gamma}_{ref}\right)}{\dot{\gamma}_{ref}}\right)^{\beta}\right]\left[\delta_{rem} + (1 - \delta_{rem})e^{-3\xi/\xi_{95}}\right]\frac{s_{u,ref}}{1+\eta} \tag{15.1}$$

where $\eta$ is the viscous property, $\dot{\gamma}$ is the soil strain rate, $\dot{\gamma}_{ref}$ is the reference strain rate, $\beta$ is the shear-thinning index, $s_{u,ref}$ is the undrained shear strength at the reference strain rate, $\delta_{rem}$ is the ratio of remolded to in situ shear strength or the inverse of remolded sensitivity, $S_t$, $\xi$ is the accumulated absolute maximum plastic shear strain, and $\xi_{95}$ is the value of $\xi$ at which soil has undergone a 95% reduction of undrained shear strength. Further details of the implementation of the VUSDFLD subroutine and verification process can be found in White [18].

## 15.4 Results

Readings from the top and bottom load cells in the drop tower experiments and simulations are shown in Figs. 15.4 and 15.5. The results were considered up to a strain of 30%, corresponding to a time of 5.2 ms. This allowed for comparison with the quasi-static unconfined compression test and the numerical simulations. It can be seen from the top load cell results shown in Fig. 15.4 that there is a sharp rise in the deviator stress with a peak at approximately three milliseconds following impact. There are then several oscillations in the deviatoric stress, after which the deviatoric stress equilibrates at approximately 250 kPa. The stress-strain response recorded at the base of the soil sample indicates a stress of 250 kPa at a strain of 15%. Stress obtained from the high strain rate test is approximately 2.5 times the stress recorded for the same soil sample under static compression.

The experiments discussed above were used to validate the numerical simulations. The sample had a diameter of 3.8 cm and a length-to-diameter ratio of two. The extended Tresca constitutive model described above was used to simulate the clay. The mass density of the clay was defined as 1860 kg/m$^3$. The elastic response of the soil was estimated using the secant modulus from a static unconfined compression test. The elastic modulus was calculated at a strain of 3% and a Poisson's ratio of 0.49 was assumed to reflect the undrained conditions of the test. Material parameters required to implement the extended Tresca constitutive model were deduced from a series of triaxial tests performed on clay at various strain rates. A reference

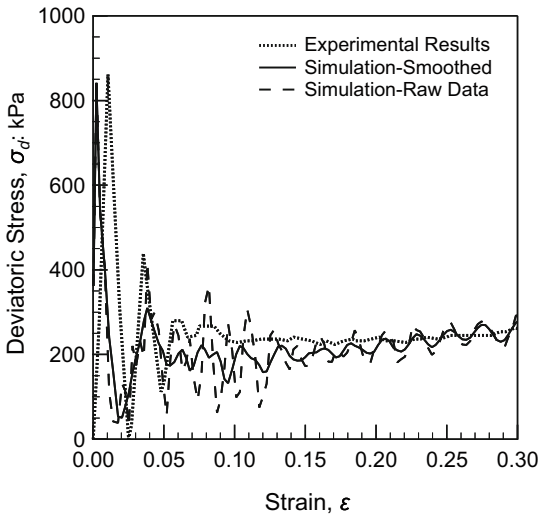


**Fig. 15.4** Comparison of vertical stresses from experiments and finite element simulations in the top load cell

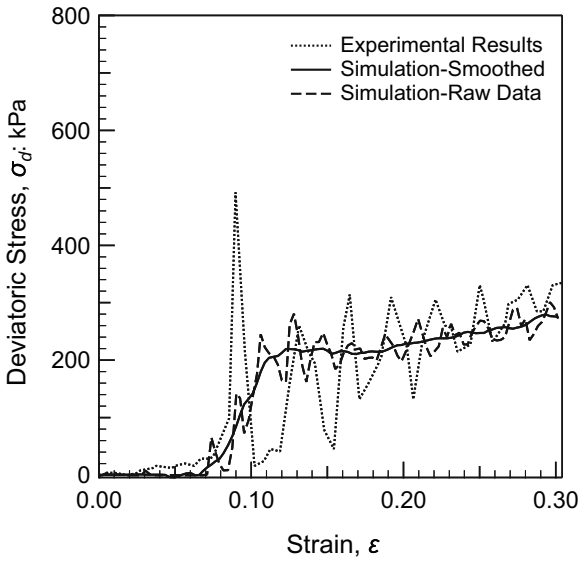


**Fig. 15.5** Comparison of vertical stresses from experiments and finite element simulations in the bottom load cell

strain rate of $\dot{\gamma}_{ref} = 0.1$/s was considered, where $s_{u,ref} = 52.5$ kPa. The rate parameters, $\eta$ and $\beta$, were determined by fitting the rate function to the undrained strength response at various strain rates. These parameters commonly range from 0.1–2.0 and 0.05–0.2, respectively, for most clays. The rate parameters acquired from experimental results were determined as $\eta = 1.0$ and $\beta = 0.15$. The strain softening parameters were adopted as $S_t = 3$ and $\xi_{95} = 20$ based on typical values reported in the literature for clay. Additional details can be found in White [18].

The stress-strain response of the soil sample recorded at the top load cell from the large deformation finite element simulations is shown in Figs. 15.4 and 15.5. Numerical results were obtained through the history output of the contact forces at the soil-damper interface. The top load cell registers a large spike in stress of 842 kPa at a time of 0.05 ms following impact. The peak in stress coincides with the time at which the clay sample experiences the total load imparted by the drop weight. This peak stress recorded at the top load cell exceeds the strength of the soil sample considerably and is related to the inertial response at impact. The amplitude of this wave attenuates as it propagates through the soil sample.

The experimental and simulation results shown in Fig. 15.5 for the bottom load cell indicate that the soil sample base begins to register stress approximately 0.5 ms after the first impact, likely an indication of elastic wave arrival at the base of the sample. The initial peak stress falls sharply to approximately 39 kPa, subsequent to which there are a number of oscillations in the stress-time history. The vertical stress oscillates at a stress of approximately 200 kPa, which is the unconfined compressive strength of the soil. The mean period of the oscillations, measured following the initial impact, from 1 to 2 ms, is approximately 0.25 ms. These oscillations can be attributed to the propagation of elastic waves in the soil, since artificial numerical mass-damping was not used in the simulations. Since the soil response enters the plastic state upon the arrival of the first peak stress, throughout the sample, these oscillations are not observed in the experiments. The magnitude of the oscillations decreases at later times, while the period of the oscillations increases. For example, the mean period of the oscillations from 3 to 4 ms, corresponding to a vertical strain of approximately 16–22%, is approximately 0.35 ms. The reduction in the period of oscillations at later times can be attributed to a decay in the stiffness of the soil as a result of a reduction in the undrained shear strength due to softening effects.

The compression of the soil sample generates both elastic and plastic waves. The plastic wave arrives at the bottom of the soil sample, where the bottom load cell is located, at a time of 1.3 ms. There is then a buildup of stress at the bottom load cell until the magnitude of the measured stress at that location reaches a mean value of 200 kPa, similar to that of the top load cell. Given that the soil sample height was 7.5 cm, the plastic wave velocity can be measured as 55 m/s. It can be seen that the stresses in the soil sample equilibrate at approximately 2.25 ms, when both the top and bottom load cells measure comparable values of vertical stress. Comparison of the experimental and simulation results confirm that the modeling procedures described in previous sections, along with the relatively simple constitutive model used, were collectively able to accurately capture the salient features of the high strain rate response of clay in unconfined compression testing using a drop tower. Such simulations can be used to gain further insight into the HSR response of clay, and to assist in the interpretation of experimental results.

## 15.5 Conclusions

Finite element simulations of high strain rate unconfined compression tests on a clay soil sample were reported. A drop tower was used to apply a constant strain rate of 56/s on the soil sample. It was found that the kaolin clay tested exhibited significant rate-dependence, with the unconfined compressive strength increasing by up to 100% at a compressive strain rate of 56/s. Three-dimensional finite element simulations of the drop tower experiments revealed that the combination of a relatively simple constitutive model and enhancements to rate dependence and strain softening was able to capture the main features of the dynamic loading of clay under unconfined compression conditions.

**Acknowledgment** The authors gratefully acknowledge the support of the Strategic Environmental Research and Development Program (SERDP) of the United States of America, Grant No. MR19-1277. The last author thanks Dr. Haixiao Liu for providing the codes.

## References


1. Holscher, P., van Tol.: Rapid load testing on piles, p. 192. CRC Press/Taylor and Francis Group, Balkema (2009)
2. Omidvar, M., Chen, Z., Bless, S., Iskander, M.: Scale bridging interactions during penetration of granular materials. Dyn. Behav. Mater. **1**, 335–340 (2014)
3. Gu, Q., Lee, F.H.: Ground response to dynamic compaction of dry sand. Geotechnique. **57**(7), 481–493 (2002)
4. Wang, Z., Lu, Y.: Numerical analysis on dynamic deformation mechanism of soils under blast loading. Soil Dyn. Earthq. Eng. **23**(8), 705–714 (2003)
5. Anderson, C.E., Behner, T., Weiss, C.E.: Mine blast loading experiments. Int. J. Impact Eng. **38**(8–9), 697–706 (2011)
6. Omidvar, M., Iskander, M., Bless, S.: Response of granular media to rapid penetration. Int. J. Impact Eng. **66**, 60–82 (2014)
7. Omidvar, M., Iskander, M., Bless, S.: Stress-strain behavior of sand at high strain rates. Int. J. Impact Eng. **49**, 192–213 (2012)
8. Casagrande, A., Shannon, W.L.: Stress-deformation and strength characteristics of soils under dynamic loads. Proceeding 2nd ICSMFE, Vol. V, pp. 29–34. Rotterdam, Netherlands (1948)
9. Suescun-Florez, E., Omidvar, M., Iskander, M., Bless, S.: Review of high strain rate testing of granular soils. Geotech. Test. J. **38**(4), 1–26 (2015)
10. Iskander, M., Bless, S., Omidvar, M.: *Rapid penetration into granular media: Visualizing the fundamental physics of rapid earth penetration*. Elsevier (2015)
11. Mostafa, K.F., Liang, R.: Numerical modeling of dynamic compaction in cohesive soils. Geo-Front. Congress, 738–747 (2011)
12. Dandekar, D.P., Green, J.L., Hankin, M., Martin, A.G., Weisgerber, W., Swanson, R.A.: Deformation of isodamp (a Polyvinyl Chloride-Based Elastomer) at various loading rates. Defense Technical Information Center, Belvoir (1991)
13. Shen, K.L., Soong, T.T.: Modeling of viscoelastic dampers for structural applications. J. Eng. Mech. **121**(6), 694–701 (1995)
14. Dassault Systemes Simulia: Abaqus 2016 Documentation. Simulia, Providence (2016)
15. Boukpeti, N., White, D.J., Randolph, M.F., Low, H.E.: Strength of fine-grained soils at the solid-fluid transition. Geotechnique. **62**(3), 213–226 (2012)
16. Zhou, H., Randolph, M.F.: Resistance of full-flow penetrometers in rate-dependent and strain-softening clay. Geotechnique. **59**(2), 79–86 (2009)
17. Liu, H., Xu, K., Zhao, Y.: Numerical investigation on the penetration of gravity installed anchors by a coupled Eulerian–Lagrangian approach. Appl. Ocean. Res. 60, 94–108 (2016). https://doi.org/10.1016/j.apor.2016.09.002
18. White, R.: *Large deformation explicit finite element simulations of high strain rate loading and rapid penetration of clay*. Master's Thesis, p. 128. Manhattan College (2021)

# Chapter 16
# A Tensile Kolsky Bar for Submillimeter Gage Lengths


**Daniel Casem, Christopher Meredith, and Daniel Magagnosc**

**Abstract** A miniature tensile Kolsky bar has been developed. The bars are steel and 1.6 mm in diameter. Because of the small size, each bar is instrumented with a normal displacement interferometer instead of strain gages. The projectile is accelerated with a spring to avoid the complexities of building a gas gun on this small scale. The bar is used to test pure aluminum samples with gage lengths of 1.0 mm and rectangular cross sections of 90 µm by 200 µm. A simple gripping design is used where the dog-bone-shaped sample is placed into recesses that are machined into the ends of the bars; the sample is then secured in place with glue. A high-speed camera is used to observe the sample deformation and failure.

**Keywords** Split Hopkinson pressure bar · Kolsky bar · Tension testing · Ductile fracture

## 16.1 Introduction

In [1], a design for a miniature tensile Kolsky bar was proposed. This paper documents initial experiments using this basic configuration. The objective of this work is to develop a capability to conduct high-strain-rate tension tests on ductile metals with sample dimensions on the order of the grain size so that the influence of microstructural features on the fracture process can be studied. Thus sample sizes in the 20 µm to 1000 µm range are of interest. A high-speed imaging capability is also desired to help study localizations in the deformation process and to confirm the measurement of sample strain. In many cases with miniature Kolsky bars, the objective is to obtain increasingly high strain rates, out of the range possible with conventional-sized bars. This is not necessarily the objective here; the main concern is accommodating small samples.

The bar is shown in Fig. 16.1. Both bars are tool steel and 1.6 mm in diameter. The input bar is 150 mm long, and the output bar is 100 mm long. There is a flange on one end of the output bar for the tubular striker to impact, generating a tensile input pulse. This is a more-or-less standard design [2] simply reduced in size. The tubular striker is also steel and dimensioned such that its impedance is slightly less than that of the input bar so that a single rectangular input pulse is generated on impact. The striker is accelerated with springs as shown, as done in [3]. This eliminates the need to use a gas gun on such a small scale.

Gripping is often a challenge in tensile testing. In the present work, miniature tension samples were cut from 90 um rolled Al via a custom fs-laser micromachining apparatus [4]. The samples have oversized tabs at each end for gripping and have a nominal gage length of 1.0 mm and a nominal width of 200 µm. Recesses are machined into the ends of each bar to accept the tabs on the sample; see Fig. 16.2. The sample is placed in these recesses and glued with cyanoacrylate. Although the samples are comparatively weak for these bars, this simple gripping method seems adequate in the preliminary experiments described here.

For bar diameters smaller than 3 mm, the use of strain gages becomes difficult, and interferometers can be used instead. The original development of this bar [1] proposed a transverse displacement interferometer (TDI) at the midpoint of the input bar to measure the input and reflected pulses, and a normal displacement interferometer (NDI) on the free end of the output bar to

D. Casem (✉) · C. Meredith
US Army Combat Capabilities Development Command Army Research Laboratory, Adelphi, MD, USA

FCDD-RLW-TC, Aberdeen Proving Ground, MD, USA
e-mail: daniel.t.casem.civ@army.mil; christopher.s.meredith3.civ@army.mil

D. Magagnosc
US Army Combat Capabilities Development Command Army Research Laboratory, Adelphi, MD, USA

FCDD-RLW-MB, Aberdeen Proving Ground, MD, USA
e-mail: daniel.j.magagnosc.civ@army.mil



S. Mates et al. (eds.), *Dynamic Behavior of Materials, Volume 1*, Conference Proceedings of the Society for Experimental Mechanics Series, https://doi.org/10.1007/978-3-031-17453-7_16

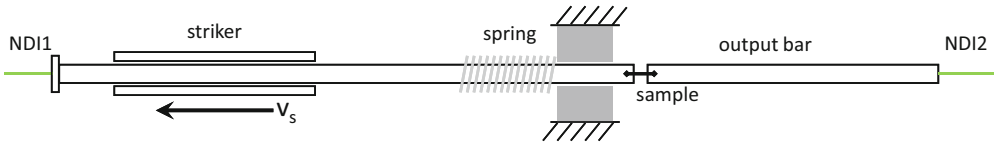


**Fig. 16.1** A miniature tensile Kolsky bar. The tubular striker is accelerated by a spring compressed against a fixed bushing. Additional bushings are used for support but not shown for clarity. The free end of each bar is instrumented by an NDI, eliminating the need for strain gages

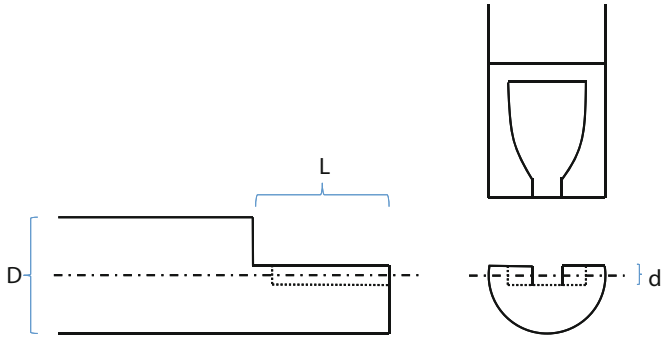


**Fig. 16.2** Dog-bone-shaped samples are glued into recesses at the ends of the bars. In the present work, L = D = 1.6 mm and d = 90 um

measure the output pulse. This is basically a tensile arrangement of the miniature compression bar described in [5]. A TDI used in this fashion requires a diffraction grating applied directly to the side of the bar. This poses a problem because the grating could easily be damaged by the passage of the striker and springs over the grating. It was therefore decided to forego the use of the TDI and instrument both bars with an NDI at the far ends, i.e., opposite the sample. The analysis of the sample then proceeds as explained in [5]. An advantage of this instrumentation is that a simple wave separation method is available which allows the force applied to each end of the sample as well as the displacement at the sample/specimen interfaces to be determined for all time, regardless of the presence of overlapping reflections. An additional advantage of the NDI is its sensitivity; this allows forces generated by small cross-sectional, low-strength samples to be measured with good resolution.

## 16.2 Experimental Results

An example experiment is now discussed. The velocity measured by each NDI is shown in Fig. 16.3a. This input pulse has a magnitude of 4.2 m/s. The next pulse is the reflection, but because it is measured at the free surface the velocity is double what might be expected. The third pulse shown is the next reverberation of this reflection and is needed for the complete analysis given below. The NDI2 trace is more complicated because of the wave overlaps but is easily converted to sample stress and strain using the analysis of [5]. As mentioned above, this is a weak sample for bars of this impedance, and so the output bar signal is much smaller than that of the input bar. The two signals are therefore plotted with two different vertical scales in the figure.

Figure 16.3b shows the stress-strain curve for this sample. The input pulse was not large enough to fail the sample with a single loading. The sample, therefore, unloads elastically and then reloads to failure upon the next reverberation of the loading pulse (the third input bar pulse in Fig. 16.3a). The free-end analysis is able to account for this unambiguously.

A Shimadzu HPVX2 high-speed camera was used to take images of the sample during deformation. Fig. 16.4 shows the necking just prior to failure (~ 32% strain).

## 16.3 Conclusion

A miniature tensile Kolsky bar has been developed and used successfully to test aluminum samples with 1 mm gage lengths. The interferometer instrumentation can accurately measure the stress-strain curve, and the gripping method using glued tabs on dog-bone samples seems adequate. A high-speed camera has been incorporated into the experiment and will be used to

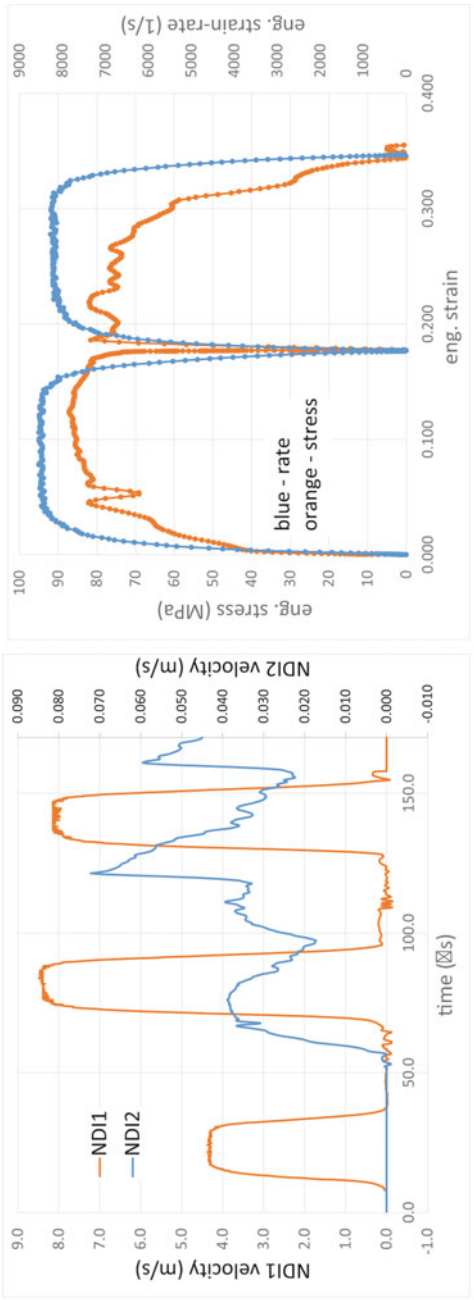


**Fig. 16.3** (**a**) The velocity measured by each NDI. Note the different scales – the velocity of the output bar is small due to the low sample force (less than 2 N). (**b**) The stress-strain and strain rate for the sample. The magnitude of the input pulse was not large enough to fail during the first loading

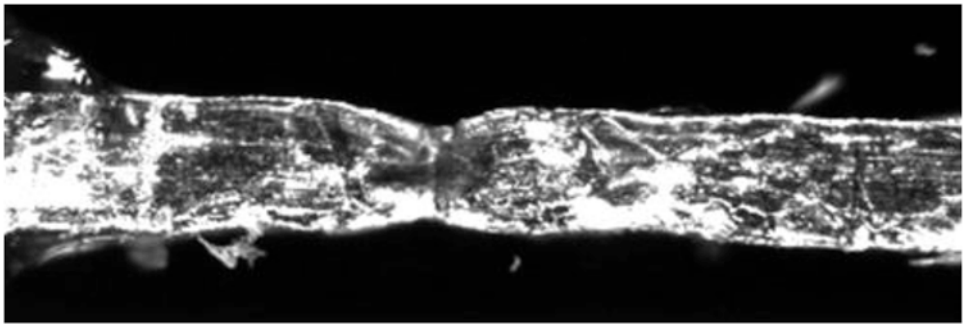

**Fig. 16.4** The neck in the sample just prior to failure

improve/confirm the measure of specimen strain in future work. Smaller samples (gage length and cross-sectional dimensions) are certainly possible, although they may need the substitution of a smaller output bar to maintain sufficient sensitivity to force. However, this is a straightforward modification to make with the existing design and instrumentation.

## References

1. Casem, D.T.: Development of a micro tensile Kolsky Bar. In: Lamberson, L., Mates, S., Eliasson, V. (eds.) Dynamic Behavior of Materials, vol. 1. Conference Proceedings of the Society for Experimental Mechanics Series. Springer, Cham (2021). https://doi.org/10.1007/978-3-030-59947-8_13
2. Nicholas, T., Bless, S.J.: High rate tension testing. ASM Metal Handbook. **8**, 208–214 (1985)
3. Lim, J., Zheng, J.Q., Master, K., Chen, W.: Mechanical behavior of A265 single fibers. J. Mater. Sci. **45**, 652–661 (2010)
4. Magagnosc, D.J., Ligda, J.P., Sano, T., Schuster, B.E.: Femtosecond laser machining of micro-tensile specimens for high throughput mechanical testing. In: Starman, L., Hay, J. (eds.) Micro and Nanomechanics, vol. 5, pp. 7–9. Springer International Publishing (2018)
5. Casem, D.T., Grunschel, S.E., Schuster, B.E.: Normal and transverse displacement interferometers applied to small diameter Kolsky bars. Exp. Mech. **52**(2), 173–184 (2012)

# Chapter 17
# A Comparison of High-Rate Tensile Failure Methods for Structural Adhesives


**Evan L. Breedlove, Ryan Powers, Michael Kennedy, Mohammed Al Tameemi, and Jordan Priester**

**Abstract** Structural adhesives are important structural elements in modern engineering design, particularly for the bonding of composites and dissimilar materials. Structural adhesives enable light-weighted structures and have long supported the use of organic structural designs common in aerospace. These applications often require designed performance under high strain-rate loading, such as crash and impact. Design and simulation with structural adhesives under these high-rate conditions require reliable mechanical failure data.

High-rate tensile failure testing of bonds, such as butt-tension and napkin ring tests, are particularly important characterizations, and several methods of preparing and loading test specimens have been proposed. However, it is not clear how specimen design and test apparatus influence measured adhesive behavior for nominally identical bond geometry.

In order to understand these effects, we evaluate three different test configurations using identical bond geometries and similar engineering strain rates. The first configuration is a conventional napkin ring specimen loaded using a Kolsky bar. The second configuration is a blister-style specimen—similar to those studied by Gollins et al. and Yildiz et al. and previously reported by Carpenter et al.—loaded using a Kolsky bar. Finally, the same blister-style specimen is evaluated using a drop tower. It is hypothesized that differences in load-train compliance and, in the case of the drop tower, apparatus dynamics will substantially influence test results. Understanding the influence of the test method on tensile failure results is critical to the development of predictive adhesive failure models and the validity of data comparisons between different test configurations.

**Keywords** Structural adhesives · Kolsky bar · Butt tension testing · Cohesive zone model · Polymer testing

## 17.1 Introduction

Structural adhesives are cure-in-place polymers which often replace traditional structural joining technologies. Thanks to their toughness and ability to join dissimilar materials, they are increasingly employed in high-performance applications such as aerospace, automobiles, and portable electronics. Many of these applications demand reliable performance at high strain rates; consequently, it is critical to establish reliable failure data at high speeds. Cohesive zone modeling is a particularly widespread technique for simulating structural adhesive failure, and such models are often calibrated using some form of butt tension test. Conventional butt tension tests, such as ASTM D2095 [1], are not well-suited to high-speed testing. Instead, a variety of analogous test geometries have been developed.

One geometry is a high-rate adaptation of a quasistatic alternative to butt-tension: the napkin ring specimen. A napkin ring specimen is an annular bond consisting of two substrates connected by a ring of adhesive. The adhesive bond is destroyed by pulling on the two substrates (Fig. 17.1). This test geometry is favorable because the bond width can be more closely matched to applications, machining tolerances for flatness and parallelism are more easily achieved, and the specimens can be alternatively loaded in torsion with a relatively uniform shear stress state [2]. Napkin ring specimens have been previously tested in a Kolsky tension bar apparatus by Yokoyama and Nakai [3].

Another test geometry is known both as the blister test [4, 5] or tensile impact [6]. This test geometry consists of a puck bonded to a window by a perimeter adhesive. A mechanical impulse is delivered to the puck through the window, causing the puck to accelerate from the window and debond (Fig. 17.1). The geometry may be tested on an instrumented falling-dart drop tower or a Kolsky bar apparatus by delivering the impulse with an incident bar rather than a falling striker.

E. L. Breedlove (✉) · R. Powers · M. Kennedy · M. Al Tameemi · J. Priester
Corporate Research Materials Laboratory, 3M Company, Maplewood, MN, USA
e-mail: elbreedlove@mmm.com



S. Mates et al. (eds.), *Dynamic Behavior of Materials, Volume 1*, Conference Proceedings of the Society for Experimental Mechanics Series, https://doi.org/10.1007/978-3-031-17453-7_17

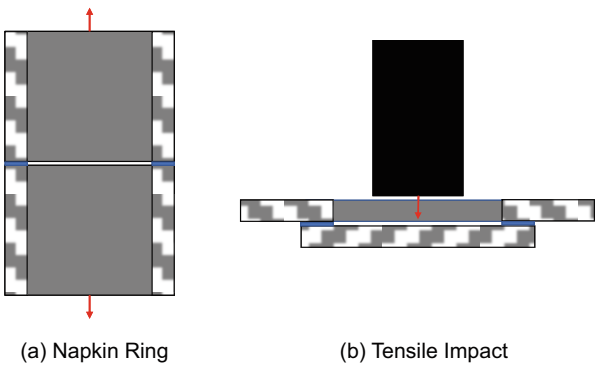


**Fig. 17.1** Schematics of (**a**) the napkin ring test and (**b**) the tensile impact test

Ideally the napkin ring and tensile impact geometries would yield the same behavior for an adhesive bond. Both geometries nominally load the adhesive in an out-of-plane tensile mode, and both geometries test a ring of adhesive. Moreover, both drop towers and the Kolsky bar are able to track dynamic forces and displacements; therefore, it would be expected that both methods would yield comparable results for the same test coupon. Nevertheless, no studies have been conducted comparing these test geometries. Therefore, it is not known whether different out-of-plane tensile failure tests will yield test results which can be substituted for engineering purposes. Consequently, this study aims to provide a preliminary investigation of this question by presenting a high-rate failure analysis for a single adhesive tested in the following modes: tensile impact on a drop tower, tensile impact on a Kolsky bar, napkin ring on a Kolsky bar using strain-gage-based displacements, and napkin ring on a Kolsky bar using DIC-based displacements.

## 17.2 Methods

***Material*** Testing was conducted on 3 M epoxy DP460NS (3 M Company; Maplewood, MN). All samples were primed with 3 M AC130 primer, then cured at 60 °C for 2 h followed by 24 h at room temperature. All samples were conditioned for at least 24 hrs at 23 °C and 50% relative humidity prior to testing.

***Tensile Impact Specimens*** Tensile impact specimens were prepared with 304 stainless steel substrates. Substrates were sand-blasted and cleaned with IPA prior to bonding. The puck consisted of a 3 mm thick disk with a diameter of 33 mm. The window was similarly 3 mm thick with an aperture of 24 mm, providing for a 4.5 mm wide bond line. Bond thickness was set at 150 μm using spacer beads. Substrate alignment was ensured using a jig which remained in place until adhesive cure was complete. Samples were checked for consistent quality following cure, yielding six samples for drop tower tensile impact and 12 samples for Kolsky bar tensile impact.

***Napkin Ring Specimens*** Napkin ring specimens were prepared with 6061 aluminum substrates. Substrates had an inner diameter of 17.4 mm and an outer diameter of 23.83 mm, resulting in a bond width of 3.12 mm. Frekote® release agent (Henkel AG; Dusseldorf, Germany) was applied to the inner and outer faces of the substrates to prevent any flashing from bonding. The bonding surface was sand-blasted and then cleaned with methyl ethyl ketone (MEK) to remove any residual release agent. Adhesive thickness was set using a jig which set the bond gap at 123 μm and applied constant pressure during cure. Flashing was easily removed with a razor. Inspection of bonds post-test confirmed that bonds were of uniform thickness with full coverage across the bonding surface for most of the tested specimens. Samples were checked for consistent quality following cure, yielding 13 samples which were tested.

***Drop Tower Apparatus*** Drop tower testing was conducted on a CEAST 9340 drop tower (Illinois Tool Works; Glenview, IL) with a steel piezoelectric striker (M3080), which has a load capacity of 22.24 kN (PCB 208A35; Depew, NY). Samples were set in a custom fixture and pneumatically clamped to prevent rebound. The carriage had a mass of 17.980 kg and was dropped from a height of 1.119 m, resulting in an impact velocity of approximately 4.68 m/s. The striker had a cylindrical profile with a flat face and a diameter of 12.7 mm. The instrumented drop tower directly records the force applied to the striker as well as the velocity just before impact by means of a light gate.

***Kolsky Bar Apparatus*** All Kolsky bar testing was conducted on a Kolsky bar apparatus designed and built by REL Inc. (Calumet, MI). Tensile impact specimens were tested in a compression configuration. A compressive force was applied to the puck using a maraging steel incident bar (3/4-in. diameter, 10-ft. length) and a 12-in. long striker bar. Copper pulse shapers

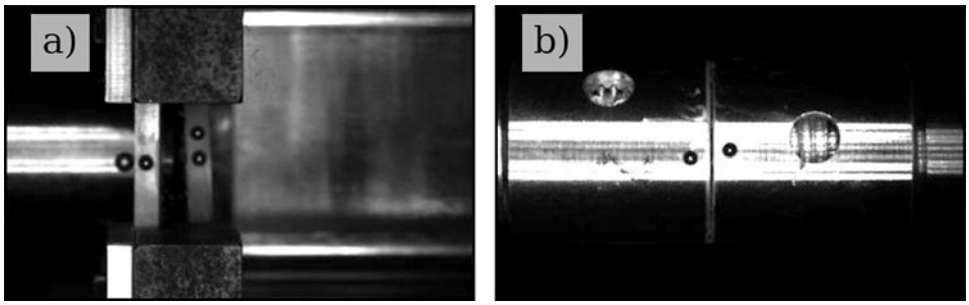


**Fig. 17.2** Images of the Kolsky bar configurations for (**a**) tensile impact and (**b**) napkin ring testing

(1/4-in diameter, 0.016-in. thick) were employed. Incident pulse was measured with an attached strain gage but was not used for data reduction. The incident bar was situated in contact with the puck at the start of testing, and incident bar displacement was measured using a high-speed camera (Shimadzu HPV-X2; Kyoto, Japan) at 500,000 fps. The reaction force of the fixture was measured using a piezoelectric load cell (Kistler 9352A; Winterthur, Switzerland) and a charge amplifier (Kistler 5010) affixed to a rigid support block (Fig. 17.2a). DIC analysis was performed using the NCORR software [7] embedded in the REL SurePulse software, version 1.22.0.

Napkin ring specimens were tested using a ¾-in. diameter, 7075 aluminum tension bar configuration. Samples were threaded onto either end of 12 ft long incident and transmission bars with Teflon® tape to dampen vibrations in the threads (Fig. 17.2b). Actuation was delivered by means of a 12-in. long annular striker bar impacting an end-cap. Copper pulse shapers were employed between the striker and end-cap. The test configuration was designed so that the bar impedance (4038.5 kg/s) was larger than the substrate impedance (86.9 kg/s), consistent with standard assumptions for one-wave data reduction techniques. Strains for incident and transmission bars were measured by strain gages. Strain gages were shunt-calibrated prior to testing. Force was measured by the transmitted wave. Displacement was measured both by the reflected wave (standard one-wave method) and by DIC tracking of dots affixed to both substrates (Shimadzu HPV-X2; 1,000,000 fps). These two methods of determining displacement are both reported for the same data as napkin ring (bar) and napkin ring (camera).

## 17.3 Results

Attempts were made to conduct tests at a consistent velocity; however, differences in apparatus configuration made this impractical. Figure 17.3 shows the velocity vs. time for all tests. Note that significant noise in the DIC measurement for napkin rings led to significant uncertainty in the test rate.

Force histories and force displacement were recorded for each of the tests (Figs. 17.4 and 17.5). While peak force amplitude was relatively consistent, the evolution of force, displacement at peak force, and general shape of the response differed significantly between geometries. A comparison between tensile impact and napkin ring tests was also made (Fig. 17.6).

Nominal stress and strain histories were also generated (Fig. 17.7). Nominal stress was computed as the force divided by the bond area. Nominal strain was computed as the displacement divided by the thickness. These nominal values served as normalization of test results. A much larger spread in peak amplitude was observed in the nominal stress. A comparison between tensile impact and napkin ring tests was also made (Fig. 17.8).

Finally, key features of the load-displacement (Fig. 17.9) and stress-strain (Fig. 17.10) curves were extracted. The comparison includes energy, which was computed as the integral under the load-displacement curve. This is a common metric for evaluating the energy dissipated by a bond during impact. The data indicate a consistent peak force, but a significant spread in all other metrics.

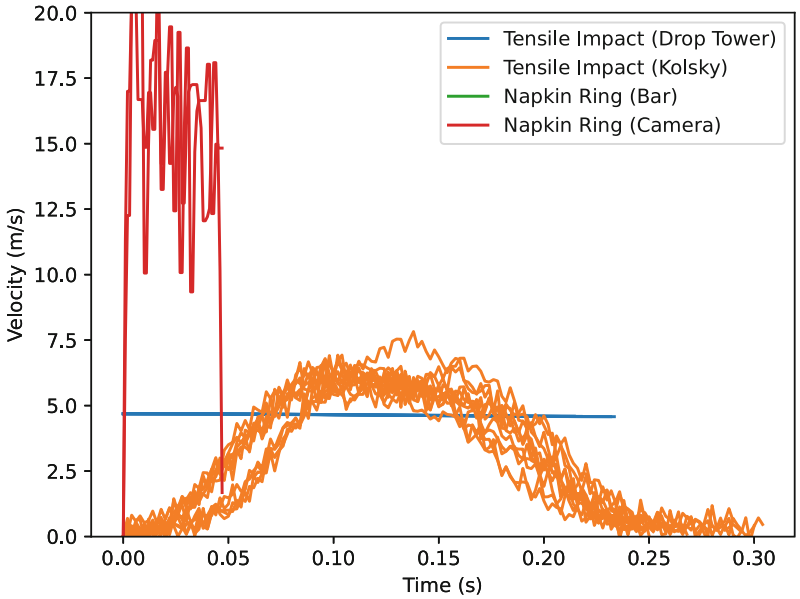


**Fig. 17.3** Test velocities for each of the test configurations. Significant noise in the camera-based napkin ring measurement was observed

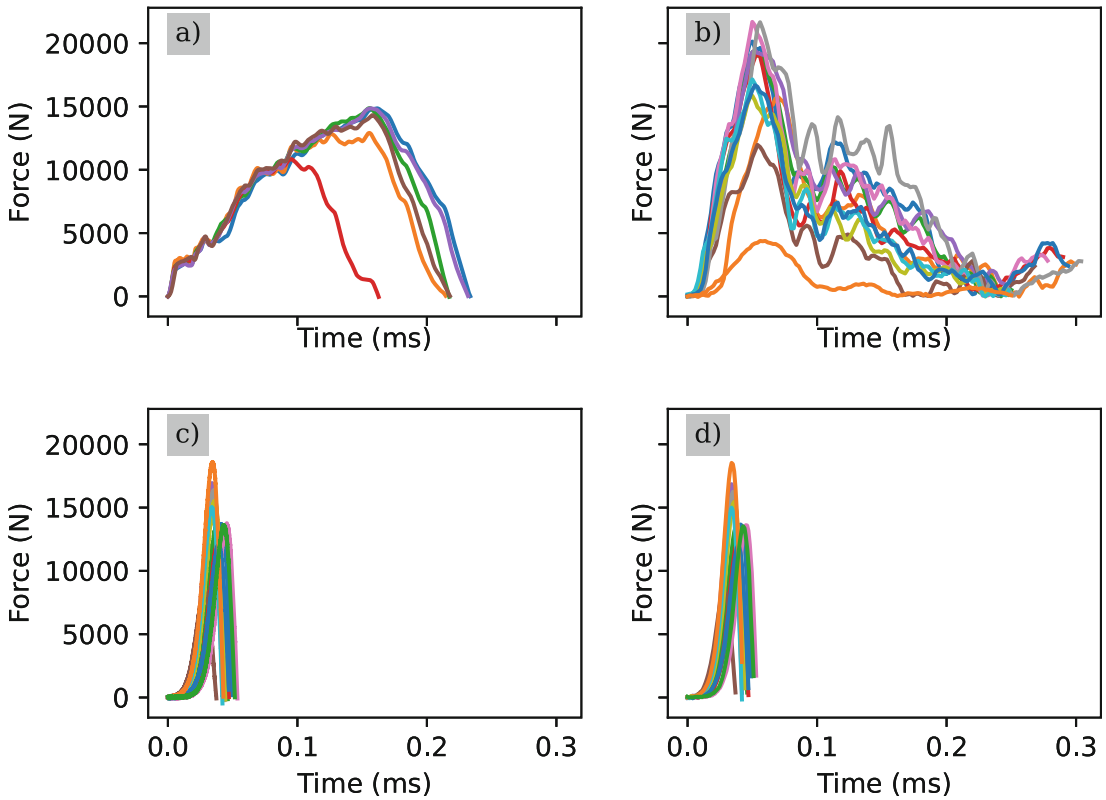


**Fig. 17.4** Force-time histories for (**a**) drop tower tensile impact, (**b**) Kolsky bar tensile impact, (**c**) bar-based napkin ring, and (**d**) camera-based napkin ring

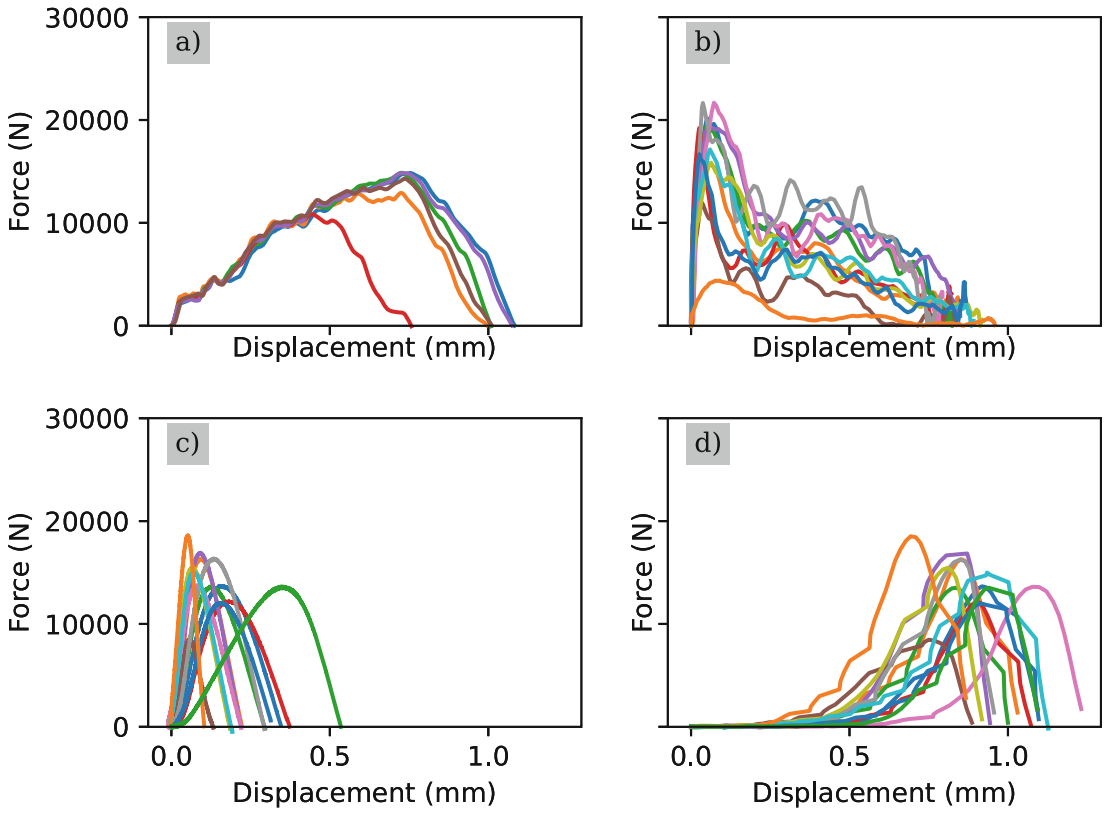


**Fig. 17.5** Force-displacement curves for (**a**) drop tower tensile impact, (**b**) Kolsky bar tensile impact, (**c**) bar-based napkin ring, and (**d**) camera-based napkin ring

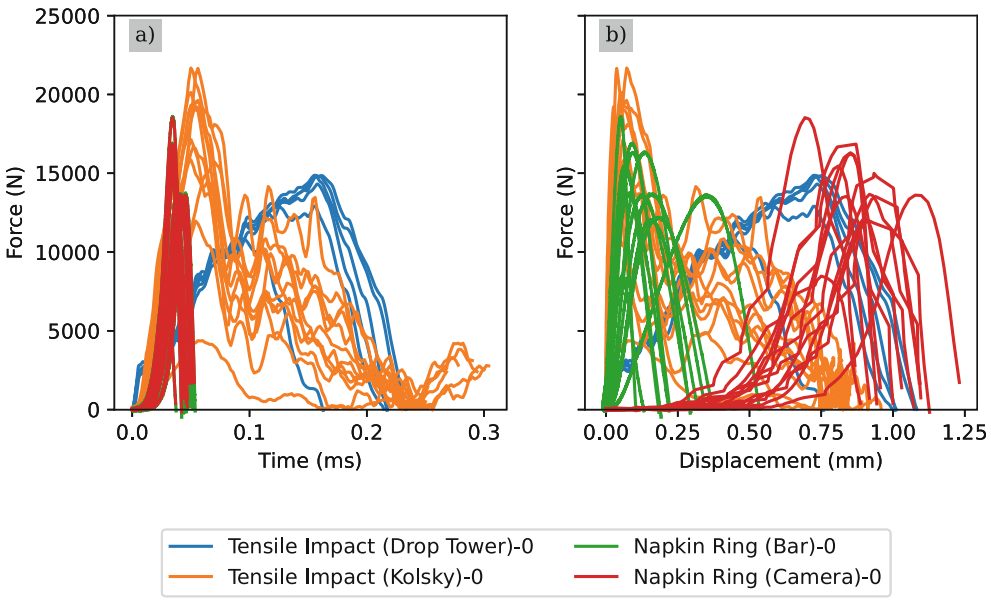


**Fig. 17.6** Comparison of (**a**) force-time and (**b**) force-displacement behavior

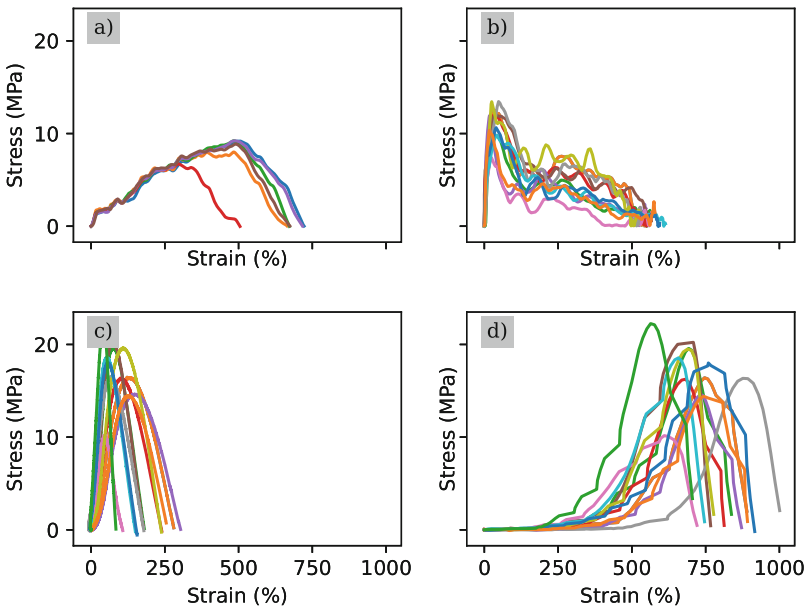


**Fig. 17.7** Nominal stress-strain curves for (**a**) drop tower tensile impact, (**b**) Kolsky bar tensile impact, (**c**) bar-based napkin ring, and (**d**) camera-based napkin ring

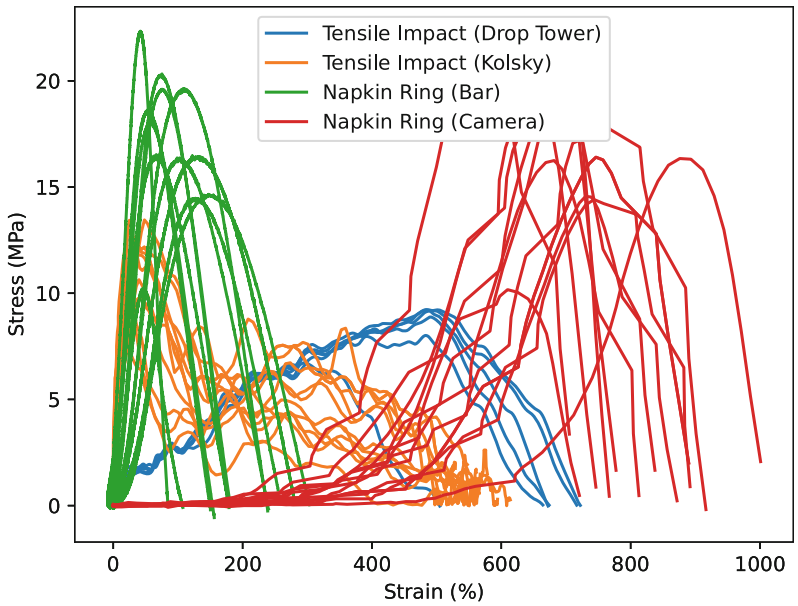


**Fig. 17.8** Comparison of nominal stress-strain behavior

## 17.4 Discussion

This study presents a novel comparison of tensile-mode failure testing for structural adhesives at high rates. Multiple test geometries and test apparatuses were evaluated for nominally identical load cases. Ideally, these data would have yielded similar force, time, and displacement histories; however, results indicate that significant differences exist between the test methods.

The most immediate difference between the test conditions is the velocity history (Fig. 17.2). Due to the relatively thin bond line, the time for sample acceleration is brief. In the case of the drop tower, the mass and velocity of the striker cause almost instantaneous acceleration of the puck. Drop tower data outputs do not actually track the puck displacement and velocity; rather, they track the striker, whose velocity is barely altered by the impact. In contrast, the same test geometry on the

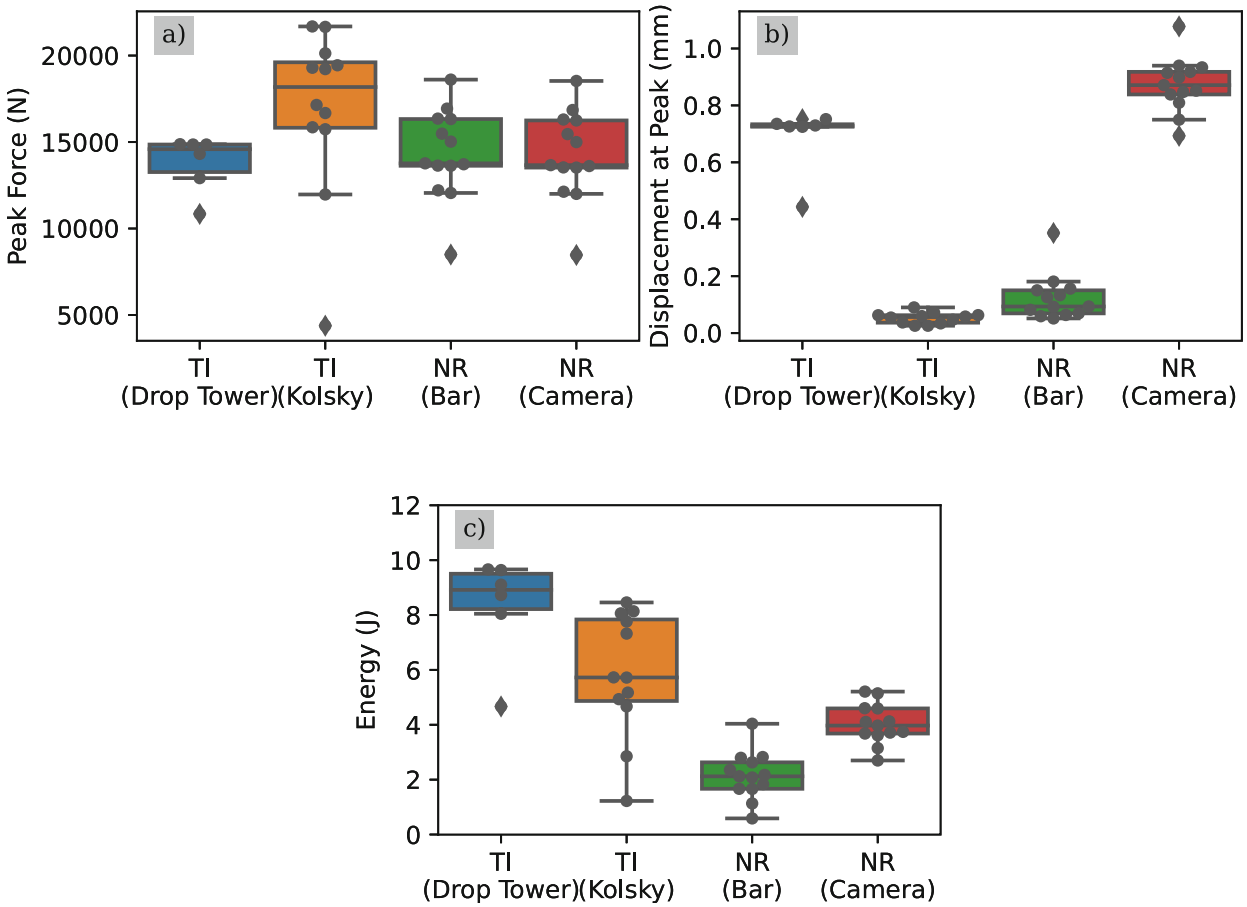


**Fig. 17.9** Comparison of (**a**) peak force, (**b**) displacement at peak force, and (**c**) dissipated energy (i.e., area under the force-displacement curve) for each of the methods (TI = tensile impact, NR = napkin ring)

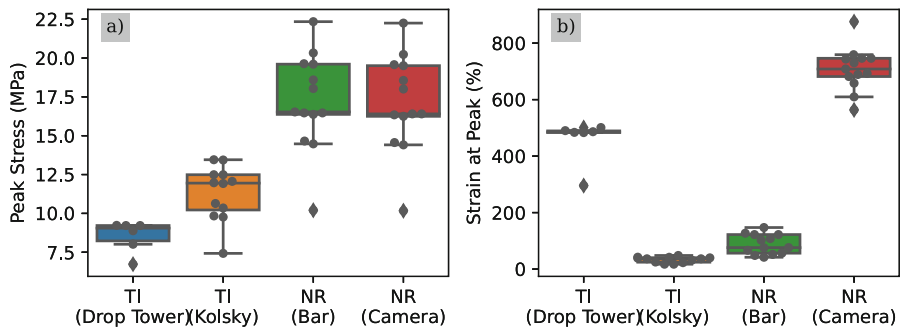


**Fig. 17.10** Comparison of (**a**) peak nominal stress and (**b**) nominal strain at peak nominal stress for each of the methods (TI = tensile impact, NR = napkin ring)

Kolsky bar is characterized by a gradual rise to a plateau velocity. As with the drop tower, this configuration tracked the displacement of the bar striking the puck, not the puck itself. The longer duration of both tensile impact configurations suggests substantial compliance in the load train (see below); in contrast, the napkin ring specimens yielded much shorter test durations. The bar-based displacements showed no constant velocity regime, with a constant rise through the end of the test. DIC-based displacement yielded significant noise but suggested a somewhat consistent velocity throughout the test.

It is worth noting how the drop tower displacement is determined. The tower does not contain any displacement sensors; rather, it records the force applied to the striker and the velocity just before impact. Provided the mass of the striker/carriage assembly is known, the velocity and displacement histories of the striker can be determined by a simple load balance on the striker load cell and integration (assuming the initial position is zero):

$$a(t) = \frac{mg - F(t)}{m} \tag{17.1}$$

$$v(t) = \int_0^t a(t)dt + v_0 \tag{17.2}$$

$$x(t) = \int_0^t v(t)dt \tag{17.3}$$

This implies that the displacement is the displacement of the striker, not the test specimen. Moreover, the displacement measurements are subject to any errors induced by treating the striker/carriage assembly as a point mass rather than a deformable body.

Significant differences were also apparent in the load-time, load-displacement, and stress-strain curves. All three of the Kolsky-bar analyses resulted in a rapid rise in force, while the drop tower yielded a much slower rise in force (Fig. 17.6a). This result is surprising given the much larger initial velocity at the start of the tests, which would necessarily cause a rapid acceleration of the puck and corresponding inertial force. The lack of a significant initial spike suggests substantial compliance in the drop tower load train. In fact, finite element simulation indicates that substantial compliance must be incorporated to yield correlation between experiments and tests, even when impacting steel plates directly with no adhesive (simulations not shown). In contrast, the Kolsky bar load train appears to be much stiffer, generating a more rapid rise in force even though the nominal test rates were slower toward the beginning of the test.

The influence of load-train compliance is even more apparent when considering the nominal stress-strain. Consistent with the load history, the drop tower exhibited lower peak stress compared with the Kolsky bar tests. Interestingly, the Kolsky-bar version of tensile impact also exhibited lower stress. Simulations indicate that significant flexure in the puck and window is expected, leading to a nonuniform stress state in the bond and contributing to the overall observed compliance (simulations not shown).

The differences in test results have significant practical implications. On one hand, data are still useful for model calibration if inverse methods are employed since differences in test geometry and load history can be accounted for. However, it is common practice in industry to rank material performance based on tests such as these. Data suggest that spurious conclusions may be reached if comparisons are made using differing test methods. Although peak force was relatively consistent across tests (Fig. 17.9a), normalized nominal peak stress indicated significant differences (Fig. 17.10a). Furthermore, differences in the load history yielded substantial variability in the displacement/strain at peak (Figs. 17.9b & 17.10b). Finally, because energy depends on both the load and displacement, notable differences in dissipated energy were observed (Fig. 17.9c). As expected because of extra compliance, the drop-tower-based tests yielded energies more than double the napkin ring geometry and even 50% greater than the energies recorded for tensile impact using the Kolsky bar. This indicates that energy-based material selection criteria could inaccurately rank materials if drop tower compliance is not accounted for.

Finally, it is notable that the napkin ring geometry yielded nominal failure stresses nearly double the tensile impact failure stresses (Fig. 17.10a). This is believed to be a consequence of puck flexure. Flexure leads to a heterogeneous stress distribution, causing some regions to fail prior to the entire bond reaching a critical stress. Loss of bonding area weakens the bond, allowing further failure to occur without increase in force. The implication is that tensile impact does not yield a true strength value. Moreover, since the degree of flexure is sensitive to the modulus and strength of the adhesive, the relative ranking of adhesive strength may not be reliable in a tensile impact mode.

This study has several notable limitations. First, the analysis was conducted on a limited sample size for only a single material. The material was selected for exhibiting relatively little rate sensitivity at high speeds; therefore, the differences in velocity profile could be more pronounced with other adhesives. Furthermore, pulse shaper selection was not optimized, which could improve velocity profile consistency between methods. Position tracking noise for DIC-based napkin ring tests could likely be improved by employing larger tracking. Finally, logistical limitations for sample preparation led to bonds which had slightly different widths and thicknesses. The differences were small, and the effects were normalized out as nominal stress and strain; however, an ideal study would consider identical bond geometries, and these differences may have influenced the comparison between methods.

## 17.5 Conclusion

This study investigates the comparability of high-rate tensile failure methods for structural adhesives. Although the deformation modes were nominally the same and tests were designed to subject bonds to the same initial velocity, results indicate that velocity history differed significantly between test methods. Moreover, data indicate that the tensile impact mode suffers from significant compliance in the load train and possible flexure of the puck, leading to low failure stresses and inflated failure strains. Consequently, nominal strength, nominal strain at break, and dissipated energy were all not comparable between methods. Furthermore, data suggest that nominal values in the tensile impact mode are not a good representation of actual strength, strain at break, or dissipated energy. While all methods may be valuable for inverse-method calibration of failure properties, care should be taken when comparing test results between different test methods.

**Acknowledgments** Thank you to Martin Rother and our other fabulous machinists. Thanks as well to our group leader, Sharon Wang, for her leadership.

## References

1. ASTM.: International, *Standard test method for tensile strength of adhesives by means of bar and rod* (2015)
2. Jeandrau, J.P.: Intrinsic mechanical characterization of structural adhesives. Int. J. Adhes. Adhes. **6**(4), 229–231 (1986)
3. Yokoyama, T., Nakai, K.: Determination of the impact tensile strength of structural adhesive butt joints with a modified Split Hopkinson pressure Bar. Int. J. Adhes. Adhes. **56**, 13–23 (2015)
4. Gollins, K., Elvin, N., Delale, F.: Characterization of adhesive joints under high-speed Normal impact: part I – experimental studies. Int. J. Adhes. Adhes. **98**(September 2019), 102529 (2020)
5. Yildiz, S., Andreopoulos, Y., Delale, F., Smail, A.: Adhesively bonded joints under quasi-static and shock-wave loadings. Int. J. Impact Eng. **143**(May), 103613 (2020)
6. Carpenter, S.; "Effects of sample preparation method on Adhesive tensile impact testing", *Annual meeting of the Adhesions society* (2018)
7. Blaber, J., Adair, B., Antoniou, A.: Ncorr: open-source 2D digital image correlation Matlab software. Exp. Mech. **55**(6), 1105–1122 (2015)

# Chapter 18
# Density-Graded 3D Voronoi Cellular Structures for Improved Impact Performance

**Vijendra Gupta, Addis Kidane, and Michael Sutton**

**Abstract** Density-graded cellular polymers have unique mechanical properties, leading to exceptional impact protection. Furthermore, they can be designed for custom requirements. The current study is part of an effort to develop efficient impact-resistant structures. The impact response of density-graded 3D Voronoi cellular structures is studied and compared to its uniform density counterpart. The specimens are fabricated via photopolymer jetting technology, an additive manufacturing technique that enables high accuracy of intricate features and complex shapes that are distinctive of Voronoi cellular structures. The density gradation is achieved by changing the cell size along the impact direction. The foam specimens are impinged by a freely falling rigid mass with the help of a drop tower that allows determining the response at intermediate strain-rate regime. A series of images are captured using a high-speed camera to capture the deformation mechanisms of the specimen, and a piezo-based load cell is used to measure the dynamic force. The performance is analyzed by studying the energy absorption and transmitted force as a function of density gradation. It is found that density-graded Voronoi cellular structures can be designed to mitigate a wide range of impact conditions.

**Keywords** 3D printing · Voronoi cellular structures · Density-graded cellular materials · Impact response · Energy absorption

## 18.1 Introduction

Cellular structures with remarkable engineering properties are commonly found in nature [1]. Exceptional performance can be derived if the key design elements of natural cellular structures are purposefully harnessed. In particular, the density gradation observed in the natural environment can be utilized in engineering structures to obtain superior functionality. As a result, density-graded Voronoi cellular structures (VCSs) that have structural similarities to naturally existing cellular structures have gained tremendous attention. These structures have excellent energy absorption capacity and provide protection from a broad range of impact situations.

There have been numerous studies on VCSs. Theoretical studies [2–5] often model the cellular material as a continuum to simplify and obtain a solution, whereas finite element studies employ either continuum-based [4, 6] or cell-based approaches [3, 7, 8]. Although the cell-based models are complex due to the manifestation of microstructural details, they provide a deep understanding of the deformation mechanisms. Experimental investigations often are performed on layered specimens that comprise a step-wise change in density [8, 9]. In addition to their tedious fabrication, layered specimens have interfaces that are prone to debonding. Cellular materials with gradually varying density eliminate the aforementioned issues. However, manufacturing such structures has been a challenge due to the geometrical complexities associated with compliance to a specified spatial density variation. This impediment can be efficiently tackled by employing additive manufacturing such as photopolymer jetting technology employed in the current study. This 3D printing technique readily addresses the fabrication of complicated parts with elaborate features and enables the production of specimens with continuous changes in properties.

This study investigates the dynamic response of additively manufactured 3D VCSs under low-impact velocities. Uniform density and density-graded specimens are prepared by controlling the local cell size. The specimens are subjected to rigid body impact with the help of a drop tower setup, and their energy absorption performance is analyzed.

V. Gupta (✉) · A. Kidane · M. Sutton
Department of Mechanical Engineering, University of South Carolina, Columbia, SC, USA
e-mail: vijendra@email.sc.edu; kidanea@cec.sc.edu; sutton@sc.edu



S. Mates et al. (eds.), *Dynamic Behavior of Materials, Volume 1*, Conference Proceedings of the Society for Experimental Mechanics Series, https://doi.org/10.1007/978-3-031-17453-7_18

## 18.2 Materials and Methods

Voronoi cells are the building blocks of VCSs. They are convex polyhedrons constructed around randomly generated points that form their cell nuclei. Each Voronoi cell has its corresponding cell nucleus. The nucleus of a particular Voronoi cell is the nearest one to all the points within that cell. The edges of the cell are the common boundaries between the adjacent cells, formed by points that are equidistant to the nearest cell nuclei. Random generation of cell nuclei is performed with a constraint such that every cell nucleus is at least a specified distance ($d_{min}$) away from all other cell nuclei. Thus, the local density can be influenced by the distance $d_{min}$. Uniform density specimens are constructed with a constant $d_{min}$, while the density-graded specimens are prepared by varying $d_{min}$. The VCS model results in large geometrical data that is processed by Python scripting. The solid model is then created and rendered in stereolithography (STL) file format using OpenSCAD, an open-sourced application program. Afterward, printing is carried out on a multi-jet 3D printer, namely, the Stratasys J750. The printer is based on a principle that takes advantage of the sensitivity of certain polymers to light. It prints a photosensitive polymer layer-by-layer that is instantly cured by ultraviolet light. The printed part is cleaned in an alkaline solution before it is completely prepared.

Both the uniform density and density-graded specimens are printed in cylindrical form with a radius of 16 mm and a height of 35 mm. The specimen photographs are shown in Fig. 18.1a. Cell size is roughly kept the same in the uniform specimens, while it is reduced gradually from top to bottom in the graded specimens (as seen in the figure). The specimens are designed such that their average densities are very close for an appropriate comparison. The average density of the uniform specimen and the graded specimen is measured to be 62.8 kg/m$^3$ and 64.4 kg/m$^3$, respectively.

The compressive dynamic response of the 3D-printed specimens is assessed by impacting them with a freely falling rigid mass made of stainless steel. Figure 18.1b shows the schematic of the experimental setup. The rigid mass is guided through a hollow tube mounted on the drop tower frame. The drop height is 9.15 cm, and the rigid mass weighs 0.857 kg. A piezoelectric-based impact load sensor is mounted below the specimen to measure the dynamic force in the specimen. To evenly transfer the load, a 5 mm thick rigid plate is placed in between the specimen and the force sensor. The load data is acquired at 0.25 MHz with the help of an amplifier and an oscilloscope. The strain in the specimen is determined by tracking the rigid mass using digital image correlation (DIC). A contrasting pattern is applied to the falling rigid mass, and its image sequence is captured using a high-speed camera to measure the displacement history. The images are recorded at an interframe time of 0.2 ms.

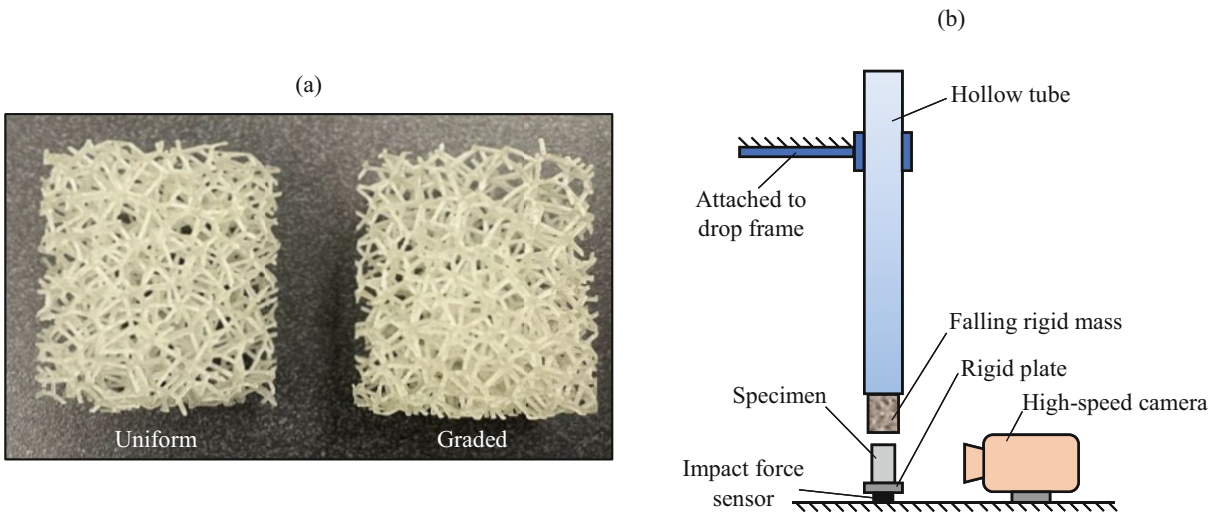


**Fig. 18.1** (**a**) Specimen photographs. (**b**) Schematic of the experimental setup

## 18.3 Results and Discussion

The recorded load data is shown in Fig. 18.2. The noise present in the raw data is removed using the Savitzky-Golay filter [10]. A second-order polynomial and a window size of 201 points, equivalent to 0.8 ms on the time scale, are used for smoothing the data. These settings give adequately smoothed data without losing key features. The raw and smoothed data for the uniform specimen are shown in Fig. 18.2a for reference. The time data is shifted such that the rigid mass strikes the specimen at time $t = 0$. Figure 18.2b shows the force data for both the uniform and the graded specimen. It should be noted that the same smoothing parameters are used for the data of both specimens.

The rigid mass displacement obtained from DIC is depicted in Fig. 18.3. It increases almost linearly with time for both specimens, with the slope of the curves gradually reducing over time as the kinetic energy of the rigid mass is dissipated.

The force and displacement data are normalized using the continuum basis. The nominal stress $\sigma$ is defined as the force per unit cross-sectional area, whereas the nominal strain $\varepsilon$ is defined as the change in length per unit original length. It should be noted that the rigid mass displacement is equal to the change in specimen length. The nominal stress-strain curve is shown in

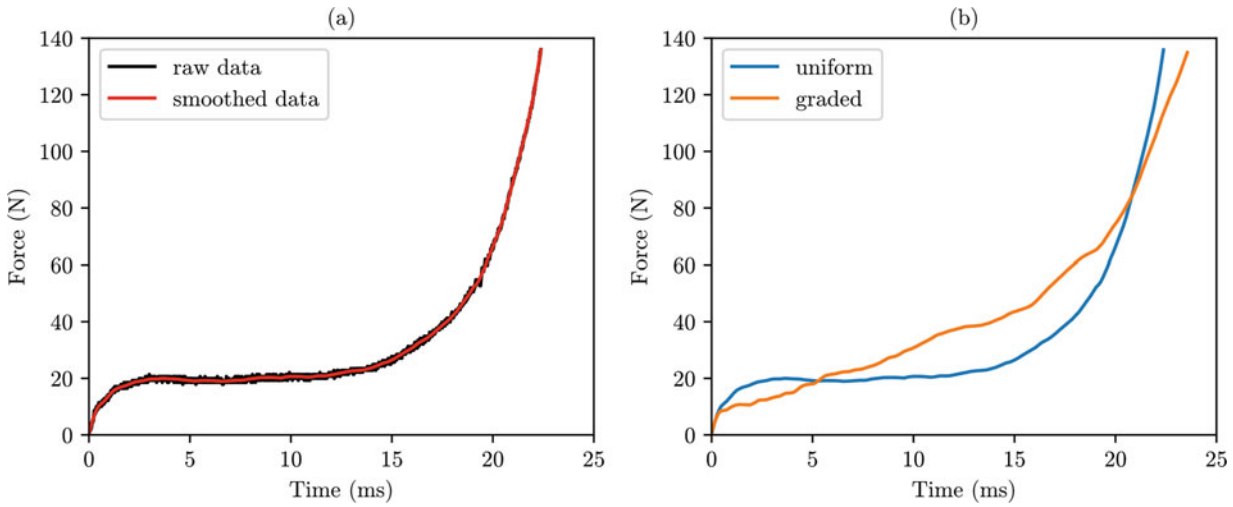


**Fig. 18.2** (**a**) Raw and filtered (smoothed) force data for the uniform specimen (**b**) Force data for both the uniform and graded specimen

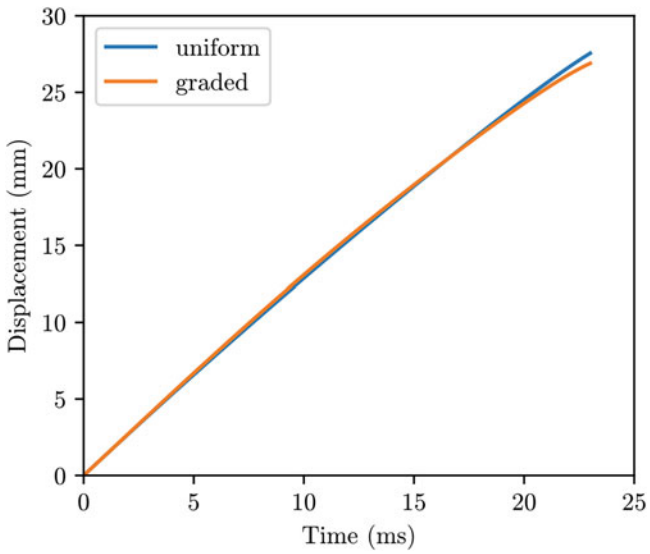


**Fig. 18.3** Displacement histories for both the uniform and graded specimen

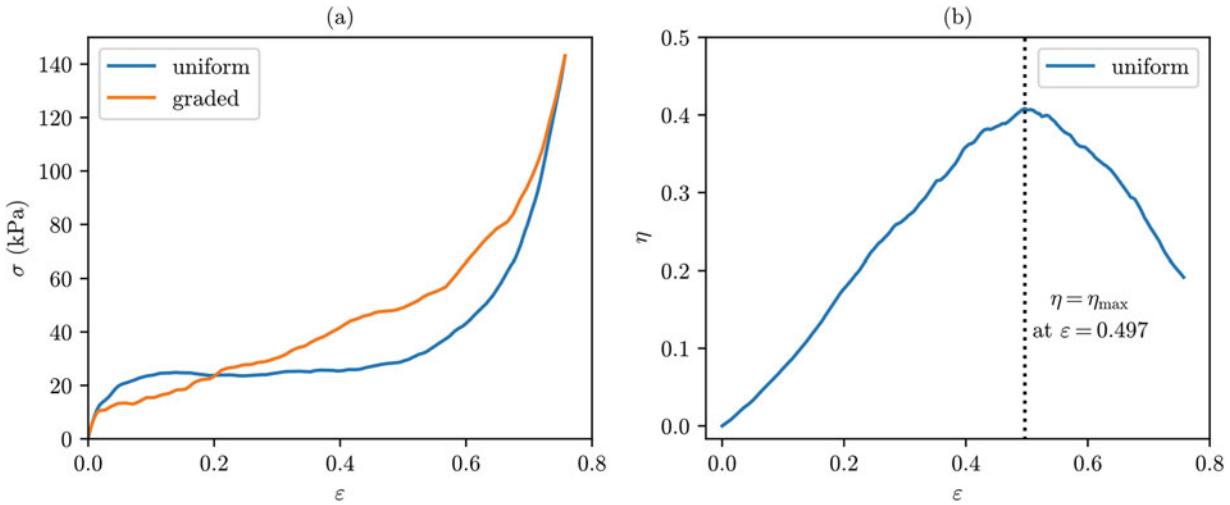


**Fig. 18.4** (**a**) Stress-strain curves (**b**) Efficiency-strain curve for the uniform specimen

Fig. 18.4a. The main difference between the response of uniform and graded specimen is seen in the plateau region. If minor aberrations are ignored, the uniform specimen has a flat plateau. In other words, the stress remains approximately constant stress in the plateau region for the uniform specimen. On the other hand, the graded specimen has a plateau with a positive slope, or the stress steadily increases in the plateau region for the graded specimen. The difference in the behavior is due to the disparity in the cell sizes that make up the specimens. Since the uniform specimen is comprised of similar-sized cells, it crushes at approximately the same stress. However, the graded specimen consists of cells that vary in size. Therefore, the cells successively collapse based on their strength. The larger cells that are weaker collapse at low stress, while the smaller cells collapse at higher stress, thus resulting in a plateau characterized by an increasing slope.

The energy absorbed by the specimen $E$ can be determined by computing the area under the stress-strain curve, and is given by the following equation:

$$E = \int_0^{\varepsilon} \sigma \mathrm{d}\varepsilon \tag{18.1}$$

The energy absorption efficiency $\eta$ defined as the ratio of the energy absorbed and the stress is given as follows.

$$\eta = \frac{E}{\sigma} \tag{18.2}$$

Figure 18.4b shows the plot for the efficiency of the uniform specimen. The densification strain $\varepsilon_{\mathrm{d}}$ can be determined using the maximum efficiency method [11]. According to this method, densification of the specimen occurs when the efficiency reaches its maximum. Therefore, the densification strain is found to be 49.7% for the uniform specimen. The plateau stress $\sigma_{\mathrm{pl}}$ is calculated by Eq. (18.3) once the densification strain is known.

$$\sigma_{\mathrm{pl}} = \frac{1}{\varepsilon_{\mathrm{d}} - \varepsilon_{\mathrm{cr}}} \int_{\varepsilon_{\mathrm{cr}}}^{\varepsilon_{\mathrm{d}}} \sigma \mathrm{d}\varepsilon \tag{18.3}$$

where $\varepsilon_{\mathrm{cr}}$ is the strain at the initial collapse stress. Since $\varepsilon_{\mathrm{cr}}$ is very small, it can be ignored for the calculation of plateau stress. Using numerical integration, the plateau stress is computed to be 23.7 kPa.

Figure 18.5a shows the graph with stress as the abscissa and absorbed energy as the ordinate. A reference line corresponding to the plateau stress of the uniform specimen is also shown in the figure. Below the plateau stress of the uniform specimen, the graded specimen absorbs a higher amount of energy than the uniform specimen. However, around the plateau stress, the energy absorption of the uniform specimen increases dramatically, exceeding that of the graded specimen.

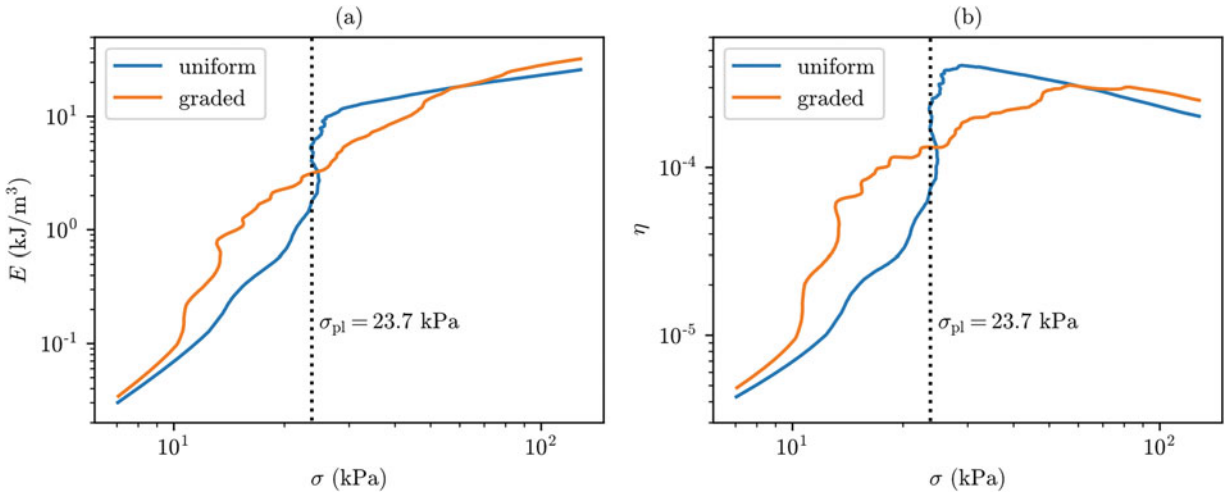


**Fig. 18.5** (**a**) Energy versus stress plot (**b**) Efficiency versus stress plot

At high stress, the graded specimen again surpasses the uniform specimen since the latter can maintain higher energy absorption only up to a certain stress level. For most of the stress spectrum, the graded specimen remains superior. The uniform specimen performs better only in the moderate stress range. Therefore, the graded specimen has better performance for a wide range of energy levels. The plot of efficiency versus stress that shows similar trends is also shown in Fig. 18.5b. A uniform density can be designed to meet an energy requirement that is known with high certainty. However, its performance is poor if there is any variation in the energy input. In practice, the requirements are often known with high uncertainty. Graded specimens remain efficient over a wide range of energy levels, thereby making them more robust and versatile.

## 18.4 Conclusions

Voronoi cellular structures with complicated features are additively manufactured using photopolymer jetting technology, which otherwise is challenging to fabricate using conventional manufacturing approaches. Their energy absorption performance is evaluated using a drop tower setup. It has been shown that the dynamic responses of the uniform-density and density-graded Voronoi cellular specimens are significantly different. The uniform specimen possesses a flat plateau in its stress-strain curve, whereas the graded specimen has a characteristic increasing slope in the plateau region. These distinctive features result in differing energy absorption capabilities. Although the energy absorption of the uniform specimen is optimized for moderate energy input, its performance deteriorates at low and high energy input levels. On the other hand, the graded specimen outperforms at low and high energy inputs, and its performance does not significantly deteriorate at moderate energy inputs. Thus, density-graded Voronoi cellular structures provide all-round energy absorption performance.

**Acknowledgments** The authors are immensely thankful for receiving the funds from the US Army Research Office via grant W911NF-18-1-0023.

## References

1. Gibson, L.J., Ashby, M.F.: Cellular Solids, Second. Cambridge University Press (1997)
2. Gupta, V., Kidane, A., Sutton, M.: Closed-form solution for shock wave propagation in density-graded cellular material under impact. Theor. Appl. Mech. Lett. **11**(5), 100288 (2021). https://doi.org/10.1016/j.taml.2021.100288
3. Wang, X., Zheng, Z., Yu, J.: Crashworthiness design of density-graded cellular metals. Theor. Appl. Mech. Lett. **3**(3), 031001 (2013). https://doi.org/10.1063/2.1303101
4. Shen, C.J., Lu, G., Yu, T.X.: Investigation into the behavior of a graded cellular rod under impact. Int. J. Impact Eng. **74**, 92–106 (2014). https://doi.org/10.1016/j.ijimpeng.2014.02.015

5. Gupta, V., Miller, D., Kidane, A., Sutton, M.: Optimization for Improved Energy Absorption and the Effect of Density Gradation in Cellular Materials, pp. 13–20 (2021). https://doi.org/10.1007/978-3-030-59765-8_4
6. Cui, L., Kiernan, S., Gilchrist, M.D.: Designing the energy absorption capacity of functionally graded foam materials. Mater. Sci. Eng. A. **507**(1–2), 215–225 (2009). https://doi.org/10.1016/j.msea.2008.12.011
7. Zhang, J., Wang, Z., Zhao, L.: Dynamic response of functionally graded cellular materials based on the Voronoi model. Compos. Part B Eng. **85**, 176–187 (2016). https://doi.org/10.1016/j.compositesb.2015.09.045
8. Gupta, V., Miller, D., Kidane, A.: Numerical and Experimental Investigation of Density Graded Foams Subjected to Impact Loading, pp. 31–35 (2020). https://doi.org/10.1007/978-3-030-30021-0_6
9. Miller, D., Gupta, V., Kidane, A.: Dynamic Response of Layered Functionally Graded Polyurethane Foam with Nonlinear Density Variation, pp. 25–30 (2020). https://doi.org/10.1007/978-3-030-30021-0_5
10. Savitzky, A., Golay, M.J.E.: Smoothing and Differentiation of Data by Simplified Least Squares Procedures. ICASSP, IEEE Int. Conf. Acoust. Speech Signal Process. – Proc. **36**(8), 1627–1639 (1964). https://doi.org/10.1109/ICASSP.2000.859059
11. Tan, P.J., Harrigan, J.J., Reid, S.R.: Inertia effects in uniaxial dynamic compression of a closed cell aluminium alloy foam. Mater. Sci. Technol. **18**(5), 480–488 (2002). https://doi.org/10.1179/026708302225002092

# Chapter 19
# Computational Design of a Simple Flyer Plate Launcher


**Brady Aydelotte**

**Abstract** The response of materials to shock loading is important to understand for a variety of applications. When shock physics emerged during and after WWII, direct explosive loading or explosively driven plate impact was the primary tool for these studies. Subsequent decades have seen the widespread use of large caliber guns for plate impact studies, laser-shock facilities, and pulsed power facilities.

INL currently lacks a gun suitable for plate impact or explosives casting and machining facilities; however, it does possess explosives use and handling capabilities. An option for performing plate impact experiments was needed. Therefore, continuum scale models were utilized to explore a few simple donor-acceptor explosive plane wave lens designs, one of which could be hand packed with plastic explosives to launch flyer plates. 2D simulations were performed to study different geometries in an effort to minimize the difference in shock arrival across the central portion of a small copper flyer plate. A shock wave arrival time difference under 50 ns across 50% of the center of the flyer was achieved with a few designs. This work summarizes the computational models and results.

**Keywords** Explosive · Lens · Shock · Flyer · Material characterization

## 19.1 Introduction

Explosives have been widely used to explosively launch flyer plates to perform shock experiments. Various approaches have been developed for doing this. Explosive lenses, precision machined from combinations of different kinds of explosives to yield a flat shock wave, were a common method for explosively driven shock-loading for many years [1, 2]. Variations on that theme have been developed for explosively launching projectiles. Marsh developed and patented a donor-acceptor plane wave lens with a variable thickness flyer to generate a plane wave without explosive machining [3]. Explosive lenses with shaped inserts [4] and even 3D printed explosive plane wave generators [5] have been demonstrated and all show good planarity.

Access to facilities which can machine, cast, or 3D print explosives was lacking, so an alternative was sought. A very simple explosive lens design was required—something which could be fabricated very simply and at low cost but still provide adequate planarity over some central region of the flyer. One design stood out, that of Xiong et al. [6], as a design that did not require complex fabrication operations. An attempt was made to replicate their results, and a few attempts were made with related designs to see if they could be improved.

## 19.2 Method

Initial efforts focused on replicating the results of Xiong et al. [6], and then some excursions were made to explore other designs. All designs considered are donor-acceptor designs where a donor explosive is detonated, resulting in a shock wave, the shock wave is modified in some fashion, and the modified shock wave ignites an acceptor explosive to provide a plane wave which then either directly loads a sample or is used to launch a flyer plate.

To explore these designs, 2D axi-symmetric computational models were constructed using the ALEGRA hydrocode [7] to explore different designs. A uniform Eulerian mesh with a cell size of 0.2 mm was utilized for these computations, and the

B. Aydelotte (✉)
Idaho National Laboratory, Idaho Falls, ID, USA
e-mail: brady.aydelotte@inl.gov



S. Mates et al. (eds.), *Dynamic Behavior of Materials, Volume 1*, Conference Proceedings of the Society for Experimental Mechanics Series, https://doi.org/10.1007/978-3-031-17453-7_19

model was run for 25 microseconds on six or eight processors. Material was allowed to advect through the mesh to address material deformation and vorticity. Material was allowed to flow out of the exterior boundary conditions. The boundary on the center axis allowed no material motion in the x direction, perpendicular to the motion of the shock front in the explosive.

The donor explosive was modeled as Composition B (Comp B) using the Jones-Wilkins-Lee equation of state model [7] and it was ignited using a programmed burn option [7] to initiate detonation at time zero on a line that was equal to the radius of an RP-1 detonator [8], 5.145 mm. The acceptor explosive was also modeled as Composition B using the History Variable Reactive Burn model [7] which detonates when shocked over its pressure threshold.

In some cases, Composition C4 (C4) was used rather than Comp B; Comp B is a castable explosive, but C4 is readily shaped by hand. When C4 was used, the donor portion of the plane wave lens was modeled using the Jones-Wilkins-Lee equation of state model [7] and it was ignited using a programmed burn option [7] to initiate detonation at time zero on a line that was equal to the radius of an RP-1 detonator [8], 5.145 mm. The acceptor explosive was also modeled as Composition C4 using the History Variable Reactive Burn model [7].

The nylon sleeve in the models derived from Xiong et al. [6] was modeled as a simple elastic-plastic material with a yield strength of 40.0 MPa and its pressure-volume response was modeled using the Mie-Grüneisen equation of state [7]. In some models, polymethyl methacrylate (PMMA) components were used instead of nylon. A sesame table was used to model the pressure-volume response of the PMMA and the strength response was modeled using the Mulliken-Boyce polymer model [7].

Where an aluminum ring was used to bridge two explosive components, it was modeled as 6061-T6 aluminum using Johnson-Cook strength and fracture models [9]; the pressure-volume response of the aluminum was modeled using a sesame table.

A 3 mm thick copper flyer plate was added. It was modeled using the Steinberg-Guinan-Lund strength model, a sesame equation of state table, and a simple void growth model to allow for failure when a critical tensile pressure threshold was exceeded.

The regions of the computational domain not occupied by other masses were filled with air, which was modeled using a sesame equation of state. Unless otherwise specified, the parameters for the various models were drawn from the library supplied with the ALEGRA hydrocode.

## 19.3 Results

A model of the plane wave lens reported by Xiong et al. [6] is shown in Fig. 19.1. It produces a reasonably flat shock front. Xiong et al. [6] reported an arrival time difference of 39 ns over 70% of the diameter or 35 mm. In this work, it was found that the arrival time difference in the flyer between the center and 70% of the diameter was 33 ns, which agrees well with the reported value. The arrival time difference in the flyer center at 50% of the diameter was 59 ns. This is somewhat surprising but is simply due to some complex curvature in the shock front. Overall, the flatness of the shock front is very good across the plane wave lens.

A half-scale version of the Xiong et al. [6] plane wave lens was modeled to see if it would scale down to reduce the amount of explosives and still produce a flat shock front. The device was scaled geometrically by ½ except for the nylon tube thickness and detonation region size, which remained the same. Arrival time difference between the center and 50% of the diameter was 18 ns, less than ½ the arrival time difference of the full-scale model, perhaps because of the fixed detonation region size. All of the model results are tabulated in Table 19.1.

Unfortunately, the ½ scale model also predicted that the copper flyer suffered from extensive spall damage, as shown in Fig. 19.2, limiting its utility as a flyer plate launcher.

Other configurations were examined as well. A parameter study was performed using Dakota [10], a toolkit for optimization and uncertainty quantification. The best design that has emerged from that study is shown in Fig. 19.1b, d. Access to facilities for casting explosives was lacking, so C4 was considered an explosive driver due to its ease of fabrication by hand. In this design, C4 was contained within PMMA cups, and the acceptor explosive was kept much smaller than the donor explosive. The cup containing the acceptor explosive had a thicker bottom to reduce spallation in the copper flyer plate and reduce the flyer plate velocity. Rather than using an aluminum ring between the donor and acceptor explosives, a PMMA plug was placed between the donor and acceptor explosives. PMMA has a lower wave speed than C4, slowing the shock from the donor explosive into the acceptor explosive. Fragments from the donor cup break off and fly into the acceptor part of the plane wave generator, igniting the explosive around the plug which, in combination with the retardation of the shock through the PMMA plug, flattens the explosive shock front.

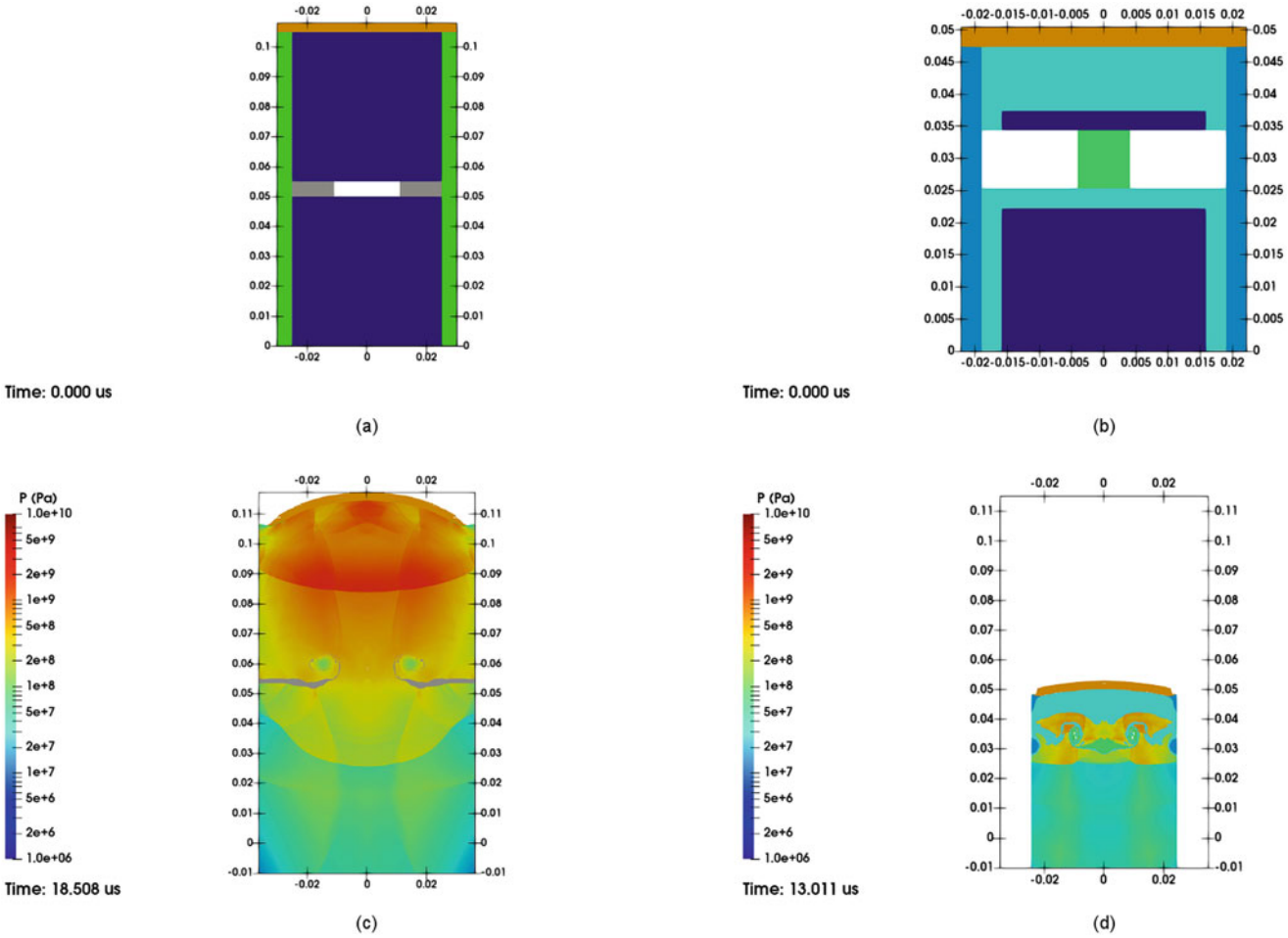


**Fig. 19.1** (**a**) A 2D model of the plane wave lens generator proposed by Xiong et al. [6]. (**b**) An alternative design using C4 explosive. The plastic components are PMMA, and a 3 mm thick flyer plate is used. (**c**) A plot of pressure 5 μs after the shock wave arrived at the copper flyer for the design from Xiong et al. [6]. (**d**) A plot of pressure 5 μs after the shock wave arrived at the copper flyer for the alternative design. Note that the flyer is somewhat flatter than the flyer launched by the plane wave lens generator proposed by Xiong et al. [6]

**Table 19.1** A summary of the difference in arrival time between the center and 50% of the diameter for three different designs

| Design | Arrival time difference at 50% of the diameter |
|---|---|
| Xiong et al. [6] | 59 ns |
| ½ Scale Xiong et al. [6] | 18 ns |
| C4 design | 42 ns |

The design using C4 didn't provide as low an arrival time difference as the half-scale design at 42 ns. The arrival time results are shown in Table 19.1 for reference; however, there is less spall damage to the flyer plate than the half-scale design, as shown in Fig. 19.2. It also yielded a flatter launched flyer plate. The reduced amount of explosive used in the design using C4 propelled the flyer at a lower velocity than either of the other designs discussed here; the time history of the flyer plate velocities of all three designs is shown in Fig. 19.3.

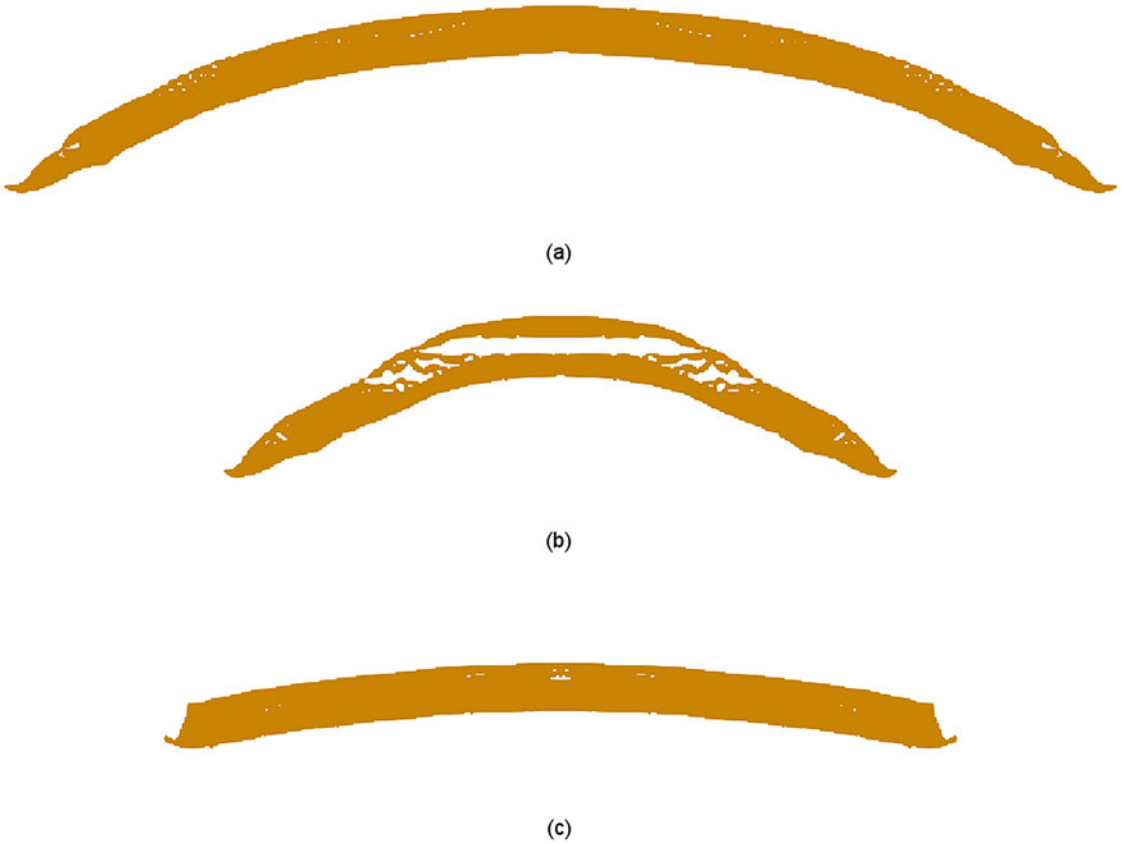


**Fig. 19.2** A comparison of the flyer plates launched by the different designs 5 microseconds after the shock front reached the flyer plate (**a**) Xiong et al. [6] design, (**b**) half-scale version of the design published by Xiong et al. [6] (**c**) and the design shown in Fig. 19.1 at the same scale

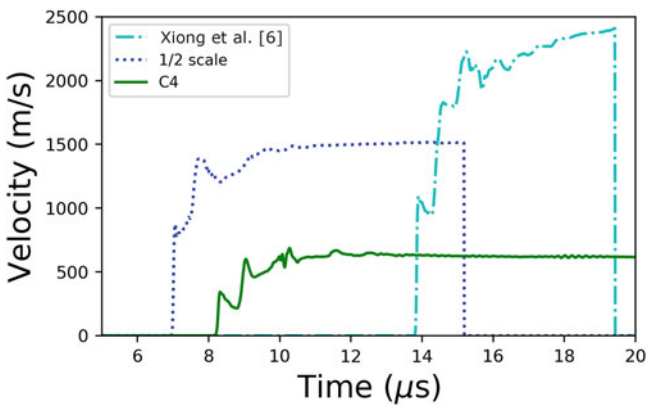


**Fig. 19.3** Velocity of the center of the flyer of each design modeled here. The velocities drop to zero when the flyer moves out of the computational domain

## 19.4 Conclusions

A simple plane wave generator design was sought to launch flyer plates. Several simple plane wave generator designs were examined. The design published by Xiong et al. [6] was modeled and found to produce a flat shock front. A half-scale version of that design was modeled as well and also found to produce a flat shock front. However, neither of these designs proved ideal for launching flyer plates. A third design was explored, and this design utilized a PMMA plug to retard the shock front in conjunction with a thick PMMA plate to reduce flyer plate velocity and damage. The computational model suggested this design would launch the flyer plate at lower velocities than the other two designs and cause less damage than the half-scale design.

**Acknowledgments** The assistance of the ALEGRA software development team at Sandia National Laboratory, particularly John Niederhaus, is gratefully acknowledged. Helpful comments and questions by K. Ryan Bratton (INL) are appreciated. This work was made possible by a grant of time from the Idaho National Laboratory High Performance Computing Center.

## References

1. Marsh, S.P. (ed.): LASL Shock Hugoniot Data. University of California Press, Berkely and Los Angeles, California (1980)
2. Brown, E.N., Borovina, D.L.: The trinity high-explosive implosion system: the Foundation for Precision Explosive Applications. Nucl. Technol. **207**(sup1), S204–S221 (2021). https://doi.org/10.1080/00295450.2021.1913954
3. S. P. Marsh, 'Explosive plane-wave lens', Art. no. US 4729318; A, 1988., Accessed 8 Feb 2022. [Online]. Available: https://www.osti.gov/doepatents/biblio/7165218-explosive-plane-wave-lens
4. Fritz, J.N.: 'A simple plane-wave explosive lens', Los Alamos National Lab., NM (USA), LA-11956-MS (1990). https://doi.org/10.2172/6430373
5. Lichthardt, J.P., Tappan, B.C., Bowden, P.R., Olinger, M.W., McDonald, D.L.: A simple 3D printed plane wave explosive lens based on Fritz parameters. AIP Conf. Proc. **2272**(1), 030018 (2020). https://doi.org/10.1063/12.0000892
6. Xiong, W., Zhang, X., Guan, Z., He, Y., Qiao, L., Guo, L.: Study of simple plane wave generator with an air-metal barrier. Def. Technol. **10**(2), 190–197 (2014). https://doi.org/10.1016/j.dt.2014.05.012
7. T. J. Fuller et al., "ALEGRA User Manual," Sandia National Laboratory, Albuquerque, NM, SAND2020-xxxx, 2021
8. RP-1 EBW Detonator. Teledyne Defense Electronics. Accessed 15 Feb 2022. [Online]. Available: https://www.teledynedefenseelectronics.com/energetics/Documents/page20.pdf
9. Johnson, G.R., Holmquist, T.J.: Test Data and Computational Strength and Fracture Model Constants for 23 Materials Subjected to Large Strains, High Strain Rates, and High Temperatures. Los Alamos National Lab, Technical LA-11463-MS, Los Alamos, NM (1989)
10. Adams, B., et al.: Dakota, A Multilevel Parallel Object-Oriented Framework for Design Optimization, Parameter Estimation, Uncertainty Quantification, and Sensitivity Analysis: Version 6.13 User's Manual. Sandia National Lab. (SNL-NM), SAND2020-12495, Albuquerque, NM (2020). https://doi.org/10.2172/1817318

# Chapter 20
# Through-Thickness Stress Wave Propagation, Delamination, and Damage in a Woven Composite

**Christopher S. Meyer, Bazle Z. Haque, and John W. Gillespie Jr**

**Abstract** At the earliest timescale after projectile impact on woven composites, stress waves propagate out from the area of impact both radially and through the thickness. At a later timescale, momentum transfer leads to the formation of a deformation cone. Studies of wave propagation in composites typically consider the radial stress wave propagation and the formation of the transverse deformation cone but neglect through-thickness stress waves. This chapter investigates the effects of through-thickness stress wave propagation on damage and delamination under a projectile in a woven composite. This investigation uses a mesoscale model of plain weave composite, validated using 1D stress wave theory. This model uses a cohesive traction-separation law to simulate delamination cracking, inelastic progressive damage composite tows, and rate-dependent matrix. The 1D stress wave theory is generalized for any number of layers. A finite element modeling approach is validated using the generalized 1D theory.

**Keywords** Dynamic · Impact · Cohesive · Mesoscale

## 20.1 Introduction

Consider high-velocity (~100–500 m/s), blunt projectile impact on a thin, plain weave glass/epoxy composite [1–3]. At the earliest timescale following this impact, stress waves propagate out from the impact location [3]. These stress waves propagate out from the area of impact radially and through the thickness. Later in time, a deformation cone wave forms as momentum transfers from the projectile to the target [4, 5].

Studies of wave propagation in woven composites typically consider radial stress wave propagation but neglect through-thickness stress waves (e.g., [4–7]). Plain weave composites include a mesoscale architecture of undulating glass fiber tows infiltrated with epoxy matrix. The mesoscale is defined as the length scale of a tow (or yarn) cross-section, as shown in Fig. 20.1. Stress waves are attenuated in fiber composites by geometric wave dispersion, which occurs when the waves interact with fiber-matrix interfaces at the microscale [8]. The microscale is defined as the length scale of a fiber diameter. Most analyses consider continuum composites and neglect geometric dispersion at lower length scales. If we consider wavelengths that are much larger than the fiber diameter, we can neglect microscale dispersion and treat discrete fiber-matrix microstructure as a continuum (see Fig. 20.1). Then we can study the effects of dispersion due to mesoscale geometry with continuum tows and matrix.

To study the through-thickness stress wave propagation in a woven composite, this chapter uses a mesoscale model of a single-layer plain weave glass/epoxy composite. The fibers and matrix in a tow are modeled as a continuum unidirectional material with properties aligned according to the undulation of the tows and the fiber direction. This chapter is primarily concerned with developing and validating the model relative to the one-dimensional (1D) stress wave propagation theory.

C. S. Meyer (✉)
U.S. Army Combat Capabilities Development Command Army Research Laboratory, Aberdeen Proving Ground, Aberdeen, MD, USA

Center for Composite Materials, University of Delaware, Newark, DE, USA
e-mail: csmeyer@udel.edu

B. Z. Haque · J. W. Gillespie Jr
Center for Composite Materials, University of Delaware, Newark, DE, USA



S. Mates et al. (eds.), *Dynamic Behavior of Materials, Volume 1*, Conference Proceedings of the Society for Experimental Mechanics Series, https://doi.org/10.1007/978-3-031-17453-7_20

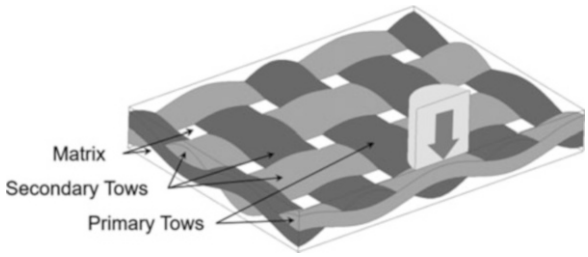


**Fig. 20.1** Schematic of a single-layer plain weave fabric composite (matrix fill shown outlined) under impact by a right circular cylindrical projectile. Here, the projectile diameter is similarly scaled to the tow width

**Table 20.1** Elastic material properties for (**a**) unidirectional S-2 glass/epoxy composite, (**b**) epoxy, and (**c**) steel projectile

| (a) Composite | | | |
|---|---|---|---|
| Density | $\rho_c$ | 1.76 | g/cm$^3$ |
| Coefficient of thermal expansion | $CTE$ | 30 | $10^{-6}$ C$^{-1}$ |
| Elastic modulus | $E_{11}$ | 55.3 | GPa |
| | $E_{22}$ | 11.8 | GPa |
| | $E_{33}$ | 11.8 | GPa |
| Wave velocity | $c_{11}$ | 5605 | m/s |
| | $c_{33}$ | 2591 | m/s |
| (b) Epoxy | | | |
| Density | $\rho_M$ | 1.14 | g/cm$^3$ |
| Coefficient of thermal expansion | $CTE$ | 30 | $10^{-6}$ C$^{-1}$ |
| Elastic modulus | $E_M$ | 2.48 | GPa |
| Wave velocity | $c_M$ | 1475 | m/s |
| (c) Steel | | | |
| Density | $\rho_P$ | 7.85 | g/cm$^3$ |
| Elastic modulus | $E_P$ | 210 | GPa |
| Wave velocity | $c_P$ | 5172 | m/s |

## 20.2 1D Stress Wave Theory

Stress waves move through a material at a velocity equal to the speed of sound in the material. The longitudinal speed of sound, $c_{Li}$, in a material, $i$, is given by Eq. (20.1), where $\rho_i$ is the density and $E_{Li}$ is the longitudinal elastic modulus of the material. Wave speeds of the materials of interest in this work are presented in Table 20.1.

$$c_{L_i} = \sqrt{\frac{E_{Li}}{\rho_i}}, i = 1,2,3\ldots \tag{20.1}$$

When a projectile impacts a target with velocity $V_I$, shown schematically in Fig. 20.2, a longitudinal compressive stress wave of constant cross-section $A$ travels out from the interface between projectile and target. Assuming materials remain in contact at the boundaries, then stress $\sigma_i$ and particle velocity $\dot{u}_j$ are continuous across the boundary, as in Eqs. (20.2) and (20.3). Here $j = I, R, T$ represent the incident, reflected, and transmitted portions, and $\dot{u}$ is the time derivative of displacement.

$$\sigma_I(z,t) + \sigma_R(z,t) = \sigma_T(z,t) \tag{20.2}$$

$$\dot{u}_I(z,t) + \dot{u}_R(z,t) = \dot{u}_T(z,t) \tag{20.3}$$

Momentum is also conserved across the boundary. For a segment $dz$, the impulse is equal to the change in momentum in Eq. (20.4). Then, for this 1D (longitudinal) system, $\sigma = F/A$ and $m = \rho Az$ gives Eq. (20.5). Finally, the longitudinal speed of sound in the material is given by $c_L = dz/dt$ so that the uniaxial stress in the material is given by Eq. (20.6) [9].

$$F\,dt = d(m\dot{u}) \tag{20.4}$$

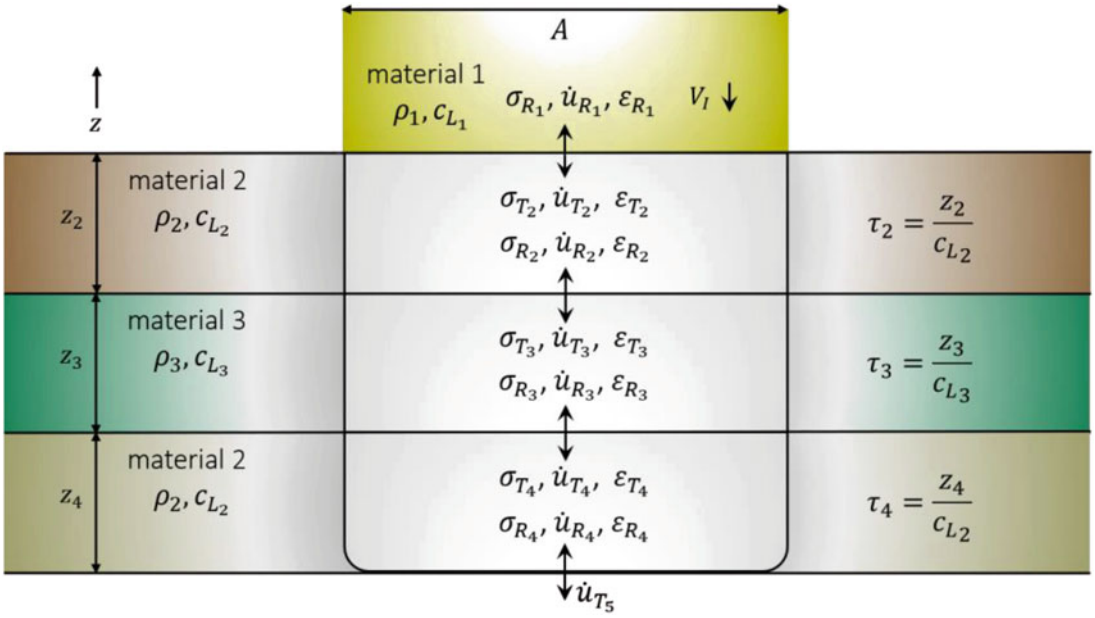


**Fig. 20.2** 1D wave propagation mechanics for a projectile impacting multilayered materials

$$\sigma = \rho \frac{dz}{dt} \dot{u} \tag{20.5}$$

$$\sigma = \rho c_L \dot{u} \tag{20.6}$$

Impedance is defined as a material's density times the sound speed in the material. If the impedance of a layer is greater than the impedance of a subsequent, neighboring layer, i.e., $\rho_i c_{Li} > \rho_{i+1} c_{Li+1}$, compressive stress will reflect as tension (i.e., sign change).

Consider the interface between the projectile, $i = 1$, and target, $i = 2$, in Fig. 20.2. From Eq. (20.6), relationships are found for the incident, reflected, and transmitted portions of the stress wave, given in Eq. (20.7). The stress transmitted into a given layer is the same as the stress incident upon the next layer. Plugging Eq. (20.7) into Eq. (20.3) and solving the resulting Eq. simultaneously with Eq. (20.2) gives Eq. (20.8).

$$\dot{u}_I = \frac{\sigma_I}{\rho_1 c_{L1}}, \; \dot{u}_R = \frac{\sigma_R}{\rho_1 c_{L1}}, \; \dot{u}_T = \frac{\sigma_T}{\rho_2 c_{L2}} \tag{20.7}$$

$$\frac{\sigma_T}{\sigma_I} = \frac{2\rho_2 c_{L2}}{\rho_1 c_{L1} + \rho_2 c_{L2}}, \; \frac{\sigma_R}{\sigma_I} = \frac{\rho_2 c_{L2} - \rho_1 c_{L1}}{\rho_1 c_{L1} + \rho_2 c_{L2}} \tag{20.8}$$

The assumption of continuity of displacement across the boundary (for constant area $A$, at time $t$) gives Eq. (20.9). Continuity of particle velocity gives Eq. (20.10). Simultaneously solving Eqs. (20.9) and (20.10) and using Eq. (20.6) gives Eq. (20.11), which is the stress in the first layer of the target, $i = 2$, following impact by the projectile, $i = 1$, at velocity $V_I$. It can be shown [3] that the stress in any subsequent layer of the target, 3,4,5,..., is given by Eqs. (20.11) and (20.12). Similarly, particle velocity may be found for any subsequent layer using Eqs. (20.6), (20.11), and (20.12). Strain in any layer may be found according to $\varepsilon_i = \dot{u}_{Ti}/c_{Li}$. Finally, the characteristic time for a stress wave to propagate across any layer is given by $\tau_i = z_i/c_{Li}$.

$$\rho_1 c_{L1} \dot{u}_{I1} = \rho_2 c_{L2} \dot{u}_{T2} \tag{20.9}$$

$$V_I - \dot{u}_{I1} = \dot{u}_{T2} \tag{20.10}$$

$$\sigma_{T2} = \frac{\rho_2 c_{L2} V_I}{1 + \frac{\rho_2 c_{L2}}{\rho_1 c_{L1}}} \tag{20.11}$$

$$\sigma_{Tk} = \frac{2\rho_k c_{Lk}}{\rho_{k-1} c_{Lk-1} + \rho_k c_{Lk}} \cdot \sigma_{Tk-1},\ k = 3,4,5,\ldots \tag{20.12}$$

## 20.3 Finite Element Models

The stress according to the 1D theory was generalized here for any number of target layers. However, there are limitations that should be considered. First, Eqs. (20.11) and (20.12) assume linear elastic response of the projectile and specimen, which is approximately correct only for low impact velocities. Second, for the response to be 1D, the projectile and target must have the same area $A$, or there will be edge effects, and Poisson effects must be neglected. Third, the assumptions of continuity and conservation of momentum across the boundaries must remain valid, so the 1D theory becomes invalid once fracture or delamination occurs. Finally, there are two limiting times. The characteristic time for the compressive wave to traverse the projectile is the first, so the projectile must be thick enough that the stress wave crosses the target before the projectile. Similarly, for a multilayered analysis, once the compressive wave returns to the impact face of the first layer, undesirable reverberations begin. For these reasons, validation involves a 1D finite element model, neglecting Poisson effects, impacted at 100 m/s (see [1]), and considers early time, before any delamination may occur and before undesirable reverberations begin. Once the finite element model is shown to produce a similar response to that predicted by the 1D theory, these requirements will be relaxed and the 1D finite element model will be extended to 3D.

The geometry of a representative volume element (RVE) of a plain weave fabric composite is shown in Fig. 20.3a. Figure 20.3b shows a mesoscale model of an RVE with dimensions given in Fig. 20.3c. The mesoscale model violates the 1D theory for two reasons. First, thin epoxy layers will lead to wave reverberations, which cause the continuity assumption to break down. Also, interfaces with impedance mismatch cause wave reflections and sign change as described earlier. Second,

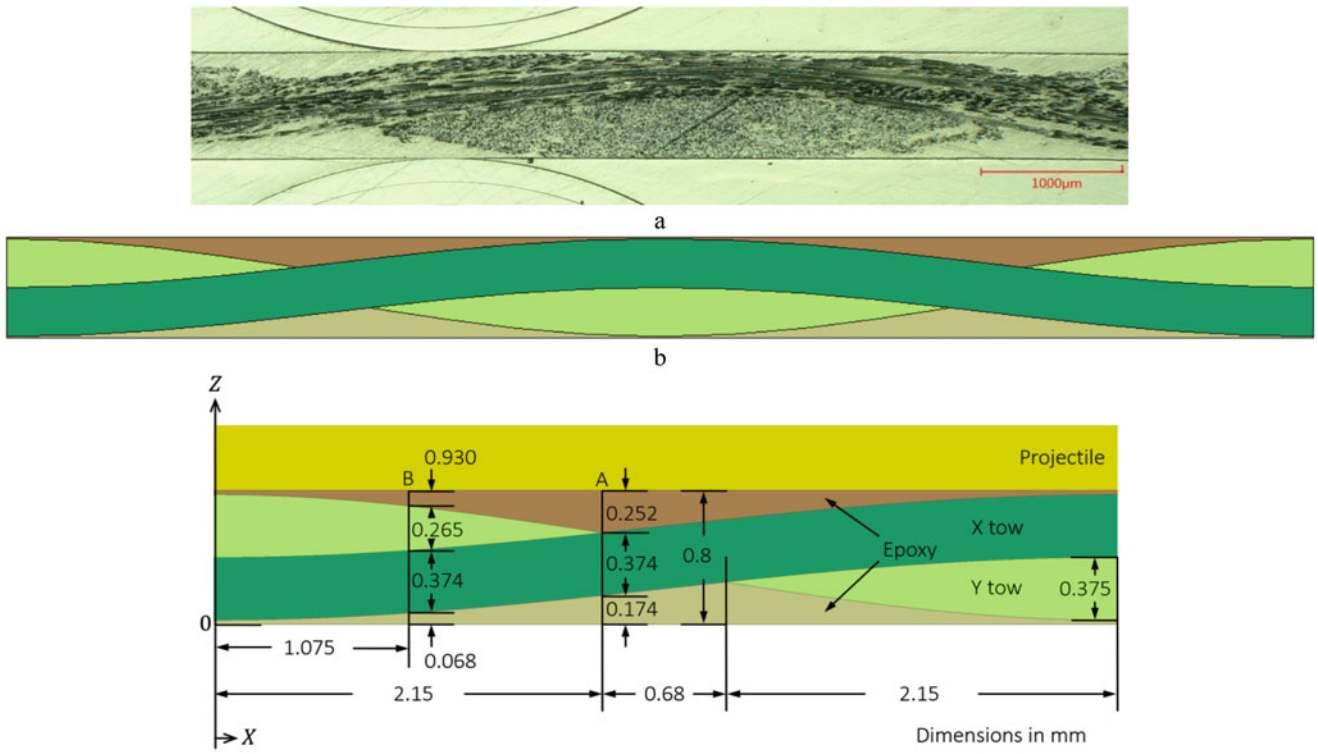


**Fig. 20.3** Mesoscale plain weave fabric composite architecture in (**a**) micrograph and (**b**) finite element model with (**c**) dimensions

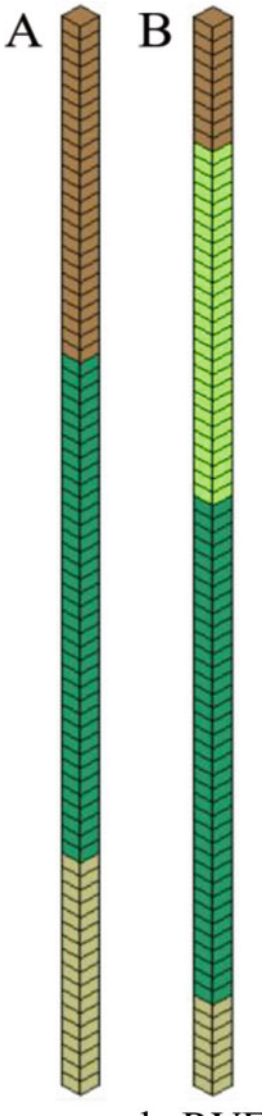


**Fig. 20.4** 1D finite element models for the lines in the mesoscale RVE at positions A and B. Colors follow from Fig. 20.3, where light/dark brown are epoxy and light/dark green are composite tows

the curvature of the layers violates the requirement of constant longitudinal cross-sectional area. However, it is reasonable to expect that if the model is well-behaved and valid for the 1D response, then the 3D response will also be well-behaved and valid. Therefore, initially, two lines are taken from the mesoscale model for validation by the 1D theory. These lines are indicated in Fig. 20.3c as A and B. Two 1D finite element models (FEMs) were developed for these two positions. These 1D FEMs are shown in Fig. 20.4. These 1D models have 80 elements of 0.01 mm in the through-thickness dimension by 0.02 mm in each of the lateral dimensions.

In all models, unless otherwise indicated, the length of the projectile was 5.6 mm. The limiting time for all validation simulations was therefore $5.6 \times 10^{-3}$ m ÷ 5172 m/s = 1.08 μs. Validation simulations were ended before this time, before the stress wave in the projectile reached the back face of the projectile. The lateral dimensions of the projectile were the same as the target model, so there were no edge effects, which will be investigated later.

The second limiting time is when stress waves begin to reverberate within any layer of the target. Stress waves will begin to reverberate in the first layer (epoxy) of the 1D model A at a time of $2 \times 0.252 \times 10^{-3}$ m ÷1475 m/s = 0.34 μs. This time is sufficient for the stress wave to have propagated into the third layer, meaning the stress in each layer may be compared to the 1D theory without concern.

Stress waves will begin to reverberate in the first layer (epoxy) of the 1D model B at a time of $2 \times 0.093 \times 10^{-3}$ m ÷1475 m/s = 0.13 μs. This time is not sufficient for the stress wave to have propagated into the third or fourth layers of 1D model B; therefore, some error is expected when comparing the stress in these layers with the 1D theory.

Since the composite impedance is greater than the epoxy, stress waves will reflect at composite-epoxy interfaces and change signs (compression to tension). However, validation considers only the wavefront of the compressive wave as it passes through the layers, and does not investigate wave reflections or reverberations.

Semi-infinite boundary conditions were used on four sides in 1D simulations. Symmetry boundary conditions were used on two faces of the one-quarter symmetry 3D model, and semi-infinite boundary conditions were used on the remaining two faces. Hence, stress waves do not reflect at model boundaries (only at material interfaces). The top of the projectile and bottom of the target were free, and contact was set between projectile and target.

Single integration point hexahedral elements were used in all simulations. Stress is computed by LS-DYNA at the integration point at the element center, and particle velocity is computed at the nodes. To compare with the 1D theory at a given time, the model elements are interrogated for stress, and model nodes are interrogated for velocity. Thus, some error is expected when comparing the stress and particle velocity with the 1D theory, which does not consider discretized geometry.

To eliminate the possibility of Poisson effects, the 1D model simulations set all Poisson's ratios to zero. In all models, the fiber tows were treated as a unidirectional continuum composite material. In 3D mesoscale models (e.g., Fig. 20.3), the material properties are oriented to follow the undulation of the tows. Taking stiffness, for example, $E_{11}$ follows the tow undulation along the length, $E_{22}$ across the width, and $E_{33}$ through the thickness. In the 1D model simulations, the through-thickness properties were important for comparison with the 1D theory, and material properties were oriented along the 1D lines indicated in Fig. 20.3c (i.e., A and B). In reality, the through-thickness properties will have some orientation bias, but assuming no bias in 1D FEMs facilitates comparison with the 1D theory in which bias is not possible.

Simulations were conducted using LS-DYNA [10]. Elastic material properties and models were described earlier. Inelastic, rate-dependent material properties for all models were taken from the literature as follows. Unidirectional S-2 glass, epoxy composite materials were modeled with MAT_162 (MAT_COMPOSITE_MSC_DMG) [11, 12] with properties given in Table 20.2 [1, 12, 13].

Layers of SC-15 epoxy were modeled with the rate-dependent MAT_003 (MAT_PLASTIC_KINEMATIC). This model accounts for strain rate with a Cowper-Symonds power law, strain hardening constitutive relation as given in Eq. (20.13). In Eq. (20.13), yield stress, $\sigma_0$, is scaled by a function of strain rate, $\dot{\varepsilon}$, and two material constants, $C$ and $p$. Parameters for the epoxy model were determined by Pankow et al. [14] and are given in Table 20.3.

A cohesive zone modeling approach for delamination used tiebreak contact (option 9) in LS-DYNA (CONTACT_AUTOMATIC_ONE_WAY_SURFACE_TO_SURFACE_TIEBREAK). The cohesive model traction-separation properties are based on the work of Carpenter et al. [15], and are provided in Table 20.4.

$$\sigma(\dot{\varepsilon}) = \sigma_0 + \sigma_0 \left( \frac{\dot{\varepsilon}}{C} \right)^{\frac{1}{p}} \tag{20.13}$$

**Table 20.2** Composite material model parameters for MAT_162 [1, 12, 13]

| $E_{11}$, GPa | $E_{22}$, GPa | $E_{33}$, GPa | $\nu_{21}$ | $\nu_{31}$ | $\nu_{32}$ | $G_{12}$, GPa | $G_{23}$, GPa | $G_{31}$, GPa |
|---|---|---|---|---|---|---|---|---|
| 55.3 | 11.8 | 11.8 | 0.05 | 0.05 | 0.45 | 4.3 | 3.7 | 4.3 |
| ρ, g/cm$^3$ | $X_{1T}$, MPa | $X_{1C}$, MPa | $X_{2T}$, MPa | $X_{2C}$, MPa | $X_{3T}$, MPa | $S_{FC}$, MPa | $S_{FS}$, MPa | $S_{12}$, MPa |
| 1.76 | 1380 | 770 | 45 | 137 | 45 | 850 | 250 | 76 |
| $S_{23}$, MPa | $S_{31}$, MPa | SFFC | PHIC | E_LIMIT | S_DELM | OMGMX | ECRSH | EEXPN |
| 38 | 76 | 0.1 | 10 | 0.2 | 1.2 | 0.999 | 0.005 | 2 |
| AM1 | AM2 | AM3 | AM4 | $C_{rate1}$ | $C_{rate2}$ | $C_{rate3}$ | $C_{rate4}$ | |
| 100 | 10 | 1.0 | 0.1 | 0.03 | 0 | 0.03 | 0.03 | |

**Table 20.3** Matrix properties for SC-15 for MAT_003 [14]

| | |
|---|---|
| Density | 1.14 g/cm$^3$ |
| Modulus | 2.48 GPa |
| Poisson's ratio | 0.36 |
| Yield stress, $\sigma_0$ | 48.3 MPa |
| $C$ | 4880 |
| $p$ | 2.883 |

**Table 20.4** Traction-separation law used for tow-tow delamination [15]

| $\dot{\epsilon}$ | 1 $s^{-1}$ |
|---|---|
| $EN$ | 520,000 MPa/mm |
| $ES$ | 1,000,000 MPa/mm |
| $T_I$ | 52 MPa |
| $T_{II}$ | 100 MPa |
| $G_{Ic}$ | 0.0026 MPa-mm |
| $G_{IIc}$ | 0.0050 MPa-mm |

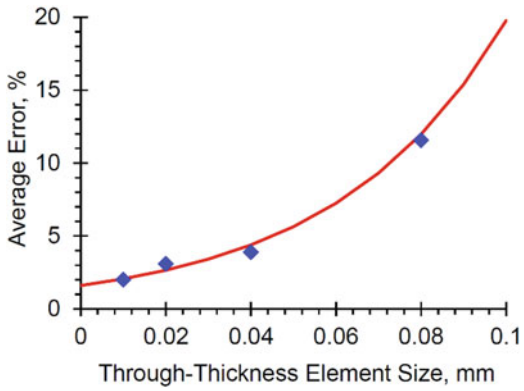


**Fig. 20.5** Results of the mesh convergence study on 1D models

## 20.4 Mesh Convergence Study

A mesh convergence study was conducted with 1D FEMs for line A in Fig. 20.3c. Models investigated element through-thickness sizes of 0.01 mm, 0.02 mm, 0.04 mm, 0.08 mm, and ≥ 0.16 mm (i.e., a single element through the thickness in each layer). Lateral element sizes of 0.016 mm were maintained for all models since only the through-thickness response is of interest here. To accurately model stress wave propagation, it is important that the stress wave does not cross one or more elements per time step, or the wave could be attenuated by stress averaging across elements. The speed of sound in the composite through-thickness layers is 2591 m/s, so considering the 0.01 mm element size, a maximum time step of ~$10^{-9}$ s was ensured for all simulations.

Each 1D FEM was impacted at $V_I = 100$ m/s, layers were perfectly bonded (i.e., layers shared nodes at each boundary, "node merged"), and elastic response was modeled and compared with the 1D theory. The stress and particle velocity produced in each of the three layers by the stress wave propagation were determined. The percent error was calculated as Error (%) = 100 × |(1D Theory Result-1D FEM Result)/(1D Theory Result)|. This error was averaged for each of the six data points (discussed later) for each of the five mesh size models. The results of the mesh convergence study are plotted in Fig. 20.5. Note that the results for the coarsest mesh, the 0.16 mm element model, are not shown since they are far off the chart (>90% error). The results in Fig. 20.5 show convergence to about 2% average error as element size decreases, so a through-thickness element size of about 0.01 mm was used for all subsequent simulations (3,335,084 elements). Smaller elements were not investigated as they could decrease the time step and thereby increase the computational cost of the simulations. Due to the short time scale of interest (~1 μs), simulations with 0.01 mm element thickness were not overly computationally expensive, so this element size is acceptable.

## 20.5 Model Validation

For an impact velocity of $V_I = 100$ m/s, the particle velocity, $\dot{u}$, and stress, $\sigma$, according to the generalized 1D theory in Eqs. (20.6), (20.11), and (20.12) were computed for each layer of 1D finite element models A and B and compared with the simulation results. Recall that stress is computed at element integration points (typically at the centroid), and velocity is computed at the nodes. As the wavefront passed through elements or nodes in each layer, these elements/nodes were interrogated and the output from at least three elements/nodes was averaged to determine stress or particle velocity at the wavefront. In general, validation simulations consider elastic material behavior since the 1D theory can only consider elastic behavior.

**Table 20.5** Comparison of results from 1D theory and 1D FEM for line A. Impact velocity 100 m/s. The model uses elastic material behavior with note-merged or cohesive zone interfaces

| | | | | Node-merged | | Cohesive zones | | | Node-merged | | Cohesive zones | |
|---|---|---|---|---|---|---|---|---|---|---|---|---|
| Layer | Thick, *mm* | $\tau$, *μs* | 1D theory $\dot{u}$, *m/s* | 1D FEM $\dot{u}$, *m/s* | Err, % | 1D FEM $\dot{u}$, *m/s* | Err, % | 1D Thry $\sigma$, *MPa* | 1D FEM $\sigma$, *MPa* | Err, % | 1D FEM $\sigma$, *MPa* | Err, % |
| Epoxy | 0.252 | 0.18 | 96.0 | 95.8 | 0.2 | 96.0 | 0.01 | 161.5 | 164.0 | 1.6 | 164.0 | 1.6 |
| Comp. | 0.374 | 0.32 | 51.8 | 53.5 | 3.3 | 53.5 | 3.3 | 235.9 | 238.8 | 1.2 | 238.8 | 1.2 |
| Epoxy | 0.174 | 0.43 | 75.6 | 77.3 | 2.2 | 77.3 | 2.1 | 127.2 | 131.6 | 3.5 | 131.6 | 3.5 |

**Table 20.6** Comparison of results from 1D theory and 1D FEM for line B. Impact velocity 100 m/s. The model uses elastic material behavior with note-merged or cohesive zone interfaces

| | | | | Node-merged | | Cohesive zones | | | Node-merged | | Cohesive zones | |
|---|---|---|---|---|---|---|---|---|---|---|---|---|
| Layer | Thick, *mm* | $\tau$, *μs* | 1D Thry $\dot{u}$, *m/s* | 1D FEM $\dot{u}$, *m/s* | Err, % | 1D FEM $\dot{u}$, *m/s* | Err, % | 1D Thry $\sigma$, *MPa* | 1D FEM $\sigma$, *MPa* | Err, % | 1D FEM $\sigma$, *MPa* | Err, % |
| Epoxy | 0.093 | 0.06 | 96.0 | 96.0 | 0.01 | 96.0 | 0.02 | 161.5 | 163.9 | 1.5 | 163.9 | 1.5 |
| Comp. | 0.265 | 0.17 | 51.8 | 53.2 | 2.7 | 53.0 | 2.4 | 235.9 | 238.5 | 1.1 | 238.4 | 1.1 |
| Comp. | 0.374 | 0.31 | 51.8 | 53.3 | 2.9 | 53.2 | 2.8 | 235.9 | 238.9 | 1.3 | 238.6 | 1.2 |
| Epoxy | 0.068 | 0.36 | 75.6 | 77.3 | 2.2 | 77.0 | 1.8 | 127.2 | 127.5 | 0.2 | 127.6 | 0.3 |

Since the tiebreak cohesive approach will be used in the 3D models to investigate delamination, tiebreak contact is introduced between layers in the 1D model to ensure it does not introduce any numerical error. Simulations were conducted with interlayer nodes merged (contact cannot be broken) and with interlayer cohesion (tied contact can be broken, but validation simulations are stopped before any separation occurs). Note that the zero-thickness cohesive approach in tiebreak contact does not have integration points, but constitutive behavior involves traction-separation rather than stress-strain.

The results for 1D model A are provided in Table 20.5. The results for 1D model B are provided in Table 20.6. In both tables, the time, $\tau$, at which the stress wave will have crossed each layer, is provided. The stress wave propagation in the 1D models is illustrated by Fig. 20.6 for model A and Fig. 20.7 for model B. Later in time, the wave reverberations become difficult to track, as seen in Fig. 20.7 after 0.42 μs.

The results show very little error for the 1D finite element models compared with the 1D theory. Error is generally less than about 3%. As discussed earlier, sources of discrepancy can include wave reverberations at a later time and computation of stress at integration points at the center of elements rather than nodes. Note that validation simulations do not continue to the point of decohesion.

## 20.6 Comparing 3D Model to 1D Theory

The through-thickness stress wave modeling approach was validated by demonstrating that the 1D finite element model responses match the 1D theory with very little error. To investigate early timescale damage in a woven composite, we must relax the requirements described earlier for the 1D theory comparison. Namely, we enable nonlinear, inelastic, and strain-rate-dependent material behavior and interfacial cohesive failure, and we consider a realistic projectile. A 3D model is shown in Fig. 20.8.

Considering inelastic material behavior and tiebreak contact, the particle velocity is determined along lines A and B from Fig. 20.3, but rather than using the 1D models in Fig. 20.4, now using the 3D models in Fig. 20.8. Note that Lines A and B are sufficiently far from the projectile edge (Fig. 20.8) so that particle velocity results are not affected by projectile edge effects. As before, two interfacial conditions are considered: node-merged (unbreakable interface) and cohesive zones (breakable interface). The particle velocities are compared to the 1D theory predictions from Eqs. (20.6), (20.11), and (20.12). Table 20.7 provides this comparison for line A, and Table 20.8 provides this comparison for line B.

As expected, the inclusion of 3D geometry, inelastic material behavior, and cohesive interfaces all increase difference from the 1D theory. Despite this, the 3D finite element model results are very close to the 1D theory, and these results provide confidence in the model predictions. This is because of the assumption of linear elastic behavior, which is approximately true for this low impact velocity of 100 m/s. Later investigations will consider impact velocities nearer to and above the ballistic limit velocity.

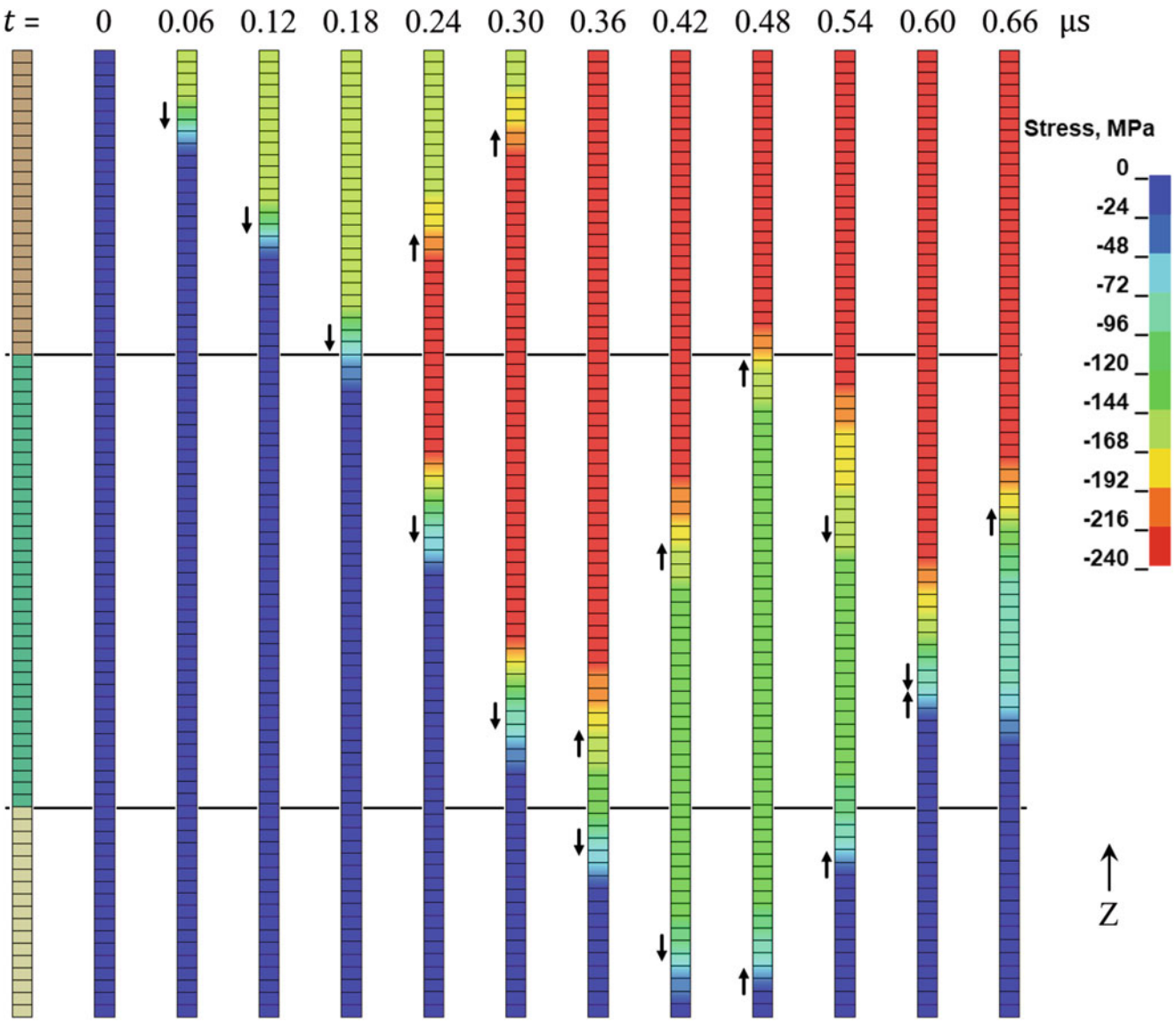


**Fig. 20.6** Elastic stress wave propagation in a 1D finite element model over time for location A

## 20.7 Conclusion

This chapter considered stress wave propagation at the earliest timescale following projectile impact on a plain weave glass/epoxy composite. First, the 1D stress wave theory was generalized for any number of layers. Then simple 1D finite element models with elastic properties were compared with the 1D theory. The 1D modeling approach was shown to provide good agreement with the theoretical model. Then a 3D model was introduced with inelastic, progressive damage material behavior and cohesive interfacial behavior. The 3D model also showed good agreement with the theoretical model. This modeling approach was validated with the 1D theory and can be used to investigate the early timescale damage evolution of plain weave composites following projectile impact.

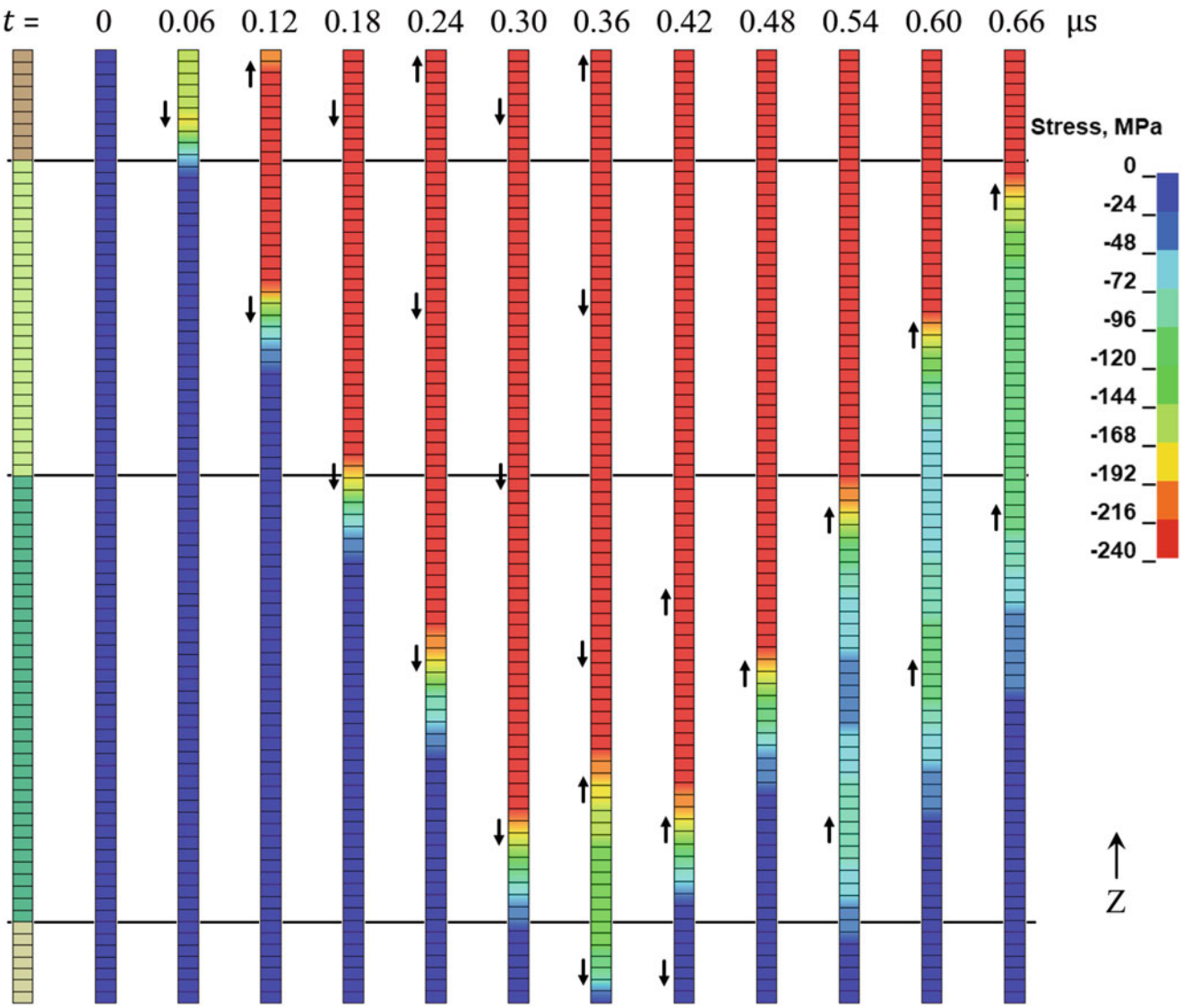


**Fig. 20.7** Elastic stress wave propagation in a 1D finite element model over time for location B

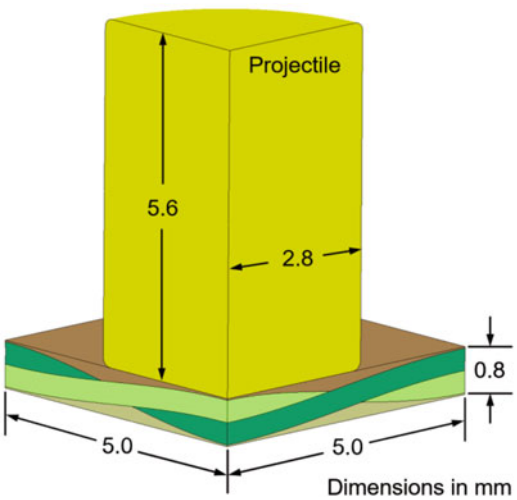


**Fig. 20.8** One-quarter symmetry, mesoscale finite element model of plain weave composite RVE impacted by a right circular cylindrical projectile

**Table 20.7** Comparison of particle velocity, $\dot{u}$, 3D FEM results to 1D theory along line A. The model uses progressive damage material behavior with node-merged or cohesive zone interfaces

| | | | | Node-merged | | Cohesive zones | |
|---|---|---|---|---|---|---|---|
| Layer | Thickness, mm | $\tau$, μs | 1D Theory $\dot{u}$ m/s | 3D FEM $\dot{u}$, m/s | Difference, % | 3D FEM $\dot{u}$, m/s | Difference, % |
| Epoxy | 0.252 | 0.18 | 96.0 | 96.1 | 0.1 | 95.9 | 0.1 |
| Composite | 0.374 | 0.32 | 51.8 | 54.7 | 5.8 | 56.3 | 8.9 |
| Epoxy | 0.174 | 0.43 | 75.6 | 79.2 | 4.8 | 80.8 | 6.9 |

**Table 20.8** Comparison of particle velocity, $\dot{u}$, 3D FEM results to 1D theory along line B. The model uses progressive damage material behavior with node-merged or cohesive zone interfaces

| | | | | Node-merged | | Cohesive zones | |
|---|---|---|---|---|---|---|---|
| Layer | Thickness, mm | $\tau$, μs | 1D Theory $\dot{u}$ m/s | 3D FEM $\dot{u}$, m/s | Difference, % | 3D FEM $\dot{u}$, m/s | Difference, % |
| Epoxy | 0.093 | 0.06 | 96.0 | 96.2 | 0.2 | 96.7 | 0.7 |
| Composite | 0.265 | 0.17 | 51.8 | 53.5 | 3.5 | 55.4 | 7.2 |
| Composite | 0.374 | 0.31 | 51.8 | 53.6 | 3.7 | 54.4 | 5.2 |
| Epoxy | 0.068 | 0.36 | 75.6 | 78.9 | 4.4 | 76.7 | 1.5 |

**Acknowledgments** The research was sponsored by the US Army Research Laboratory and was accomplished under Cooperative Agreement Number W911NF-12-2-0022. The views and conclusions contained in this document are those of the authors and should not be interpreted as representing the official policies, either expressed or implied, of the US Army Research Laboratory or the US Government.

## References

1. Meyer, C.S., Haque, B.Z.G., O'Brien, D.J., Getinet, N., Yu, J.H., Bonyi, E., Aslan, K., Gillespie Jr., J.W.: Mesoscale ballistic damage mechanisms of a single-layer woven glass/epoxy composite. Int. J. Impact Eng. **113**(August 2017), 118–131 (2018)
2. Meyer, C. S., Bonyi, E., Haque, B. Z., O'Brien, D. J., Aslan, K., Gillespie, J. W.: "Ballistic impact experiments and quantitative assessments of mesoscale damage modes in a single-layer woven composite," Conference Proceedings of the Society for Experimental Mechanics Series, **1**, 9–17 (2019)
3. Meyer, C. S., (Gama) Haque, B. Z., O'brien, D. J., & Gillespie Jr, J. W.: "Mesoscale and Continuum Models of Wave Propagation in a Woven Composite," In: *Proceedings of the American Society for Composites 34th Technical Conference* (2019)
4. Leigh Phoenix, S., Porwal, P.K.: A new membrane model for the ballistic impact response and V50 performance of multi-ply fibrous systems. Int. J. Solids Struct. **40**(24), 6723–6765 (2003)
5. Haque, B.Z., Gillespie Jr., J.W.: A combined theoretical-semiempirical penetration model of ballistic penetration of thick section composites. J. Thermoplast. Compos. Mater. **25**(5), 631–659 (2012)
6. Naik, N.K., Shrirao, P., Reddy, B.C.K.: Ballistic impact behaviour of woven fabric composites: formulation. Int. J. Impact Eng. **32**(9), 1521–1552 (2006)
7. Chocron, S., Carpenter, A.J., Scott, N.L., Bigger, R.P., Warren, K.: Impact on carbon fiber composite: ballistic tests, material tests, and computer simulations. Int. J. Impact Eng. **131**, 39–56 (2019)
8. Moon, F. C.: A critical survey of wave propagation and impact in composite materials, NASA Lewis Research Center, NASA CR-121226 (1973)
9. Meyers, M.A.: Dynamic Behavior of Materials. Wiley, New York (1994)
10. Hallquist, J.O.: LS-DYNA® Keyword User's Manual, vol. I. Livermore Software Technology Corporation, Livermore (2016)
11. Yen, C.F.: A ballistic material model for continuous-fiber reinforced composites. Int. J. Impact Eng. **46**, 11–22 (2012)
12. (Gama) Haque, B. Z.: "A progressive composite damage model for unidirectional and woven fabric composites," Materials Sciences Corporation and University of Delaware Center for Composite Materials, MAT_162 User Manual (2017)
13. Gama, B.A., Gillespie, J.W.: Finite element modeling of impact, damage evolution and penetration of thick-section composites. Int. J. Impact Eng. **38**(4), 181–197 (2011)
14. Pankow, M., Waas, A.M., Yen, C.F., Ghiorse, S.: Modeling the response, strength and degradation of 3D woven composites subjected to high rate loading. Compos. Struct. **94**(5), 1590–1604 (2012)
15. Carpenter, A.J., Chocron, S., Anderson, C.E.: Mesoscale modeling of S-2 glass/SC-15 epoxy composites: plain-weave architecture. J. Compos. Mater. **50**(5), 685–700 (2016)

# Chapter 21
# Structure of Shock Waves and Inelasticity in Shock-Compressed Cemented Tungsten Carbides

**Bingsen Wang and Vikas Prakash**

**Abstract** In the present study, shock wave experiments are conducted on General Carbide cemented tungsten carbide with 3.7 wt.% cobalt binder to determine its shock-induced compression behavior up to 100 GPa. The measured wave profiles indicate the cemented tungsten carbide undergoes elastic-plastic deformation during shock compression. A three-stage particle velocity profile is observed in the experiments – an initial elastic rise to the Hugoniot elastic limit (HEL), an elastic-plastic ramp indicating substantial post-yield hardening, and finally a rise to the peak shocked Hugoniot state. The results of the experiments are used to determine the HEL, the shock velocity ($U_s$) vs. particle velocity ($u_p$) Hugoniot relation, and the longitudinal stress ($\sigma_x$) vs. specific volume (V) curve for the samples. The HEL of the material was determined to lie between 4.41 and 4.58 GPa. The $U_s - u_p$ relation was determined to be $U_s = 4.97 + 1.457u_p$ for particle velocities greater than 0.75 km/s. The measured plastic shock velocities for particle velocities less than 0.7 km/s were found to be larger than those predicted using the linear $U_s - u_p$ Hugoniot relationship, indicating the cemented WC samples to preserve substantial shear strength in the post-yield deformation region. No phase transformation was observed up to 100 GPa.

**Keywords** Cemented tungsten carbide · Normal shock compression · Shock profiles · In-material Hugoniot quantities

## 21.1 Introduction

Cemented tungsten carbides are metal matrix composites in which a large fraction of hard tungsten carbide (WC) grains are embedded in a soft transition metal matrix, e.g., cobalt, nickel, iron, etc., commonly referred to as the binder. A compromise of high hardness and toughness is achieved by optimizing the composition of the primary constituents (i.e., WC grains and the binder) and the material microstructure. Because of their high density and hardness, these composites have been particularly attractive in applications where high-rate mechanical loading, high hardness, and high wear resistance are important. However, to date, very little fundamental information is available on their shock and impact properties in the open literature [1–3].

The primary objective of the present work is to better understand the structure of shock waves and their associated thermodynamic equilibrium states in shock-compressed cemented WC with 3.7 wt.% Co binder. The peak shocked state of interest for this study is up to 100 GPa, which is more than fifteen times the Hugoniot elastic limit (HEL) reported for WC ceramics in the literature [4]. Besides the calculation of in-material quantities in the elastic limit and the peak shocked Hugoniot states, Hugoniot relations for the cemented WC sample in terms of the shock velocity vs. particle velocity ($U_s - u_p$) and longitudinal stress vs. volume compression ($\sigma_x - V/V_o$) are determined over the stress range of interest.

## 21.2 Experimental Methods

Cemented tungsten carbide samples with 3.7 wt.% cobalt binder were obtained from General Carbide, PA. The samples were manufactured by powder metallurgy, where tungsten carbide powder is mixed with the binder metal, compacted in a die, and then sintered in a furnace. The process results in cementing the tungsten grain particles with the metallic binder, forming a strong metallurgical bond between the tungsten carbide grains and the metal binder. During sintering, the microstructure of the

B. Wang · V. Prakash (✉)
Institute for Shock Physics, Washington State University, Pullman, WA, USA
e-mail: vikas.prakash@wsu.edu



S. Mates et al. (eds.), *Dynamic Behavior of Materials, Volume 1*, Conference Proceedings of the Society for Experimental Mechanics Series, https://doi.org/10.1007/978-3-031-17453-7_21

**Table 21.1** Physical properties of General Carbide cemented WC–3.7 wt.% cobalt

| Physical properties | |
|---|---|
| Density (g/cm$^3$) | 15.17 |
| Bulk modulus (GPa) | 375.1 |
| Poisson's ratio | 0.209 |
| Longitudinal wave speed (km/s) | 6.97 |
| Shear wave speed (km/s) | 4.23 |
| Bulk wave speed (km/s) | 4.97 |

**Table 21.2** Summary of plate impact experiments conducted on the cemented WC–3.7 wt.% Co samples used in the present experiment. In all experiments, the elastic shock wave in the buffer was overdriven by the plastic shock wave

| Shot # | Driver | Impact vel. (km/s) | WC sample thickness (mm) | Impactor/ thickness (mm) | Buffer/ thickness (mm) | Window/ thickness (mm) | Peak stress (GPa) | Impact tilt (mrad) |
|---|---|---|---|---|---|---|---|---|
| 01 (103-01) | 30 mm powder gun | 1.400 | 2.588 | C101-Cu/ 1.707 | C101-Cu/ 1.072 | ⟨100⟩ LiF/ 6.389 | 42.98 | 1.12 |
| 02 (103-03R) | 30 mm powder gun | 2.667 | 2.565 | C101-Cu/ 1.710 | C1011-Cu/ 1.132 | ⟨100⟩ LiF/ 6.397 | 94.13 | 1.22 |
| 03 (103-04) | 30 mm powder gun | 1.695 | 2.566 | C101-Cu/ 1.733 | C101-Cu/ 1.115 | ⟨100⟩ LiF/ 6.384 | 53.77 | 0.73 |
| 04 (103-05) | 30 mm powder gun | 2.360 | 2.571 | C101-Cu/ 1.718 | C101-Cu/ 1.124 | ⟨100⟩ LiF/ 6.402 | 80.42 | 1.59 |
| 05 (103-06) | 30 mm powder gun | 1.994 | 2.572 | C101-Cu/ 1.743 | C101-Cu/ 1.132 | ⟨100⟩ LiF/ 6.391 | 65.78 | 1.90 |
| 06 (103-07) | 100 mm gas gun | 0.545 | 2.558 | Al-1010/ 2.336 | a-cut Sapphire/ 3.191 | ⟨100⟩ LiF/ 6.385 | 8.97 | 0.57 |
| 07 (103-08) | 100 mm gas gun | 0.909 | 2.562 | Al-1010/ 2.378 | a-cut Sapphire/ 3.191 | ⟨100⟩ LiF/ 6.389 | 15.66 | 1.12 |
| 08 (103-09) | 30 mm powder gun | 1.818 | 2.564 | Al-1010/ 2.528 | Al-1010/ 0.984 | ⟨100⟩ LiF/ 6.389 | 29.25 | 0.65 |

WC cermet samples was controlled such that the average grain size lies in a narrow band of 1–2 microns. All samples were characterized by density and sound speed measurements at ambient conditions. The physical properties of the cemented WC samples are presented in Table 21.1.

A summary of the shock experiments conducted in the present study is provided in Table 21.2. The table lists the Shot number, the driver used, impact velocity, the impactor and buffer materials, peak stress attained, and the estimated impact tilt in each experiment. A schematic of the experimental configuration is shown in Fig. 21.1. Experiments at peak stress higher than 15.66 GPa (Shots 01, 02, 03, 04, 05, and 08) were conducted using a 30 mm powder gun, while experiments at peak stress of 8.97 and 15.66 GPa (Shots 06 and 07) were conducted using the 100 mm single-stage light gas gun at the Institute for Shock Physics, Washington State University. A typical impactor and target plate assembly for the low peak stress experiments (Shots 06 and 07) comprised an Al-1050 impactor, an a-cut sapphire buffer that is bonded to the cemented WC sample, and a <100> LiF window. For the intermediate peak stress experiments (Shot 08), an Al-1050 impactor, an Al-1050 buffer bonded to the WC sample, and a LiF window were used. For the higher peak stress experiments (Shots 01–05), the impactor and the buffer materials in the intermediate peak stress configuration were replaced by C-101 copper. The use of the same impactor and buffer materials in the experiments helps to limit wave interactions due to wave reflections at the impactor/buffer interface. Prior to bonding the various target components, a thin aluminum mirror is vapor deposited onto the front surface of the LiF window, which serves as a reflector for laser interferometry (VISAR-Velocity Interferometer System for Any Reflector) measurements [5–7]. In all experiments, the VISAR measurements used a dual velocity-per-fringe configuration to unambiguously determine the peak particle velocity [8]. The central VISAR probe, shown by the red arrow in Fig. 21.1, provides the shock wave transit times through the sample along with the particle velocity profiles at the WC sample/window interface. The three (outer) radial VISAR probes (Fig. 21.1 – black arrows), focused on the back of the polished buffer at 120°

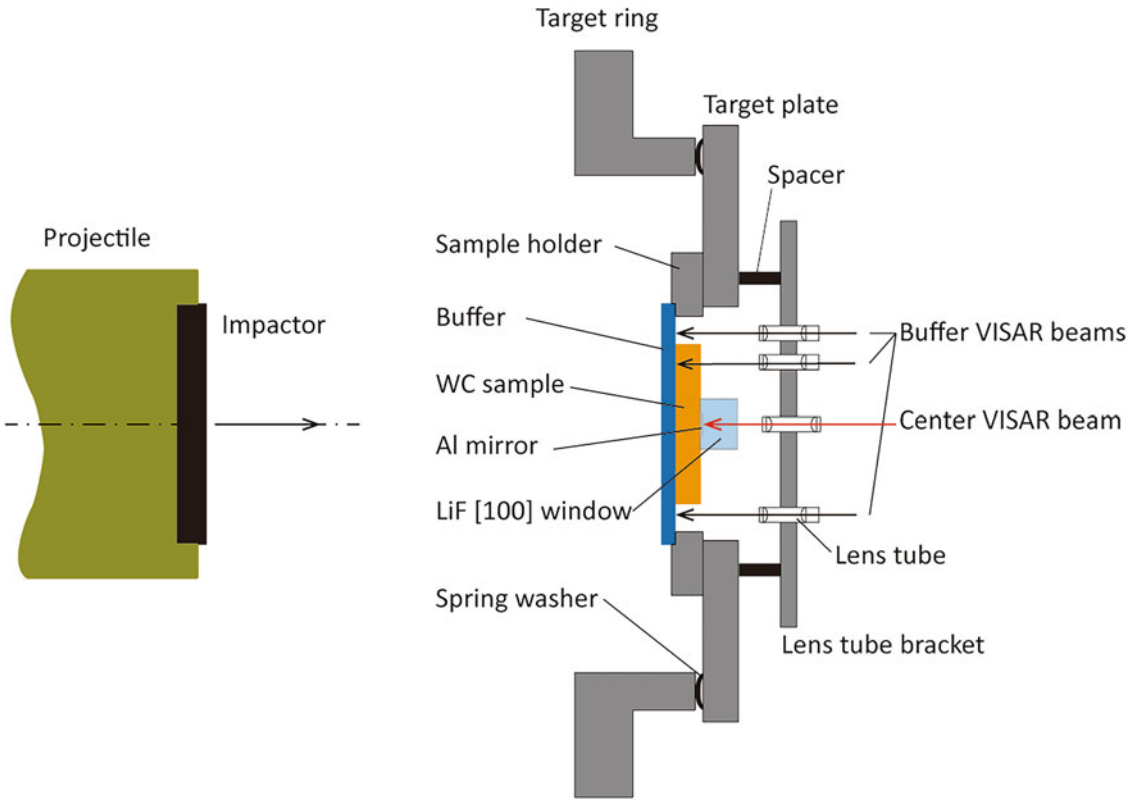


**Fig. 21.1** Schematic of the experimental configuration used in the present experiments

intervals, allow determination of the shock arrival times at the sample/buffer interface and the impact tilt in the experiments. The maximum impact tilt in the experiments was estimated to be 1.9 mrad.

## 21.3 Wave Propagation in the Flyer and Target Assembly: Lagrangian Time – Distance Diagram

For the high peak stress experiments, the copper (buffer) − WC (sample) − LiF (window) target assemblies were impacted with copper impactors, launched using a light powder gun. Upon impact, a single overdriven shock wave propagates into the copper buffer and impactor. The forward propagating shock in the buffer interacts with the buffer/sample interface, resulting in both elastic and plastic shock waves propagating through the WC sample and a reflected re-shock wave travelling backward into the buffer. Due to the impedance contrast between the sample and the window, the propagating elastic and plastic waves in the WC sample undergo further transmission and reflection at the WC sample/window interface. The shock wave in the impactor eventually reaches its back surface and reflects from it as a rarefaction wave. The corresponding Lagrangian time vs. distance diagram is shown in Fig. 21.2.

For the low and intermediate peak stress experiments, the copper impactor is replaced by Al-1010 while the buffer is replaced by either a-cut sapphire (Shots 06 and 07) or Al-1010 (Shot 08). For the impact configuration used in Shots 06 and 07, a two-wave structure is developed in the impactor while only a single elastic shock wave is generated in the a-cut sapphire, which loads the sample.

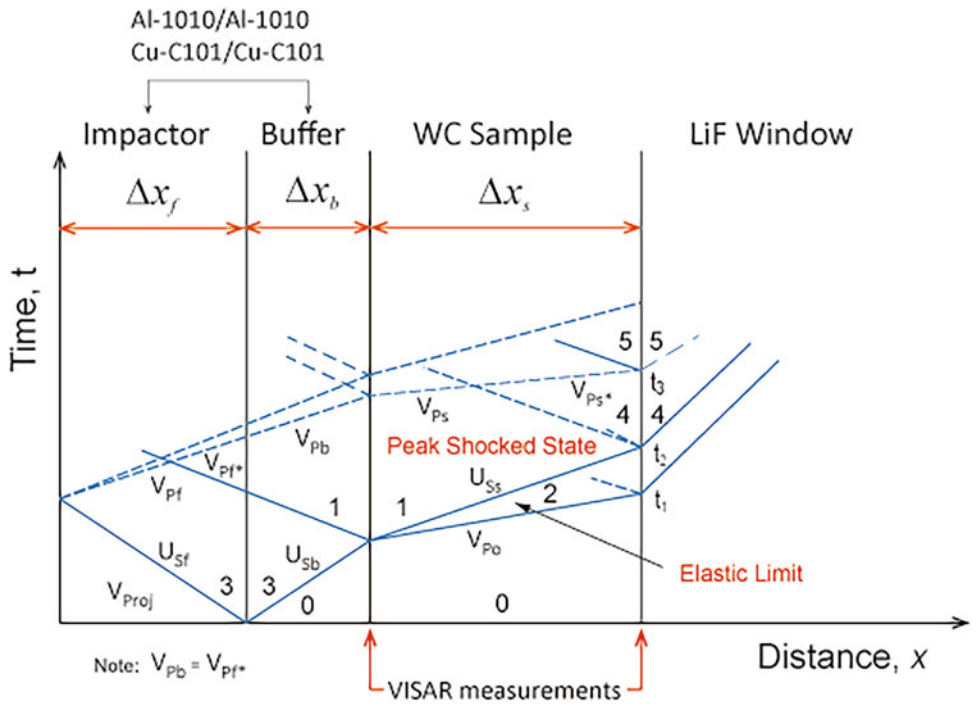


**Fig. 21.2** Lagrangian distance-time diagram for the high-impact experiments conducted in the present study. $U_s$ is shock velocity, $V_P$ is the compressional sound velocity and $V_{Po}$ is the elastic precursor velocity and $t_1$, $t_2$ and $t_3$ are wave arrival times at the sample-window interface. The subscripts *f*, *b*, and *s* refer to the flyer, buffer, and sample, respectively

## 21.4 Experimental Results

Eight normal shock compression plate impact experiments were conducted on the cemented tungsten carbide samples in the present study. These experiments were designed to impart peak stress levels in the range of 8.97–94.13 GPa in the shocked state. The experimental parameters relevant to these eight experiments are summarized in Table 21.2. The intermediate and high Hugoniot (peak) stress plate impact experiments were conducted using a 30 mm bore powder gun, while the low peak stress experiments were conducted using the 100 mm single-stage gas-gun facility at the Institute for Shock Physics, Washington State University. For the low peak stress experiments, a-axis sapphire (HEL ~ 18 GPa) was used as the buffer with Al-1050 as the impactor, while for the intermediate and high peak stress experiments, either Al-1050 or OFE Cu plates were employed as both impactor and buffer plates. In all experiments, a <100> LiF window is used behind the WC sample. Projectile velocities were chosen such that the elastic wave in the buffer is overdriven and a single shock wave is incident at the buffer/WC sample interface, resulting in a constant peak stress state in the WC samples.

Figure 21.3 shows the wave profiles measured at the sample/window interface using VISAR interferometry. In all experiments, a two-wave structure comprising an elastic precursor and a trailing plastic wave is observed. The elastic precursor amplitude (HEL) is nearly constant (within the experimental scatter) at all impact velocities [9]. No yield drop (stress relaxation) immediately behind the elastic wave front is observed in the particle velocity profiles. Beyond the HEL, the longitudinal stress rises continuously to the peak stress state, with the rate of increase in stress being higher for larger stress in the peak state. The quantitative measurements of primary interest to this work are the particle velocity at the sample/window interface at the elastic limit (corresponding to the Hugoniot elastic limit) and the peak stress state, from which the in-material Hugoniot properties can be calculated [10–12].

## 21.5 Analysis

Figure 21.4 shows the longitudinal stress vs. particle velocity diagram for a typical experiment conducted using a copper impactor and copper buffer combination in the present study. A two-wave structure is considered in the analysis of the Hugoniot states in the WC samples – elastic limit behind the leading elastic precursor and a peak shocked state behind the

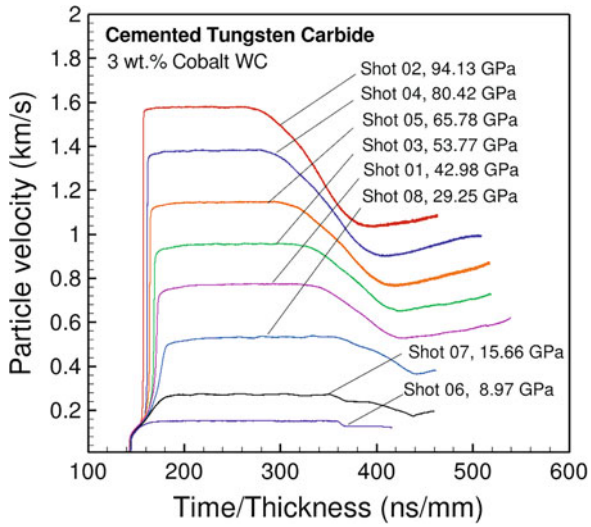


**Fig. 21.3** Measured particle velocity profiles at the WC/LiF window for WC samples shocked up to 100 GPa. Time is normalized with the sample thickness

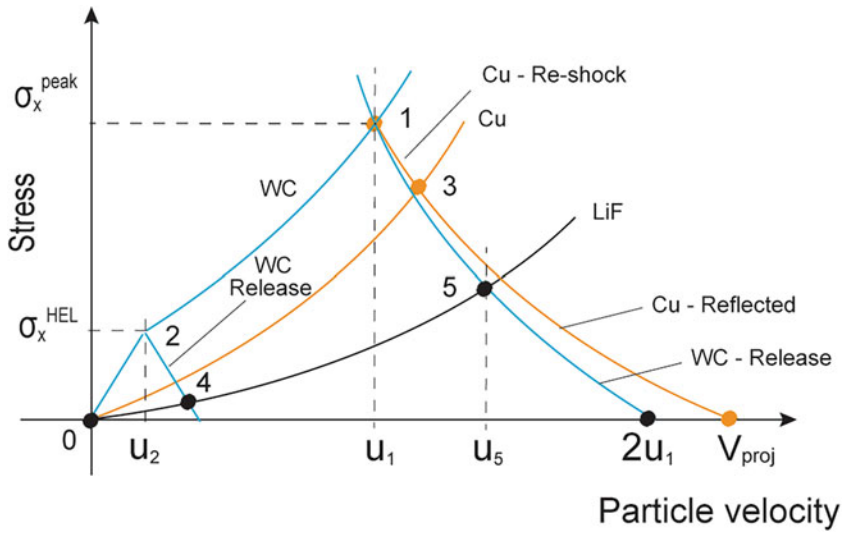


**Fig. 21.4** Stress vs. particle velocity diagram showing the various Hugoniot shock and release states achieved in the WC sample, the impactor, and the buffer plates in a typical shock experiment

**Table 21.3** Hugoniot $U_s - u_p$ relationship for the impactor, buffer, and window materials used in the present study

| Material | $U_s - u_p$ Hugoniot |
|---|---|
| Cu-C101 | $U_s = 3.97 + 1.479\ u_p$ |
| Al-1050 | $U_s = 5.35 + 1.32\ u_p$ |
| a-cut sapphire | $U_s = 11.213 + 0.97\ u_p$ |
| LiF <100> | $U_s = 5.215 + 1.351\ u_p$ |

trailing plastic shock wave. The objective of the analysis is to calculate the in-material Hugoniot quantities of interest (i.e., longitudinal stress, particle velocity, elastic shock wave speed, and density compression) in the elastic limit (State 2) and the peak shocked state (State 1) using impedance matching procedures and the Rankine-Hugoniot jump conditions. The principal Hugoniot ($U_s - u_p$) relations for the impactor, the buffer, and the window used in the calculations are summarized in Table 21.3.

To facilitate the calculation of the in-material quantities at the elastic limit and peak stress state, the cemented WC samples were idealized as rate-independent, elastic, and perfectly plastic materials; accordingly, the measured particle velocity profiles were idealized as a two-step function. Because of this assumption, the time dependence of material behavior on the structure of the shock waves was not considered in the present analysis.

**For $\sigma_x \le \sigma_x^{HEL}$**

Since the material ahead of the elastic precursor in the WC samples is stationary, the Eulerian elastic shock wave speed in the sample, $D_{0\,\to\,2}$, is the same as the Lagrangian (measured) elastic shock wave speed $D^L_{0\to 2} = \Delta x_s/(t_1 - t_0)$, where $\Delta x_s$ represents the un-deformed thickness of the WC sample and $(t_1 - t_{0)}$ is the transit time of the elastic shock wave in the sample.

Using the $\sigma - u$ Hugoniot relationship connecting States 0 and 2 in WC, gives

$$\sigma_{x2}^{HEL} = \rho_0^{WC}\, D_{0\to 2} u_2 = \rho_0^{WC} D^L_{0\to 2} u_2 \tag{21.1}$$

where $\sigma_{x2}^{HEL}$ is the peak stress at the elastic limit, $\rho_0^{WC}$ is the (ambient) density of the WC sample in State 0, and $u_2$ is the particle velocity in State 2.

The longitudinal stress in the shocked WC after release at the WC/LiF interface (State 4) gives

$$\sigma_{x4} = \rho_0^{WC} D^L_{0\to 2}(2u_2 - u_4) \tag{21.2}$$

In Eq. (21.2), $\sigma_{x4}$ and $u_4$ are the longitudinal stress and particle velocity states in State 4 at the WC/LiF window interface.

Moreover, principal Hugoniot for shocked LiF connecting State 0 to 4 gives

$$\sigma_{x4} = \rho_0^{LiF}\left(A^{LiF} + B^{LiF}\, u_4\right) u_4 \tag{21.3}$$

where $\rho_0^{LiF}$ is the ambient density of LiF in State 0, and $A^{LiF}$and $B^{LiF}$ are the known $U_s - u_p$ Hugoniot parameters for LiF.

Conservation of mass for shocked WC from State 0 to State 2 gives

$$\rho_0^{WC}\, D_{0\to 2} = \rho_2^{WC}(D_{0\to 2} - u_2) \tag{21.4}$$

Using Eqs. (21.1) to (21.4) along with the measured particle velocity at the WC/LiF window interface, the longitudinal stress at the elastic limit $\sigma_{x2}^{HEL}$, material density $\rho_2^{WC}$, and the particle velocity $u_2$, can be calculated.

**For $\sigma_x > \sigma_x^{HEL}$**

The Lagrangian plastic shock wave speed in the shocked WC, $D^L_{2\to 1}$, can be expressed as

$$D^L_{2\to 1} = \frac{\Delta x_s}{(t_2 - t_0)} \tag{21.5}$$

where $(t_2 - t_{0)}$ is the transit time of the plastic shock wave in the shocked sample.

Accordingly, the Eulerian plastic shock wave speed connecting the elastic limit (State 2) to the peak shocked state (State 1) in the WC samples, i.e., $D_{2\,\to\,1}$, can be written as

$$D_{2\to 1} = u_2 + \frac{\rho_0^{WC}}{\rho_2^{WC}}\, D^L_{2\to 1} \tag{21.6}$$

Using the $\sigma - u$ Hugoniot relationship for shocked WC, the longitudinal stress $\sigma_{x1}$ in the peak stress state can be expressed in terms of the measured plastic shock wave speed $D^L_{2\to 1}$ and the particle velocity $u_1$, as

$$\sigma_{x1} - \sigma_{x2}^{HEL} = \rho_2^{WC}(\, D_{2\to 1} - u_2\,)(u_1 - u_2) = \rho_0^{WC} D^L_{2\to 1}(u_1 - u_2) \tag{21.7}$$

To calculate the particle velocity $u_1$ in the peak stress state (State1), consider the plastic release of the shocked WC from State 1 to State 5 (at the LIF/WC window interface) using the reflected Hugoniot from State 1. Using the principal Hugoniot for shocked LiF connecting States 0 to 5, the longitudinal stress at the WC/LiF interface can be expressed as

$$\sigma_{x5} = \rho_0^{WC} D^L_{2\to 1}(2u_1 - u_5) = \rho_0^{LiF}\left(A^{LiF} + B^{LiF} u_5\right) u_5 \tag{21.8}$$

Also, considering the elastic release of WC from State 1 to State 5, the stress at the WC/LiF window interface can be expressed as

$$\sigma_{x5} = \rho_0^{WC} D^L_{2\to 1}(u_1 - u_2) + \sigma_{x2}^{HEL} - \rho_0^{WC} D^L_{0\to 2}(u_5 - u_1) = \rho_0^{LiF}\left(A^{LiF} + B^{LiF} u_5\right) u_5 \tag{21.9}$$

Then, the particle velocity $u_1$ at the peak stress state (State 1) is then taken to be the average of the two values calculated using Eqs. (21.8) and (21.9). Knowing $u_1$, the peak stress in State 1 can be calculated.

**Table 21.4** In-material quantities in shocked cemented WC samples at the elastic limit and the peak stress state calculated using impedance matching procedures and the measured particle velocity at the WC/LiF window interface. Note $D_{0\rightarrow 2}$ and $D^{L}_{2\rightarrow 1}$ are the measured elastic and plastic shock wave speeds, respectively, and $D_{2\rightarrow 1}$ is the Eulerian plastic wave speed

| | | Wave speeds | | | Elastic limit | | | Peak shocked state | | |
|---|---|---|---|---|---|---|---|---|---|---|
| Shot # | Impact vel. (km/s) | $D_{0\rightarrow 2}$ (km/s) | $D_{2\rightarrow 1}$ (km/s) | $D^{L}_{2\rightarrow 1}$ (km/s) | Stress (GPa) | Density (GPa) | Particle vel. (km/s) | Stress (GPa) | Density (GPa) | Particle vel. (km/s) |
| 01 (103–01) | 1.40 | 6.9862 | 5.8659 | 5.8590 | 4.5804 | 15.2545 | 0.0433 | 42.9788 | 16.4222 | 0.4756 |
| 02 (103-03R) | 2.667 | 6.9338 | 6.3671 | 6.3635 | 4.6222 | 15.2972 | 0.0440 | 94.1319 | 17.9350 | 0.9716 |
| 03 (103–04) | 1.695 | 6.9712 | 5.9537 | 5.9476 | 4.4057 | 15.2310 | 0.0417 | 53.7652 | 16.7833 | 0.5892 |
| 04 (103–05) | 2.360 | 6.8962 | 6.1904 | 6.1816 | 4.4506 | 15.2642 | 0.0426 | 80.4193 | 17.5809 | 0.8524 |
| 05 (103–06) | 1.994 | 6.9788 | 6.0906 | 6.0850 | 4.6108 | 15.2553 | 0.0436 | 65.7804 | 17.1343 | 0.7067 |
| 06 (103–07) | 0.545 | 6.9000 | 6.5880 | 6.5860 | 4.6212 | 15.2877 | 0.0441 | 8.9681 | 15.3899 | 0.0875 |
| 07 (103–08) | 0.909 | 6.8988 | 6.1466 | 6.1419 | 4.5028 | 15.2952 | 0.0429 | 15.6624 | 15.6008 | 0.1625 |
| 08 (103–09) | 1.818 | 6.9446 | 5.8463 | 5.8391 | 4.5454 | 15.2655 | 0.0433 | 29.2480 | 16.0507 | 0.3247 |

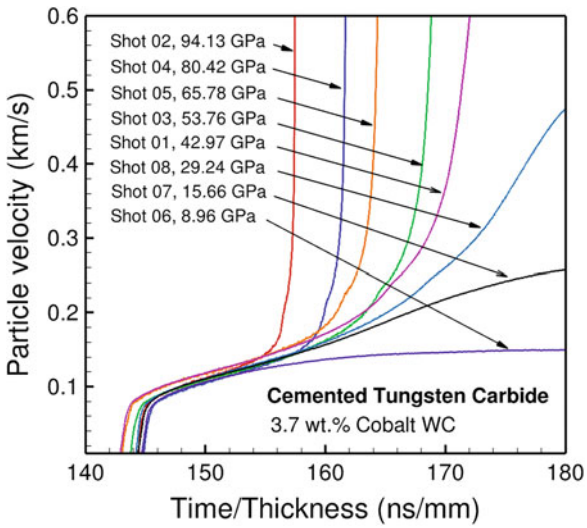


**Fig. 21.5** Precursor characteristics of General Carbide cemented WC with 3.7 wt.% cobalt binder

Also, conservation of mass in the shocked WC between States 1 and 2, gives

$$\rho_2^{WC}(D_{2\rightarrow 1}-u_2)=\rho_1^{WC}(D_{2\rightarrow 1}-u_1) \tag{21.10}$$

Using Eqs. (21.5) to (21.10) and the measured particle velocity at the WC/LiF window interface, the longitudinal stress, $\sigma_{x1}$, material density, $\rho_1^{WC}$, and the particle velocity, $u_1$, can be calculated in the peak stress state in the WC samples.

The calculated in-material quantities at both the elastic limit and the peak stress state in the cemented WC samples are summarized in Table 21.4.

## 21.6 Results and Discussion

Details of the measured particle velocity profiles immediately following the elastic precursor and preceding the attainment of the final peak stress state for all experiments in the present study, are shown in Fig. 21.5. The wave profiles show a diffused change in slope in the particle velocity profiles in the stress range from 4.41 to 4.581 GPa. This change in slope is identified as the HEL for the WC cermet used in the present investigation. The average stress at HEL is calculated to be 4.52 GPa. Since the precision for measurements of particle and free surface velocity is 1–2%, the statistical uncertainty associated with the average value of the HEL is likely to arise from the variability in the material microstructure.

Following the elastic precursor, a distinct ramp in the measured particle velocity is observed in all experiments. This ramp in particle velocity is followed by a relatively sharp increase in particle velocity at ca. 0.165 km/s. This sudden change in particle velocity following the ramp occurs at ca. 7 GPa, which is approximately equal to the HEL of pure WC ceramics.

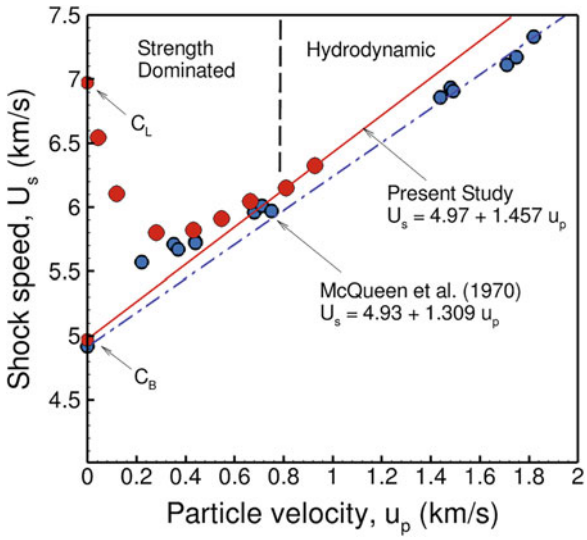


**Fig. 21.6** Shock speed vs. particle velocity Hugoniot relation for cemented WC–3.7 wt.% cobalt (present work) and WC–5 wt.% cobalt. (McQueen et al. [15])

Similar features in the measured particle velocity profiles immediately following the HEL in shocked cemented WCs with cobalt and nickel binders were noted by Grady [13] and Appleby-Thomas [14], where they attributed the initial break-in particle velocity to the elastic limit of the cemented WC and the second sharper break (rise) in particle velocity to the elastic limit of the WC grains comprising the material microstructure. The shock waves following the second break-in particle velocity travel in the shocked cemented WC samples with velocities in the range of 5.839 km/s and 6.586 km/s. These Eulerian shock velocities are much higher than the bulk sound wave speed in the cemented WC at ambient conditions, i.e., 4.97 km/s, suggesting the role of pressure and the associated density compression in the shocked cemented WC samples.

The shock speed vs. particle velocity relation for cermet WC–3.7 wt.% Co binder is shown in Fig. 21.6 together with the ultrasonic wave speed data and the results of shock wave experiments by McQueen et al. [15] on WC–5 wt.% Co binder. The measured elastic shock wave speeds in the cemented WC samples used in the present study were consistent with the zero-pressure longitudinal sound velocity obtained from ultrasonic measurements, as shown in Table 21.4. In the plastic region, the shock velocities were much larger compared with the bulk sound velocity and for those less than 0.75 km/s particle velocity were larger than those predicted by the linear Hugoniot relation – indicating that the samples preserve a high shear strength in the post-HEL plastic region.

The $U_s - u_p$ curve for cemented WC–3.7 wt.% cobalt was obtained by following an approach similar to the one used in the work by McQueen et al. [15] on cemented WC–5% cobalt binder. The density of the samples used by McQueen et al. was 15.01 g/cm$^3$. The longitudinal and shear wave velocities were reported to be 6.89 km/s and 4.18 km/s, respectively. The calculated bulk sound wave speed and Poisson's ratio were 4.92 km/s and 0.209, respectively. These values are not very different from the measured values of sound speeds in the WC–3.7 wt.% cobalt samples used in the present study. Careful examination of the experimental data in Fig. 21.5 and considering that hydrodynamic equilibrium in the shocked cemented WC samples is not attained until a longitudinal stress of ca. 75 GPa yields the following linear relation between the shock velocity ($U_s$) and the particle velocity ($u_p$) for particle velocities greater than 0.75 km/s

$$U_s = 4.97 + 1.457\ u_p \tag{21.10}$$

In determining this equilibrium $U_s - u_p$ Hugoniot relation, the intercept of the Hugoniot fit is forced to coincide with the bulk sound speed obtained from the measured longitudinal and shear wave speeds; the slope of the $U_s$ - $u_p$ relation is determined by the high-stress data alone.

The experimental Hugoniot-compression data for General Carbide cemented WC–3.7 wt.% Co used in the present study, WC–5 wt.% Co used by McQueen et al., and Cercom pure WC ceramic used in the work by Dandekar and Grady [4] are shown along with their calculated hydrodynamic-compression curves in Fig. 21.7. The hydrodynamic compression curves were calculated using the bulk modulus of 375.1 GPa with s = 1.42 (present work) and bulk modulus of 363.33 GPa with s = 1.309 for the case of WC samples used by McQueen et al. [15] and by Dandekar and Grady [4]. The Hugoniot data from the present work and from McQueen et al. fall on their respective hydrodynamic-compression curves for longitudinal stresses greater than ca. 75 GPa, while data from Dandekar et al. for the WC ceramic samples show retention of substantial shear strength when shocked to stresses ca. 80 GPa.

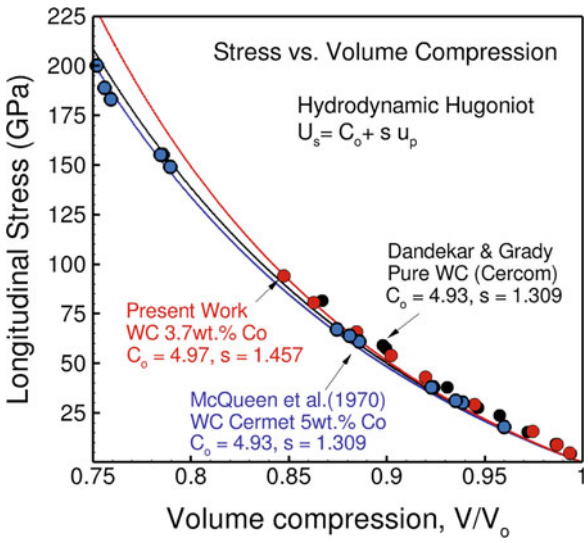


**Fig. 21.7** Longitudinal stress versus volume compression curves for cemented WC–3.7 wt.% cobalt (present work), WC–5 wt.% cobalt. (McQueen et al. [15]) and pure WC ceramic (Dandekar and Grady [4])

## 21.7 Conclusion

In the present study, shock wave experiments are conducted on General Carbide cemented tungsten carbide with a 3 wt.% cobalt binder to determine its shock-induced compression behavior up to ca.100 GPa. The measured wave profiles indicate the cermet will undergo elastic-plastic deformation during its shock compression. A three-stage particle velocity profile is observed in the experiments – an initial elastic rise to the (HEL), an elastic-plastic ramp indicating substantial post-yield hardening, and finally a rise to the peak shocked Hugoniot state. The results of the experiments are used to determine the Hugoniot elastic limit (HEL), and the shock velocity ($U_s$) vs. particle velocity ($u_p$), and longitudinal stress ($\sigma_x$) vs. volume (V) Hugoniot relations for the cermet. The HEL of the material was determined to lie between 4.41 and 4.58 GPa. The $U_s - u_p$ relation was determined to be $U_s = 4.97 + 1.457u_p$ for particle velocities greater than 0.75 km/s. The measured shock velocities for shocks with particle velocities less than 0.7 km/s were larger than those predicted using the linear $U_s - u_p$ Hugoniot relationship, indicating the WC cermet samples preserve substantial shear strength in the post-yield deformation region. No phase transformation was observed up to 100 GPa.

**Acknowledgments** The authors would like to thank Kurt Zimmerman, Yoshi Toyoda, and Nate Arganbright for their assistance in conducting the experiments. This work was supported by the US Department of Energy/National Nuclear Security Administration (Cooperative Agreement No. DE-NA0003957).

## References

1. Zuanetti, B., Wang, T., Prakash, V.: Plate impact investigation of the dynamic response of commercial tungsten carbide under shock-induced compression and combined compression-and-shear loading. Int. J. Impact Eng. **131**, 200–208 (2019)
2. Gooch, W.A., Burkins, M.S., Palicka, R.: Ballistic development of U.S. high density tungsten carbide ceramics. J. Phys. **IV**(10), 741–746 (2000)
3. Kettenbeil, C., Lovinger, Z., Jiao, T., Mello, M., Clifton, R.J., Ravichandran, G.: Inelastic behavior of tungsten carbide at high pressures. J. Mech. Phys. Solids. **159**, 104762 (2022)
4. Dandekar, D.P., Grady, D.E.: Shock equation of state and dynamic strength of tungsten carbide. In: *AIP conference proceedings*, vol. 620, pp. 783–786. American Institute of Physics (2002)
5. Barker, L.M., Hollenbach, R.E.: Laser interferometer for measuring high-velocities of any reflecting surfaces. J. Appl. Phys. **43**(11), 4669–4675 (1972)
6. Zuanetti, B., Wang, T., Prakash, V.: A compact fiber-optics based heterodyne combined normal and transverse displacement interferometer. Rev. Sci. Instrum. **88**, 033108 (2017)
7. Yuan, F., Prakash, V.: Plate impact experiments to investigate shock-induced inelasticity in westerly granite. Int. J. Rock Mech. Min. Sci. **60**, 277–287 (2013)
8. Dolan, D.H.: SAND2006–1950: Foundations of VISAR Analysis. Sandial National Laboratory, Alburquerque, NM (2006)
9. Zuanetti, B., McGrane, S.D., Bolme, C.A., Prakash, V.: Measurement of elastic precursor decay in pre-heated aluminum films under ultra-fast laser generated shocks. J. Appl. Phys. **123**(19), 195104 (2018)

10. Oniyama, T., Gupta, Y.M., Ravichandran, G.: Shock compression of molybdenum single crystals to 110 GPa: elastic-plastic deformation and crystal anisotropy. J. Appl. Phys. **127**(20), 205902 (2020)
11. Mandal, A., Gupta, Y.M.: Elastic-plastic deformation of molybdenum single crystals shocked along [100]. J. Appl. Phys. **121**(4), 045903 (2017)
12. Sunny, G., Yuan, F., Prakash, V., Lewandowski, J.J.: Effect of high strain rates on peak stress in a Zr-based bulk metallic glass. J. Appl. Phys. **104**, 093522 (2008)
13. Grady, D.: Impact failure and fragmentation properties of tungsten carbide. Int. J. Impact Eng. **23**, 307–317 (1999)
14. Appleby-Thomas, G.J., Hazell, P.J., Stennett, C., Cooper, G., Helaar, K., Diederen, A.M.: Shock propagation in a cemented tungsten carbide. J. Appl. Phys. **105**(6), 064916 (2009)
15. McQueen, R.G., Marsh, S.P., Taylor, J.W., Fritz, J.N., Carter, W.J.: Chapter VII: the equation of state of solids from shock wave studies. In: Kinslow, R. (ed.) High-Velocity Impact Phenomena, pp. 293–417. Academic Press, New Yok (1970)